ATOMIC AND PLASMA-MATERIAL INTERACTION DATA FOR FUSION

VOLUME 10

INTERNATIONAL ATOMIC ENERGY AGENCY, VIENNA, 2002

The volumes of ATOMIC AND PLASMA-MATERIAL INTERACTION DATA FOR FUSION are published by the International Atomic Energy normally once a year.

For these volumes, papers, letters and reviews are accepted which deal with the following topics:

- Elementary collision processes in fusion plasmas involving photons, electrons, ions, atoms and molecules;
- Collision processes of plasma particles with surfaces of fusion relevant materials;
- Plasma-material interaction phenomena, including the thermophysical response of materials.

Each submitted contribution should contain fusion relevant data and information in either of the above areas. Original contributions should provide new data, using well established methods. Review articles should give a critical analysis or evaluation of a wider range of data. They are normally prepared on the invitation by the Editor or on prior mutual consent. Each submitted contribution is assessed by two independent referees.

Every manuscript submitted must be accompanied by a *disclaimer* stating that the paper has not been published and is not being considered for publication elsewhere. If no copyright is claimed by the authors, the IAEA automatically owns the copyright of the paper.

Guidelines for the preparation of manuscripts are given on the inside back cover. Manuscripts and correspondence should be addressed to: The Editor, ATOMIC AND PLASMA-MATERIAL INTERACTION DATA FOR FUSION, International Atomic Energy Agency, Wagramer Strasse 5, P.O. Box 100, A-1400 Vienna, Austria.

Publisher: International Atomic Energy Agency, Wagramer Strasse 5, P.O. Box 100, A-1400 Vienna, Austria

Editor: R.E.H. Clark, Atomic and Molecular Data Unit, Division of Physical and Chemical Sciences

---

ATOMIC AND PLASMA-MATERIAL INTERACTION DATA FOR FUSION, VOLUME 10
IAEA, VIENNA, 2002
STI/PUB/023/APID/10

FOREWORD

Charge exchange (or charge transfer, or electron capture) processes between generic plasma ions (protons) and plasma impurity ions on one side, and neutral plasma constituents (such as H and impurity atoms and molecules) on the other play an important role in the physics of edge and divertor plasmas of toroidal fusion devices. These processes change the charge states of the ion and the neutral particle, and that has important consequences for the transport of both the ions and neutral particles in a magnetized plasma. If the ion is multiply charged (such as He^{2+}, or some impurity ion A^{q+}, $q > 1$), more than one target electron can be captured by the ion, or the electron capture can be accompanied by a simultaneous ejection of another target electron in the continuum (transfer-ionization). If the neutral target particle is a molecule, the electron capture process may be accompanied by dissociation of the molecular ion produced in the charge transfer process (dissociative charge transfer). All these processes take place in the plasma edge of toroidal fusion devices (tokamaks, stellarators) and in their divertors, where the plasma temperature is sufficiently low (~ 1-100 eV) to support the existence of neutral particles (including molecules).

Aside from their obvious impact on the neutral particle and impurity transport in the edge and divertor plasmas, the charge exchange processes also play an important role in the attenuation kinetics of neutral atomic beams (H, He, Li) injected into the plasma for heating or diagnostic purposes. Even in the hot core plasma region, the charge exchange processes of plasma protons or fusion alpha particles with incompletely stripped impurity ions are of greatest importance for the production of energetic neutrals (and alpha particle escape from the core plasma region).

When the ionic charge is greater than 2–3, the captured electron populates excited levels of the product $A^{(q-1)+}$ ions, which then decay by radiation. The emitted radiation from the excited charge exchange ionic products provides a unique tool for determining the radial distribution of impurities in a plasma, and is the basis for the presently widely used charge exchange recombination spectroscopy in all toroidal fusion devices.

The present volume of Atomic and Plasma-Material Interaction Data for Fusion represents the result of a co-ordinated effort of 12 leading experimental and theoretical groups within the IAEA Co-ordinated Research Project (CRP) on Charge Exchange Cross Section Data for Fusion Plasma Studies. The contributions of the participants of this CRP, contained in the present volume, significantly enlarge the cross-section information on charge exchange processes taking place in different regions of fusion plasmas. This information is an important ingredient in many modeling and diagnostic studies of fusion plasmas.

The IAEA is taking this opportunity to acknowledge the CRP participants for their dedicated effort and contribution to this volume.

EDITORIAL NOTE

This publication has been prepared from the original material as submitted by the authors. The views expressed do not necessarily reflect those of the IAEA, the governments of the nominating Member States or the nominating organizations.

The use of particular designations of countries or territories does not imply any judgement by the publisher, the IAEA, as to the legal status of such countries or territories, of their authorities and institutions or of the delimitation of their boundaries.

The mention of names of specific companies or products (whether or not indicated as registered) does not imply any intention to infringe proprietary rights, nor should it be construed as an endorsement or recommendation on the part of the IAEA.

The authors are responsible for having obtained the necessary permission for the IAEA to reproduce, translate or use material from sources already protected by copyrights.

CONTENTS

Recommended partial cross sections for electron capture in $C^{6+} + H(1s)$ collisions

J. Caillat[1,2], A. Dubois[1], J.P. Hansen[2]

[1)] Laboratoire de Chimie Physique — Matière et Rayonnement, UMR 7614 du CNRS — Université Pierre et Marie Curie, Paris, France

[2)] Institute of Physics, University of Bergen, Bergen, Norway

Abstract. We report $n\ell$-selective capture cross sections for the C^{6+}– $H(1s)$ collision system at low and intermediate impact energies. The present converged results take into account important trajectory effects for $C^{5+}(n = 5)$ capture channels and allow for the extension of the analytical fits proposed by Janev *et al.* in *At. Data Nucl. Data Tables* **55** 201 in the 0.1 – 60 keV amu^{-1}energy range.

An important limitation to the heating of fusion plasmas arises from the presence of non-negligible impurity ions in the medium [1, 2]. Among others, plasma modeling and diagnostics require the knowledge of accurate cross sections of electron transfer from atomic hydrogen to fully stripped carbon and oxygen ions. For both systems Janev *et al.* [2] proposed analytical fits of capture cross sections based on reliable theoretical and experimental data, when available in the 0.1 – 1000 keV amu^{-1} impact energy range.

Since the seventies, the C^{6+}– $H(1s)$ collision system has been widely studied which makes it a benchmark system for atomic collisions involving highly charged ions [3]. The two main capture channels are the C^{5+} $(n = 4)$ and C^{5+} $(n = 5)$ manifolds,

$$C^{6+} + H(1s) \rightarrow C^{5+}(4\ell) + H^{+}$$

$$C^{6+} + H(1s) \rightarrow C^{5+}(5\ell) + H^{+}$$

For the dominant C^{5+} $(n = 4)$ capture cross sections, experimental data and theoretical predictions were found to be in good agreement and the fits covered the entire energy domain of interest, cf. figure 1. However, severe discrepancies were reported for electron capture to the $C^{5+}(n = 5)$ shell at low impact energies (0.1 – 10 keV amu^{-1}). These disagreements, as well as the lack of data for minor channels, prevented Janev *et al.* to extend their fits to the low energy range [2].

We have recently reported new results for that system [4, 5] with special emphasize in the low energy range where the above mentioned discrepancies were observed. By a detailed analysis of the mechanisms responsible for the capture processes and of the inter nuclear trajectory effects [4], we have proposed a set of cross sections reliable in this range. These data are reported in the present paper.

We use a non-perturbative semi-classical approach, within the straight-line inter nuclear trajectory approximation. The electron wave function is expanded on a set of target- and projectile-centered atomic orbitals. The projectile orbitals are furthermore

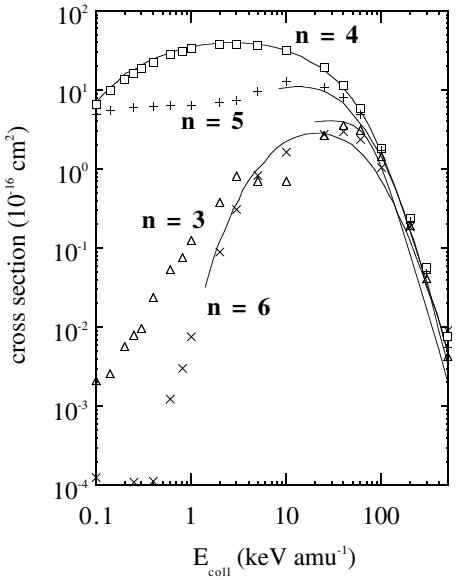

FIG. 1. Electron capture cross sections from H(1s) to C^{5+}(n=3–6). Our results: △, n=3; □, n=4; +, n=5; ×, n=6. Recommended data [2]: ___, n=3–6.

modified with Electron Translational Factors in order to take into account the relative motion of the two atomic centers. Inserting this expansion in the time-dependent Schrödinger equation leads to a set of coupled differential equations for the coefficients c. These coupled equations are solved numerically for given impact energies E_{coll} and a well chosen set of trajectories, characterized by the impact parameter b. From the expansion coefficients after collision the probabilities and cross sections for transition from initial atomic state i to final atomic states f can be evaluated, respectively

$$P_{i\to f}\left(E_{coll},b\right)=\left|c_f\left(t\to\infty,E_{coll},b\right)\right|^2 \tag{1}$$

$$\sigma_{i\to f}\left(E_{coll}\right)=2\pi\int_0^\infty b\;db\,P_{i\to f}\left(E_{coll},b\right) \tag{2}$$

However, for $C^{5+}(n=5)$ capture, the small impact parameter range (b $\leq$ 4 a.u.) is very dominant in the integration of eq. 2, and trajectory effects due to the strong repulsive interaction between the collision partners in the final channel were found very important [4]. To take into account the departure from straight-line trajectory, we have performed Classical Trajectory Monte Carlo (CTMC) [9] calculations to obtain realistic deflection functions. The trajectory effects were then introduced in the semi-classical results by replacing the impact parameter b in $P_{i\to f}\left(E_{coll},b\right)$ (eq. 2) by an averaged closest approach distance evaluated from the CTMC results [4].

Table 1. Electron transfer cross sections (in 10^{-16} cm^2) from H($1s$) to $C^{5+}(n\ell)$, n = 3–6 at low collision energies E_{coll} (in keV amu^{-1}). For transfer to $C^{5+}(5\ell)$ the trajectory modified cross sections are shown by "$\rightarrow$" and pure straight-line results are reported underneath in smaller font

E_{coll}	0.05	0.0625	0.1	0.14	0.2*	0.25	0.3*	0.4	0.6	0.81*
$3s$	1.88^{-6}	2.32^{-6}	1.46^{-5}	5.06^{-5}	2.30^{-5}	2.13^{-5}	1.85^{-5}	1.37^{-5}	4.12^{-4}	7.28^{-4}
$3p$	3.00^{-6}	7.83^{-6}	2.91^{-5}	2.13^{-5}	2.99^{-5}	4.49^{-5}	4.74^{-5}	3.92^{-5}	2.67^{-4}	1.21^{-3}
$3d$	5.93^{-6}	5.08^{-6}	8.23^{-5}	1.24^{-5}	3.58^{-5}	4.41^{-5}	6.30^{-6}	6.00^{-5}	5.61^{-4}	1.09^{-3}
n=3	1.08^{-5}	1.52^{-5}	1.26^{-4}	8.42^{-5}	8.88^{-5}	1.10^{-4}	7.22^{-5}	1.13^{-4}	1.24^{-3}	3.02^{-3}
$4s$	3.70^{-1}	3.72^{-1}	4.90^{-1}	6.48^{-1}	8.94^{-1}	1.05^{+0}	1.34^{+0}	1.61^{+0}	2.12^{+0}	2.07^{+0}
$4p$	8.38^{-1}	9.51^{-1}	1.46^{+0}	1.97^{+0}	2.79^{+0}	3.30^{+0}	4.01^{+0}	4.69^{+0}	6.42^{+0}	7.23^{+0}
$4d$	9.95^{-1}	1.15^{+0}	1.87^{+0}	2.22^{+0}	3.01^{+0}	3.93^{+0}	4.91^{+0}	7.06^{+0}	9.49^{+0}	1.12^{+1}
$4f$	1.13^{+0}	1.43^{+0}	2.67^{+0}	5.06^{+0}	7.07^{+0}	7.93^{+0}	8.42^{+0}	9.29^{+0}	1.00^{+1}	1.07^{+1}
n=4	3.34^{+0}	3.90^{+0}	6.49^{+0}	9.90^{+0}	1.38^{+1}	1.62^{+1}	1.87^{+1}	2.26^{+1}	2.80^{+1}	3.13^{+1}
$5s \rightarrow$	1.83^{-1}	1.87^{-1}	5.46^{-1}	5.79^{-1}	5.59^{-1}	3.15^{-1}	2.55^{-1}	3.34^{-1}	6.58^{-1}	7.51^{-1}
	5.44^{-1}	4.39^{-1}	8.53^{-1}	7.83^{-1}	6.81^{-1}	3.66^{-1}	2.88^{-1}	3.64^{-1}	6.89^{-1}	7.71^{-1}
$5p \rightarrow$	1.98^{-1}	3.75^{-1}	5.16^{-1}	8.76^{-1}	1.12^{+0}	1.09^{+0}	8.36^{-1}	6.78^{-1}	1.29^{+0}	1.59^{+0}
	5.89^{-1}	8.78^{-1}	8.06^{-1}	1.19^{+0}	1.37^{+0}	1.26^{+0}	9.45^{-1}	7.39^{-1}	1.35^{+0}	1.63^{+0}
$5d \rightarrow$	3.26^{-1}	5.68^{-1}	5.05^{-1}	6.72^{-1}	1.17^{+0}	1.12^{+0}	1.12^{+0}	1.45^{+0}	1.77^{+0}	1.83^{+0}
	9.71^{-1}	1.33^{+0}	7.89^{-1}	9.10^{-1}	1.43^{+0}	1.30^{+0}	1.27^{+0}	1.59^{+0}	1.85^{+0}	1.88^{+0}
$5f \rightarrow$	8.67^{-1}	1.12^{+0}	1.68^{+0}	1.26^{+0}	1.32^{+0}	1.69^{+0}	2.09^{+0}	2.28^{+0}	1.74^{+0}	1.51^{+0}
	2.58^{+0}	2.62^{+0}	2.63^{+0}	1.70^{+0}	1.61^{+0}	1.97^{+0}	2.36^{+0}	2.49^{+0}	1.82^{+0}	1.55^{+0}
$5g \rightarrow$	9.65^{-1}	1.10^{+0}	1.69^{+0}	2.08^{+0}	1.64^{+0}	1.78^{+0}	1.79^{+0}	1.45^{+0}	8.77^{-1}	6.96^{-1}
	2.87^{+0}	2.57^{+0}	2.64^{+0}	2.81^{+0}	2.00^{+0}	2.07^{+0}	2.02^{+0}	1.59^{+0}	9.17^{-1}	7.15^{-1}
n=5 $\rightarrow$	2.54^{+0}	3.35^{+0}	4.94^{+0}	5.46^{+0}	5.82^{+0}	6.00^{+0}	6.09^{+0}	6.21^{+0}	6.34^{+0}	6.37^{+0}
	7.55^{+0}	7.84^{+0}	7.72^{+0}	7.39^{+0}	7.10^{+0}	6.97^{+0}	6.89^{+0}	6.77^{+0}	6.64^{+0}	6.54^{+0}
$6s$	6.03^{-5}	1.13^{-5}	4.91^{-5}	1.22^{-4}	5.71^{-4}	1.04^{-3}	8.54^{-4}	1.32^{-3}	3.14^{-3}	4.74^{-3}
$6p$	7.77^{-5}	1.71^{-5}	9.23^{-5}	3.51^{-4}	1.07^{-3}	1.03^{-3}	2.65^{-3}	3.06^{-3}	8.01^{-3}	1.21^{-2}
$6d$	2.03^{-4}	3.81^{-5}	1.79^{-4}	2.77^{-4}	6.03^{-4}	2.16^{-3}	2.01^{-3}	4.32^{-3}	1.31^{-2}	1.20^{-2}
$6f$	2.33^{-4}	1.13^{-4}	3.50^{-4}	3.99^{-4}	8.52^{-4}	1.31^{-3}	1.43^{-3}	5.91^{-3}	1.48^{-2}	2.16^{-2}
$6g$	4.26^{-4}	1.93^{-4}	5.41^{-4}	5.08^{-4}	1.01^{-3}	1.23^{-3}	1.58^{-3}	5.56^{-3}	9.62^{-3}	1.65^{-2}
$6h$	6.58^{-4}	2.52^{-4}	8.93^{-4}	9.33^{-4}	1.60^{-3}	1.22^{-3}	1.18^{-3}	3.61^{-3}	4.73^{-3}	9.19^{-3}
n=6	1.66^{-3}	6.24^{-4}	2.10^{-3}	2.59^{-3}	5.70^{-3}	8.00^{-3}	9.70^{-3}	2.38^{-2}	5.34^{-2}	7.62^{-2}

The basis set used in the calculations consists of the H($1s$) initial state and of all the states spanning the $C^{5+}(n = 1 - 6)$ shells. This basis set does not include hydrogen excitation and ionisation channels so that it is not expected to give very accurate cross sections above 60 keV amu^{-1}[7]. Indeed Figure 1 shows that the capture cross sections are slightly overestimated (typically 50% at 200 keV amu^{-1}) in our model compared to the recommended data [2]. However in the low energy range the basis set is adequate and describes correctly the $(CH)^{6+}$ molecular curves and the important avoided crossings [4]. Our results are in excellent agreement with recent molecular-orbital calculations of Harel *et al.* [6]: for example at 0.3 keV amu^{-1}, differences between the two data sets are less than 5% for the important channels and below 50% for the minor $C^{5+}(n = 3)$ and $C^{5+}(n = 6)$ channels.

The $n\ell$-partial and n-partial ($n = 1-6$) capture cross sections are reported in table for 10 impact energies from .05 keV amu^{-1} to .81 keV amu^{-1} and in table for 10 impact energies from 1 keV amu^{-1} to 200 keV amu^{-1}. As concluded in [4] for electron

Table 2. Electron transfer cross sections (in 10^{-16} cm^2) from H($1s$) to $C^{5+}(n\ell)$, $n = 3$–6 at medium collision energies E_{coll} (in keV amu^{-1})

E_{coll}	1.0	2.0	3.0	5.0	10.0	25.0	40.0	60.0	100.	200.
$3s$	1.07^{-3}	1.40^{-2}	7.23^{-2}	2.34^{-1}	3.32^{-1}	3.58^{-1}	3.52^{-1}	1.06^{-1}	5.09^{-2}	1.29^{-2}
$3p$	4.05^{-3}	4.66^{-2}	1.45^{-1}	3.94^{-1}	7.54^{-1}	1.07^{+0}	1.16^{+0}	8.98^{-1}	1.99^{-1}	1.82^{-2}
$3d$	2.47^{-3}	2.88^{-2}	9.07^{-2}	2.03^{-1}	5.56^{-1}	1.31^{+0}	1.48^{+0}	1.37^{+0}	7.97^{-1}	1.56^{-1}
n=3	7.60^{-3}	8.94^{-2}	3.08^{-1}	8.31^{-1}	1.64^{+0}	2.74^{+0}	2.99^{+0}	2.38^{+0}	1.05^{+0}	1.87^{-1}
$4s$	3.13^{+0}	2.40^{+0}	2.52^{+0}	1.80^{+0}	1.04^{+0}	3.99^{-1}	1.56^{-1}	9.54^{-2}	6.88^{-2}	1.15^{-2}
$4p$	8.21^{+0}	9.03^{+0}	8.54^{+0}	7.31^{+0}	4.22^{+0}	1.66^{+0}	1.04^{+0}	5.96^{-1}	1.27^{-1}	1.69^{-2}
$4d$	1.15^{+1}	1.37^{+1}	1.36^{+1}	1.39^{+1}	1.06^{+1}	5.44^{+0}	2.16^{+0}	8.62^{-1}	4.43^{-1}	1.10^{-1}
$4f$	1.11^{+1}	1.29^{+1}	1.28^{+1}	1.31^{+1}	1.55^{+1}	1.20^{+1}	8.15^{+0}	4.26^{+0}	1.18^{+0}	9.91^{-2}
n=4	3.40^{+1}	3.80^{+1}	3.74^{+1}	3.61^{+1}	3.13^{+1}	1.95^{+1}	1.15^{+1}	5.82^{+0}	1.81^{+0}	2.37^{-1}
$5s$	6.98^{-1}	2.60^{-1}	2.26^{-1}	1.81^{-1}	1.54^{-1}	1.30^{-1}	8.05^{-2}	1.02^{-1}	6.51^{-2}	9.80^{-3}
$5p$	1.55^{+0}	7.21^{-1}	6.26^{-1}	6.16^{-1}	6.58^{-1}	5.51^{-1}	5.53^{-1}	3.31^{-1}	9.17^{-2}	1.42^{-2}
$5d$	1.79^{+0}	1.20^{+0}	1.04^{+0}	1.29^{+0}	1.53^{+0}	1.36^{+0}	7.75^{-1}	5.64^{-1}	3.36^{-1}	8.08^{-2}
$5f$	1.60^{+0}	2.46^{+0}	2.17^{+0}	2.72^{+0}	3.17^{+0}	2.61^{+0}	2.36^{+0}	1.76^{+0}	7.26^{-1}	8.50^{-2}
$5g$	7.89^{-1}	2.39^{+0}	3.41^{+0}	4.79^{+0}	7.27^{+0}	5.98^{+0}	4.26^{+0}	2.10^{+0}	4.93^{-1}	2.69^{-2}
n=5	6.42^{+0}	7.03^{+0}	7.47^{+0}	9.61^{+0}	1.28^{+1}	1.06^{+1}	8.04^{+0}	4.86^{+0}	1.71^{+0}	2.17^{-1}
$6s$	4.46^{-3}	1.60^{-2}	3.20^{-2}	1.65^{-2}	2.21^{-2}	4.22^{-2}	5.64^{-2}	8.76^{-2}	6.09^{-2}	9.19^{-3}
$6p$	2.16^{-2}	4.60^{-2}	9.25^{-2}	5.30^{-2}	5.15^{-2}	1.88^{-1}	2.51^{-1}	2.16^{-1}	8.89^{-2}	1.25^{-2}
$6d$	3.41^{-2}	9.44^{-2}	1.28^{-1}	8.64^{-2}	1.11^{-1}	3.33^{-1}	3.40^{-1}	3.81^{-1}	2.65^{-1}	6.34^{-2}
$6f$	2.66^{-2}	4.72^{-2}	2.19^{-1}	8.65^{-2}	1.42^{-1}	5.52^{-1}	8.67^{-1}	9.16^{-1}	5.04^{-1}	7.15^{-2}
$6g$	2.31^{-2}	5.29^{-2}	2.24^{-1}	2.67^{-1}	1.44^{-1}	7.46^{-1}	1.18^{+0}	1.01^{+0}	3.89^{-1}	3.10^{-2}
$6h$	1.56^{-2}	1.23^{-1}	1.23^{-1}	2.00^{-1}	2.35^{-1}	7.94^{-1}	8.84^{-1}	5.20^{-1}	1.24^{-1}	5.15^{-3}
n=6	1.25^{-1}	3.80^{-1}	8.19^{-1}	7.09^{-1}	7.06^{-1}	2.66^{+0}	3.58^{+0}	3.13^{+0}	1.43^{+0}	1.93^{-1}

capture to $C^{5+}(n\ell)$ we recommend the use of the trajectory modified cross sections, in good agreement with the data of Green *et al.* [8] (for information pure impact-parameter results are also reported in smaller font).

Trajectory effects were interpolated from figure 4 in [4] for 3 impact energies (.2, .3 and .81 keV amu^{-1}) marked by "*" in table (CTMC predictions not available). These effects were considered identical for the different ℓ states in the $C^{5+}(n = 5)$ shell. Note finally that trajectory effects are not significant for all other channels ($C^{5+}(n = 3, 4, 6)$) compared to the uncertainty of the data. Thus trajectory-modified cross sections are not reported in these cases.

Part of the computations have been performed at Institut du Développement et des Ressources en Informatiques Scientifiques (IDRIS). We acknowledge also the support of the Bergen Training Center for Theoretical and Computational Physics, EU contract: HPMT-CT-2000-00154.

REFERENCES

[1] FONCK, R.J,, DARROW, D.S., JAEHNIG, K.P. (1984) *Phys. Rev. A* **29** 3288.

[2] JANEV, R.K., PHANEUF, R.A., TAWARA, H., SHIRAI, T. (1993) *At. Data Nucl. Data Tables* **55** 201.

[3] FRITSCH, W., LIN, C.D. (1991) *Phys. Rep.* **202** 44.

[4] CAILLAT, J., DUBOIS, A., HANSEN, J.P. (2000) *J. Phys. B: At. Mol. Opt. Phys.* **33** L715.

[5] CAILLAT, J., DUBOIS, A., HANSEN, J.P., 2000 in press *Proc. IVth European Workshop on Quantum Systems in Chemistry and Physics* (Dordrecht, The Nederlands: Kluwer Academic Publishers).

[6] HAREL, C., JOUIN, H., PONS, B. (1998) *At. Data Nucl. Data Tables* **68** 279.

[7] TOSHIMA, N. (1994) *Phys. Rev. A* **50** 3940.

[8] GREEN, T.A., SHIPSEY, E.J., BROWN, J.C. (1982) *Phys. Rev. A* **25** 1364.

[9] OLSON, R.E., SCHULTZ, D.R., 1989 *Phys. Scr.* T **28** 71.

Cross-sections for electron capture by multiply charged ions from hydrogen atoms and molecules and population of electronic states of created ions

M.N. Panov, V.V. Afrosimov, A.A. Basalaev
A.F. Ioffe Physical-Technical Institute,
St. Petersburg, Russian Federation

Abstract. The cross-sections for single electron capture by alpha-particles and multiply charged ions Ne^{3+}, Ne^{4+}, Ar^{4+}, Ar^{5+}, Ar^{6+} from hydrogen atoms and molecules have been measured using registration of coincidences between incident and recoil ions after collision to separate this process [1]. Population of different electronic states of ions with lower charges produced at single electron capture has been measured by collision spectroscopy method [1]. Cross-sections for one electron capture by He^{2+}, Ar^{Z+} (Z = 6, 5, 4) and Ne^{Z+} (Z = 3–4) have been measured in the kinetic energy range of incident multiply charged ions from 1×Z to 12×Z keV (Z is charge of multiply charged ions). Cross-sections for the population of electronic states at electron capture from H_2 molecules have been measured in the velocity range from V = $1{\cdot}10^7$ cm/s to V= $5{,}5{\cdot}10^7$ cm/s (in the collision energy range 3.0×Z Kev - 21.0×Z KeV) at collisions of Ar^{Z+} ions (Z= 3–6) and Ne^{Z+} (Z= 3– 4). The double electron capture cross-sections at incident alpha-particles and hydrogen molecules collision have been measured in the energy range from 1 KeV up to 100 KeV ($V = 0,235 \div 2,58{\cdot}10^8$ cm/s). Errors of measured values of cross-sections are $\sim$10–15% The results of the measurements are presented below in Tables 1–8.

1. Introduction

The purpose of experimental measurements is to check and to enrich the available data on the processes of Single-Electron Capture (SEC) by alpha-particles and multiply charged ions from hydrogen molecules and atoms.

The experiment includes state selective measurements of absolute values of cross-sections of reaction product formation in collisions of hydrogen atoms and molecules with alpha particles (product of thermonuclear reaction) and with multiply charged ions of Ar and Ne as possible artificial impurities added to cool outer edge of thermonuclear plasma [2].

The data concerning ionization of hydrogen molecules by alpha-particles are needed also for estimation of potentialities of method of determination of magnetic field direction and current density distribution over tokamak plasma column cross section (q-factor) using hydrogen molecule diagnostic beams [3].

2. Experimental method

For the measurements of cross-sections of the processes of particle charge and electronic state change in collisions the well known method of collision spectroscopy has been used.

The initial ion beam is passed through a gas target. On the first step of the experiment slow recoil ions formed in the target gas were extracted by an electric field and

analyzed in mass and charge by a magnetic analyzer and registered in current mode. At this stage of the experiment the absolute cross-sections of production of recoil ions with definite charge have been measured. In the next stage, fast particles were analyzed after interaction in scattering angle with resolution of a few angular minutes and in kinetic energy by electrostatic analyzer with a resolution about 4000. Both recoil and scattered particles with definite charge states formed in one binary ion-atom collision were registered in counting mode and selected by a time delayed coincidence circuit to separate certain process of charge state change. Registration efficiency of detectors of fast particles with different charges was defined experimentally. The initial multiply charged ion beam had energy spread about 0,4 eV×Z.

The hydrogen atom target was provided by the use of a high temperature tungsten gas cell. Absolute values of hydrogen atom density and degree of dissociation of molecular hydrogen in the cell was ascertained using comparison of temperature dependencies of double electron capture efficiency in heated hydrogen and rare gas target when an alpha-particle beam passed through the gas cell [4]. Population of final electron states in one electron capture by multiply charged projectile ions was determined by collision spectroscopy, i.e. by precise analysis of kinetic energy of projectiles after collision.

Thus, this device allowed us to measure absolute values of cross-sections of elementary processes of charge state change as well as population of electronic states of ions with lower charge formed in the processes of one or two electron capture.

3. Results

TABLE 1. POPULATION OF ELECTRONIC STATES OF He^+(nl) IONS IN He^{2+} – H(1s) COLLISIONS (ERRORS OF MEASURED VALUES OF CROSS-SECTION ARE ±15%)

V	σ(n,l)		σ_{total}
	n=2	n=3	
(10^7 cm/s)	(10^{-16} cm^2)		(10^{-16} cm^2)
5,13	3,88	–	3,88
6,16	4,97	0,19	5,16
7,56	5,86	0,342	6,20
9,21	8,35	0,540	8,89
10,6	11,3	0,716	12,0
12,3	11,1	0,765	11,9
15,3	–	–	11,75
13,9	9,85	0,947	10,8

TABLE 2. POPULATION OF ELECTRONIC STATES OF Ar^{3+*} IONS IN Ar^{4+} ($3s^2$ $3p^2$) – H(1s) COLLISIONS (ERROR OF MEASURED VALUES OF CROSS-SECTION ARE ±15%)

V (10^7 cm/s)	σ (10^{-16} cm^2)				σ_{tot} (10^{-16} cm^2)
	$3s^23p^24p$	$3s^23p^24s$	$3s^23p^23d$	$3s3p^4$	
0,982	6,28	-	-	-	6,28
1,39	17,9	-	-	-	17,9
1,96	30,2	2,59	-	-	32,8
2,41	36,6	6,20	1,42	-	44,2
2,91	31,7	12,2	2,59	-	46,5
3,40	23,9	8,52	1,98	1,03	35,4
4,21	22,5	10,6	4,66	1,24	38,9
4,79	17,1	12,5	5,9	2,47	38,0

TABLE 3. POPULATION OF ELECTRONIC STATES OF Ar^{4+}($3s^23pnl$) IONS IN Ar^{5+}($3s^23p$) – H(1s) COLLISIONS (ERROR OF MEASURED VALUES OF CROSS-SECTION ARE ±15%)

V (10^7 cm/s)	σ_{nl} (10^{-16} cm^2)							σ_{tot} (10^{-16} cm^2)
	4f	4d	4p	4s	3d	$5s+4f$ $+5p$	$5s+4f$ $+5p$ $+4d+4p$	
1,55	3,27	33,4	6,58	-	-	35,2	41,5	43,2
2,20	5,55	30,8	8,29	-	-	35,9	44,1	44,6
2,69	5,74	31,0	10,3	-	-	34,6	44,3	47,0
3,26	3,29	25,7	11,3	0,86	-	31,0	43,0	41,1
3,80	-	-	11,6	14,3	0,49	16,8	28,4	-
4,71	-	-	12,6	12,5	1,33	7,73	23,6	32,4
5,35	-	-	-	17,2	7,78	-	18,0	45,6
1,10	-	-	-	-	-	-	36,9	36,9

TABLE 4. POPULATION OF ELECTRONIC STATES OF $Ar^{5+}(3s^2nl)$ IONS IN $Ar^{6+}(3s^2)$ – H(1s) COLLISIONS (ERROR OF MEASURED VALUES OF CROSS-SECTION ARE ±15%)

V (10^7 cm/s)	σ_{nl} (10^{-16} cm^2)					
	5d	5s	4f	4d	4p	4s
0,80	22,10	2,24	1,00	-	-	-
1,20	5,01	12,90	-	-	-	-
1,65	1,00	18,41	6,80	2,29	-	-
2,40	-	22,65	11,40	7,41	-	-
2,95	-	25.10	15,50	8,13	0,98	-
3,50	-	25,70	15,40	10,50	-	-
4,20	-	24,55	12,60	12,90	2,45	-
5,00	-	-	-	-	6,31	1,23
5,90	-	-	-	-	5,37	3,85

TABLE 5. POPULATION OF ELECTRONIC STATES OF $Ne^{3+}(2s^22p^2nl)$ IONS IN $Ne^{4+}(2s^22p^2)$ – H(1s) COLLISIONS (ERROR OF MEASURED VALUES OF CROSS-SECTION ARE ±15%)

V (10^7 cm/s)	σ_{nl} (10^{-16} cm^2)			σ_{tot} (10^{-16} cm^2)
	3d	3p	3s	
1,96	-	-	-	18,9
2,78	26,8	4,70	-	31,5
3,40	24,0	4,02	-	28,0
4,19	23,6	5,20	-	28,8
4,79	27,1	6,0	0,674	33,8
5,96	20,0	10,4	2,46	32,8
6,74	12,7	14,5	4,00	31,2

TABLE 6. POPULATION OF ELECTRONIC STATES OF $Ne^{2+}(2s^22p^3nl)$ IONS IN $Ne^{3+}(2s^22p^3)$ – H(1s) COLLISIONS (ERROR OF MEASURED VALUES OF CROSS-SECTION ARE ±15%)

V (10^7 cm/s)	σ_{nl} (10^{-16} cm^2)		σ_{tot} (10^{-16} cm^2)
	3p	3s	
1,70	14,6	1,79	16,4
2,41	23,2	8,14	31,3
2,95	17,2	8,48	25,7
3,63	23,2	18,4	41,6
4,13	22,7	17,5	40,2
5,16	20,1	17,4	37,5
5,84	16,1	19,4	35,4

TABLE 7. THE DOUBLE ELECTRON CAPTURE CROSS-SECTION – $He^{2+} + H_2$ – $He^0(1s^2) + H^+ + H^+$ (ERROR OF MEASURED VALUES OF CROSS-SECTION ARE ±10%)

V (10^8) cm/s	0,235	0,33	0,41	0,50	0,58	0,71	0,81	1,00	1,15
σ (10−17 cm^2)	1,15	4,98	6,08	4,33	2,98	2,01	1,59	1,71	2,28
V (10^8 cm/s)	1,63	1,41	1,63	1,83	2,00	2,16	2,31	2,45	2,58
σ (10^{-17} cm^2)	2,69	3,20	4,15	4,71	5,09	5,41	5,34	5,86	5,72

The population of electronic states of neutral helium atoms formed in double electron capture (DEC) processes can not be determined by standard collision spectroscopy method because sufficiently precise analysis of kinetic energy of neutral particles cannot be provided. Therefore we can suppose only that at velocity about $5{\cdot}10^7$ cm/s (the position of low energy maximum of cross-section as function of velocity) helium atoms are created in excited 1snl states. During population of these electronic states of helium atoms the process of double electron capture has the lowest energy defect and maximum double electron capture cross section corresponds to small values of collision velocities. One can suppose that the high energy peak at velocities of alpha-particles more than $3{\cdot}10^8$ cm/s corresponds to production of helium atoms in ground states.

TABLE 8. POPULATION OF VARIOUS EXCITED STATES OF IONS FORMED IN ONE ELECTRON CAPTURE PROCESSES

$He^{2+} + H_2 \rightarrow He^{+}(nl)$

V (10^7 cm/s)	σ_{nl} (10^{-16} cm^2)	
	$\sigma(1s)$	$\sigma(2l)$
4.43	2.2	0.06
6.26	1.95	0.56
8.08	1.45	1.92
9.90	1.30	3.45
11.4	1.25	5.0
12.8	1.30	6.35
14.0	1.35	8.0
16.2	1.45	10
18.0	1.55	11
19.8	1.65	11.2

$Ne^{4+} + H_2 \rightarrow Ne^{3+}(nl)$

V (10^7 cm/s)	σ_{nl} (10^{-16} cm^2)			σ_{tot} (10^{-16} cm^2)
	$\sigma(3d)$	$\sigma(3p)$	$\sigma(3s)$	
1.96	19.9	8.6	-	29.1
2.78	16.6	12.8	0.59	30.0
3.40	15.7	16.4	0.99	-
3.49	-	-	-	34.2
4.19	14.6	18.5	1.47	35.2
4.79	17.3	15.7	2.02	-
5.96	16.2	16.6	1.82	35.3
6.74	13.9	19.9	4.38	38.8

$Ar^{4+} + H_2 \rightarrow Ar^{3+}(nl)$

V (10^7 cm/s)	σ_{nl} (10^{-16} cm^2)			σ_{tot} (10^{-16} cm^2)
	$\sigma(4p)$	$\sigma(4s)$	$\sigma(3d) + \sigma(3s3p^4)$	
0.982	13.1	10.2	-	26.3
1.39	11	18.3	2.48	34.8
1.96	9.91	21.2	3.49	37.6
2.41	7.04	23.8	5.66	39.5
2.91	5.05	23.4	8.65	40.1
3.4	5.63	21.8	8.57	39.0
4.21	4.32	19.8	8.88	36.0

$Ar^{5+} + H_2 \rightarrow Ar^{4+}(nl)$

V (10^7 cm/s)	σ_{nl} (10^{-16} cm^2)				$\sigma(T.I.)$ (10^{-16} cm^2)	σ_{tot} (10^{-16} cm^2)
	$\sigma(4d)$	$\sigma(4p)$	$\sigma(4s)$	$\sigma(3d)$		
1.10	9.24	13.5	-	-	5.46	28.2
1.55	7.48	21.4	-	-	3.67	32.5
2.20	6.86	24.3	-	-	4.24	-
2.69	7.26	24.4	-	-	5.65	37.3
3.26	6.72	24.8	2.38	-	-	38.3
3.80	6.98	22.5	5.02	-	-	-
4.71	8.14	10.9	11.6	4.21	-	39.3
5.35	-	-	17.0	7.20	-	38.6

$Ar^{6+} + H_2^0 \rightarrow Ar^{5+}(nl)$

V (10^7 cm/s)	σ_{nl} (10^{-16} cm^2)				
	$\sigma(5p)$	$\sigma(5s)$	$\sigma(4f)$	$\sigma(4d)$	$\sigma(4p) + \sigma(4s) + \sigma(3d)$
1.2	2.16	16.6	12.3	6.84	-
1.7	1.91	12.8	12.6	16.8	-
2.41	1.82	8.02	11.9	20.5	0.81
2.95	2.07	3.58	14.3	18.5	2.9
3.57	-	-	-	25.1	5.8
4.17	-	-	-	22.6	7.1

4. CONCLUSIONS

We have obtained SEC, DEC cross-sections which may be used for modelling of processes involving alpha-particles in fusion plasma, processes in divertors of CTR devices and for the development and use of particle and spectroscopic methods of plasms diagnostic.

ACKNOWLEDGEMENTS

The work was supported by International Atomic Energy Agency, CRM Research Contract # RUS–10088 and by RFBR (project 99–02–17970).

REFERENCES

[1] AFROSIMOV, V.V., BASALAEV, A.A., PANOV, M.N., SAMOILOV, A.V., JETP **91** (1986) 465 (Sov. Phys. JETP **64** (1987) 273).
[2] ITER Physics Expert Group on Divertor Modelling and Database, Nuclear Fusion **39**, N 12 (1999) 2391.
[3] AFANAS'EV, V.I., KISLYAKOV, A.I., et al., English Transl. – JETP Letters **50** (1989) 453.
[4] AFROSIMOV, V.V., BASALAEV, A.A., DONETZ, E.D., ZINOV'EV, A.N., LOZHKIN, K.O., PANOV, M.N., English Transl. – JETP Letters **37** (1983) 21.

Extension of model potential methods to treat charge transfer in open shell systems. Application to the Si^{3+}/He, He^{2+}/He (2^1S) and He^{2+}/He (2^3S) systems

D. Rabli, R. McCarroll
Laboratoire de Dynamique des Ions, Atoms et Molécules (ESA 7066 du CNRS),
Université Pierre et Marie Curie, Paris, France

M. Gargaud
Observatoire de l'Université de Bordeaux I (UMR 5804 du CNRS), Floirac, France

Abstract
Charge transfer reactions in ion-atom collisions are investigated theoretically for systems involving open-shell configurations. Both model potential and *ab-initio* methods are used to treat the adiabatic states of the collision complex. A quantum mechanical treatment of the collison dynamics is used. Electron capture cross sections for two representative systems (He^{2+} in collsion with either 2^1S or 2^3S metastable He and for Si^{3+} with ground state He) are calculated in the eV-keV energy range.

1. Introduction

Model potential methods have proved very successful in the theoretical treatment of the dynamics of charge transfer by multiply charged ions A^{q+} from atomic H targets. Experiments show that these methods are excellent not only for closed shell ions such as C^{4+}, N^{5+}, O^{6+}, Al^{3+}, $Si^{4+}$and Ar^{8+}[1-6] but also for closed sub-shells such as N^{3+}, $Si^{2+}$and Ar^{6+} [7,8]. Basically, the reason is that charge transfer occurs at relatively large internuclear distances, primarily by electron capture into excited Rydberg states of $A^{(q-1)+}$. As a consequence, the ionic core A^{q+} plays a passive role and its effect can often be adequately described by an effective (or model) potential. This greatly simplifies the computation of the network of adiabatic molecular potentials (and non-adiabatic matrix elements) of the collision complex. For ions with charge $q \geq 2$ charge units, such networks reveal a finite number of effective avoided crossings, which control the charge transfer process. And since the non-adiabatic coupling is dominant only in the vicinity of avoided energy crossings, a fairly small (usually less than 10) basis set of adiabatic states is sufficient to describe the charge transfer process (at least for $q \leq 6$). With a simple modification [8], the model potential methods can also be adapted to deal with a restricted class of two active electron systems involving single electron capture from ground state He targets. Systems such as Si^{4+}/He and Ar^{6+}/He have been successfully treated in this way [8, 9]. In this presentation, we consider an extension of the model potential approach to treat systems in which either the ion or the neutral target has an open-shell configuration. We shall consider two such systems, which are representative of two different types of processes. The first involves capture by a structureless ion from a neutral target in an excited open-shell configuration, the second capture by an open-shell ion from a ground state neutral target.

1.1 He^{2+}/metastable He

One of the simplest (and most instructive) examples of single electron capture from an excited neutral target is that of He^{2+} ions in collision with neutral He in an excited metastable state. The conversion of He^{2+} to He^{+} by charge exchange in collisions with ground state He is inefficient for energies below 10 keV/amu, the most favourable reaction at lower energies being double electron capture (which of course leads to no net change in the ionic abundance). On the other hand, it is expected that He^{2+} can easily capture an electron from metastable He, leading to the production of two singly charged He^{+} ions. From elementary considerations based on the over-barrier model [10], electron capture takes place mainly to the n=3 quantum level of He^{+} according to reactions [12]

$$He^{2+}+He(1s2s)^1S \rightarrow He^{+}(n=3,l)+He^{+}(1s)^2S \quad (1)$$
$$He^{2+}+He(1s2s)^3S \rightarrow He^{+}(n=3,l)+He^{+}(1s)^2S \quad (2)$$

Because of the proximity of the excitation channels corresponding to the (1s2p) configuration of He, it is also necessary to take account of the excitation processes

$$He^{2+}+He(1s2s)^1S \rightarrow He^{2+} + He(1s2p)^1P \quad (3)$$
$$He^{2+}+He(1s2s)^3S \rightarrow He^{2+} + He(1s2p)^3P \quad (4)$$

These reactions occur in the vicinity of avoided crossings of the adiabatic energies of the collision complex He_2^{2+} at internuclear distances beyond $10\,a_0$. An accurate description of the adiabatic potentials of the excited states of the He_2^{2+} system is therefore required. Some simplification can of course be expected since for internuclear distances greater than about $5a_0$, the overlap of the 1s orbital centred on different nuclei is negligible.

Calculations by Fritsch [11] would suggest that the cross section for the single electron capture for electron capture from the metastable He (2^1S) state attains cross sections of the order of $10^{-14}cm^2$ an energy of 4 keV/amu..

Since the He_2^{2+} system only involves two electrons, it is fairly straightforward to carry out an accurate configuration interaction calculation of the adiabatic potentials. It therefore provides an ideal testing ground for a model potential approach, which is considerably easier to implement than a full *ab-initio* calculation. In order to obtain the correct asymptotic energy limits of both the singlet and triplet channels, it is necessary to introduce spin dependent potentials. Of course, the introduction of such spin dependent potentials has been used before, but the procedure has never really been tested in a rigorous way.

1.2. Si^{3+}/He

The Si^{3+}/He system is a typical example of capture by an open shell ion from a ground state atom. This system has been the subject of several extensive theoretical investigations [13,14] based on ab-initio calculations of the adiabatic potentials and non-adiabatic coupling matrix element of the Si^{3+}/He system. The results of [14] are consistent with the measured

rate constant [15] of 6×10^{-10} cm^3 s^{-1} at an effective temperature of 4000K On the other hand, the results of [13] are a factor of 3 smaller at these low energies. We should remark, that in comparing theory with experiment, Si^{3+} is of particular interest for ion-trap experiments since it has no long-lived metastable states which might interfere with the interpretation of the ionic decay and its charge to mass (3/28) ratio avoids possible confusion with other contaminants.

The aim of the present work is to re-examine the theoretical calculations on the Si^{3+}/He system to analyse the difference between the different theoretical calculations. From the network of reaction channels in the Si^{3+}/He system [13,14] it is clearly established that at low energies, electron capture takes place primarily according to the reaction

$$Si^{3+}(3s)^2S+He(1s^2)^1S\rightarrow Si^{2+}(3s^2)^1S+He^+(1s)^2S \quad (5)$$

via a $^2\Sigma$ avoided crossing with the entry channel at $6a_0$. All the calculations exhibit a well defined peak in the non-adiabatic radial coupling in the vicinity of the crossing. From the earlier calculations, it is seen that there is a maximum in the cross section for a centre of mass energy of around 17 eV (ion energy in the laboratory system of 120 eV). For higher energies, the calculated cross sections are not too sensitive to the height of the radial coupling peak value $A(R_X)$. But on the lower energy side of the Landau-Zener maximum, the cross section depends quite critically on $A(R_X)$. It may be remarked that as a general rule, $A(R_X)$. is related to the minimum energy separation Δ_X in the case of an isolated avoided crossing according to the formula

$$A(R_x)=(q\text{-}1)/2R_x^2\Delta_x \quad (6)$$

The calculations [13] yield a minimum energy separation, which is not compatible with (6). So while the results of [13] are reliable for energies greater than a centre of mass energy of 10eV, they are susceptible to error at lower energies. On the other hand, in the calculations [14] the radial coupling peak and minimum energy separations are compatible with (6). Rather than attempt to refine the *ab-initio* calculations, we have opted in this work for a model potential method.

2. Methods

Both model potential and *ab-initio* methods have been used to calculate the adiabatic potential energies of the collision complex. In the model potential approach, an effective two-centre Hamiltonian is constructed from a superposition of the model potentials of the ionic core and the neutral atom. When one or both of the colliding partners have an open-shell configuration, the atomic (and/or ionic) model potentials are spin dependent and it may be necessary as in the case of electron capture by He^{2+} from metastable He, to make two separate calculations, one for the singlet series, the other for the triplet series. However, in the Si^{3+}/He system, the dominant reaction channel involves only capture to the ground singlet state of Si^{2+} and capture to the triplet states is negligible. For that reason it is only necessary to treat the

case of a model potential for the singlet series of Si^{2+}. The parameters used to describe the different potentials may be found in [16].

In the *ab-initio* calculations, the adiabatic energies are determined by standard variational techniques using a basis of Slater-type orbitals expressed in prolate spheroidal coordinates, (of the same type as in the model potential caclulations). A complete configuration-interaction calculation using all the basis set orbitals is adopted. The main originality of our calculations arises from the method used to compute the bielectronic matrix elements [17].

Non-adiabatic matrix elements are calculated in a standard way and the transformation from an adiabatic to a diabatic basis set is carried out as described in [2], with Galilean invariance being insured by the introduction of appropriate reaction coordinates [18]. The coupled dynamical equations are solved in a fully quantum mechanical calculation.

Results and discussion

3.1. He^{2+}/He metastable

By and large, the *ab-initio* and model potential calculations are in excellent agreement both for the position and energy separations of the avoided crossings. The largest apparent difference concerns the position of the long distance singlet avoided crossing. It is seen from Table 1 that the error of the *ab-initio* calculation for the dissociation limit is about 0.25% in the singlet case and 0.05% in the triplet case. This is sufficient to explain the differences between the *ab-initio* and model potential determinations of the crossing radii. Since the model potential parameters are chosen to give the correct dissociation limit it is probable that the model potential results are more precise than the *ab-initio* results for both the position and energy separation of the avoided crossings. In any case, even without any adjustment of the dissociation limit, both the *ab-initio* and model potential calculations will yield very similar results for the collision process.

Table 1 Comparison of *ab initio* and model potential avoided crossing parameters for the system He^{2+}/metastable He

		Model Potential		Ab-initio	
Symmetry	Crossing	$R_x(a_0)$	Δ_x(eV)	$R_x(a_0)$	Δ_x(eV)
Singlet	Σ_1-Σ_4	18.38	0.85	18.17	0.89
	Σ_4-Σ_5	11.45	0.58	11.55	0.57
Triplet	Σ_1-Σ_4	19.93	0.26	19.77	0.27
	Σ_2-Σ_4	10.83	0.18	10.84	0.16

In view of the excellent agreement of the model-potential adiabatic energies with the *ab-initio* calculations, we have chosen to calculate the non-adiabatic matrix elements using model-potential wave functions. This choice was dictated not only by the desire to simplify

the calculations. The main reason is that reactions (1-3) are governed by very long range interactions (avoided crossing radii in the range 10-20 a_0). Past experience with such calculations [19] indicate that, under such conditions, model potential techniques have the advantage, in that they guarantee the numerical accuracy of the matrix elements (within the physical limitations of the method). Another reason was the need to modify the adiabatic basis to take account of the lack of Galilean invariance of the standard scattering equations. One way to do so is to introduce appropriate reaction coordinates such that all non-adiabatic coupling terms vanish in the asymptotic limit. This procedure has given satisfactory results and we have been able to use the programme developed by Gargaud et al.[2] without any major modification.

The results for the electron capture and excitation cross sections are presented graphically in figures 1 and 2.

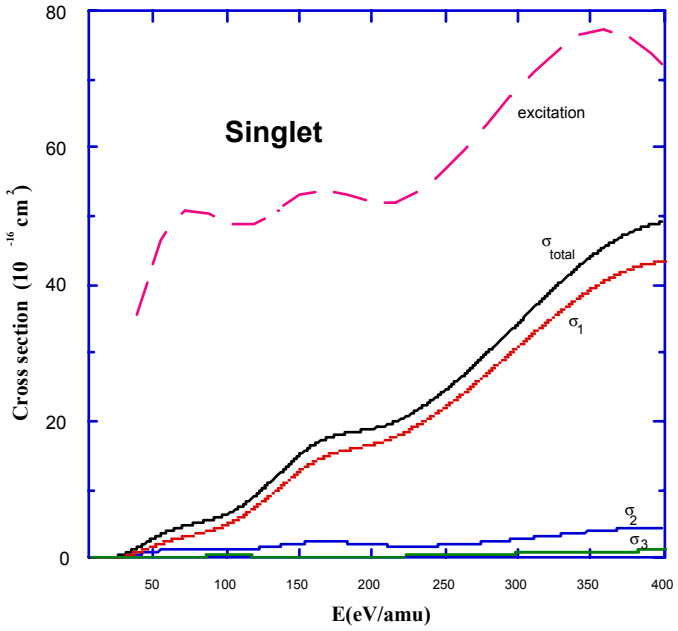

Figure 1. Cross sections in units of 10^{-16} cm^2 for electron capture and excitation in collisions of He^{2+} with $He(2^1S)$. The quantities σ_1, σ_2 and σ_3 refer to electron capture into the individual Stark states of $He^+(n=3)$, σ_{total} designates the electron capture cross section summed over all Stark states and $\sigma_{excitation}$ designates the excitation cross section of $He(1s,2p)^1P$.

The most striking aspect of the results concerns the very different behaviour of the singlet and triplet systems. The onset of electron capture by He^{2+} from $He(2^1S)$ occurs at about 30 eV/amu and the cross section rises uniformly with increasing energy, attaining a value of about 5×10^{-16} cm^2 at 400eV/amu. Above 400eV/amu, the cross-section levels off and it is reasonable to expect that our calculations are consistent with those of Fritsch [11] at energies above 4 keV/amu. The onset of electron capture by He^{2+} from $He(2^3S)$ occurs at much lower energies (about 1 eV /amu) and the cross section rises to a maximum of about $2\times10^{-14}cm^2$ at a collision energy of 350eV/amu.

One other notable feature concerns the excitation channels. The cross-section for excitation of He$(1s,2p)^1P$ in the singlet system is much larger than the electron capture cross-section, ranging from 5×10^{-15} cm^2 at 60 ev/amu to a maximum of 8×10^{-15} cm^2 at 350 eV/amu. The dominance of the excitation channel is also found in the calculations of Fritsch. On the other hand, excitation of the He$(1s,2p)^3P$ in the triplet system is negligible. The dominant electron capture channel for both the singlet and triplet systems is the Stark Σ state (n_1=0,n_2=2). The cross-section for electron captures to the Stark Σ state (n_1=1,n_2=1) is an order of magnitude smaller than the cross section for the dominant channel. Electron capture to the (n_1=2,n_2=0) Stark State is negligible.

It would be of great interest to have some experimental measurements on this relatively system involving collisions of He^{2+} with metastable He. The electron capture and excitation mechanisms are highly selective in the energy range below 1 keV/amu.

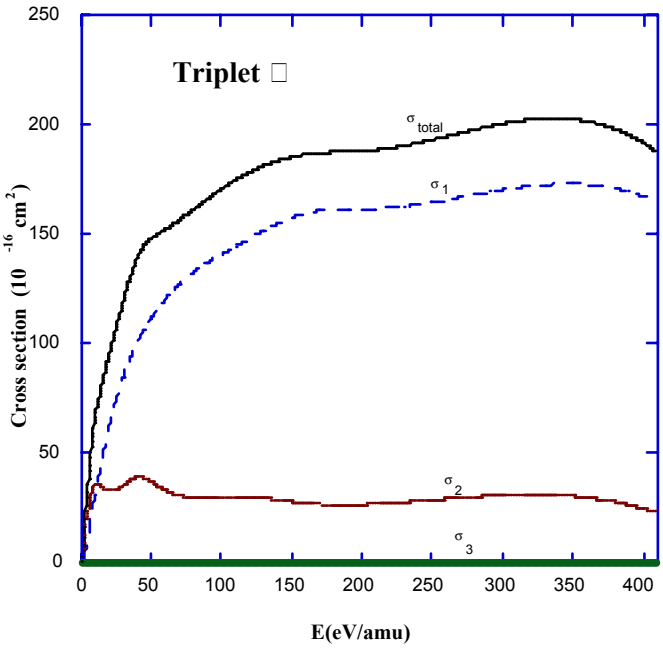

Figure 2. Cross sections in units of 10^{-16} cm^2 for electron capture and excitation in collisions of He^{2+} with He(2^3S). The quantities σ_1, σ_2 and σ_3 refer to electron capture into the individual Stark states of $He^+(n=3)$, σ_{total} designates the electron capture cross section summed over all Stark states. Excitation cross section of He$(1s,2p)^3P$ is negligible.

3.2. Si^{3+}/He

An indication of the accuracy of the model potential method can be ascertained by a comparison with [13, 14] for the location of the avoided crossing R_x, the minimum energy separation Δ_x in eV, and the peak of the radial coupling matrix $A(R_x)$ in a.u. Our calculations [14] are in satisfactory agreement with [14]. In [13], the peak intensity of the radial coupling appears to be a little too small.

Our calculated electron capture cross sections [16] are listed in table 3. A comparison of the results [13,14] is presented in graphical form in figure 3.

The rate constant k_{ct} for charge transfer has been calculated from the cross sections by averaging over a Maxwellian distribution of the collision partners. The results are presented in tabular form in Table (4) and in graphical form in figure (6), where a comparison is made with our theoretical and experimental values.

Table 2. Comparison of curve crossing parameters and maximum peak intensity of radial coupling

	R_x(a.u.)	Δ_x(eV)	$A_x(R_x)$ (a.u.)
Present work [16]	6.28	0.33	2.25
Honvault et al. [13]	6.00	0.25	1.80
Stancil et al. [14]	6.3	0.27	2.5

Table 3. Si^{3+}/He electron capture cross sections in units of $10^{-16}cm^2$

E(eV/amu)	Total cross section
0.039	4.28
0.078	5.73
0.155	7.92
0.233	9.96
0.582	13.5
1.25	16.0
2.50	16.8
4.36	16.8
10.0	15.3
22.5	12.9
40.0	11.1
125.0	7.83
187.9	6.98
250.0	6.49

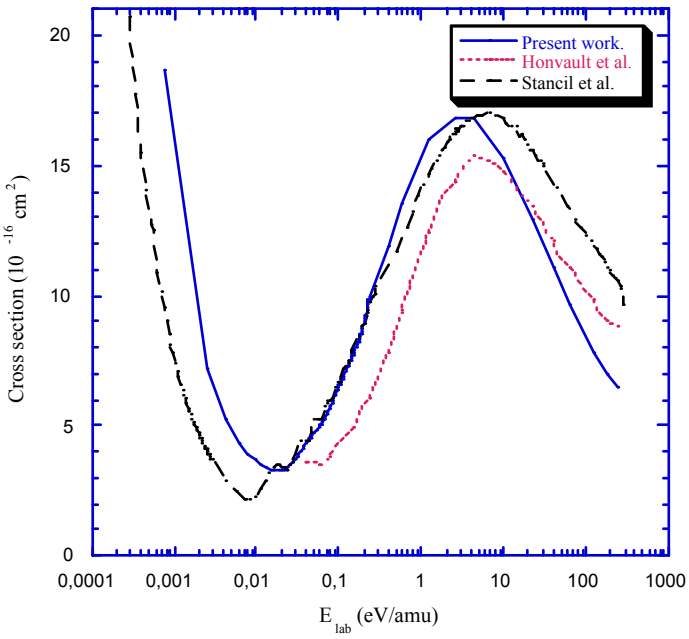

Figure 3. Si^{3+}/He total electron capture cross section (units of $10^{-16}cm^2$) as a function of the ion energy in the laboratory system.

Table 4. Si^{3+}/He electron capture rate coefficient (units of $10^{-9}cm^3s^{-1}$)				
T(K)	Present work [16]	Stancil et al. [14]	Honvault et al. [13]	Fang et al. [15]
10	9.38×10^{-2}			
50	6.44×10^{-2}			
100	5.63×10^{-2}	2.92×10^{-2}		
200	5.51×10^{-2}			
500	7.34×10^{-2}	6.34×10^{-2}		
1000	1.17×10^{-1}	1.15×10^{-1}	0.2×10^{-1}	
4000	4.09×10^{-1}	4.07×10^{-1}		6×10^{-1}
10000	9.10×10^{-1}	8.81×10^{-1}	4.8×10^{-1}	
30000	2.03	1.96	1.46	
50000	2.76	2.71	2.19	
100000	3.95	4.06	3.59	

In making a comparison between the different theoretical models, it should be borne in mind that our present calculations take no account of the influence of non adiabatic coupling with the excited $^2\Sigma^+$ state, whose asymptotic separated atoms corresponds to the $Si^{3+}(3p)^2P$+He$(1s^2)^1S$. This channel is closed for centre of mass energies less than 8 eV and in the thermal energy range of astrophysical interest (100-10^5K), its influence is negligibly

small. Indeed the calculations [13] indicate that the two-state model should be valid up to energies of the order of eV/amu (well beyond the excitation threshold). For energies less than the excitation threshold of the $Si^{3+}(3p)^2P$ +$He(1s^2)^1S$ a two-state model was used in [14]. In this energy range, where the cross section undergoes a strong variation with energy, their results are in excellent agreement with [15]. The discrepancy at very low energies (less than 0.01 eV) is of little physical significance. The upturn of the cross section at 0.02 eV/amu is an indication of a Langevin-type trajectory effect [5], which depends sensitively on very long-range interactions, which have not been optimised in our calculations. It would seem that the results of [13] are not reliable below 10 eV/amu).

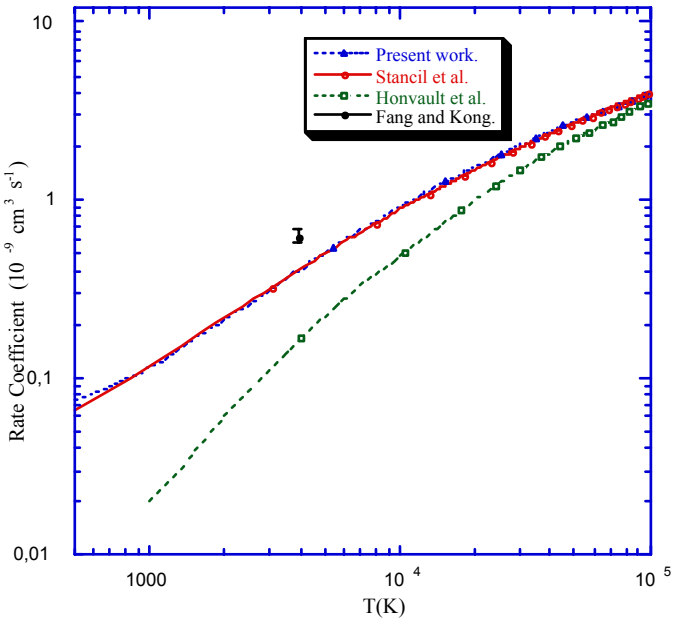

Figure 4. Si^{3+}/He charge transfer rate (units of $10^{-9}cm^3s^{-1}$) as a function of temperature.

For energies above the excitation threshold a 5-state model was used in [14] and calculated cross sections tend to be larger than ours for energies greater than about 10eV/amu. It is surprising that the difference with [14] should be so large, given that the two-state model is expected to be valid up to the highest energies presented in the Table 3.

Our calculated charge transfer rate constants [16] (for the whole range of temperatures studied) are in excellent agreement with [14] and they are also consistent with the experimental result [15] (bearing in mind the difficulty of defining the effective ion-trap temperature).

REFERENCES

[1] M. Gargaud and R. McCarroll, J. Phys.B: Atom. Mol. Phys. **18**, 463 (1985).

[2] M. Gargaud, R. McCarroll and P. Valiron, J. Phys.B: Atom. Mol. Phys. **20**, 1555 (1987).

[3] M. Gargaud, R. McCarroll and L. Opradolce, J. Phys.B: Atom. Mol. Phys. **21**, 521 (1988).

[4] M. Gargaud and R. McCarroll, J. Phys.B: Atom. Mol. Phys. **21**, 513 (1988).

[5] M. Pieksma, M. Gargaud, R. McCarroll and C.C. Havener, Phys. Rev. A **54**, R13 (1996).

[6] M. Gargaud and R. McCarroll, Atomic and Plasma Material Interaction Data for Fusion **6**, 163 (1995).

[7] M. Gargaud, S.F.C O'Rourke, R. McCarroll and L. Andersson, Physica Scripta **48**, 436 (1993).

[8] M. Gargaud, R. McCarroll and L. Benmeuraiem, Physica Scripta **51**, 752 (1995).

[9] L. Opradolce, R. McCarroll and P. Valiron, Astron. Astrophys. **148**, 229 (1985).

[10] A. Niehaus, J. Phys. B: At. Mol. Opt. Phys. **19**, 2925 (1986).

[11] W. Fritsch, J. Phys. B: At. Mol. Opt. Phys. **27**, 3461 (1994).

[12] D. Rabli, M. Gargaud and R. McCarroll, Phys. Rev. A **64**, to appear shortly.

[13] P. Honvault, M.-C. Bacchus-Montabonel, M. Gargaud and R. McCarroll, Chem. Phys. **238**, 401 (1998).

[14] P.C. Stancil, N.J. Clarke, B. Zygelman and D.L. Cooper, J. Phys. B: At. Mol. Opt. Phys. **32**, 1523 (1999).

[15] Z. Fang and V.H.S. Kwong, Astrophys. J. **483**, 527 (1997).

[16] D. Rabli, M. Gargaud and R. McCarroll, J. Phys. B: At. Mol. Opt. Phys. **34**, 1395 (2001).

[17] A. Henriet, C. Lesech and F. Masnou-Seeuws, Chem. Phys. Lett. **158**, 389 (1989).

[18] R. McCarroll and D.S. F. Crothers, Adv. At. Mol. Opt. Phys. **32**, 253 (1993).

[19] L. Opradolce, L. Benmeuraiem, R. McCarroll and R.D. Piacentini, J. Phys. B: At. Mol. Opt. Phys. **21**, 501 (1988).

Line emission spectroscopy of low-energy charge transfer reactions

Z. Juhász, G. Lubinski, R. Morgenstern, R. Hoekstra
KVI, Atomic Physics,
Groningen, Netherlands

Abstract. We present state-selective charge-transfer cross sections obtained by means of a combined RF-guided ion beam and photon emission spectroscopy method. Interaction energies have been varied from 1000 eV/amu down to energies as low as 5 eV/amu. Concerning state-selective charge transfer the energy range below ∼100 eV/amu is almost fully unexplored. Here we present a detailed discussion of absolute state-selective cross sections for one- and two-electron transfer in He^{2+} collisions on molecular hydrogen. In addition to the He^{2+} results some selected results for multicharged low-Z ions are discussed to illustrate the inappropriateness of using simple scaling laws to estimate charge transfer cross sections at energies well below 1 keV/amu.

1. Introduction

The main objective of the KVI Atomic Physics group was the production of charge-exchange data for the diagnostics and modelling of divertor and edge-plasma regions and to check the quality of theoretical predictions. In the scrape-off-layers and divertors of fusion plasma machines interaction energies range from 1 keV/amu down to energies as low as 1 eV/amu. At these low energies interactions between multiply charged ions, A^{q+}, and neutrals, B, are dominated by single electron capture into excited states, which subsequently decay under photon emission. This sequence of processes is given by:

$$A^{q+} + B \rightarrow A^{(q-1)+}(nl) + B^{+}$$

and

$$A^{(q-1)+}(nl) \rightarrow A^{(q-1)+}(n'l') + h\nu$$

From this it is clear that the photon emission spectrum can be regarded as a "fingerprint" of the nl-state-selective electron capture processes. Therefore, the photon emission of the subsequent decay of the excited states is an important passive diagnostics for fusion plasma, but also for astrophysical environments. In order to use the information contained in the intensity and spectral distribution of the light it is necessary to quantitatively understand the underlying processes (e.g. [1]). Therefore, in particular a lot of theoretical studies have been performed. In general the numerous theoretical predictions of state selective charge transfer cross sections well below 1000 eV/amu could be tested only partly or not at all. Furthermore, different calculations are frequently not in accordance with each other. A typical example is electron capture by O^{3+} (e.g. [2])

When neutral particles are approached by multiply charged ions they become strongly polarized, leading to a mutual attraction which increases with the charge state

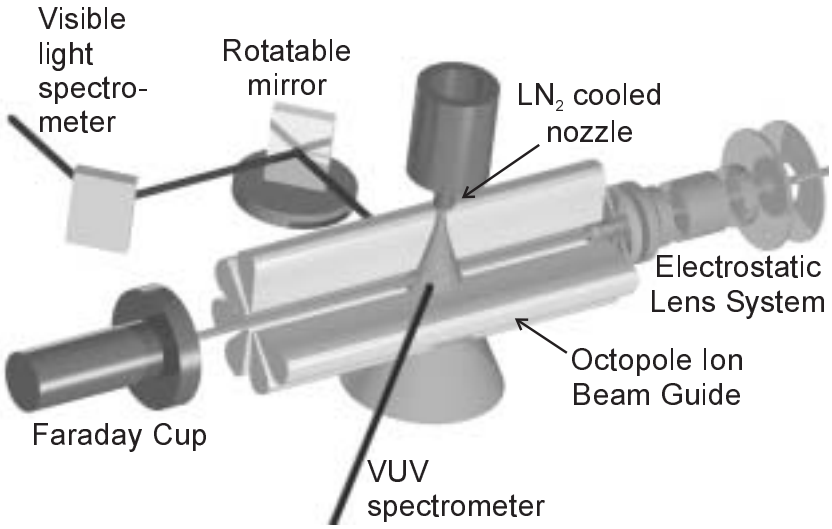

FIG. 1. Artistic representation of the experimental set-up for photon emission spectroscopy studies of low-energy collisions of multiply charged ions with neutrals.

of the ion. At collision energies above some ten eV/amu this hardly influences the interaction dynamics. At lower energies it has dramatic consequences. It means that the collision trajectories are strongly influenced and that large impact parameters can result in relatively small distances of closest approach. This implies that cross sections for electron transfer strongly increase with decreasing collision energies. In a classical approach the electron capture cross sections increase with the charge state of the ions and are inversely proportional to the velocity. Quantum mechanically even more interesting features are predicted to occur which are connected with the so called orbiting resonances: at specific collision energies charge transfer proceeds via discrete ro-vibrational states of the transient molecular ion [3].

2. Experimental set up

We developped an experimental method, which facilitates state-selective charge-transfer measurements at energies of direct relevance for fusion-plasma diagnostics and modelling. The method combines the technique of RF ion guiding with crossed-beam photon emission spectroscopy as schematically depicted in figure 1. Details of the experiment and experimental procedures are presented elsewhere [4, 5]. Briefly, ions extracted at 3.5 kV from our electron cyclotron resonance (ECR) ion source installed at the KVI atomic physics facility are injected via a five-element lens system into a RF multipole ion guide [6], in our case an 8-pole system. The method of RF multipole ion guiding was pioneered by Teloy and Gerlich [7] for singly charged ions and for the first time applied to multicharged ion beams by Okuno *et al.* [8]. Our RF octopole is a far more open system to allow for injecting a neutral target beam and observing the photon emission resulting from charge transfer reactions. Because of possible field penetration, the openness of the system prevented the standard usage of rods as RF poles. Instead special shaped, rigid 10 cm long poles were designed and made by spark erosion.

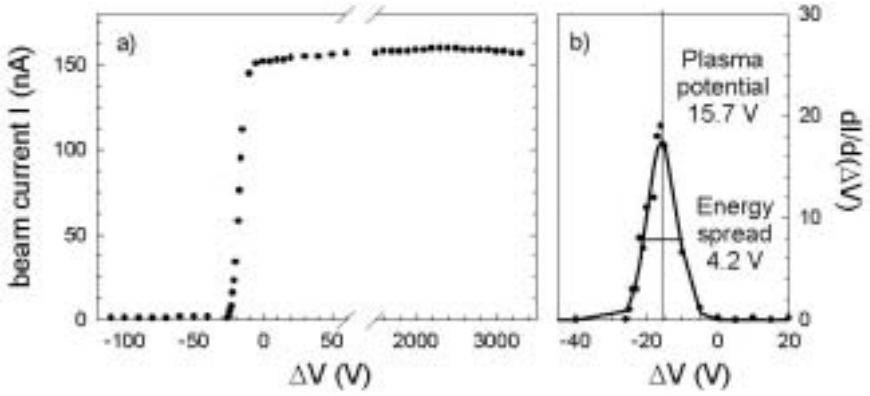

FIG. 2. a). Measured ion beam current through the octopole ion guide as a function of the DC potential difference between ECR ion source and octopole. Initial ion beam: 17.5 keV N^{5+}. b). Off-set energy due to the internal plasma potential of the ECR ion source and the energy spread of the ion beam as determined from the derivative of the beam current.

The interaction energy with the target is defined by the difference between the source potential and the DC potential at which the octopole is floated (plus an offset due to the plasma potential of the source, ∼15 V (cf. figure 2 and ref. [4]). Down to a beam energy of basically 0, the ion beam can be guided through the system without intensity loss. However there is a lower limit for performing well-defined experiments which is set by the energy spread of the primary beam. For our ECR ion source typical spreads are of the order of 5×q eV [4]. For the example shown in figure 2, the energy spread is slightly smaller. A typical energy spread of 5×q eV sets the lower limit for a well-defined collision energy to ∼ 5 eV/amu. In combination with a source from which ions can be extracted with smaller energy spreads, experiments can be performed at lower energies. As such a source, a recoil ion source might be considered which can produce cold ions (∼0.1 eV/amu [9]).

The photon emission following charge transfer reactions can be observed by two monochromators on opposite sides of the interaction region. The positioning is similar to the one used previously in our lab (e.g. [10]). The VUV spectrometer, which is used in the present experiments, covers a spectral range from 5 - 80 nm and is mounted under the double-magic angle to cancel polarization effects. The VUV system is calibrated absolutely on wavelength and sensitivity by cross-reference measurements on systems with well-known cross sections [10]. The spectrometer is equipped with a position-sensitive detector detecting a spectral range of almost 20 nm in one measurement.

3. The $He^{2+} - H_2$ collision system

Inelastic collisions of He^{2+} have attracted a lot of attention in connection with the modelling of He ash removal in the divertor region of tokamaks [11]. A point of interest is the charge state of the helium. If it is readily neutralized it is no longer magnetically confined and it may diffuse back into the core plasma thereby deteriorating the plasma. To

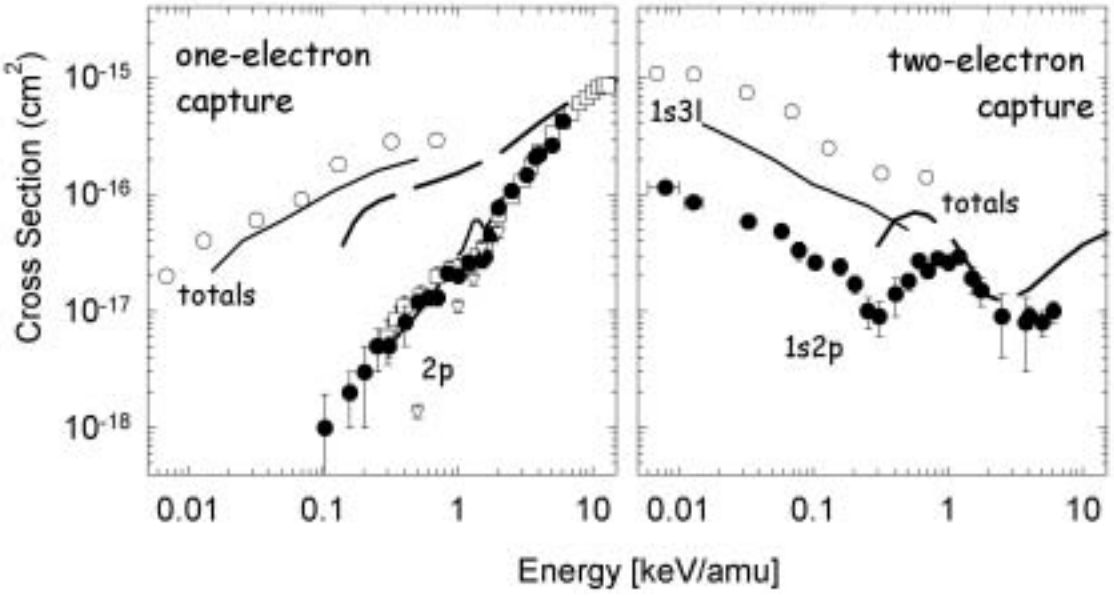

FIG. 3. $He^{2+} - H_2$. Comparison of our HeII($2p \rightarrow 1s$) and HeI($1s2p \rightarrow 1s^2$) line emission cross sections (closed symbols labelled as 2p and 1s2p, respectively) with total one- and two-electron capture cross sections: open circles: Okuno et al. [17], solid line: Shimakura et al. [21], long-dashed line: recommended cross sections [16]. In addition previous experimental data by our group [22, 23] (open squares) and theoretical data by Saha et al. [24] (solid line) for the HeII($2p \rightarrow 1s$) line emission are included. The inverted triangles represent the $He^{1+}(n = 2)$ cross sections of Hodgkinson et al. [25].

study the behavior of a recombining plasma for divertor and edge-region applications, at NIFS (Japan) a lot of work has been performed on cold recombining He plasmas resulting from the interaction with neutral gasses puffed into a He plasma [12–15]. To explain the direct response and the anomalously high intensity of the HeI($1s3l \rightarrow 1s2l'$) line emission when cold hydrogen molecules were brought into contact with the He plasma, strong double-electron capture, preferably directly into the He($1s3l$) states, has been invoked.

For energies above approximately 0.5 - 1 keV/amu a lot of experimental data exists and shows that one-electron capture dominates over two-electron capture ([16], long-dashed curves in figure 3). In the energy range of 1 keV/amu down to less than 1 eV/amu, a whole series of total charge changing cross section measurements was performed by Okuno *et al.* [17]. They showed that while being of the same order of magnitude around 0.5 keV/amu, two-electron capture dominates over the one-electron transfer processes by a factor of 50 around 10 eV/amu. Dominance of two-electron capture over one-electron capture is very rare (to our knowledge the only other system is C^{4+} - He [18–20]). Although underestimating the total charge changing cross sections by a factor of 2 (see figure 3), molecular orbital (MO) calculations in the energy range of 10 - 1000 eV/amu by Shimakura *et al.* [21] gave more or less the correct ratios between single- and double-electron transfer. In addition the MO calculations predicted that at energies below 100 eV/amu, where two-electron capture dominates, singly excited He(1s3l) states are populated.

Table 1. Measured HeII($2p \rightarrow 1s$) and HeI($1s2p \rightarrow 1s^2$) line emission cross sections (in units of 10^{-16} cm^2) resulting from He^{2+} + H_2 collisions. The errors represent statistical errors only. The systematic absolute uncertainty is approximately 20%. Energies are given in eV/amu

E	HeII	HeI	E	HeII	HeI
8	-	1.14±0.06	838	0.21±0.02	0.28±0.04
13	-	0.85±0.09	1008	0.20±0.02	0.26±0.04
33	-	0.58±0.06	1203	0.26±0.02	0.29±0.04
58	-	0.48±0.05	1508	0.27±0.02	0.19±0.05
78	-	0.33±0.06	1600	0.29±0.02	-
103	0.01±0.01	0.26±0.03	1758	0.45±0.03	0.15±0.05
158	0.02±0.01	0.24±0.04	2008	0.76±0.09	-
203	0.03±0.02	0.17±0.03	2508	1.06±0.07	0.09±0.05
253	0.05±0.02	0.10±0.03	3258	1.45±0.10	-
308	0.05±0.01	0.09±0.03	3758	2.04±0.10	0.08±0.05
408	0.08±0.03	0.14±0.05	4008	2.18±0.11	0.09±0.02
508	0.12±0.02	0.18±0.03	5008	2.62±0.13	0.08±0.02
608	0.13±0.02	0.27±0.04	6008	4.21±0.21	0.10±0.02
708	0.13±0.02	0.22±0.03			

To obtain state-selective information on the He^{2+}–H_2 collision system, we have measured the VUV spectrum of such interactions. In the VUV spectral range the Lyman series HeII($np \rightarrow 1s$) and HeI($1snp\,^1\mathrm{P} \rightarrow 1s^2\,^1\mathrm{S}$) can be observed [5]. The first series of lines is associated with one-electron capture while the second one results from two-electron capture.

3.1. *One − electron capture*

Below about 1 keV/amu HeII($np \rightarrow 1s$) line emission from np states with $n \geq 3$ becomes negligible in comparison to the Lyman-α emission [10, 23]. In figure 3, (left panel) the present HeII(2p → 1s) line emission cross sections are seen to present a smooth extension of previous data towards lower energies. The theoretical results by Saha *et al.* [24] are in good agreement with the data, except maybe just above 1 keV/amu where they exhibit a small local maximum, which is not observed in the data.

By means of translational energy spectroscopy (TES) Hodgkinson *et al.* [25] determined cross sections for capture into $He^{1+}(n = 2)$, i.e. the sum of capture into the degenerate $He^{1+}(2s)$ and $He^{1+}(2p)$ states. In the energy range in which the TES experiments were performed (0.5–2 keV/amu), the cross section for capture into the $2s$ state is small as compared to the cross section for capture into $2p$ [23, 26]. Therefore, at least by and large the TES measurements should yield cross sections similar to our HeII($np \rightarrow 1s$) line emission cross sections. This is indeed the case for energies above 1 keV/amu. However at

lower energies the TES and PES data diverge strongly. At the lowest energy of the TES measurements, 0.5 keV/amu, the difference is already a factor of 8, see figure 3.

Considering the absolute calibration of the cross sectional data it is of note that our PES data were calibrated to previous data from our group at 5 keV/amu [22, 23]. By this procedure we obtain an absolute systematic uncertainty of 20% associated to the PES data. The TES results are put on an absolute scale by normalizing the sum of all reaction channels to the total one-electron capture cross sections determined by Nutt *et al.* [27]. It is to be realized that the work by Nutt *et al.* is also the main source in the 0.5–2 keV/amu energy range on which the recommended cross sections for one-electron capture are based [16]. The theoretical and experimental one-electron capture cross sections by respectively Shimakura *et al.* [21] and Okuno *et al.* [17] exceed the data of Nutt *et al.* [27] by a factor of 2 to 3. Assuming the unlikely scenario that the data by Nutt *et al.* would be off by a factor of 2 to 3, there remains a difference of approximately a factor of 3 between the PES and TES data. Together with the Queen's University of Belfast group (McCullough *et al.*) we will attempt to resolve these inconsistencies between different experimental and theoretical data sets.

The difference between the cross sections for HeII($np \rightarrow 1s$) line emission and those for total charge transfer increases for lower impact energies. The total one-electron capture cross section σ_{tot} is equal to the sum of all Lyman transitions, the metastable $He^+(2s)$ production cross section $\sigma_p(2s)$, and the cross section for direct capture into the $He^+(1s)$ ground state, $\sigma_c(1s)$ (see e.g. [23]), i.e.,

$$\sigma_{tot} = \sum\nolimits_n \sigma(np \rightarrow 1s) + \sigma_p(2s) + \sigma_c(1s) \tag{1}$$

As mentioned before, at low impact energies $\sigma_p(2s)$ is small compared to $\sum_n \sigma(np \rightarrow 1s)$ [23, 26] and there is no significant contribution from np states with $n \geq 3$ to Lyman emission. Thus the HeII($2p \rightarrow 1s$) emission cross section might be compared directly to the total cross sections (see figure 3). The increasing difference between the respective cross sections towards lower impact energies indicates that one-electron capture goes fully into the $He^+(1s)$ ground state when decreasing the projectile energy. This is in line with our previous conclusions [23] based on measurements above 1 keV/amu and existing TES [28] and fragmentation work [27], that the dominant charge transfer channel swaps around a few keV/amu from non-dissociative capture into $2p$

$$He^{2+} + H_2 \rightarrow He^{1+}(2p) + H_2^+ \tag{2}$$

to capture into the ground state associated with target-ion dissociation and excitation

$$He^{2+} + H_2 \rightarrow He^{1+}(1s) + H^+ + H(n \geq 2). \tag{3}$$

The fact that the dissociative channel produces mainly excited atomic hydrogen was inferred from our H Lyman-α measurements. The H Lyman-α cross sections were of similar magnitude as the $He^+(1s)$ cross sections [23]. This indirect evidence was later confirmed in the TES measurements by Hodgkinson *et al.* [25]. The importance of this

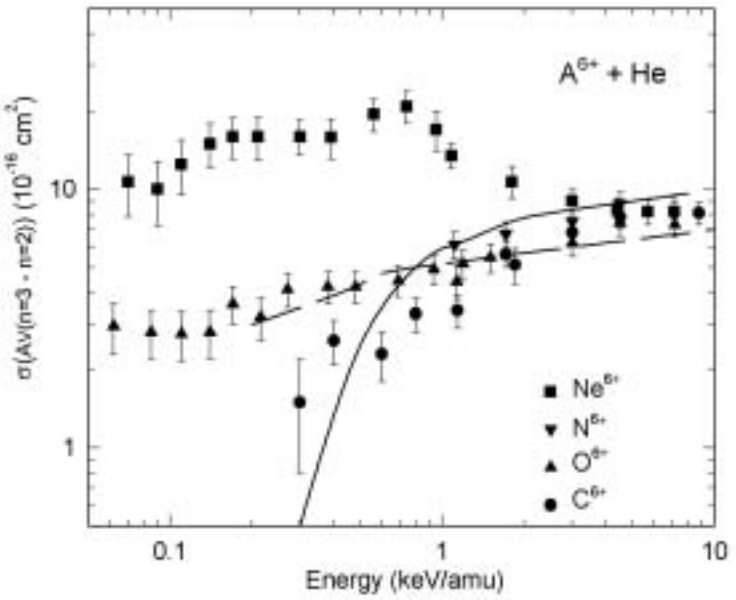

FIG. 4. Comparison of $n = 3 \rightarrow n = 2$ line emission cross sections following one-electron capture in collisions of six-fold charged C, N, O, and Ne ions colliding on He (partly from our previous work [30–33]. The theoretical curves are constructed from AO calculations for C^{6+} [34] and MO calculations for O^{6+} [35].

reaction channel mandates that theoretical calculations of one-electron transfer at low energies need to include an appropriate description of both electrons and the molecular nature of the target.

3.2. *Two − electron capture*

Results for two-electron capture are depicted in the right panel of figure 3. In the overlapping energy range of 0.5–1 keV/amu, the results of Okuno *et al.* [17] exceed the recommended data [16] by a factor of 2–3, just as for one-electron capture. The MO calculations by Shimakura *et al.* [21] predict a two-electron capture cross section approximately half of the ones measured by Okuno *et al.* [17]. Our measured HeI($1s2p \rightarrow 1s^2$) line emission cross sections (cf. figure 3) follow the same energy dependence as the total two-electron capture cross sections by Okuno *et al.* [17] and Shimakura *et al.* [21], but are smaller by a factor of 10 and 5, respectively. This seems to imply that capture into He(1s2p) is a weak two-electron capture channel. It is of note that capture into the He(1s3s) and He(1s3d) states is included in the HeI($1s2p \rightarrow 1s^2$) line emission because they decay to the He(1s2p) state. Therefore, capture processes into He(1s3s) and He(1s3d) states are also minor reaction channels. In our spectra we do not observe any appreciable emission from HeI($1snp \rightarrow 1s^2$) lines with $n \geq 3$ [4].

From this it is concluded that two-electron capture proceeds mainly into either the He($1s^2$) ground state or the He($1s2s\,^1$S) metastable state. In our opinion the latter state

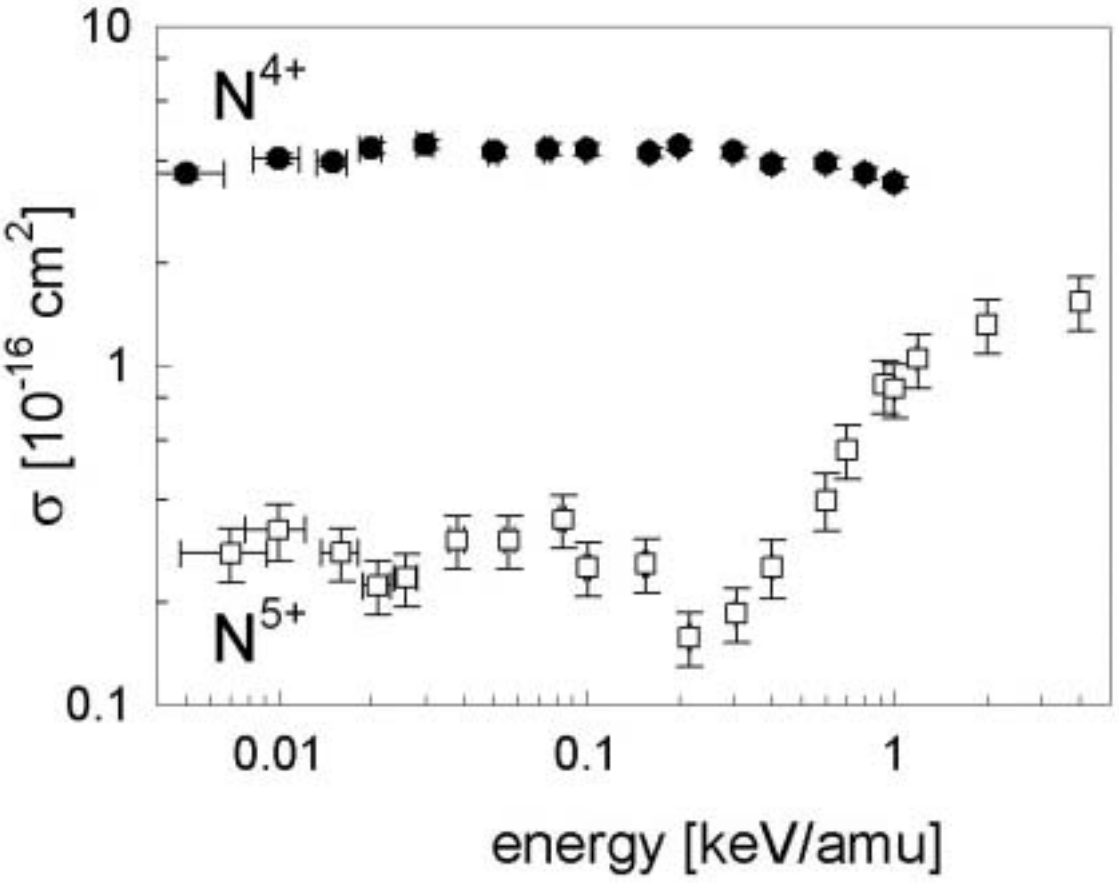

FIG. 5. Comparison of our total one-electron capture cross sections for $N^{4+} - H_2$ and $N^{5+} - H_2$. The total cross sections are determined from the relevant line emission cross sections.

seems the most likely, since the total amount of energy needed to remove the electrons from H_2 molecules is 50.8 eV (assuming Franck-Condon type transitions). This should be compared with the binding energies of the He($1s^2$) and He($1s2s\,^1$S) states which are 79 and 58.4 eV, respectively. From the potential-energy curves of the He^{2+} - H_2 system it is seen that the He($1s^2$) state can only be populated at small impact parameters [21] and therefore a large cross section is unlikely. We conclude that the difference between our partial cross section results and the total two-electron capture cross sections of Okuno *et al.* must be due to capture into the He($1s2s\,^1$S) metastable state.

The MO calculations [21] did predict that at energies below 100 eV/amu where two-electron capture dominates over one-electron capture, singly excited He($1s3l$) states are populated. The predicted strong population of these He($1s3l$) states has been used to explain the aforementioned anomalously intense HeI($1s3l \rightarrow 1s2l'$) emission observed when helium plasmas are brought in contact with cold hydrogen molecules. There are two possible explanations for the apparent discrepancy. 1) Ion temperatures in the helium plasmas, i.e., the corresponding ion energies are much lower than the energies in both our experiment and in the MO calculations. This may shift the electron capture distribution

to higher levels, which is a trend well-known from Landau-Zener type of calculations. 2) The energy gap between the He($1s2s\,^1$S) state and the He($1s3l$) states is so small that the He($1s3l$) states can very efficiently be populated from He($1s2s\,^1$S) by low-energy plasma electrons. At low temperatures electron impact excitation of HeI($1s2s\,^1$S$\rightarrow 1s3l'$) transitions is associated with large collision strengths [29].

4. Multicharged, low-Z ion – H_2 collision systems

Recently we performed a series of PES experiments on He-like ions (C^{4+}, N^{5+} and O^{6+}) colliding with molecular hydrogen. The $3l$-state selective cross sections are presented elsewhere both in graphical and tabular form [5]. On this state selective level large discrepancies with sparse theoretical results are observed, in particular for the N^{5+}–H_2 system for which orders of magnitude differences are found. Here we want to stress the near-impossibility of finding and of reliably using scaling laws at energies below 1 keV/amu, not only on a state selective but even on a total cross section level.

In figure 4 we summarize ($n = 3 \rightarrow n = 2$) line emission results for six-fold charged ions colliding on He. For Ne^{6+}, O^{6+} and N^{6+} ($n = 3 \rightarrow n = 2$) line emission cross sections are the sum of the separate ($3l \rightarrow 2l'$) line emission results to allow for a direct comparison with the capture results from C^{6+} - He interactions, for which the ($3l \rightarrow 2l'$) transitions are degenerate. The ($3l \rightarrow 2l'$) line emission is equal to $\sigma(3s) + 0.12\sigma(3p) + \sigma(3d)$. From the figure it is clear that above 1 keV/amu the results are all similar, but at lower energies the results for the different ionic species are diverging strongly. This implies that the core-electronic structure of the projectiles strongly influences the charge transfer processes, thereby hampering simple classical scaling relations (see e.g. ref. [36]) which give a proportionality to the charge state of the ions.

It may be argued that at least partly the differences might be due to changes in the distribution over the $3l$ states, for example a large cross section for capture into $3p$ for the ion with the lowest ($n = 3 \rightarrow n = 2$) line emission cross sections. Our state selective results (not shown) do indeed show that there are differences in the distribution over the angular momentum states within the $n = 3$ shell, but these differences can by far not explain the large variety in cross sections between the different six-fold charged ions. To illustrate this further figure 5 depicts the total cross sections for N^{4+} and N^{5+} ions colliding on molecular hydrogen. The cross sectional behavior is very different for N^{4+} and N^{5+} ions. Over the full energy range the total one-electron capture cross section for N^{4+} ions clearly exceed the ones for N^{5+} ions. According to the q-scaling law the cross sections for N^{5+} should exceed the ones for N^{4+} by a factor of 5/4.

Finally, figure 6 shows the fact that also ions in the same charge state do not need to have similar cross sections. While the total charge transfer cross sections are almost equal for C^{4+} and N^{4+}, they strongly differ for five-fold charged oxygen and nitrogen ions. This implies again that at low-energy every collision system may need to be treated separately.

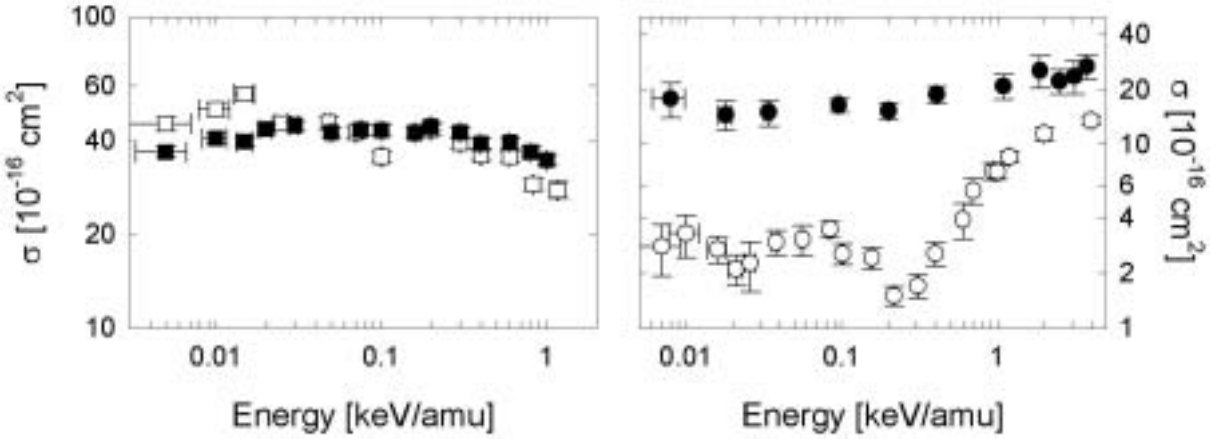

FIG. 6. Left panel: Comparison of our total one-electron capture cross sections for N^{4+} – H_2 (closed squares) and C^{4+} – H_2 (open squares). Right panel: Comparison of our total one-electron capture cross sections for N^{5+} – H_2 (open circles) and O^{5+} – H_2 (closed circles). The total cross sections are determined by summing the relevant line emission cross sections.

5. Conclusions

We have presented state-selective charge-transfer cross sections obtained by means of a combined RF-guided ion beam and photon emission spectroscopy method. Interaction energies have been varied from 1000 eV/amu down to energies as low as 5 eV/amu. From a detailed treatment of the absolute cross sections for He^{2+} colliding on molecular hydrogen, it is found that large uncertainties exist concerning one and two-electron transfer processes. Results for different multicharged low-Z ions show that simple q-scaling laws for charge transfer are not valid below approximately 1 keV/amu.

ACKNOWLEDGEMENTS

This work is part of the research programme of the Association Agreement EURATOM-FOM (stichting voor Fundamenteel Onderzoek der Materie) and performed in conjunction with the IAEA Co-ordinated Research Project (CRP) on "Charge Exchange Cross Section Data for Fusion Plasma Studies".

REFERENCES

[1] O'MULLANE, M.G., MATTIOLI, M., GIANELLA, R., PEACOCK, N.J., Plasma Phys. Control. Fusion **41**, 105 (1999).
[2] GARGAUD, M., McCARROLL, R., J. Physique Coll. **50**, 127 (1989) and Astron. Astrophys. **208**, 251 (1989).

[3] SHIMAKURA N., KIMURA, M., Phys. Rev. A **44**, 1659 (1991).
[4] LUBINSKI, G., JUHÁSZ, Z., MORGENSTERN, R., HOEKSTRA R., J. Phys. B: At. Mol. Opt. Phys. **33**, 5275 (2000).
[5] LUBINSKI, G., JUHÁSZ, Z., MORGENSTERN, R., HOEKSTRA R., J. Phys. Rev. Lett. **86**, 616 (2001).
[6] GERLICH, D., Adv. Chem. Phys. **LXXXII**, 1 (1992).
[7] TELOY, E., GERLICH, D., Chem. Phys. **4**, 417 (1974).
[8] OKUNO, K., SOEJIMA, K., KANEKO, Y., Nucl. Instr. Meth. **53**, 387 (1991).
[9] COCKE, C.L., OLSON, R.E., Phys. Rep. **205**, 153 (1991).
[10] HOEKSTRA, R., DE HEER, F.J., MORGENSTERN, R., J. Phys. B: At. Mol. Opt. Phys. **24**, 4025 (1991).
[11] JANEV, R.K., Comm. At. Mol. Phys. **26**, 83 (1991).
[12] SATO, K., TAKIYAMA, K., ODA, T., FURUKANE, U., AKIYAMA, R., MIMURA, M., OTSUKA, M., TAWARA, H., J. Phys. B: At. Mol. Opt. Phys. **27**, L651 (1994).
[13] ODA, T., FURUKANE, U., TAKIYAMA, K., SATO, K., TAWARA, H., Fusion. Eng. Design. **34–35**, 773 (1997).
[14] ODA, T., SATO, K., NAMBA, S., KUSAKABE, S., TAKAHARA, K., TAWARA, H., KATSUTA, T., TAKIYAMA, K., FURUKANE, U., J. Nucl. Mater. **241–243**, 1238 (1997).
[15] NAMBA, S., NOMURA, I., IWASAKI, K., TAKIYAMA, K., FURUKANE, U., ODA, T., SATO, J. Nucl. Mater. **266–269**, 1157 (1999).
[16] BARNETT, C.F., HUNTER, H.T., KIRKPATRICK, M.I., ALVAREZ, I., CISNEROS, C., PHANEUF, R., *Atomic Data for Fusion*, vol. 1 (Oak Ridge National Laboratory, ORNL–6086/V1, 1990).
[17] OKUNO, K., SOEJIMA, K., KANEKO, Y., J. Phys. B: At. Mol. Opt. Phys. **25**, L105 (1992).
[18] CRANDALL, D.H., OLSON, R.E., SHIPSEY, E.J., BROWNE, J.C., Phys. Rev. Lett. **36**, 858 (1976).
[19] CRANDALL, D.H., Phys. Rev. A **16**, 958 (1977).
[20] HANSEN, J.P., J. Phys. B: At. Mol. Opt. Phys. **25**, L17 (1992).
[21] SHIMAKURA, N., KIMURA, M., LANE, N.F., Phys. Rev. A **47**, 709 (1993).
[22] HOEKSTRA, R., SCHLATMANN, A.R., DE HEER, F.J., MORGENSTERN, R., J. Phys. B: At. Mol. Opt. Phys. **22**, L603 (1989).
[23] HOEKSTRA, R., FOLKERTS, H.O., BEIJERS, J.P.M., MORGENSTERN, R., DE HEER, F.J., J. Phys. B: At. Mol. Opt. Phys. **27**, 2021 (1994).
[24] SAHA, B.C., LANE, N.F., KIMURA, M., Phys. Rev. A **44**, R1 (1991).
[25] HODGKINSON, J.M., McLAUGHLIN, T.K., McCULLOUGH, R.W., GEDDES, J., GILBODY, H.B., J. Phys. B: At. Mol. Opt. Phys. **28**, L393 (1995).
[26] SHAH, M.B., GILBODY, H.B., J. Phys. B: At. Mol. Phys. **11**, 121 (1978).
[27] NUTT, W.L., McCULLOUGH, R.W., BRADY, K., SHAH, M.B., GILBODY, H.B., J. Phys. B: At. Mol. Phys. **11**, 1457 (1978).
[28] AFROSIMOV, V.V., LEIKO, G.A., PANOV, M.N., Sov. Phys. Tech. Phys. **25**, 313 (1980).
[29] DE HEER, F.J., BRAY, I., FURSA, D.V., BLIEK, F.W., FOLKERTS, H.O., SUMMERS, H.P., Nucl. Fusion. Suppl. **6**, 7 (1995).
[30] DIJKKAMP, D., ĆIRIĆ, D., VLIEG, E., DE BOER, A., DE HEER F.J., J. Phys. B: At. Mol. Phys. **18**, 737 (1985).

[31] DIJKKAMP, D., ĆIRIĆ, D., VLIEG, E., DE BOER, A., DE HEER F.J., J. Phys. B: At. Mol. Phys. **19**, 4763 (1985).
[32] BEIJERS J.P.M., HOEKSTRA, R., SCHLATMANN, A.R., MORGENSTERN, R., DE HEER F.J., J. Phys. B: At. Mol. Opt. Phys. **25**, 463 (1992).
[33] BEIJERS J.P.M., HOEKSTRA, R., MORGENSTERN, R., DE HEER F.J., J. Phys. B: At. Mol. Opt. Phys. **25**, 4851 (1992).
[34] FRITSCH, W., LIN, C.D., J. Phys. B: At. Mol. Phys. **19**, 2683 (1986).
[35] KIMURA M, OLSON, R.E., J. Phys. B: At. Mol. Phys. **17**, L713 (1984).
[36] JANEV, R.K., WINTER, HP., Phys. Rep. **117**, 265 (1985).

Measurements of state-selective electron capture by slow multiply charged ions in specified ground or metastable states

H.B. Gilbody, R.W. McCullough

Department of Pure and Applied Physics, The Queen's University of Belfast,
Belfast, United Kingdom

Abstract

The technique of double translational energy spectroscopy (DTES) has been used in this laboratory to study state-selective electron capture by slow state-prepared ions in collisions with a variety of targets including atomic hydrogen. Measurements are described involving one-electron capture by C^{2+} ^1S ground state and C^{2+} ^3P metastable ions, N^{2+} ^2P ground state ions and O^{2+} ^3P ground state ions in the range 0.8 – 6 keV. Use of DTES overcomes the difficult problem of interpretation inherent in the many previous measurements carried out with ion beams containing unknown fractions of metastable ions.

1. INTRODUCTION

A detailed understanding of one-electron capture processes of the type

$$X^{q+} + Y \rightarrow X^{(q-1)+}(n, l) + Y^{+}(n', l')$$

leading to product ions in specified excited states is directly relevant to the accurate modelling of the behaviour of edge plasmas in fusion devices. At velocities $v < 1$ au, it is well known that, in processes with moderate exothermicity, electron capture may take place very effectively through a limited number of pseudocrossings of the adiabatic potential energy curves describing the initial and final molecular systems. In many such processes, experimental measurements have provided both identification and a quantitative assessment of the main excited product channels. Since accurate calculations are difficult, particularly for partially ionized primary ions, where a number of curve crossings may be important, reliable experimental data are of particular value in determining the range of validity of the approximations used in the theoretical models.

In this laboratory we have used the well-established technique of translational energy spectroscopy (TES) to obtain detailed information on state-selective electron capture in many different processes. In the TES approach, the X^{q+} primary ion beam of well defined energy T_1 is passed through the target gas and the kinetic energy T_2 of the forward scattered $X^{(q-1)+}$ ions formed as products of single collisions is then measured. The difference in kinetic energy ΔT is then given by

$$\Delta T = T_2 - T_1 = \Delta E - \Delta K$$

where ΔK is a small recoil correction of the target. Provided that the ratio $\Delta E/T_1 << 1$ and the scattering is confined to small angles, the measured change in translational energy $\Delta T \approx \Delta E$. The relative importance of collision product channels characterised by particular values of ΔE may then be assessed from a careful analysis of the energy change spectra subject to the limitations of the available energy resolution.

The TES approach has been extremely successful in providing definitive data for many different processes including collisions in atomic hydrogen. However, in many processes, TES studies have revealed the presence of collision channels associated with metastable ions in addition to ground state ions in the primary ion beam (cf. review by Gilbody [1]). For example, in the case of one-electron capture in C^{2+} - H(1s) collisions, our TES measurements [2] identified collision product channels associated with both ground state C^{2+} $(2s^2)$ ^1S and metastable C^{2+} (2s2p) $^3P^o$ primary ions. In the range 2 – 8 keV, between 60% and 65% of the observed C^+ product yield arose from channels associated with C^{2+} $^3P^o$ metastable primary ions. In such cases, a detailed quantitative analysis is precluded unless the metastable content of the beam can be specified. These TES measurements also indicate that many previous measurements of total electron capture cross sections carried out with ion beams containing unknown fractions of metastable ions must be interpreted with caution. Indeed, in some cases, large discrepancies between total cross sections measured in different laboratories seem likely to be due to the use of beams containing different and unknown fractions of metastable ions.

In the modelling of edge plasmas in fusion devices, there is a need for data on electron capture by both ground state and metastable species. An attractive solution to this difficult problem is provided, in principle, by the use of the technique of double translational energy spectroscopy (DTES). In this approach, primary ions in a particular ground or metastable state are prepared by electron capture collisions in a suitable gas target and then selected and identified by TES. The selected ions in well defined states are then used as primary ions in a second stage of TES to study electron capture in the target gas of interest without any ambiguities in the interpretation of the collision product channels. The feasibility of DTES was first demonstrated by Huber *et al* [3] in 1984, but was not seriously applied until the recent series of measurements carried out in this laboratory. To date, we have studied one-electron capture by C^{2+} ^1S ground state and C^{2+} ^3P metastable ions in He, Ne, Ar, H_2, N_2 and O_2 [4, 5] by N^{2+} ^2P ground state ions in He, Ne, Ar and H_2 [6, 7] and by O^{2+} ^3P ground state ions in He, Ne and Ar [8]. Recently, we have also succeeded in carrying out DTES measurements in atomic hydrogen for one-electron capture by C^{2+} ^1S ground state and C^{2+} ^3P metastable ions [9], by N^{2+} ^2P ground state ions [10] and by O^{2+} ^3P ground state ions [11]. Unlike our previous TES measurements, which employed a tungsten tube furnace to provide a target of highly dissociated hydrogen, we have used a specially developed aluminium target cell fed with highly dissociated hydrogen from a microwave-driven discharge source. All the measurements to date have been carried out within the range 0.8 – 6 keV. In this review, we shall describe the results obtained for a few representative processes.

2. EXPERIMENTAL APPROACH

A schematic diagram of the basic DTES apparatus is shown in figure 1. In order to provide a state-prepared beam of X^{2+} ions, an intense beam of X^{3+} ions is first extracted from an ECR ion source. This beam is focused, momentum analysed by a double focusing magnet and then enters the electrostatic lens system L1 of the double translational energy spectrometer. After focusing and deceleration by L1, the beam passes though the hemispherical electrostatic energy analyser EA1 at an energy of 40q eV (where q = 3). The emerging energy resolved beam of intensity about 0.2 nA and with an energy spread corresponding to about 1 eV FWHM , is accelerated by lens L2 to an energy of qV_{01} eV. It then enters the first target cell T1 containing helium where the gas pressure is adjusted to maximise the transmitted yield of X^{2+} ions formed by electron capture collisions.

The X^{2+} products emerging from T1 are decelerated and focused by the lens system L3 before entering the hemispherical analyser EA2. Application of an appropriate positive bias

voltage V_{R1} to EA2 and the associated lenses L3 and L4 ensures passage of the X^{2+} ions while rejecting X^{3+} primary ions. The acceptance energy of EA2 is 60(q - 1) eV. By adjusting the scanning voltage V_{S1} the translational energy change spectrum obtained from EA2 in this first stage of TES can be displayed and used to select X^{2+} ions in either the ground or metastable state. This is illustrated in figure 2 which shows the energy change spectrum obtained for C^{2+} ions formed by one-electron capture by 15 keV C^{3+} ions in helium. In this case, a beam of either ^{1}S ground state or ^{3}P metastable C^{2+} ions could be produced from the ions comprising peaks A or B respectively. Actually, peak A corresponds to the C^{2+} ($1s^2 2s2p$) ^{1}P excited product channel but this is known to decay very rapidly (see [4]) to the ^{1}S ground state before reaching the second target. In contrast, less than 0.1% of the long-lived ^{3}P metastables in peak B decay in transit to the second target.

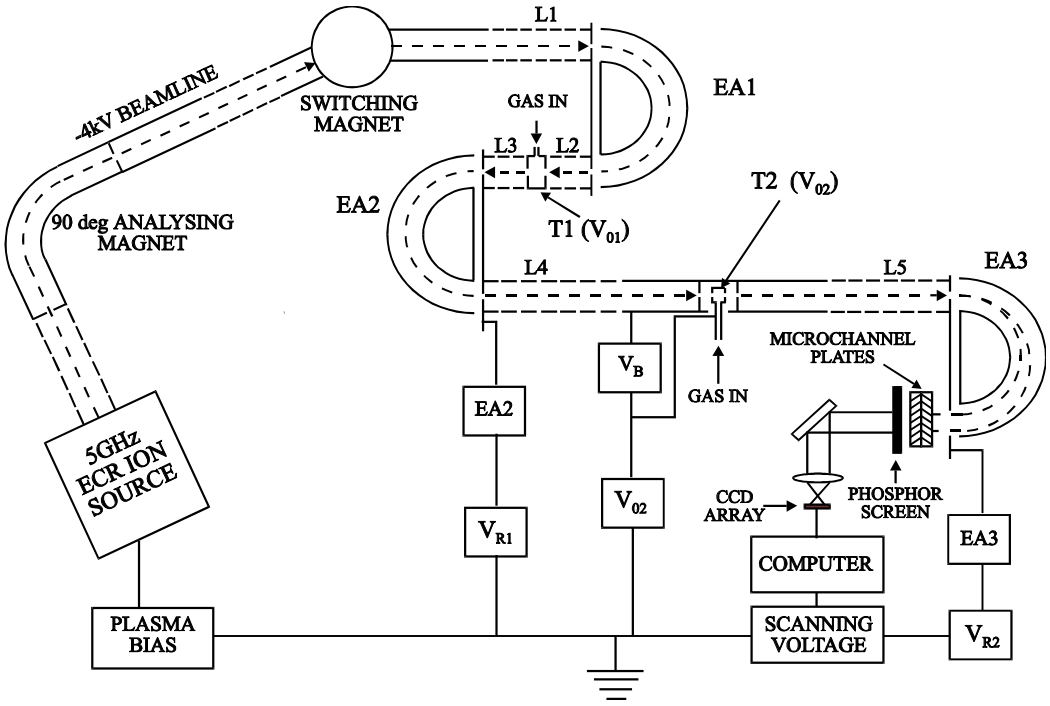

Figure 1. Schematic diagram of the DTES apparatus (from [4]).

A pure beam of either ^{1}S ground state or ^{3}P metastable C^{2+} ions emerging from EA2 is accelerated and focused by lens system L4 into the main target gas cell T2. The gas pressure in T2 is low enough to ensure single collision conditions. The forward-scattered C^{2+} products emerging from T2 are decelerated and focused by lens L5 into the final electrostatic analyser EA3. As in the case of electron capture in the target cell T1, appropriate potentials were applied to L5 and EA3 to allow product C^+ ions to enter with an energy of 40(q - 2) eV. The energy analysed product C^+ ions from EA3 are counted by a computer controlled position sensitive detector.

Our DTES measurements with N^{2+} and O^{2+} ions were carried out with beams in well-defined states prepared in a similar way. However, unlike C^{2+} ions where yields of both the ground state and metastable species were adequate, only the ground state components of the N^{2+} and O^{2+} beams have usually been intense enough to be able carry out the second stage TES measurements.

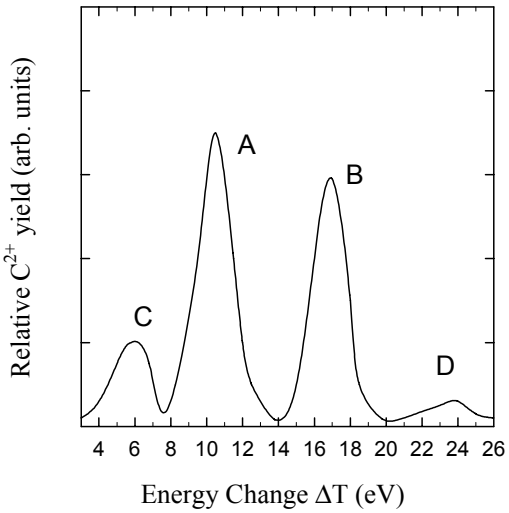

Figure 2. Energy change spectrum of C^{2+} ions formed in one-electron capture by 15 keV C^{3+} ions in helium (from [4]).

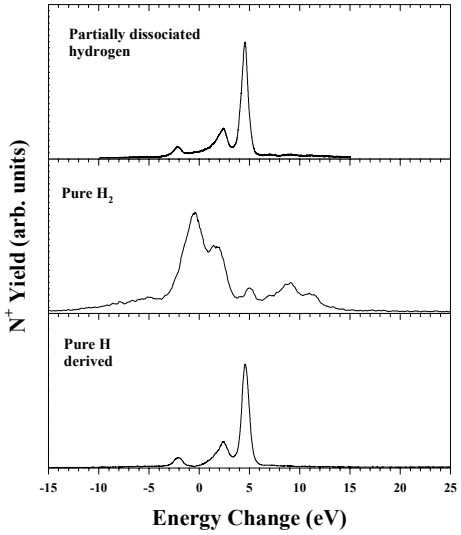

Figure 3. Energy change spectra at 3 keV measured for one-electron capture by pure N^{2+} $^2P^o$ ions in highly dissociated hydrogen, in pure H_2 and derived (see text) for pure H atoms.

In order to carry out DTES measurements in an atomic hydrogen target, the gas cell T2 in figure 1 is replaced by an aluminium target cell fed by a microwave-driven hydrogen discharge source (see [10]). The tube is held typically at a potential of + 50V with respect to the surrounding region. This voltage labelling ensures that the collisions occurring in the region outside the cell do not contribute to the observed energy change spectrum.

Although highly dissociated hydrogen is injected into the target cell, H_2 molecules are formed by collisions with the cell walls so that the spectra obtained reflects the mixture of H and H_2 present in the cell. Energy change spectra for atomic hydrogen alone can be derived from the measured spectra by subtracting the molecular contribution from the spectra obtained in the 'mixed' target. The accurate subtraction process is facilitated by the ability of the hydrogen source to be rapidly switched from highly dissociated hydrogen to pure H_2.

Typical energy change spectra obtained at 3 keV for one-electron capture by pure N^{2+} $^2P^o$ ground-state ions are shown in figure 3. The spectra for highly dissociated (about 70 %) hydrogen and pure molecular hydrogen can be seen to be very different while the derived spectrum for a pure atomic hydrogen target exhibits clearly defined product channels suitable for quantitative analysis..

Our DTES apparatus does not yet allow absolute measurements of the total one-electron capture cross sections for state-prepared ions. However, in a few measurements with C^{2+} ions it has been possible to use a simple beam attenuation technique to determine the ratios $\sigma(\,^3P\,)/\sigma(\,^1S\,)$ of the total cross sections for metastable and ground state species. Figure 4 shows the attenuation of a beam of pure metastable or ground state C^{2+} ions in helium as the target thickness μ is increased so that the total recorded beam intensity follows the simple relation $I = I_0\, e^{-\mu\sigma}$. Analysis [4] of plots of this type in helium, neon and argon at 4 keV, provide ratios $\sigma(\,^3P\,)/\sigma(\,^1S\,) = 11.5 \pm 3.0,\ 3.1 \pm 0.2$ and 3.5 ± 0.3 respectively. These observations indicate the need for cautious interpretation of any measurements of cross sections carried out with ion beams of unknown metastable content.

3. RESULTS AND DISCUSSION

3.1. DTES measurements with C^{2+} ions

As already noted, our previous TES studies [2] of the electron capture process

$$C^{2+} + H(1s) \rightarrow C^{+}(n, l) + H^{+}$$

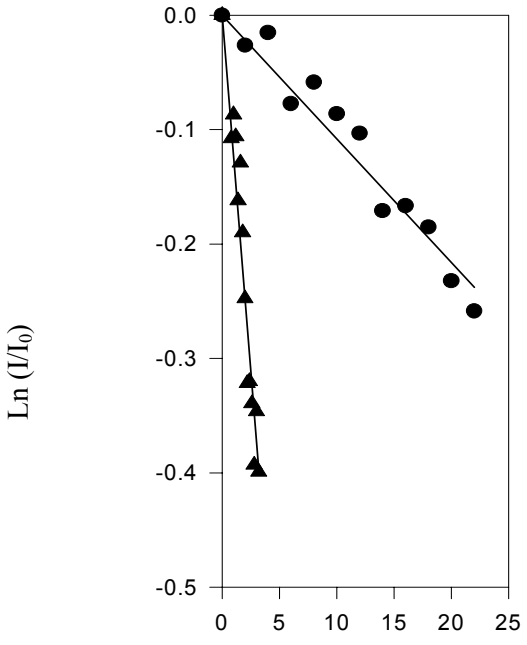

Figure 4. Attenuation by one-electron capture collisions in helium of pure ground state C^{2+} ^1S (●) and pure metastable C^{2+} ^3P (▲) ion beams at 4 keV as the target thickness μ is increased (from [4]).

were carried out with ion beams of unknown metastable content and the observed energy change spectra exhibited channels associated with both $C^{2+}(2s^2)^1S$ ground state and $C^{2+}(2s2p)^3P^o$ metastable primary ions. Our recent DTES measurements [9] carried out at 6 keV, remove the ambiguity of interpretation of the earlier measurements and allow the relative importance of the product channels to be determined for both $C^{2+}\ ^1S$ ground state and $C^{2+}\ ^3P^o$ primary ions. Figure 5 shows the energy change spectra observed for each of these selected ions in a highly dissociated hydrogen target, in a pure H_2 target and the derived spectra for a pure H atom target after the molecular contributions have been subtracted.

In figure 5 we include for comparison, relative cross sections for specific product channels based on our calculations [9], using an impact parameter semi-classical treatment and a molecular expansion including a common translation factor, and those of Gu *et al* [12] which considered only the case of $C^{2+}\ ^1S$ ions. To facilitate this comparison, the maximum calculated partial cross sections have been normalised to the maximum observed peak in the energy spectra. In the $C^{2+}\ ^1S$ - H case, the observed dominance of the G2 channel is confirmed by theory, and there is reasonable accord between experiment and theory for relative magnitudes of the exothermic channels G1 and G2. This is also true in the case of the two endothermic channels G4 and G5 but observed channels G3 and G6 are smaller than the calculated values.

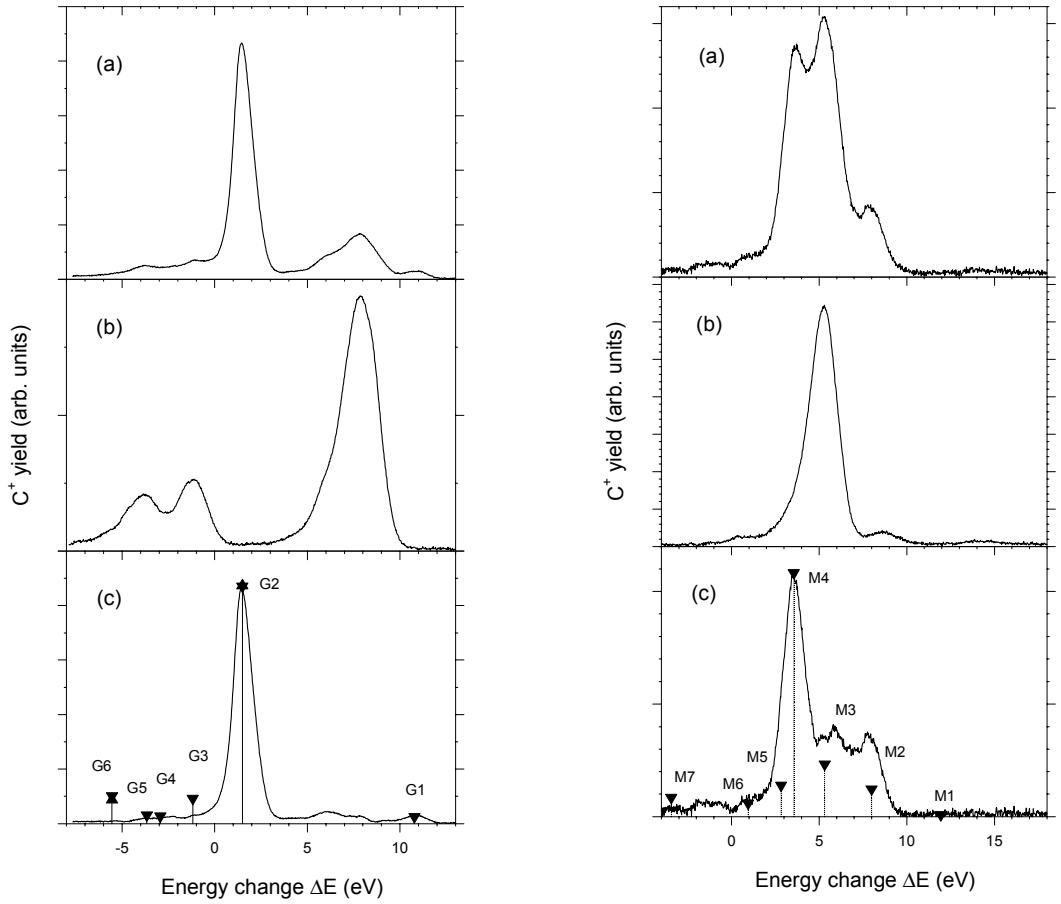

Figure 5. Energy change spectra (from [9]) for one-electron capture by 6 keV $C^{2+\ 1}S$ ions (left hand block) and by $C^{2+\ 3}P^o$ ions (right hand block) in (a) highly dissociated hydrogen, (b) in pure H_2 and (c) derived for pure H. In (c) relative values (▼) and(▲) are based on calculations [9] and [12] respectively. Collision product channels designated G and M are identified in table 1.

TABLE 1. MEASURED YIELDS OF ELECTRON CAPTURE CHANNELS IN ATOMIC HYDROGEN FOR 6 KEV C^{2+} ^1S IONS (DESIGNATED BY G) AND FOR C^{2+} ^3P IONS (DESIGNATED BY M) COMPARED WITH CALCULATED VALUES [9].

Peak	Product Channels	Energy Defect ΔE (eV)	Percentage of total yield	
			Measurement	Calculation
G1	$C^+ (2s^2 2p)\ ^2P^o + H^+$	10.78	3.5	2.2
G2	$C^+ (2s2p^2)\ ^2D + H^+$	1.49	88	75.9
G3	$C^+ (2s2p^2)\ ^2S + H^+$	-1.18	4	8.0
G4	$C^+ (2s2p^2)\ ^2P + H^+$	-2.94	2	2.4
G5	$C^+ (2s^2 3s)\ ^2S + H^+$	-3.66	1.5	2.7
G6	$C^+ (2s^2 3p)\ ^2P^o + H^+$	-5.54	1	8.8
M1	$C^+ (2s2p^2)\ ^4P + H^+$	11.95	0.5	0.5
M2	$C^+ (2s2p^2)\ ^2D + H^+$	7.99	18	7.1
M3	$C^+ (2s2p^2)\ ^2S + H^+$	5.32	20.5	13.5
M4	$C^+ (2s2p^2)\ ^2P + H^+$	3.56	46	62.5
M5	$C^+ (2s^2 3s)\ ^2S + H^+$	2.83	6	8.1
M6	$C^+ (2s^2 3p)\ ^2P^o + H^+$	0.95	4	3.5
M7	$C^+ (2s^2 3d)\ ^2D + H^+$	-0.78	3	0.0
M8	$C^+ (2s2p3s)\ ^4P + H^+$	-3.43	2	4.8

In the C^{2+} $^3P^o$ - H spectrum, the dominant channel M4 is correctly predicted by theory, but there are differences between experimental and calculated relative values for all the channels.

Figure 6 shows the energy change spectra obtained [5] for one-electron capture by 4 keV C^{2+} ions in collisions with H_2. The spectrum obtained using a beam of C^{2+} ions with unknown metastable content obtained directly from our ECR ion source exhibits the same main features observed in the TES measurements of Unterreiter *et al* [13]. Our DTES spectra in figure 6 exhibit evidence of H_2^+ being formed in vibrationally excited states and we show the position of channels up to $v = 11$. For C^{2+} ^1S ground state ions, electron capture involves only the three product channels:

$$C^{2+1}S + H_2 \rightarrow C^+ (2s^2 2p)\ ^2P + H_2^+ X^2\Sigma_g^+ (v = 0 \rightarrow 11) + 8.96 \rightarrow 6.84 \text{ eV} \quad \text{designated G1}$$

$$C^+ (2s2p^2)\ ^2D + H_2^+ X^2\Sigma_g^+ (v = 0 \rightarrow 11) - 0.33 \rightarrow -2.54 \text{ eV} \quad \text{designated G2}$$

$$C^+ (2s2p^2)\ ^2S + H_2^+ X^2\Sigma_g^+ (v = 0 \rightarrow 11) + 6.15 \rightarrow 3.94 \text{ eV} \quad \text{designated G3}$$

The electron capture process for C^{2+} $^3P^o$ ions is highly selective with only one significant channel

$$C^{2+}\ ^3P^o - H_2 \rightarrow \quad C^+(2s2p^2)\ ^2D + H_2^+ X^2\Sigma_g^+ (v = 0 \rightarrow 11) \quad + 6.15 \rightarrow 3.94 \text{ eV designated M1.}$$

The well separated G and M collision product channels in the DTES spectra allows us to confirm the absence of the spin - forbidden product channel $C^+ (2s2p^2)\ ^4P + H_2^+ X^2\Sigma_g^+ (v)$. It is also worth noting that the asymmetry evident in the observed peaks reflect the influence of the Franck-Condon factors for $H_2X^1\Sigma_g^+(v = 0) \rightarrow H_2^+X^2\Sigma_g^+(v)$ transitions on the probability for electron capture into a particular level. The positions of the maxima in G2, G3 and M1 can be seen to be close to v = 2 where the Franck-Condon factor is known to have a maximum value [14]. However, the maximum in peak G1 is closer to v = 5. Recently,

calculations by Errea *et al* [27] have predicted a maximum in the vibrational distribution after capture in $C^{2+}\,{}^3P^o - H_2$ collisions near v = 3 at 4 keV.

We have calculated a reaction window (see [15]) for one-electron capture in $C^{2+}\,{}^1S - H_2$ collisions based on the dependence of the single crossing Landau-Zener cross section for a series of crossings in the range covered by the energy change spectra. The calculated reaction window extends from ΔE = 3.0 to 7.4 eV. However, in figure 6, it can be seen that such a window can only accommodate the products in the higher vibrationally excited states within peak G1 while the products within peaks G2 and G3 lie completely outside this window.

Energy change spectra obtained for C^{2+} - He collisions [4] are shown in figure 7. Here, results obtained using a C^{2+} ion beam of unknown metastable content derived directly from our ECR ion source may be compared with DTES spectra for pure $C^{2+}\,{}^1S$ ground state and pure $C^{2+}\,{}^3P$ metastable ions. In the case of ground state $C^{2+}\,{}^1S$ ions, the two exothermic peaks G1 and G2, surprisingly, both arise from collisions with an unidentified trace impurity species.

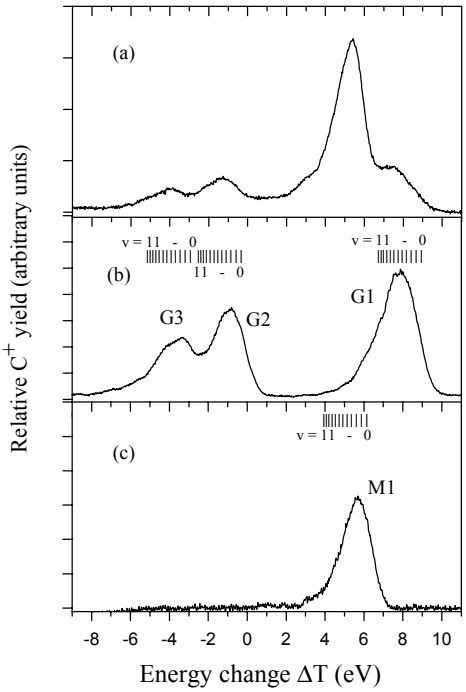

Figure 6. Energy change spectra for one-electron capture in 4 keV C^{2+}- H_2 collisions (from [5]). The spectrum (a) for C^{2+} ions of unknown metastable content obtained directly from the ion source is compared with the DTES measurements (b) for pure $C^{2+}\,{}^1S$ ground state ions and (c) for pure $C^{2+}\,{}^3P$ metastable ions. Positions of product channels corresponding to the formation of vibrationally excited $H_2^+\,X^2\Sigma_g^+(v)$ which accompany the $C^+(n, l)$ products are shown for v = 0 to 11.

These peaks account for 29% of the total product signal in spite of the fact that the background pressure in the collision region was about 100 times lower than the helium target gas pressure. Only the following two G channels, which are both endothermic, arise from collisions with He:

$$C^{2+}\,{}^1S + He \rightarrow C^+\,(1s^2 2s^2 2p)^2P + He^+\,(1s)^2S - 0.20\ eV \quad \text{designated G3}$$

$$C^{+}\,(1s^2 2s 2p^2)^2D + He^{+}(1s)^2S - 9.50\ eV \quad \text{designated G4}$$

The dominant contribution to the C^{+} product ion yield arises from the G3 channel while the much smaller contribution from G4 channel involves core electron rearrangement.

In the case of $C^{2+}\ ^3P$ metastable ions, electron capture occurs mainly via the exothermic channel

$$C^{2+}\,^3P + He \rightarrow \quad C^{+}\,(1s^2 2s^2 2p)^2P + He^{+}(1s)^2S + 6.28\ eV \quad \text{designated M1}$$

A minor peak is associated with the channel

$$C^{2+}\,^3P + He \rightarrow \quad C^{+}\,(1s^2 2s 2p^2)^4P + He^{+}(1s)^2S + 0.95\ eV \quad \text{designated M2.}$$

Our DTES studies of electron capture in C^{2+} - He collisions resolve some ambiguities in previous TES measurements carried out with primary beams of unknown metastable content. For example, the peak G2 at 2.8 eV, which corresponds to a trace contaminant, was also observed by Lee e*t al* [16] who suggested that it might be associated with 'metastable' $C^{2+}(2p^2)\ ^3P$ ions in the primary beam, although (see [4]) this state has a lifetime of only 7.7×10^{-10} s.

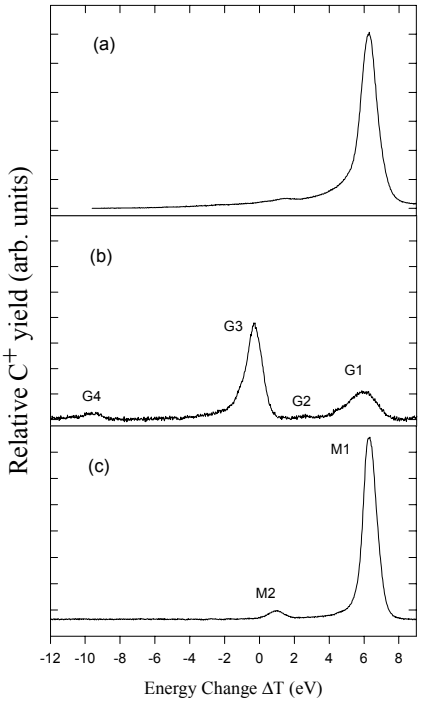

Figure 7. Energy change spectra for one-electron capture in 4 keV C^{2+}-He collisions (from [4]). The spectrum (a) for C^{2+} ions of unknown metastable content obtained directly from the ion source is compared with the DTES measurements (b) for pure C^{2+} ground state ions and (c) for pure $C^{2+}\ ^3P$ metastable ions.

We have also carried out DTES studies of one-electron capture by C^{2+} ions in Ne, Ar [4], N_2 and O_2 [5] which allow the relative importance of the product channels for C^{2+} ^1S ground state and C^{2+} $^3P^o$ primary ions to be determined unambiguously for the first time. Figure 8 shows energy change spectra for C^{2+}- Ar collisions at 4 keV. The spectrum shown

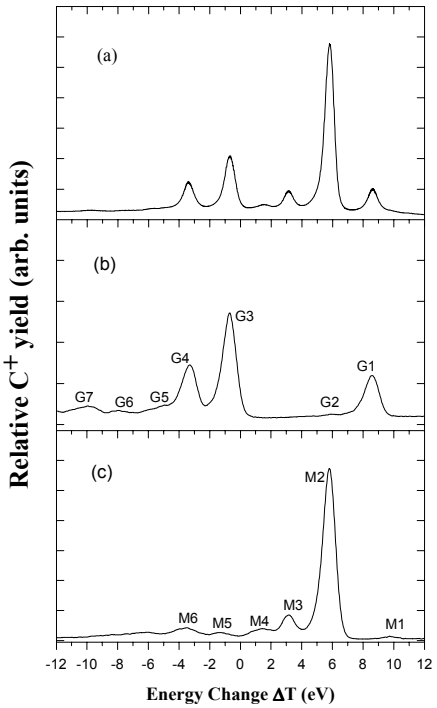

Figure 8. Energy change spectra for one-electron capture in 4 keV C^{2+}- Ar collisions (from [4]). The spectrum (a) for C^{2+} ions of unknown metastable content obtained directly from the ion source is compared with the DTES measurements in (b) for pure C^{2+} ground state ions and (c) for pure C^{2+} ^3P metastable ions.

for an ion beam of unknown metastable content direct from the ion source contains unresolvable contributions associated with one-electron capture by both ground and metastable C^{2+} ions. However, these contributions are clearly identified as peaks G1 – G7 and M1 – M6 in the DTES spectra. A detailed discussion of the channels corresponding to these peaks has been given by Greenwood *et al* [4]. The main peaks G3 in the C^{2+} ^1S ground state spectrum and M2 in the C^{2+} $^3P^o$ metastable spectrum both arise from the product channel C^+ $(2s\ 2p^2)$ ^2D + Ar^+ $(3s^2 3p^5)$ ^2P which involve energy defects of –0.67 eV and + 5.82 eV respectively

3.2 DTES measurements with N^{2+} ions

Recently, we have carried out DTES measurements [10] of the process

$$N^{2+} + H(1s) \rightarrow N^+(n, l) + H^+$$

at energies within the range 0.8 – 6.0 keV using a beam of pure ground-state $N^{2+}(2s^2 2p)$ $^2P^o$ primary ions. These new measurements allow comparison with current theoretical predictions and a re-evaluation of previous TES measurements [17] of this process carried out in this laboratory with ion beams containing an unknown fraction of metastable $N^{2+}(2s2p^2)$ ^4P ions.

Figure 9 shows energy change spectra obtained for one-electron capture by 6 keV N^{2+} ions in atomic hydrogen. The 'mixed' beam spectrum for N^{2+} ions obtained directly from the ion source containing an unknown fraction of metastable ions may be compared with the spectrum obtained using a state-prepared pure N^{2+} ^2P ground-state beam. In this case, the 'mixed' beam and pure ground state spectra are very similar evidently because collision product channels with not greatly different energy defects provide the dominant contributions to both.

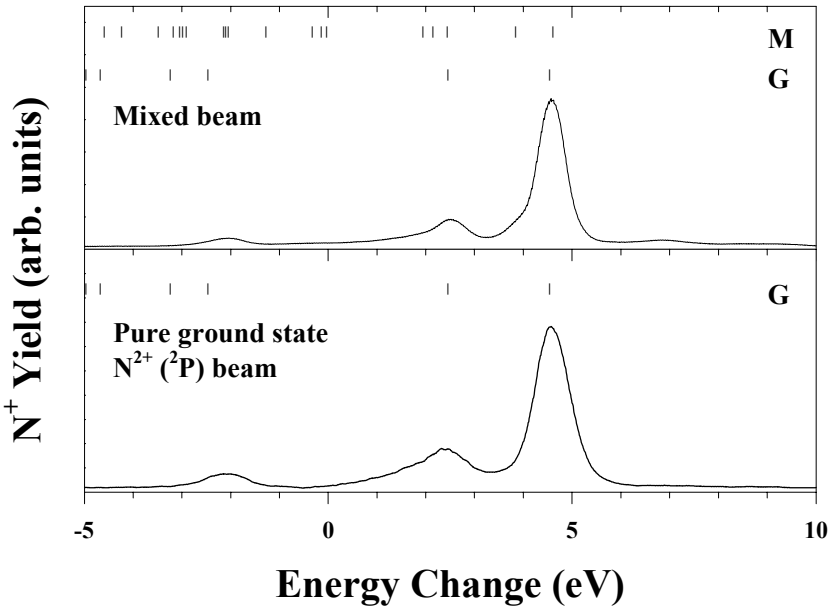

Figure 9. Energy change spectra (from [10]) obtained for one-electron capture by 6 keV N^{2+} ions in atomic hydrogen. The 'mixed' beam spectrum for N^{2+} ions obtained with ions containing an unknown fraction of metastable ions is compared with the DTES spectrum obtained using a pure N^{2+} $^2P^o$ ground-state beam. Positions of possible product channels corresponding to ground-state primary ions (G) and metastable primary ions (M) are also shown.

In the case of ground-state primary ions, the three main product channels can be identified as:

$$N^{2+}\,{}^2P^o + H(1s) \rightarrow \quad N^+(2s2p^3)\,{}^3D^o + H^+ + 4.57\ \text{eV}$$

$$\rightarrow N^+(2s2p^3)\,{}^3P^o + H^+ + 2.46\ \text{eV}$$

$$\rightarrow N^+(2s^22p3s)\,{}^1P^o \text{ or } {}^3P^o + H^+ - 2.49 \text{ or } -2.46\ \text{eV}$$

$$\rightarrow N^+(2s2p^3)\,{}^1D^o + H^+ - 1.87\ \text{eV}$$

of which the two exothermic channels (which involve core excitation) are dominant.

In the case of metastable primary ions, the channels which seem most likely to contribute to the observed 'mixed' beam spectrum are:

$$N^{2+}(2s2p^2)\,^4P + H(1s) \rightarrow N^+(2s^2\,2p3s)\,^3P^o + H^+ + 4.63\ eV$$

$$\rightarrow N^+(2s\,2p^3)\,^3S^o + H^+ + 3.86\ eV$$

$$\rightarrow N^+(2s^2\,2p3p)\,^3D + H^+ + 2.45\ eV$$

$$\rightarrow N^+(2s^2\,2p4p)\,^3D,\ ^3P, \text{or } ^3S + H^+ - 2.04, -2.10 \text{ or } -2.14\ eV$$

The close similarity between the 'mixed' beam and pure ground-state energy change spectra using DTES confirms the results of our earlier TES measurements [17] in the range 0.6 – 8.0 keV using N^{2+} beams which contained an admixture of metastable ions. In those measurements, changes in the metastable fraction were found to have no detectable effect on the measured total electron capture cross sections leading us to conclude that the total cross sections for ground and metastable ions N^{2+} in atomic hydrogen were not greatly different. In view of the lack of dependence of these total cross sections on the metastable content of the primary beam, we have normalised the DTES data obtained at different energies (table 2) to our previously measured total electron capture cross sections [17]. The latter values are in good agreement with measurements by Seim *et al* [18] and by Phaneuf *et al* [19] in the energy ranges of overlap.

TABLE 2. CROSS SECTIONS FOR FORMATION OF $N^+\,^3D^O$, $^3P^O$ AND ($^1P^O + ^3P^O + ^1D^O$) IN $N^{2+}\,^2P^O$ – H(1S) COLLISIONS [10].

Energy (keV)	Cross sections (10^{-16} cm^2)		
	$N^+\,^3D^o$	$N^+\,^3P^o$	$N^+(\,^1P^O + ^3P^O + ^1D^O)$
0.8	3.19 ± 0.26	0.32 ± 0.26	-
1.2	2.97 ± 0.36	0.40 ± 0.37	-
1.5	3.16 ± 0.31	0.30 ± 0.31	-
3.0	3.80 ± 0.63	0.88 ± 0.51	0.15 ± 0.68
6.0	3.53 ± 0.53	1.70 ± 0.45	0.43 ± 0.62

In figure 10, these cross sections for $N^+\,^3D^o$, $^3P^o$ and $N^+(\,^1P^O + ^3P^O + ^1D^O)$ formation can be seen to be in good accord with the values obtained in our previous TES measurements [17]. However, it is important to note that, in the lower resolution measurements of [17], the small peak comprising the N^+ ($^1P^o + ^3P^o + ^1D^o$) contributions from endothermic channels were incorrectly identified as due to the N^+ ($^1D^o$) product channel alone. In addition, the measurements of [17] also recorded at and above 6 keV very small contributions from a $N^+(2s^2 2p3p)\,^3P$ product channel corresponding to ΔE = - 5.17 eV; these are absent in the higher resolution DTES measurements. Figure10 also includes cross sections for the main $^3D^o$ product channel calculated by Bienstock *et al* [20] using a molecular approach which extends earlier theoretical work by Heil *et al* [21]. These calculations predict the $^3D^o$ product channel is the only significant electron capture channel at the energies considered and are therefore at variance with experiment. More recent quantal calculations carried out by Herrero *et al* [22], in which molecular states were obtained using *ab initio* SCF-CI methods, correctly predict contributions from channels other than the dominant $^3D^o$ product channel.

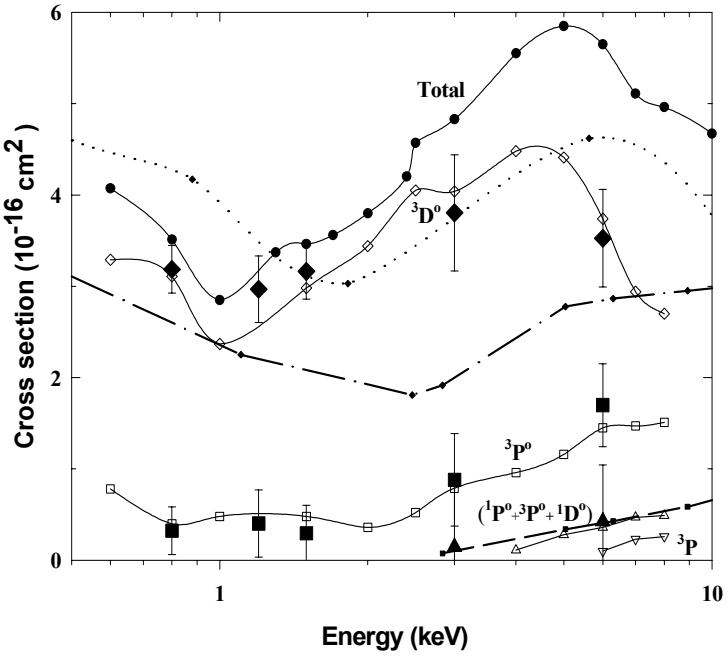

Figure 10. Cross sections for one-electron capture by N^{2+} ions in atomic hydrogen leading to specified $N^+(n, l)$ products. DTES measurements [10] with pure ground-state N^{2+} $^2P^o$ ions, ◆, $^3D^o$; ■, $^3P^o$;▲, ($^1D^o$ + $^1P^o$ + $^3P^o$). Previous TES measurements [17] using an N^{2+} beam containing an unknown fraction of metastable ions, ●, total; ◊ , $^3D^o$; □, $^3P^o$; Δ, ($^3P^o$ + $^1P^o$ + $^1D^o$); ∇, ^3P. Theory by Bienstock et al [20], · · · · · · · ·, ^{3}D^o. Theory by Herrero et al [22], — · — · , $^3D^o$; — — —, $^3P^o$.

However, in the energy range shown in figure 10, their calculated cross sections for the ^{3}D^o and ^{3}P^o channels are not in very satisfactory agreement with the experimental values.

Although our measurements have shown that cross sections for one-electron capture in N^{2+} - H collisions at keV energies are insensitive to the metastable content of the ion beams used, this is certainly not the case for collisions with H_2. We have carried out DTES studies of one-electron capture by N^{2+} ^{2}P^o ground state ions in collisions with H_2 at energies within the range1.75 - 8 keV [7] which resolve discrepancies and serious ambiguities in previous measurements carried out with N^{2+} beams containing unknown fractions of metastable ions. At the energies considered, both non-dissociative and dissociative electron capture channels of the type

$$N^{2+} + H_2 \rightarrow N^+ (n, l) + H_2^+ (\Sigma)$$

$$\rightarrow N^+ (n, l) + H^+ + H(n', l')$$

are found to be significant. In figure 11, which shows DTES data obtained at 6 keV, the pure ground state and 'mixed' N^{2+} beam energy change spectra can be seen to be very different.

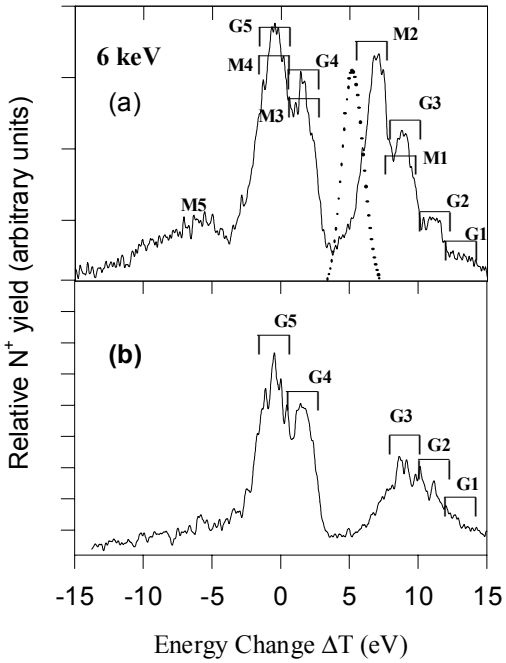

Figure 11. Energy change spectra for one-electron capture in 6 keV N^{2+}- H_2 collisions (from [7]). The spectrum in (a) for N^{2+} ions of unknown metastable content obtained directly from the ion source is compared with the DTES measurements in (b) for pure N^{2+} $^2P^o$ ground state ions. Peaks designated G and M correspond to primary ions in the respective $^2P^0$ ground state and ^4P metastable states. A calculated Landau-Zener reaction window is shown by a dotted line.

While the pure ground state spectrum can be interpreted unambiguously, the prominent peak M2 around 7 eV in the mixed beam spectrum illustrates the strong influence of an unknown admixture of metastable ions. In addition, the long endothermic tail, which is less prominent in the pure ground state spectrum, extends back to about -15 eV and makes a significant contribution to the total N^+ signal. This includes many contributing channels including dissociative one-electron capture via the H_2^+ $A^2\Sigma_u^+$ repulsive state. The G and M channels shown in Figure 11 are identified in table 3. While a full quantitative analysis of the G peaks in our energy change spectra obtained with pure ground N^{2+} ions is precluded by insufficient energy resolution, the peaks (G1+G2+G3), G4 and G5 account for about 37%, 18% and 32% respectively of the total N^+ yield at 8.0 keV and about 31%, 18% and 35% of the total at 6.0 keV. The substantial differences between the pure ground state and mixed beam energy change spectra indicate that interpretations of previous TES measurements and, indeed total cross section measurements, in terms of an assumed 100% ground state primary ion beam are invalid. For example, the energy change spectrum published by Rajgara *et al* [23] at 1.75 keV is considerably different from both our mixed beam spectrum (with a likely different metastable content) and our pure ground state spectrum. Their spectrum, unlike ours, shows no evidence of collision channels in the range -2 to 1 eV. In addition, while they do observe a peak near 7 eV (which our measurements clearly show corresponds to the metastable channel M2) they wrongly attribute this to a ground state primary ion channel. The DTES data are also at variance with our earlier TES measurements (McCullough *et al* [24]) at 8 keV where no channels associated with metastable primary ions were observed.

TABLE 3. COLLISION PRODUCT CHANNELS FOR ONE-ELECTRON CAPTURE IN N^{2+} - H_2 COLLISIONS. PEAKS DESIGNATED G AND M (FIGURE 11) CORRESPOND TO PRIMARY IONS IN THE RESPECTIVE $^2P^o$ GROUND STATE AND ^4P METASTABLE STATES. THE ENERGY DEFECTS SHOWN ALLOW FOR VIBRATIONAL EXCITATION OF H_2^+($\nu = 0 \rightarrow$ D.L) WHERE D.L IS THE DISSOCIATION LIMIT

Peak	Collision product channels	Energy defect (eV)
G1	$N^+ 2s^2 2p^2 (^3P) + H_2^+ (X\ ^2\Sigma_g^+ \nu = 0 \rightarrow$ D.L)	$11.51 \rightarrow 14.16$
G2	$N^+ 2s^2 2p^2 (^1D) + H_2^+ (X\ ^2\Sigma_g^+ \nu = 0 \rightarrow$ D.L)	$9.61 \rightarrow 12.26$
G3	$N^+ 2s^2 2p^2 (^1S) + H_2^+ (X\ ^2\Sigma_g^+ \nu = 0 \rightarrow$ D.L)	$7.46 \rightarrow 10.11$
G4	$N^+ 2s2p^3 (^3D) + H_2^+ (X\ ^2\Sigma_g^+ \nu = 0 \rightarrow$ D.L)	$0.07 \rightarrow 2.72$
G5	$N^+ 2s2p^3 (^3P) + H_2^+ (X\ ^2\Sigma_g^+ \nu = 0 \rightarrow$ D.L)	$-2.03 \rightarrow 0.62$
M1	$N^+ 2s2p^3 (^3D) + H_2^+ (X\ ^2\Sigma_g^+ \nu = 0 \rightarrow$ D.L)	$7.12 \rightarrow 9.77$
M2	$N^+ 2s2p^3 (^3P) + H_2^+ (X\ ^2\Sigma_g^+ \nu = 0 \rightarrow$ D.L)	$5.02 \rightarrow 7.67$
M3	$N^+ 2s^2 2p3s (^3P) + H_2^+ (X\ ^2\Sigma_g^+ \nu = 0 \rightarrow$ D.L)	$0.10 \rightarrow 2.75$
M3	$N^+ 2s2p^3 (^3S) + H_2^+ (X\ ^2\Sigma_g^+ \nu = 0 \rightarrow$ D.L)	$-0.67 \rightarrow 1.98$
M3	$N^+ 2s^2 2p^2 (^3P) + [H_2^+ (A^2\Sigma_u^+) \rightarrow H^+ + H]$	3.0 ± 2.0
M4	$N^+ 2s^2 2p3p (^3P) + H_2^+ (X\ ^2\Sigma_g^+ \nu = 0 \rightarrow$ D.L)	$-2.09 \rightarrow 0.56$
M4	$N^+ 2s2p^2 (^5S) + [H_2^+ (A^2\Sigma_u^+) \rightarrow H^+ + H]$	-3.0 ± 2.0

Since there are no detailed theoretical studies of the N^{2+} - H_2 system, we have calculated Landau-Zener windows (see McCullough *et al* [15] for N^{2+} $^2P^o$ impact as shown in figure 11. These windows are found to be seen to be centred on energies which shift from about 4.5 eV at 1.75 keV to about 5.2 eV at 8 keV. As in the case shown in figure 11, the main observed collision channels are not well described by these reaction windows.

We have also carried out DTES studies of one-electron capture in collisions of N^{2+} with He, Ne and Ar [6] which also provide a more detailed and reliable assessment of the main collision product channels than has been possible in previous studies.

3.3 DTES measurements with O^{2+} ions

The interpretation of previous total electron capture cross sections and TES measurements with O^{2+} ions has been complicated by the possible presence of O^{2+} $(2s^2 2p^2)$ ^1D and O^{2+} $(2s^2 2p^2)$ ^1S metastable ions in addition to O^{2+} $(2s^2 2p^2)$ ^3S ground state ions in the primary ion beams. For example, our previous TES studies [25] of one-electron capture in O^{2+}- H(1s) collisions at energies in the range 2 – 8 keV, revealed two peaks in the energy change spectra.. The main peak, which accounts for about 70% of the total O^+ yield could be identified with the ground state primary ion channel

$$O^{2+} (2s^2 2p^2)\ ^3S + H(1s) \rightarrow O^+ (2s2p^3) 2p\ ^4P + H^+ + 6.64\ eV$$

but the available energy resolution could not exclude a possible small contribution from O^{2+} ^1S metastable primary ion channel

$$O^{2+} (2s^2 2p^2)\ ^1S + H(1s) \rightarrow O^+ (2s2p^3) 2p\ ^2D + H^+ + 6.29\ eV$$

The second smaller peak in the observed spectra was correlated with the O^{2+} ^1D metastable primary ion channel

$$O^{2+}(2s^2 2p^2)\ ^1D + H(1s) \rightarrow O^+(2s2p^3)2p\ ^2D + H^+ + 3.45\ eV$$

Figure 12 shows a DTES energy change spectrum [11] obtained at 6 keV for a beam of pure O^{2+} ^3S ground state ions compared with a 'mixed' beam spectrum measured for O^{2+} ions of unknown metastable content direct from the ion source. In the 'mixed' beam spectrum, the O^+ $(2s2p^3)2p$ ^2D contribution in the smaller of the two peaks arising from electron capture by O^{2+} ^1D metastable ions can be clearly seen while, in the pure O^{2+} ^3S spectrum, the single peak corresponds to the O^+ $(2s2p^3)2p$ ^4P product channel. These measurements confirm the low energy quantal calculations by Butler *et al* [26] which predict that only the O^+ $(2s2p^3)2p$ ^4P product channel should be significant for O^{2+} ^3S ground state ion impact.

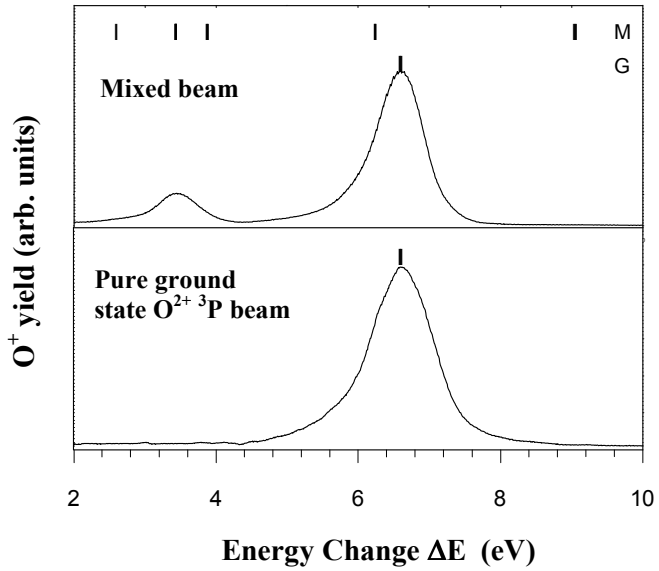

Figure 12. Energy change spectra (from [11]) for one-electron capture in O^{2+} - H(1s) collisions (a) by a beam of O^{2+} ions of unknown metastable content obtained directly from the ion source and (b) by pure O^{2+} ^3S ground state ions prepared by DTES. Possible product channels associated with O^{2+} ^1D metastable ions and O^{2+} ^3S ground state ions are indicated as M and G respectively.

We have also carried out preliminary DTES studies of one-electron capture by O^{2+} ions in He, Ne and Ar [8]. Only in the case of the measurements in He has it so far been possible to obtain energy change spectra for O^{2+} ^1D metastable ions as well as O^{2+} ^3S ground state ions. However, the measurements again demonstrate the advantages of DTES over previous TES measurements where peak assignments have been in doubt.

4. CONCLUSION

Our measurements with state-prepared C^{2+}, N^{2+} and O^{2+} have demonstrated that DTES is a powerful technique capable of providing detailed information on state-selective electron capture without the ambiguities of interpretation associated with previous measurements carried out with ion beams of unknown metastable content. DTES measurements in several atomic and molecular gases of fusion interest and in atomic hydrogen have been made. Our apparatus does not yet provide absolute cross sections for each selected ground or metastable species but the collision product channels can be identified unambiguously and their relative

importance determined. The data provide a much more reliable assessment of the range of validity of a number of theoretical predictions than has been possible previously and help to resolve some of the serious discrepancies in both TES measurements and in total cross sections obtained previously in different laboratories.

This work forms part of the IAEA Co-ordinated Research Project (CRP) on 'Charge Exchange Cross Section Data for Fusion Plasma Studies'. The project has relied on financial support from the U.K. Engineering and Physical Sciences Research Council and it also forms part of the LEIF 2000 and E.C. Framework 5 Thematic Network on Low Energy Ion Facilities.

REFERENCES

[1] GILBODY, H.B., in Advances in Atomic, Molecular and Optical Physics BEDERSON, B., WALTHER, H., Eds.), Academic Press, New York Vol. 33, 1994, 149.
[2] MCCULLOUGH, R.W., WILKIE F.G., GILBODY, H.B., J.Phys.B: At. Mol. Phys.**17** (1984) 1373.
[3] HUBER, B.A., KAHLERT, H.J., WIESEMANN, K.J. Phys.B: At. Mol. Phys.**17** (1984) 2883.
[4] GREENWOOD, J.B., BURNS, D., MCCULLOUGH, R.W., GEDDES, J., GILBODY, H.B. J.Phys.B: At. Mol. Opt. Phys. **29** (1996) 5867.
[5] BURNS, D., GREENWOOD, J.D., BAJAJOVA, K.R., MCCULLOUGH, R.W., GILBODY H B J. Phys. B: At. Mol. Opt. Phys. **30**, (1997) 1531.
[6] BURNS, D., THOMPSON, W.R., GREENWOOD, J.B., MCCULLOUGH, R.W., GEDDES, J., GILBODY, H. B., J. Phys. B: At. Mol. Opt. Phys. **30** (1997) 4559.
[7] BURNS, D., GREENWOOD, J. B., MCCULLOUGH, R.W., GEDDES, J., GILBODY, H.B, J. Phys. B; At. Mol Opt. Phys. **30** (1997) L323.
[8] THOMPSON, W. R., BURNS, D., VOULOT, D., MCCULLOUGH, R.W., GEDDES, J. GILBODY, H.B., Physica Scripta, **T80** (1999) 362.
[9] VOULOT, D., GILLEN, D.R., THOMPSON, W.R., GILBODY, H.B., MCCULLOUGH R.W.,ERREA L., MACÍAS A., MÉNDEZ L., RIERA A., J. Phys.B: Atom.Molec.Opt. Phys. **33** (2000) L187.
[10] VOULOT, D., GILLEN, D.R., KEARNS, D., MCCULLOUGH, R.W., GILBODY, H.B.,J. Phys.B: Atom.Molec.Opt.Phys. 34 (2001) 1039.
[11] MCCULLOUGH, R.W., GILLEN, D.R., VOULOT, D., KEARNS, D., GILBODY, H.B., Physica Scripta – in course of publication.
[12] GU, J-P., HIRSCH, BUENKER, R.J., KIMURA, M., DUTTA, C.M., NORDLANDER, P., Phys. Rev.A. **57** (1998) 4483.
[13] UNTERREITER, E., SCHWEINZER, J., WINTER, H.P., J. Phys. B. At. Mol. Opt. Phys. **24** (1991) 1003.
[14] DUNN, G.H., J. Chem. Phys. **44** (1966) 2592.
[15] MCCULLOUGH, R.W., WILSON, S.M., GILBODY, H.B., J.Phys.B: At. Mol. Phys.**20** (1987) 2031.
[16] LEE, A.R., WILKINS, A.C.R., ENOS, C.S., BRENTON, A.G., Int. J. Mass, Spectrom. Ion. Process**. 134** (1994) 213.
[17] WILKIE, F. G., YOUSIF, F. B., MCCULLOUGH, R.W., GEDDES, J., GILBODY, H.B. J. Phys B: At. Mol. Phys. **18** (1985) 479.
[18] SEIM, W., MULLER, A., WIRKNER-BOTT, I., SALZBORN, E., J. Phys. B. At. Mol. Phys. **14** (1981) 3475.
[19] PHANEUF, R.A., MEYER, F.W., MCKNIGHT, R.A., Phys. Rev.A **17** (1978) 534.

[20] BIENSTOCK, S., DALGARNO, A., HEIL, T.G., Phys. Rev. A **33** (1986) 2078.
[21] HEIL, T. G., BUTLER, S. E., DALGARNO, A., Phys. Rev. A **23** (1981) 1100.
[22] HERRERO, B., COOPER, I. L., DICKINSON, A. S., FLOWER, D.R., J. Phys.B: At. Mol. Opt. Phys. **28** (1995) 711.
[23] RAJARA, F.A., BADRINATHAN, C., MATHUR, D., Int. J. Mass Spectrom. Ion. Process. **134** (1988) 229.
[24] MCCULLOUGH, R.W., LENNON, M., WILKIE, F.G., GILBODY, H.B., J.Phys B: At. Mol. Phys. **16**, (1983) L173.
[25] MCLAUGHLIN, T.K., WILSON, S.M., MCCULLOUGH, R.W., GILBODY, H.B., J.Phys. B: Atom. Molec. Opt. Phys. **23** (1990) 737.
[26] BUTLER, S.E., HEIL, T.G., DALGARNO, A., Astrophys. J. **241** (1980) 442.
[27] ERREA, L.F., MACÍAS, A., MÉNDEZ, L.,RABADÁN, I., RIERA, A., J. Phys.B: Atom.Molec.Opt. Phys. **33** (2000) L165.

Charge exchange between slow doubly charged ions and simple molecules: Translational energy spectroscopy and data survey

M. Albu[b], F. Aumayr[a], J.P. Klein[a], L. Mrazek[c], R. Wörgötter-Plunger[a], Hp. Winter[a]

[a]Institut für Allgemeine Physik, Technische Universität Wien, Vienna, Austria
[b]Permanent Address: National Institute for Physics and Nuclear Engineering "Horia Hulubei", Bucharest-Magurele, Romania
[c]Permanent Address: J. Heyrovsky Institute of Physical Chemistry, Academy of Sciences of the Czech Republic, Prague, Czech Republic

Abstract
We present the final report from TU Wien on our participation in the 1998-2000 IAEA Coordinated Research Program „Charge Exchange Cross Section Data for Fusion Plasma Studies". After shortly pointing out the relevance of CX processes for the fusion plasma edge region, in particular its diagnostics and modelling, we present so far unpublished results from studies conducted by means of TES (translational energy spectroscopy) for single electron capture in edge-plasma relevant collision systems (impact of slow doubly charged ions C^{2+}, N^{2+}, O^{2+} on simple molecules H_2, N_2, O_2, CO). In addition, a collection of recent low impact energy CX data of relevance for plasma edge modelling has been set up.

1. INTRODUCTION

The edge region of magnetically confined fusion plasmas from, e.g., tokamak- or stellarator discharges couples the hot plasma core to the SOL (scrape-off layer) and finally the first-wall surface. It has typically a thickness of some centimeters only but features tremendous gradients for the plasma density and –temperature. The plasma edge is fed by hot plasma constituents (fast particles, radiation) from the inside of the plasma and by slow neutral particles from the outside. The neutral particles are desorbed and sputtered from the first wall and will become rapidly excited and ionized in the plasma edge. A basically similar situation is given in the tokamak divertor region studied for future exhaust of fusion-generated power and -particles. While understanding of the role of the plasma edge for global energy balance and stability of fusion plasma discharges is still far from satisfactory, its decisive importance has been highlighted in the course of numerous recent experimental and theoretical fusion plasma studies. A particular important point concerns the content and transport of impurity ions in the plasma edge which by electron capture from neutrals can strongly influence the local radiation power and thus via „radiation cooling" the steepness of plasma density- and temperature profiles. The importance of these profiles in conjunction with strong magnetic shear for achieving improved plasma confinement by formation of internal transport barriers is evident.
It is with this rather complex background in mind that we are interested in atomic collisions between slow impurity ions and relevant neutral atoms and molecules, as such processes modify the properties of edge plasmas quite significantly. Moreover, characteristic radiation emitted from such collision processes serves for passive and active plasma edge diagnostics which can provide useful insight for edge plasma formation, modification and -behaviour.

2. TRANSLATIONAL ENERGY SPECTROSCOPY FOR SINGLE ELECTRON CAPTURE FROM MOLECULES BY SLOW DOUBLY CHARGED IONS

Motivation

Ion translational energy spectroscopy with comparably high resolution (≤ 100 meV) has been applied at TU Wien for studying single electron capture (SEC) by ground state- and metastable C^{2+} ions from H_2, N_2, O_2 and CO molecules (ion impact energy ≤ 1 keV). It could be shown that the such obtained results agreed satisfactorily with multichannel-Landau-Zener calculations [1, 2]. In continuation of this work, similar measurements have been carried out for impact of N^{2+} and O^{2+} on atomic (He, Ar) and molecular target particles (H_2, N_2, O_2, CO). SEC reactions involving these primary ions and molecular target particles are of interest for a number of reasons, in particular the energy balance of edge plasmas in thermonuclear fusion research and the kinetics of low-temperature plasmas for various technical applications. A sufficiently detailed understanding of these SEC reactions and comparison of the respective experimental data with theory can only be achieved if state-selective information on the electronic states of both collision partners is available. For the molecular targets also vibrational-state selectivity with respect to the final reaction channels is of interest, whereas for the initial channel the molecular particles can be assumed in the vibrational ground state. For the here regarded projectile ion species apart from the ground state two (N^{2+}) or three metastable states (O^{2+}) may be present in the primary ion beam, whereas C^{2+} has only one metastable state. Since at low impact energy the SEC cross sections depend critically on the involved reaction energy defects, the presence of metastable primary ions can be of decisive influence [3]. For O^{2+}-He collisions important SEC channels were only seen for the O^{2+} ground state, but for SEC from Ar the ground-state and the metastable O^{2+} ions were found to be of comparable importance. For O^{2+} impact on N_2 and CO the important features in the observed translational energy spectra (TES) could be attributed to SEC into the ground state ion, but minor participation by metastable ions could be clearly identified. As for C^{2+} impact [1,2] also for N^{2+} and O^{2+} the „reaction window“ for SEC moves for lower impact energy to smaller energy defects which generally increases the relative importance of SEC by the metastable ions. However, not for all of the here studied collision systems an unanimous identification of the prominent TES features could be achieved. For such cases an attenuation cell in front of the translational energy spectrometer can be activated. With suitable attenuation gas species and -densities the different primary ion beam fractions may be strongly varied which results in conspicuous changes in the resulting TES.
As will be explained below, under favourable conditions even absolute total primary-ion state-selective SEC cross sections can be measured in this way. Such pre-attenuation of primary ion beams provides a simple alternative to translational energy spectroscopy with state-prepared primary ions which requires, e.g., electron impact ionization with controlled electron energy [3] or tandem translational energy spectroscopy [4].

Experimental techniques

The applied experimental setup (translational energy spectrometer **LIBUSSA** for **L**ow-energy **I**on **B**eam **U**nit for **S**cattering **S**tudies and -**A**pplications) is sketched in fig. 1. X^{2+} primary ions (in the present case X = N or O) are extracted with an acceleration voltage of 1 kV from a 5 GHz ECR ion source at IAP Wien [5] and transported through the attenuation stage (see below) via sets of steering plates and electrostatic lenses toward an ion monochromator. Before entering the latter the ions are decelerated to their appropriate pass energy (usually a few tens of eV).

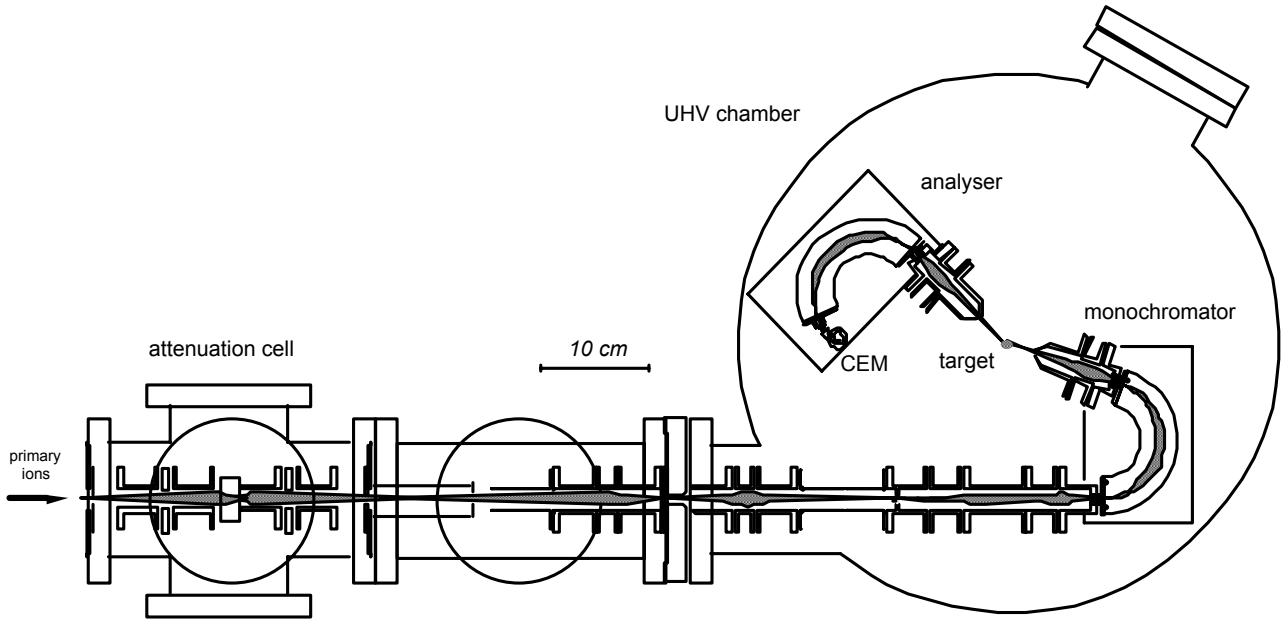

Fig. 1 Sketch of translational energy spectrometer LIBUSSA with pre-attenuation cell.

Between the monochromator and the target gas cell the ions are re-accelerated to the actually desired collision energy and thereafter again decelerated to the pass energy of the ion energy analyzer. The necessary deceleration voltage has to be adjusted for passing those ions through the analyser which have captured an electron from the target particle. The translational energy spectra (TES) are obtained by varying the deceleration voltage by means of a small linear ramp on the analyzer side. In this way the ions which suffer an energy defect characteristic for the respective SEC reaction channel can pass the analyzer and be detected by means of a channel electron multiplier. The kinetic energy of the primary ions can be defined within a FWHM of typically 50 meV per charge state which was found sufficient for resolving post-collisional ions according to the final vibrational states in which the target molecular ions have been left after the SEC. Ion beams delivered by the ECR ion source may also contain long-lived excited (metastable) ions apart from the respective ground state. The electron energy distribution in the ECR plasma is rather broad and can hardly be influenced by the ion source parameters (magnetic field, RF power, working gas pressure) in order to control the metastable fractions. For this reason non-negligible metastable fractions of 10 - 30 %, depending on the respective excitation energy, can be assumed as typical. By means of the pre-attenuation cell (cf. fig. 1) positioned in front of the translational energy spectrometer we may control the absolute fractions of metastable admixture(s) in the primary ion beams.
This can be achieved, if ground state- and metastable components can be attenuated with different efficiency on their passage through a suitably selected attenuation gas. The attenuation gas pressure in the differentially pumped and electrically isolated attenuation cell is set by a piezo-driven UHV gas valve controlled by a Baratron capacitance manometer between typically 10^{-4} and 10^{-3} mbar, with the baqckground pressure outside of the cell being around 10^{-6} mbar. Primary ions are accelerated or decelerated in front of the attenuation cell and thereafter reset to the original kinetic energy before passing on to the translational energy spectrometer.
A set of deflection plates and a small Faraday cup situated behind the attenuation cell permit measurement of current ratios of primary and charge-exchanged ions, from which the corresponding total SEC cross sections may be evaluated. As explained in some detail in

chapter 2.4, combined operation of this attenuation cell and the translational energy spectrometer permits under favourable conditions the determination of respective metastable ion beam fractions. With such information at hand also respective total primary-ion state-selective SEC cross sections can be measured. Inside the vacuum chamber which houses the attenuation cell the primary ion beam is guided by four sets of stearing plates through the attenuation cell and thereafter towards the translational energy spectrometer.

Experimental results and interpretation

The following table shows electronic configurations of ground- and metastable states for the N^{2+} and O^{2+} primary ions of our present interest (data from [6]).

Ion species	ground state	rec. energy (eV)	metastable state	exc. energy (eV)
N^{2+}	$2s^2\ 2p\ ^2P^o$	29,60	$2s\ 2p^2\ ^4P$	7,10
			$2s\ 2p^2\ ^2D$	12,53
			$2s\ 2p^2\ ^2S$	16,24
O^{2+}	$2s^2\ 2p^2\ ^3P$	35,12	$2s^2\ 2p^2\ ^1D$	2,51
			$2s^2\ 2p^2\ ^1S$	5,35
			$2s\ 2p^3\ ^5S^o$	7,48

Furthermore, we list the configurations, ionization energies and vibrational energy distributions of target molecular species of present interest. Approximate energy differences (in eV) for ionization of H_2 and N_2 and for vibrational excitation of H_2^+ and N_2^+ respectively were taken from Herzberg 1950 and Fukuroda et al. 1989, and for ionization of O_2 and CO and vibrational excitation of O_2^+ and CO^+ from Herzberg and Huber 1979, respectively (loc. cit. in [1, 2]).
From the data contained in both tables the reaction energy defects ΔE for various SEC channels can be calculated („gs“ and „ms_i“ refer to the ground- and the i-th metastable state of involved primary ion species, respectively).

$$X^{2+}(gs) + YZ \rightarrow X^+(n,l) + YZ^+(n',l',v') + \Delta E$$

$$X^{2+}(ms_i) + YZ \rightarrow X^+(n,l) + YZ^+(n',l',v') + \Delta E$$

The such calculated reaction energy defects ΔE have to be compared with the energy position of particular TES peaks in order to identify the corresponding SEC reaction channels.

SEC by N^{2+} ions

For N^{2+}+H_2 no clearly structured TES could be measured and the signal intensity was considerably weaker than for all other collision systems, a fact also proven by attenuation measurements. This remarkable finding can only partially be explained by an unfavourable situation for SEC into the ground state (ΔE ≤ 2,73 eV) and the not spin-forbidden SEC into the first metastable state (ΔE ≤ 2,47 eV) with respect to the reaction window. Interestingly, we do also not see the SEC channel involving the highly excited $H_2^+(B\ ^2\Sigma_g^+)$ system according to the reaction $N^{2+}(ms_1) + H_2 \rightarrow N^+(2s2p^3\ ^5S^o) + H_2^+(B\ ^2\Sigma_g^+)$; ΔE = 3,89 eV, nor any contributions from the higher N^{2+} metastable states.

Molecular State	Vibrational transitions v'→ v''						
	0→1	**1→2**	**2→3**	**3→4**	**4→5**	**5→6**	**6→7**
H_2 ($X\ ^1\Sigma_g^+$)	0.52	0.49	0.46	0.43	0.40		
ionization energy to H_2^+ ($X\ ^2\Sigma_g^+$) 15.43 eV, H_2^+ ($B\ ^2\Sigma_g^+$) 27.06 eV.							
H_2^+ ($X\ ^2\Sigma_g^+$)	0.27	0.25	0.24	0.22	0.21	0.19	0.17
H_2^+ ($B\ ^2\Sigma_g^+$)	0.053	0.051	0.050	0.049	0.047		
N_2($X\ ^1\Sigma_g^+$)	0.29	0.29	0.28	0.28	0.27		
ionization energy to N_2^+ ($X\ ^2\Sigma_g^+$) 15.58 eV, N_2^+ ($A\ ^2\Pi_{ui}$) 16.70 eV, N_2^+ ($B\ ^2\Sigma_u^+$) 18.74 eV, N_2^+ ($D\ ^2\Pi_g$) 22,07 eV, N_2^+ ($C\ ^2\Sigma_u^+$) 23,59 eV.							
N_2^+($X\ ^2\Sigma_g^+$)	0.27	0.27	0.26	0.26	0.25		
N_2^+($A\ ^2\Pi_{ui}$)	0.23	0.23	0.22	0.22	0.22		
N_2^+($B\ ^2\Sigma_u^+$)	0.29	0.29	0.28	0.28	0.27		
N_2^+($D\ ^2\Pi_g$)	0.11	0.10	0.10	0.10	0.10		
N_2^+($C\ ^2\Sigma_u^+$)	0.25	0.25	0.25	0.25	0.24		
O_2($X\ ^3\Sigma_g^-$)	0.19	0.19	0.19	0.18	0.18		
ionization energy to O_2^+ ($X\ ^2\Pi_g$) 12.07 eV, O_2^+ ($a\ ^4\Pi_{ui}$) 16.10 eV, O_2^+ ($A\ ^2\Pi_u$) 17.11 eV, O_2^+ ($b\ ^4\Sigma_g^-$) 18.21 eV, O_2^+ ($C\ ^2\Phi_u$) 18.72 eV, O_2^+ ($D\ ^2\Sigma_g$) 19.85 eV, O_2^+ ($B\ ^2\Sigma_g^-$) 20.43 eV, O_2^+ ($c\ ^4\Sigma_u^-$) 24.58 eV.							
O_2^+ ($X\ ^2\Pi_g$)	0.23	0.23	0.22	0.22	0.22		
O_2^+ ($a\ ^4\Pi_{ui}$)	0.13	0.12	0.12	0.12	0.12		
O_2^+ ($A\ ^2\Pi_u$)	0.11	0.10	0.10	0.10	0.09		
O_2^+ ($b\ ^4\Sigma_g^-$)	0.14	0.14	0.14	0.13	0.13		
O_2^+ ($B\ ^2\Sigma_g^-$)	0.14	0.13	0.13	0.12	0.12		
CO($X\ ^1\Sigma_g^+$)	0.27	0.26	0.26	0.26	0.25		
ionization energy to CO^+ ($X\ ^2\Sigma^+$) 14.01 eV, CO^+ ($A\ ^2\Pi_i$) 16.58 eV, CO^+ ($B\ ^2\Sigma^+$) 19.70 eV.							
CO^+($X\ ^2\Sigma^+$)	0.27	0.27	0.26	0.26	0.26		
CO^+($A\ ^2\Pi_i$)	0.19	0.19	0.18	0.18	0.18		
CO^+($B\ ^2\Sigma^+$)	0.21	0.20	0.19	0.19	0.18		

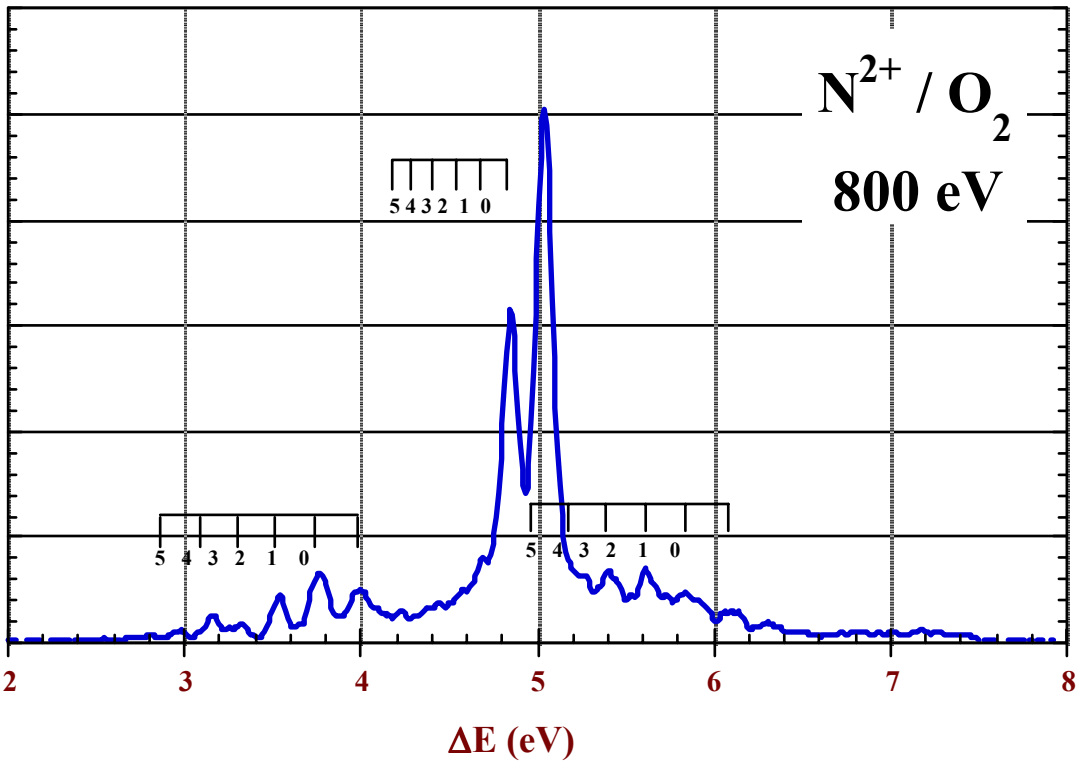

Fig. 2 TES for impact of 800 eV N^{2+} on O_2.
Combs labelled „0, 1, etc." indicate vibrational state distributions of involved final molecular ions (further explanation in text).

$N^{2+}+O_2$

However, these higher states are probably only weakly populated because of a relatively high excitation energy. Anyhow, the apparent „transparency" of H_2 for doubly charged nitrogen ions is remarkable, probably of interest for plasma chemistry and therefore deserves further investigation.

Fig. 2 shows a TES for 800 eV impact energy (for the principal peak at ΔE = 5,02 eV no vibrational states have been indicated as they are not known to us). Four distinct features lie inside or near the reaction window which here is situated between 4,1 eV and 5,2 eV. Three of them, in particular the dominant one, can be attributed to SEC into N^{2+} ground state ions:

$$N^{2+}(gs{:}2s^2 2p\ ^2P^0) + O_2(X\ ^3\Sigma_g^-) \rightarrow N^+(2p^2\ ^3P^o) + O_2^+(c\ ^4\Sigma_u^-);\ \Delta E_{v=0} = 5{,}02\ eV$$

$$N^{2+}(gs{:}2s^2 2p\ ^2P^0) + O_2(X\ ^3\Sigma_g^-) \rightarrow N^+(2p^3\ ^3P^0) + O_2^+(X\ ^2\Pi_g);\ \Delta E_{v=0} = 3{,}99\ eV$$

$$N^{2+}(gs{:}2s^2 2p\ ^2P^0) + O_2(X\ ^3\Sigma_g^-) \rightarrow N^+(2p^3\ ^3D^0) + O_2^+(X\ ^2\Pi_g);\ \Delta E_{v=0} = 6{,}09\ eV$$

However, the second-largest TES peak can only be attributed to SEC into the first metastable state of N^{2+}:

$$N^{2+}(ms_1{:}2s2p^2\ {}^4P) + O_2 \rightarrow N^+(2p^3\ {}^3D^0) + O_2{}^+(B\ {}^2\Sigma_g^-);\ \Delta E_{v=0} = 4{,}83\ eV$$

This last peak proves the presence of a relatively large first metastable ion beam fraction, and its above assignment could be further corroborated by pre-attenuation studies. Given the numerous electronically excited O_2^+ systems (see respective table above), various other SEC reaction channels are also conceivable but obviously not of great importance.

N^{2+}+CO

In the TES shown in fig. 3 (impact energies of 600 and 800 eV), the two largest peaks can be ascribed to SEC into N^{2+} ground state ions:

$$N^{2+}(gs) + CO(X\ {}^1\Sigma_g{}^+) \rightarrow N^+(2p^3\ {}^3D^0) + CO^+(X\ {}^2\Sigma^+);\ \Delta E_{v=0} = 4{,}15\ eV$$
$$N^{2+}(gs) + CO(X\ {}^1\Sigma_g{}^+) \rightarrow N^+(2p^3\ {}^5S^0) + CO^+(B\ {}^2\Sigma^+);\ \Delta E_{v=0} = 4{,}15\ eV$$

(note, however, that the second reaction is spin-forbidden !)

$$N^{2+}(gs) + CO(X\ {}^1\Sigma_g{}^+) \rightarrow N^+(2p^2\ {}^1S) + CO^+(B\ {}^2\Sigma^+);\ \Delta E_{v=0} = 5{,}85\ eV$$

At least three other reaction channels can be identified which all involve the first metastable $N^{2+}(2s2p^2\ {}^4P)$ state:

$$N^{2+}(ms_1) + CO(X\ {}^1\Sigma_g{}^+) \rightarrow N^+(2p^3\ {}^3S^0) + CO^+(X\ {}^2\Sigma^+);\ \Delta E_{v=o} = 3{,}46\ eV$$
$$N^{2+}(ms_1) + CO(X\ {}^1\Sigma_g{}^+) \rightarrow N^+(2p^3\ {}^3P^0) + CO^+(B\ {}^2\Sigma^+);\ \Delta E_{v=o} = 3{,}46\ eV$$
$$N^{2+}(ms_1) + CO(X\ {}^1\Sigma_g{}^+) \rightarrow N^+(3p\ {}^3D^0) + CO^+(B\ {}^2\Sigma^+);\ \Delta E_{v=0} = 5{,}56\ eV$$
$$N^{2+}(ms^1) + CO(X\ {}^1\Sigma_g{}^+) \rightarrow N^+(3p\ {}^3P^0) + CO^+(A\ {}^2\Pi_i);\ \Delta E_{v=0} = 6{,}58\ eV$$

As expected, with lower impact energy all reaction channels become relatively less important with respect to the principal one, for which the energy defect of 4,15 eV lies in the center of the reaction window (cf. fig. 3).

SEC by O^{2+} ions

O^{2+}+H_2

Only one SEC reaction channel is clearly identifiable, starting from the ground state (cf. fig. 4):

$$O^{2+}(gs{:}2p^2\ {}^3P) + H_2(X\ {}^1\Sigma_g{}^+) \rightarrow O^+(2p^4\ {}^4P) + H_2{}^+(X\ {}^2\Sigma_g{}^+);\ \Delta E_{v=0} = 4{,}81\ eV$$

For impact energies between 600 and 1000 eV no particular changes in the population of the different H2+ vibrational states could be observed, obviously because the respective reaction energy defects correspond to the center of the SEC reaction window (maximum at 4,6 eV for

500 eV /2/). Another hint for this conclusion is the relative weak $H_2^+(v=0)$ peak. We cannot rule out, however, that other SEC reaction channels involving the highly excited $H_2^+(B\ ^2\Sigma_g^+)$ system and/or SEC into metastable O2+ ions provide some background to the above main reaction.

O^{2+}+N_2

For O^{2+}+N_2 three channels related to the O^{2+} ground state can be clearly identified in fig. 5.

$$O^{2+}(gs{:}2p^2\ ^3P) + N_2(X\ ^1\Sigma_g^+) \rightarrow O^+(2p^3\ ^2P^0) + N_2^+(C\ ^2\Sigma_u^+);\ \Delta E_{v=0} = 6{,}51\ eV$$

$$O^{2+}(gs{:}2p^2\ ^3P) + N_2(X\ ^1\Sigma_g^+) \rightarrow O^+(2p^4\ ^4P) + N_2^+(X\ ^2\Sigma_g^+);\ \Delta E_{v=0} = 4{,}66\ eV$$

$$O^{2+}(gs{:}2p^2\ ^3P) + N_2(X\ ^1\Sigma_g^+) \rightarrow O^+(2p^4\ ^4P) + N_2^+(A\ ^2\Pi_{ui});\ \Delta E_{v=0} = 3{,}54\ eV$$

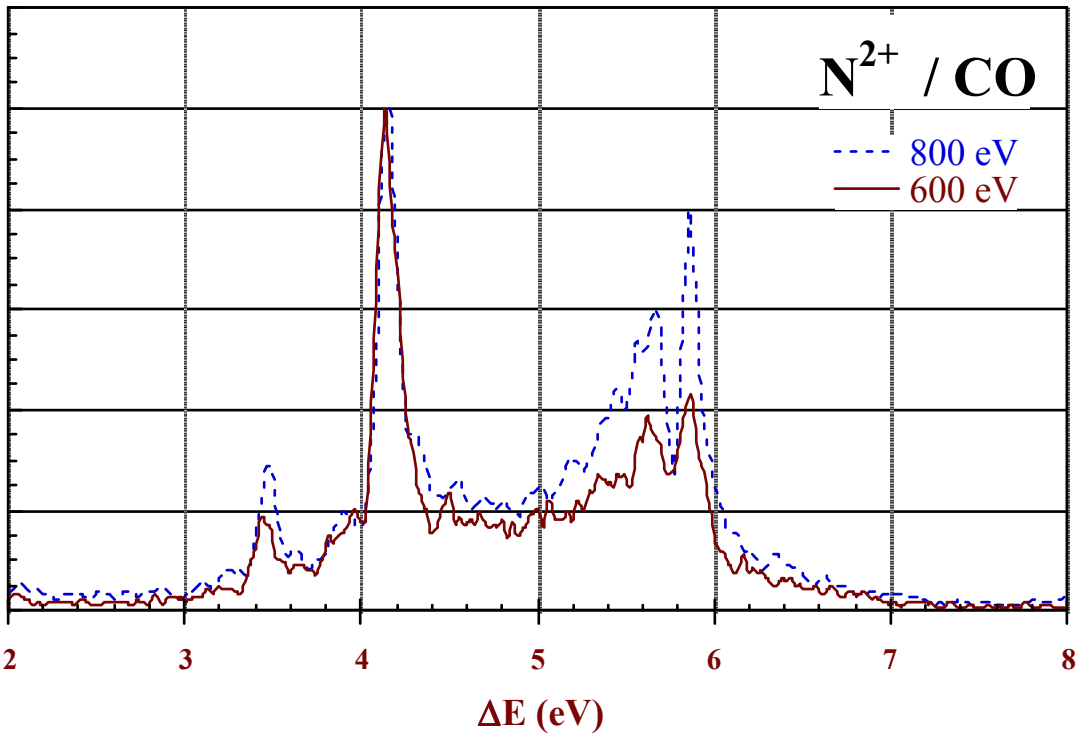

Fig. 3 TES for impact of 600 and 800 eV N^{2+} on CO, respectively (further explanation in text).

The conspicuously dominant peak at ΔE = 4,66 eV lies next to the calculatd maximum of the reaction window (4,5 eV for 500 eV) and exhibits a rather low probability for excited vibrational states of $N_2^+(C^2\Sigma_g^+)$. The other two peaks become relatively more important with increasing impact energy, since they lie on opposite wings of the reaction window. The tail of the TES in the higher energy defect region can either be related to another SEC channel involving the ground state:

$$O^{2+}(gs{:}2p^2\ ^3P) + N_2(X\ ^1\Sigma_g^+) \rightarrow O^+(2p^3\ ^2D^0) + N_2^+(C\ ^2\Sigma_u^+);\ \Delta E = 8{,}21\ eV,$$

and/or to SEC into metastable O^{2+} ions.

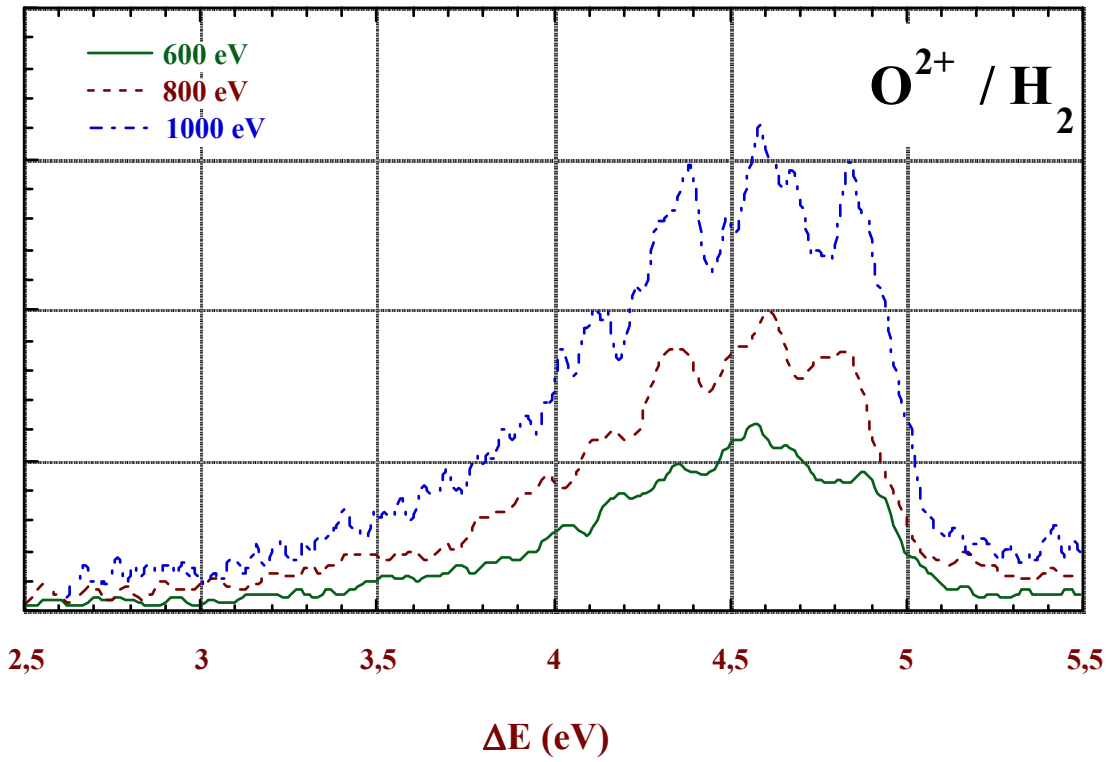

Fig. 4 TES for impact of 600, 800 and 1000 eV O^{2+} on H_2, respectively (further explanation in text).

O^{2+}+CO

For SEC from CO the dominant TES peak involves the ground state (fig. 6):

$$O^{2+}(gs{:}2p^2\ ^3P) + CO(X\ ^1\Sigma_g^+) \rightarrow O^+(2p^4\ ^4P) + CO^+(X\ ^2\Sigma^+)\ ;\ \Delta E_{v=0} = 6{,}23\ eV$$

The second most important peak corresponds to two SEC channels starting with the first metastable state, and its relative importance increases strongly with lower impact energy:

$$O^{2+}(ms1{:}2p^2\ ^1D) + CO(X\ ^1\Sigma_g^+) \rightarrow O^+(2p^4\ ^2D) + CO^+(X\ ^2\Sigma^+);\ \Delta E_{v=0} = 3{,}04\ eV$$
$$O^{2+}(ms1{:}2p^2\ ^1D) + CO(X\ ^1\Sigma_g^+) \rightarrow O^+(2p^4\ ^4P) + CO^+(B\ ^2\Sigma^+);\ \Delta E_{v=0} = 3{,}05\ eV$$

A third series of peaks starting at about ΔE = 3,7 eV is due to SEC from the O^{2+} ground state:

$$O^{2+}(gs{:}2p^2\ ^3P) + CO(X\ ^1\Sigma g^+) \rightarrow O^+(2p^4\ ^4P) + CO^+(A\ ^2\Pi_i);\ \Delta E_{v=0} = 3{,}66\ eV$$

However, two underlying SEC channels may be related to the second metastable O^{2+} state:

$$O^{2+}(ms2{:}2p^2\ ^1S) + CO(X\ ^1\Sigma_g^+) \rightarrow O^+(3s\ ^4P) + CO^+(X\ ^2\Sigma^+);\ \Delta E_{v=0} = 3{,}48\ eV$$
$$O^{2+}(ms2{:}2p^2\ ^1S) + CO(X\ ^1\Sigma_g^+) \rightarrow O^+(2p^4\ ^2D) + CO^+(A\ ^2\Pi_i);\ \Delta E_{v=0} = 3{,}31\ eV.$$

Structures between $4 \leq \Delta E \leq 5$ eV possibly result from SEC by the third O^{3+} metastable state, e.g. the spin-forbidden reaction channel:

$$O^{2+}(ms3{:}2p^3\ ^5S^0) + CO(X\ ^1\Sigma_g^+) \rightarrow O^+(2p^4\ ^2S) + CO^+(X\ ^2\Sigma^+);\ \Delta E = 4{,}32\ eV.$$

There are also possible contributions at the low ΔE side of the main TES peak:

$$O^{2+}(ms2{:}2p^2\ ^1S) + CO(X\ ^1\Sigma_g^+) \rightarrow O^+(2p^4\ ^2D) + CO^+(X\ ^2\Sigma^+);\ \Delta E = 5{,}88\ eV$$

$$O^{2+}(ms3{:}2p^3\ ^5S^0) + CO(X\ ^1\Sigma_g^+) \rightarrow O^+(3s\ ^4P) + CO^+(X\ ^2\Sigma^+);\ \Delta E = 5{,}61\ eV.$$

Maxima of the reaction window are located at 4,4 eV, 4,7 eV and 5,1 eV for the X, A and B states of CO^+ at a collision energy of 500 eV /2/, respectively. Both dominant peaks are therefore situated relatively far away from these maxima.

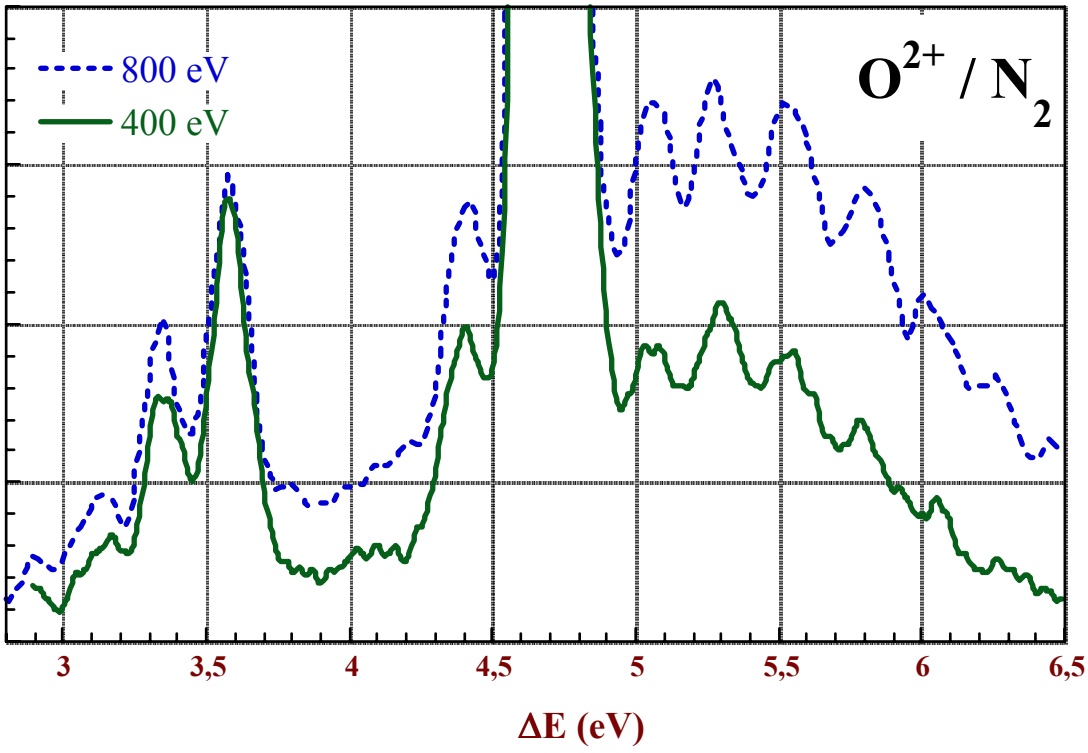

Fig. 5 TES for impact of 400 and 800 eV O^{2+} on N_2, respectively (further explanation in text).

Determination of metastable doubly charged ion beam fractions via „capture attenuation translational spectroscopy" (CATS)

In order to clarify the role of metastable primary ion beam admixtures for SEC by N^{2+} and O^{2+} projectiles, we have supplemented our ion translational energy spectrometer LIBUSSA with a gas-attenuation cell (cf. fig. 1). The following explanation applies to primary ion beams with one metastable component only, but extension to more than one metastable fraction is feasible. Primary ions enter the attenuation cell (attenuation gas density n_{att} and -length l; attenuation target thickness $\Pi_{att} \equiv n_{att}.l$). If SEC causes dominant attenuation (SEC cross sections $Q_{21,g}$, $Q_{21,m}$ for ground- and metastable state ions, respectively), the fluxes F_{go} and

F_{mo} of the two ion beam fractions will be attenuated to F_g and F_m according to

$$F_{g;m}/F_{go;mo} = \exp(- Q_{21,g;m}.\Pi_{att}). \qquad (1)$$

Change of ion beam fractions due to their different attenuation leads to a corresponding change in the translational energy spectra, as is qualitatively demonstrated by a low-resolution TES measurement for $C^{2+}+N_2$ as shown in fig. 7. Since SEC by the metastable ions $C^{2+}(2p\ ^3P^o)$ from He is much more probable than by the ground state ions $C^{2+}(2s^2\ ^1S)$ [7], the metastable primary ion beam fraction will be preferentially attenuated and, as a consequence, its related TES peaks become accordingly less prominent (for corresponding higher-resolution TES see fig. 6 in ref. [1]).

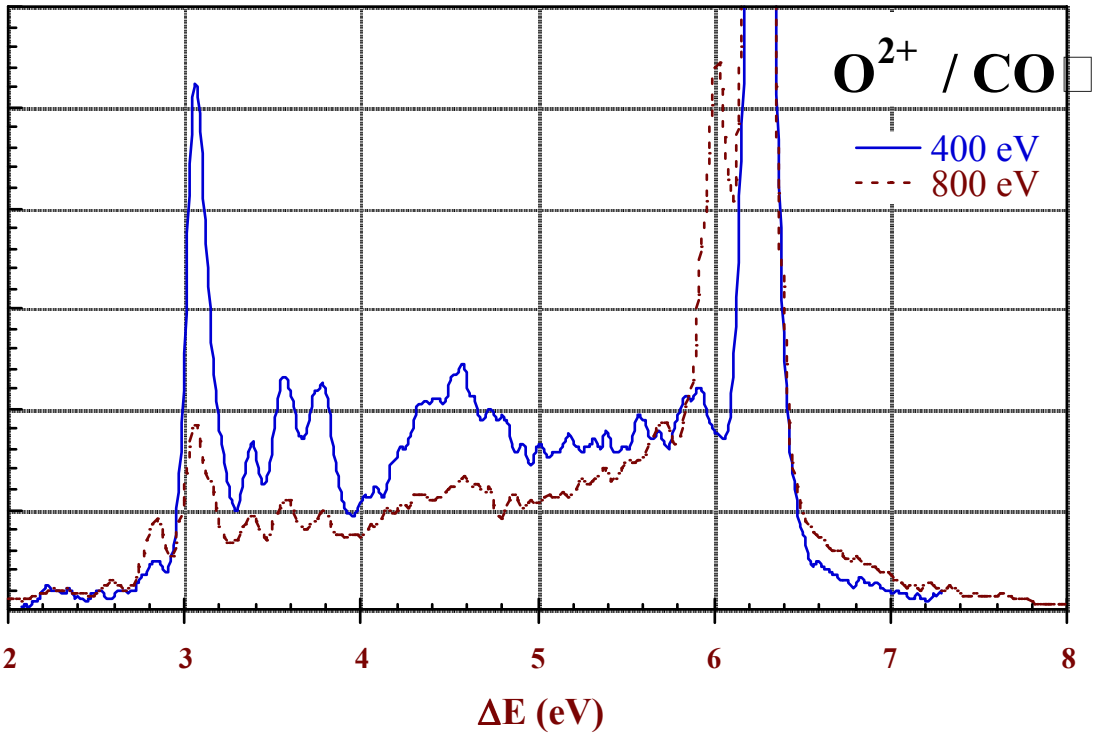

Fig. 6 TES for impact of 400 and 800 eV O^{2+} on CO, respectively. (further explanation in text).

With some additional efforts the metastable fraction itself may be determined in the following way. The translational energy spectrometer is operated with target gas in order to produce TES which feature suitable peaks S_g and S_m for SEC into the ground state- and the metastable primary ions, respectively. The ratios of corresponding TES peak heights without ($s \equiv S_m/S_g$) and with ($s' \equiv S_m'/S_g'$) attenuation yield an attenuation-gas pressure dependent entity $\Sigma(\Pi_{att})$:

$$\Sigma \equiv s'/s = (S_m'/S_g')/(S_m/S_g) = (S_m'/S_m)/(S_g'/S_g = \exp(- Q_{21,m}.\Pi_{att})/\exp(- Q_{21,g}.\Pi_{att}) =$$
$$= \exp[(Q_{21,g} - Q_{21,m}).\Pi_{att}] \rightarrow (Q_{21,g} - Q_{21,m}) = \ln[\Sigma(\Pi_{att})]/\Pi_{att}, \qquad (2)$$

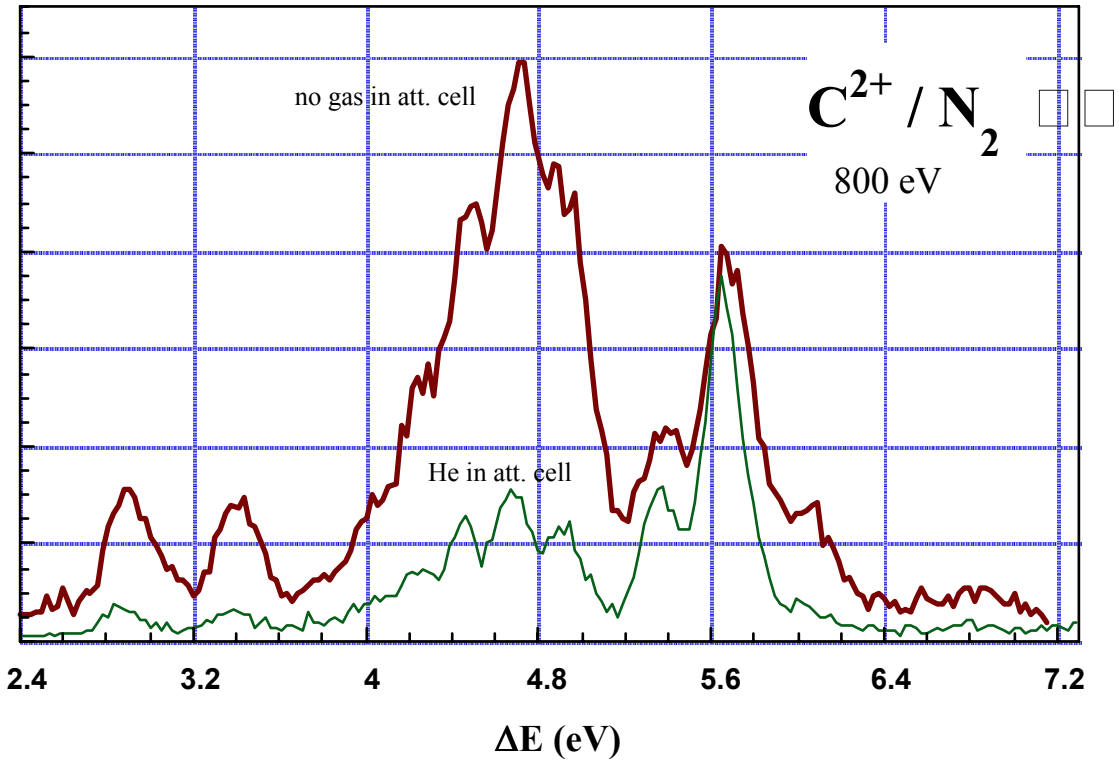

Fig. 7 Qualitative demonstration of working principle for pre-attenuation analysis of metastable ion state contribution to SEC in low-resolution TES for impact of C^{2+} on N_2

(further explanation in text).

from which the difference of the two attenuation cross sections $Q_{21,g}$ and $Q_{21,m}$ is obtained. An absolute measurement of the attenuation target thickness Π_{att} is needed, for which the attenuation gas pressure has to be determined with a capacitance manometer. Measurements for different attenuation pressures will provide useful consistency checks.
With a second „state-preparation cell“ in front of the attenuation cell we may produce an almost pure one-component ion beam if $Q_{21,g} << \text{or} >> Q_{21,m}$. For such a beam we can determine the SEC cross section Q_{21} by means of the attenuation cell if it is followed by a Faraday cup for measuring the respective singly charged ion current vs. Π_{att}, and by making use of equ. (1). Having one of the two SEC cross sections determined, we can obtain the other one from equ. (2). No precise gas pressure measurements in the preparation cell are needed for this procedure.

3. CX DATABASE FOR COLLISION OF SLOW SINGLY AND MULTIPLY CHARGED IONS WITH NEUTRAL ATOMS AND MOLECULES OF RELEVANCE FOR FUSION EDGE PLASMAS

Motivation

State-selective electron capture by slow multiply charged ions from atoms and molecules is considered an important process for the understanding and control of fusion- and astrophysical plasma properties. In colder plasma regions such collisions of ions with neutral

molecules can play an important role for the ionization balance and radiative energy loss and -cooling by impurity ions which are copiously present in these plasmas. The radiation loss from high-temperature plasmas is strongly dependent upon emission from impurity ions in moderately ionized states which in part can be formed by capture of electrons into excited states and decay by emitting characteristic radiation usually in the soft-x ray and VUV regions.
A number of experimental and theoretical investigations of cross sections for electron transfer processes involving slow multicharged ions have been made in the last ten years. Measured cross sections for electron capture have been found to be in satisfactory agreement with various theoretical calculations. In most cases, the total cross sections and also the principal quantum numbers of the electronic states of captured electrons can correctly be reproduced by models ranging from the simple classical over-barrier one to fully quantal calculations. In addition, experimental setups for measuring total and partial cross sections have been improved.
Charge exchange spectroscopy and photon-emission spectroscopy in the VUV, X-ray and visible regions are now well established techniques for such measurements, which are also of interest for impurity ion diagnostics. Time-of-flight (TOF) spectroscopy, translation energy spectroscopy (TES) and, in the very low energy range, state-selected ion flow-drift tube (SIFDT) mass spectrometers, multipole ion guiding systems and Penning quadrupole ion traps have been made available for measuring cross sections data with reasonable accuracy. Errors in such measurements resulting from unknown metastable state admixtures in ion beams produced from plasma multicharged ion sources (most notably Electron Cyclotron Resonance Ion Sources – ECRIS) are discussed in some theoretical and experimental papers. At low impact energy another source of uncertainty for electron transfer cross sections results from the repulsive interaction between post-collision partners which may be scattered into larger angles and thus a non-neglible fraction of charge-exchanged projectiles will not be collected. Consequently, experimentally determined cross sections can become too small which influence becomes progressively more important toward lower impact energy. E.g., fusion-relevant charge-changing collisions of $\leq$ 1 keV C^{2+} and O^{2+} ions with H, H_2, He and other atomic and molecular targets are affected by this errrors and the unknown metastable primary ion fractions causes further problems [8]. Finally, only few studies have been devoted to isotopic effect for H_2 vs. D_2, the possible influence of an initial vibrational excitation of such target molecules, etc.

General information about the database

In the following we present a data base containing measured and calculated cross sections for single electron capture in fusion-relevant collision systems involving slow singly and multiply-charged ions. This database has been set up for reactions like

$$\mathbf{X^{q+} + Y \rightarrow X^{(q-1)+}(\mathit{n,l}) + Y^{+}},$$

where X = H, H_2, He, Be, B, C, N, O, Ne, Ar with charge states q $\leq$ 8, and atomic and molecular targets Y = H, He, Li, Be, B, C, N, O, H_2, N_2, O_2, H_2O, CO, NO, CO_2, CH_4 and C_2H_2. The considered impact energy range is below 10 keV/amu. The regarded papers for experimental and theoretical data were published in the period 1989 to June 2000. The used program is named „FileMaker Pro“ and the files are called „*h_he_cap.data“* for H- and He projectiles, „*be_ne_cap.data“* for Be-, B-, C-, N-, O- and Ne projectiles and „*ar_cap.data“* for Ar projectiles. The files contain the following information about the reaction partners:
Charge states of the projectiles and the atomic and molecular targets, the kind of work (experimental and/or theoretical), the energy range and the kind of data (electron capture cross

sections, electron capture rate coefficients, translation energy spectra etc.). The experimental setups and the theoretical treatments are shortly described, and the first author and the name of the publishing journal are listed as well.
We have retrieved 232 relevant papers, 131 for the experimental and 146 for the theoretical data. File *h_he_cap.data* contains in total 130 papers: 96 with data for electron capture cross sections and 34 with other kind of data like TE spectra (11 papers), rate coefficients for electron capture (5 papers), alignment parameters (2 papers), excitation and ionization cross sections (17 papers). File *be_ne_cap.data* contains 102 papers: 87 for electron capture cross sections and 16 for TE spectra, and *ar_cap.data* contains 20 for electron capture cross sections and 4 for other kind of data.

For projectiles in specific charge states q we have found a number of experimental and theoretical papers as indicated in the following table.

	H *q=1*	He *q=1,2*	Be *q=1÷4*	B *q=1÷5*	C *q=1÷5*	N *q=1÷4*	O *q=1÷8*	Ne *q=1÷5*	Ar *q=1÷8*
E	19	36	2	1	28	16	19	10	20
T	46	44	10	5	22	12	7	-	4

The full version of our database can be downloaded from our homepage

http://www.iap.tuwien.ac.at/www/atomic/cxdatabase

Databases for Atomic and Molecular Physics accessible on the Internet

Most useful databases for electron capture processes in the low energy range are ORNL - Controlled Fusion Atomic Data Center, http://www-cfadc.phys.ornl.gov, and
NIFS - Atomic Databases-Data Planing Center, National Institute for Fusion Science, Japan, http://amdata.nifs.ac.jp
For experimental and theoretical electron capture cross sections for H-, H_2- and He- like projectiles on H, He, Ne, Ar, Kr, Xe, H_2, N_2, O_2, H_2O, C, CH_4, C_2H_4, C_2H_6, C_4H_{10}, CO, CO_2 we have found the following database especially useful:
JEAMDL - Japanese Evaluated Atomic and Molecular Data, Library - JAERY (Japan Atomic Energy Research Institute), http://wwwndc.tokai.jaeri.go.jp/JEAMDL/images/.
This database covers a large energy range (1 - 10^8 eV) for the period from 1950 until present. All cross sections contained are plotted and interpolated.
Further useful databases for Atomic and Molecular Physics are listed below.
NIST - Physical Reference Data, http://physics.nist.gov/PhysRefData/contents.htm
e + H, He, H_2, N_2, O_2, CO, CO_2, NO, NH_3, C_nH_m (n = 1 - 6, m = 1 - 8)
AMDIS (Atomic and Molecular Data Information System) Bibliographic Database (AMBDAS), http://www-amdis.iaea.org/: H, He, B, Be, Ne, C, N, O + H, He, Li, Na, Be, B, C, N, O, H_2, N_2, O_2, CO, CO_2, NO, CH_4, C_2H_2.
AMODS (Atomic, Molecular and Optical Database System) Library - KAERY
(Korea Atomic Energy Research Institute), http://amods.kaeri.re.kr/:
e + H, He, O, H_2, N_2, O_2, H_2O, CO_2, SO_2, CH_4

GAPHYOR - Data Center, http://gaphyor.lpqp.u-psud.fr/: H, He, B, Be, Ne, C, N, O + H, He, Li, Na, Be, B, C, N, O, H_2, N_2, O_2, CO, CO_2, NO, CH_4, C_2H_2.
WEIZMANN - Databases for Atomic and Plasma Physics
http://plasma-gate.weizmann.ac.il/DBfaPP.html
EDP Sciences, http://www.ed-phys.fr/docinfos/journals.html
Institute of Physics - INSPEC Database from the IEE, http://www.iop.org/JR/.

ACKNOWLEDGEMENT

This work has been conducted within Association EURATOM-OEAW, with measurements described in chapter 2 supported by Austrian FWF.

REFERENCES

[1] P. Leputsch, D. Dumitriu, F. Aumayr and HP. Winter, J. Phys. B: At. Mol. Opt. Phys. **30**(1997)5009
[2] P. Leputsch, Thesis, TU Wien (1998, unpublished)
[3] HP. Winter, J. Phys. Chem. **99**(1995)15448
[4] R.W. McCullough, Int.J. Mass Spectrom. **192**(1999)141
[5] M. Leitner, D. Wutte, J. Brandstötter, F. Aumayr and HP. Winter, Rev. Sci. Instrum. **65**(1994)1091
[6] S. Bashkin and J.O. Stoner, jr., Atomic Energy Levels and Grotrian Diagrams I, North Holland, Amsterdam 1975
[7] E. Unterreiter, J. Schweinzer and HP. Winter, J.Phys.B:At.Mol.Opt.Phys. **24**(1991)1003
[8] L.F. Errea, A. Macias, L. Mendez and A. Riera, J.Phys.B:At.Mol.Opt.Phys. **32**(1999)4065.

Vibrationally resolved charge transfer and ionisation cross sections for ion-H_2(D_2, DT, T_2) collisions

D. Elizaga, L.F. Errea, J.D. Gorfinkiel, C. Illescas, A. Macías[1], L. Méndez, I. Rabadán, A. Riera, A. Rojas, P. Sanz
Departamento de Química, Universidad Autónoma de Madrid,
Madrid, Spain

Abstract. Theoretical (*ab initio* and CMTC) cross sections for charge transfer and ionization in ion-H_2 collisions are presented. Vibrationaly resolved cross sections are obtained for some ions using the sudden and Franck-Condon approximations alongwith some vibrational close-copling calculations. Our results are compared with experimental data and other theoretical results.

1. Introduction

Charge transfer cross sections in collisions of multicharged ions with molecules are of interest in the outer regions of the plasma in fusion devices, particularly near divertors. In this paper we summarize calculated cross sections for collisions of ions with H_2 (also D_2, DT and T_2) for energies above 40 eV/amu. Our methods are based on the sudden approximation for the treatment of the ro-vibrational motion of the diatom. In some cases, we have used the additional Franck-Condon (FC) approximation and the cross sections have been obtained from calculations at only the target equilibrium distance ρ_0. Partial vibrational cross sections can be obtained in this case, by multiplying the FC ones by the FC factors of Table 1 [1]. At low velocities, we have employed a close-coupling expansion for the electronic wavefunction in terms of *ab initio* molecular functions (see [2]).

State-to-state vibrational cross sections have been calculated in collisions of Be^{4+}[3], C^{4+} [4], H^+ and $C^{2+}(^3P)$ [5] with H_2 in the impact energy range 50 eV/amu–2 keV/amu. Significant deviations from the simple FC approximation were found; hence, explicit comparison with vibrationally resolved measured data is useful.

In each case, the molecular states used in the dynamical study were chosen from consideration of the adiabatic correlation diagrams. The asymptotic energy differences between the electronic states and the corresponding experimental ones [6] are always smaller than 10^{-2} Hartree.

When the corrrelation diagram is too complex or at intermediate impact velocities, when a large number of molecular states are required in the dynamical treatment, a model potential approach has been applied.

At high impact energies (9–625 keV/amu for charge transfer and 9 keV/amu–2.5 MeV/amu for ionisation) classical trajectory calculations have been carried out [7].

Comparison with other experimental results and calculations (not shown in the figures) are included in the published papers mentioned in the corresponding sections.

[1] Also at Instituto de Estructura de la Materia CSIC, Serrano 113 bis, 28006 Madrid, Spain.

Cross sections are tabulated as a function of the relative impact velocity, v (in a.u.), and the corresponding energies are $E = 24.982\ v^2$ keV/amu.

2. Theory

The method we use is described in detail in [3]. Here we only summarize the procedure:

1. Molecular data (energies and dynamical couplings) for the triatomic AH_2^{q+} are obtained *ab initio* using MELD [2], modified as explained in [8].
2. The sudden approximation for rotation and vibration is employed to obtain the vibrational state-to-state cross sections. The electronic transitions are calculated using the semiclassical eikonal method (see e.g. [9]): for fixed H_2 target position, the ion follows rectilinear trajectories with impact parameter $\boldsymbol{b}$ and velocity $\boldsymbol{v}$, $\boldsymbol{R} = \boldsymbol{b} + \boldsymbol{v}t$. The wavefunction Ψ describing the collision is solution of

$$\left(H_{\rm int} - {\rm i}\ \frac{\partial}{\partial t}\bigg|_{r,\rho} \right) \Psi(\boldsymbol{r}, \boldsymbol{\rho}, t) = 0 \tag{1}$$

where $H_{\rm int} = H_{\rm el} + T_\rho$ is the total Hamiltonian without the kinetic energy term associated to the coordinate R . The wavefunction Ψ is expanded as:

$$\Psi(\boldsymbol{r}, \boldsymbol{\rho}, t) = \chi_0(\rho) Y_{JM}(\hat{\boldsymbol{\rho}}) \sum_k a_k(\boldsymbol{\rho}, t) \phi_k(\boldsymbol{r}; \boldsymbol{R}, \boldsymbol{\rho}) \exp\left(-{\rm i} \int_0^t \epsilon_k {\rm d}t' \right) \tag{2}$$

where $\chi_0(\rho) Y_{JM}(\hat{\boldsymbol{\rho}})$ is the initial rovibrational wavefunction of H_2, and $\phi_k(\boldsymbol{r}; \boldsymbol{R}, \boldsymbol{\rho})$ are electronic wavefunctions of the triatomic quasimolecule with energies ϵ_k.

These functions ϕ_k depend on three parameters: R, the distance from the projectile to the H_2 centre of mass; ρ, the H-H internuclear distance; and θ, the angle between $\boldsymbol{R}$ and $\boldsymbol{\rho}$.

2.1. *Isotropic approximation*

When charge transfer transitions occur at relatively large R, anisotropy effects in the projectile-target interactions are small and both the hamiltonian and the dynamical couplings may be substituted by those obtained for a fixed value of θ.

Substituting (2) in (1) leads to a set of differential equations for the coefficients a_k. The probability $P_{\nu f}$ for transition from the vibronic state $\{0i\}$ to $\{\nu f\}$ is given by

$$P_{\nu f}(b, v) = \left| \int {\rm d}\rho \chi_0 \chi_\nu \exp\left[-{\rm i} \int_0^\infty {\rm d}t (\epsilon_f - E_f) \right] a_f(\infty, \rho) \right|^2 \tag{3}$$

where E_f is the asymptotic energy of the vibronic state $\{\nu f\}$. The total cross section for the transition $\{0i\} \rightarrow \{\nu f\}$ is, in the isotropic approximation [1],

$$\sigma_{\nu f}(v) = 2\pi \int_0^\infty b P_{\nu f} \mathrm{d}b \,. \tag{4}$$

It is useful to define the quantities $P_n^e(\rho, b, v)$ and $\sigma_n^e(\rho, v)$ for a fixed ρ and v as

$$P_f^e(\rho, b, v) = |a_f(\infty, \rho)|^2 \tag{5}$$

$$\sigma_f^e(\rho, v) = 2\pi \int_0^\infty b P_f^e(\rho, b, v) \, \mathrm{d}b. \tag{6}$$

When $\rho = \rho_0$, the target equilibrium distance, equations (5) and (6) yield the familiar FC transition probability and cross section respectively.

From equation (4), and using the closure relations for the vibrational functions χ_ν, the total cross section for transition to the electronic state f is given by

$$\sigma_f(v) = \sum_\nu \sigma_{\nu f} = \int_0^\infty \chi_0^2 \, \sigma_f^e \, \mathrm{d}\rho \,. \tag{7}$$

2.2. *Anisotropic behaviour*

When transitions occur at small R distances, the isotropic approximation is not longer accurate and an average over the relative orientations must be performed. Then, the vibronic probabilities (equation (3)) and cross sections (equation (4)) become (see e.g. Errea et al. [3])

$$P_{\nu f}(\boldsymbol{v}, \hat{\boldsymbol{\rho}}) = \left| \int \mathrm{d}\rho \chi_0 \chi_\nu \exp\left[-\mathrm{i} \int_0^\infty \mathrm{d}t (\epsilon_f - E_f) \right] a_f(\infty, \boldsymbol{\rho}) \right|^2 \tag{8}$$

and

$$\sigma_{\nu f}(v) = \frac{1}{4\pi} \int d\boldsymbol{b} \int d\hat{\boldsymbol{\rho}} P_{\nu f}(\boldsymbol{v}, \hat{\boldsymbol{\rho}}). \tag{9}$$

The presence of divergent rotational couplings at the conical intersections between adiabatic states was solved by removing the divergent components from the rotational couplings [10].

2.3. *Model potential calculations*

The *ab initio* calculation of charge transfer cross sections in collisions of multiply charged ions with H_2 molecules becomes cumbersome when a large number of coupled states has to be included in the basis. This is always the case at higher impact velocities.

An alternative approach, (see e.g. [9] and references therein), is the use of effective potentials to treat the interaction of the active electron, described by a model wavefunction $\psi^m(\boldsymbol{r},t)$, with the cores.

Firstly, we solve the one-electron impact parameter model equation

$$\left(h^m - \mathrm{i}\frac{\partial}{\partial t}\right)\psi^m(\boldsymbol{r},t) = 0 \tag{10}$$

where h^m includes model potentials of the form:

$$V_k = -\frac{Z-N_c}{r_k} - \frac{N_c}{r_k}(1+\alpha_k r_k)\exp(-\alpha'_k r_k) \tag{11}$$

to describe the interaction of the active electron with the X^{q+} projectile and H_2^+ cores respectively. $\psi^m(\boldsymbol{r},t)$ is expanded in terms of (approximate) MO χ_j, eigenfunctions of h^m with energies ϵ_j:

$$\psi^m(\boldsymbol{r},t) = D(\boldsymbol{r},t)\sum_j a_j(t)\chi_j \exp(-\mathrm{i}\int_0^t \epsilon_j \mathrm{d}t') \tag{12}$$

where D($\boldsymbol{r}$,t) is a common translation factor (CTF) [11–13].

Then, a two-electron interpretation is required to evaluate transition probabilities and cross sections. In the usual equivalent-electron independent particle model (IPM) approach, [14–16], the two-electron impact parameter equation:

$$\left[H - \mathrm{i}\frac{\partial}{\partial t}\right]\Psi(\boldsymbol{r}_1,\boldsymbol{r}_2,t) = 0 \tag{13}$$

is simplified by replacing H by the IPM Hamiltonian H^{IPM}

$$H^{\mathrm{IPM}} = h^m(1) + h^m(2) \tag{14}$$

and the solution of (13) is approximated by

$$\Psi^{\mathrm{IPM}}(\boldsymbol{r}_1,\boldsymbol{r}_2,t) = ||\psi^m\overline{\psi^m}|| \tag{15}$$

where $||\ ||$ denotes a Slater determinant.

The IPM transition probabilities for single electron capture (SEC) ($P^{\rm SEC}$), double electron capture (DEC) ($P^{\rm DEC}$) and excitation (EX) ($P^{\rm EX}$) are obtained by projecting $\Psi^{\rm IPM}$ onto the corresponding asymptotic forms of the electronic states in the limit $t \rightarrow \infty$. This method has been previously applied to ion-H_2 collisions in ref. [7]. However, this standard IPM interpretation, leads to inaccurate results at low velocities. For example, $P^{\rm SEC}$ is always less than 0.5 which points to a limitation of the IPM.

2.3.1. IPM-SEC approximation

To improve the IPM in the treatment of SEC at low velocities, we have applied a modified technique, the IPM-SEC method. We construct a set of diabatic MOs ,$\{\chi_j^d\}$ [17], by a unitary transformation of the set $\{\chi_j\}$. We then construct the set of two-electron wavefunctions $\phi_{kl}(\boldsymbol{r}_1, \boldsymbol{r}_2, t)$:

$$\phi_{kl} \;=\; \frac{N_{kl}}{\sqrt{2}}\left[||\chi_k^d\,\overline{\chi_l^d}|| \,+\, ||\chi_l^d\,\overline{\chi_k^d}||\right] \tag{16}$$

where $N_{kl} = 2^{-1/2}$ for $k = l$ and $N_{kl} = 1$ for $k \neq l$. The IPM-SEC wavefunction $\Psi^{\rm IPM-SEC}$ is then expanded as:

$$\Psi^{\rm IPM-SEC} = D(\boldsymbol{r}_1, \boldsymbol{r}_2, t)\sum_{kl} a_{kl}(t)\phi_{kl}(\boldsymbol{r}_1, \boldsymbol{r}_2)\exp[-{\rm i}\int_0^t E_{kl}{\rm d}t'] \tag{17}$$

with $E_{kl} =< \phi_{kl}|H|\phi_{kl} >$.

For systems where the interactions between both the entrance channel and SEC functions with DEC functions are not effective, these DEC functions can be removed from expansion (17).

As in the standard IPM approach, [18], the matrix elements of H can be replaced by those of $H^{\rm IPM}$ of eq. (14). Time integration of the ensuing system of differential equations then yields the expansion coefficients a_{jk}, and hence the SEC and excitation transition probabilities.

3. Results

3.1. $\mathbf{H^+ + H_2(X^1\ \Sigma_g^+,\ \nu)}$

We have obtained single electron capture (SEC) vibrationally resolved cross section using the sudden approximation. The basis set includes the lowest two states of H_3^+. SEC cross sections from ν=0 and ν=1 of $H_2(X\ ^1\Sigma_g^+)$ are given in Table 2 and plotted in Figure 1. Also plotted in this figure are the capture to dissociative vibrational states (DC), total vibrational excitation (VE) and dissociative excitation (DE) cross sections.

Comparison with experimental data for capture of Gealy and van Zyl [19] shows a good agreement at impact velocities above 0.1 a.u., while a sizeable difference may be observed at lower values with Sudden calculations. To ascertain the origin of this discrepancy, we have carried out a vibronic close-coupling calculation (CC) using 7 states corresponding to the entrance H^++H_2 channel and other 7 states corresponding to the capture H(1s)+H_2^+ state. The excelent agreement obtained with experimental measurements shows the region of validity of the Sudden approach.

State-to-state vibrational cross sections are shown in figures 2 (capture) and 3 (excitation), (see also [1]), for H_2, D_2, DT, and T_2 targets.

3.2. $Li^+ + H_2$

A 5-electronic-state calculation for the system LiH_2^+ was performed [1] in the framework of the FC approximation. Orientation averaged cross sections (eq. 8-9) for SEC to Li(2s,2l)+H_2^+ and excitation to $H_2(B\ ^1\Sigma_u^+)$ are given in Table 3 and plotted in Figure 4.

3.3. $C^{2+} + H_2$

13- and 16- state calculations were performed for the ground ($2s^2$;^{1}S) and metastable (2s2p;^{3}P) states of C^{2+} respectively. The collinear geometry and the FC approximation were employed [20]. Results are shown in Figure 5 and Table 4. More accurate calculations, using the sudden approximation, have been also carried out for collisions with the metastable projectile [5]. In this case, cross sections to individual vibrational states of H_2^+ have been obtained in the process:

$$C^{2+}(2s2p;^3\,P) + H_2(X^1\Sigma_g^+, \nu = 0) \rightarrow C^+(2s2p^2;^2\,D) + H_2^+(X^2\Sigma_g^+, \nu'). \tag{18}$$

and compared to measured distributions [21], obtained after increased the resolution of the experiment.

We also include in figure 5 the more accurate sudden total cross section $\sigma_{^2D}$ calculated using (7) from $C^{2+}(^3P)$. Good agreement between this and the FC approximation is found for high energies, but differences are noticeable at the low impact energies.

In figure 6, we show the vibrational distributions of $H_2^+(X^2\Sigma_g^+, \nu')$ for reaction (18) at four impact energies. As in [21], in the range of impact energies (0.6–1 keV), our *sudden* distributions show a maximum at $\nu' = 4$, which moves to smaller ν' as the impact energy increases, approaching the FC prediction.

This behaviour can be explained by expanding $a_f(\rho)$ in powers of $(\rho - \rho_c)$ in equation (3) and (4). Corrected FC cross sections are obtained as explained in [5], and plotted in figure 6, where they display a better agreement with the more exact results.

The calculated state-to-state charge transfer cross sections are compared to the experimental TES of [21] at $E = 1$ keV in figure 7.

Very good agreement is obtained for the vibrational distribution of H_2^+ associated with the $C^+(^2D)$ ions, which confirms the accuracy of the vibrational sudden approximation method for this energy range and of the experimental data. The small values obtained for the $C^+(^2S)$ band, do not allow to get any conclusion when compared to the experimental values.

3.4. $C^{3+} + H_2$

Calculations have been carried out using the FC approximation, collinear geometry and a basis of 8 electronic states. DEC leading to Coulomb explosion of the diatom is competitive with SEC and the corresponding cross sections are listed in Table 5 and plotted in Figure 8.

3.5. $C^{4+} + H_2$

Calculations using the sudden approximation and a basis of 8 electronic states were reported in [4]. Our results include state-selected (vibrational and electronic) cross sections in SEC, as well as cross sections for transfer dissociation and vibrational excitation in collisions with H_2, D_2 and DT. We give cross sections for SEC into the main exit electronic channels in Table 6 and Figure 9.

IPM-SEC treatment

To extend the energy range, to 50 eV/amu$\leq E \leq$6 keV/amu, we have employed the IPM-SEC model approach. The interaction with the H_2^+ core (see [18]) is described by a one-center model potential (eq. (11)). Details on the model potential parameters are described in [18]. A semiclassical impact parameter treatment, in the framework of the Franck-Condon approximation calculation is carried out, whose accuracy for total and partial SEC cross sections was discussed in ref. [4]. Our basis set includes 20 MOs and the CTF of ref. [12].

In figure 10 we have included the IPM-SEC cross section.

3.6. $N^{5+} + H_2$

A model potential IPM-SEC treatment has been used in the FC framework. In this case, a more sophisticated two-center model potential (of (11)) has been used, to improve the representation of the H_2 target, as anisotropy effects are expected to be important. The basis set included 8 MOs: five dissociating into $N^{4+}(n{=}3)+H_2^+$, the two most important molecular orbital dissociating into $N^{4+}(n{=}4)+H_2^+$ and the entrance channel. Our results are given in Table 7 and plotted in Figure 11 together with experimental data of [22].

Although comparison with experimental data shows an overall agreement for the total single capture cross section to $N^{4+}(n{=}3)+H_2^+$, further calculations using *ab initio* data and the Sudden approach should be performed at lower velocities, as for this system, the double capture transitions to $N^{3+}(3l3l')$ compete with single capture.

3.7. *CTMC calculations*

We have calculated SEC and single ionisation (SI) cross sections for H^+, He^{2+}, Li^{3+}, Be^{4+}, B^{5+}, C^{6+}, N^{7+} and O^{8+} in collisions with H_2, using the improved impact parameter CTMC treatment (see [7]). The calculation employs the FC approximation and a model potential for the H_2 target. Results for SI are plotted in Figure 12 and tabulated in Table 8. The corresponding SEC results are given in Figure 13 and Table 9. In these figures, the results are compared with experimental and other theoretical data (see [7] for details).

Analogously to the ion-atom case, we have obtained scaling laws of the SEC and SI cross sections as functions of the charge q of the projectile and velocity v.

$$\sigma_{\mathrm{SEC}}^{\mathrm{scaled}}(q, vq^{0.11}) = \sigma_{\mathrm{SEC}}(1, v)q \tag{19}$$

$$\sigma_{\mathrm{SI}}^{\mathrm{scaled}}(q, v) = \sigma_{\mathrm{SI}}(1, v)q^{2\left\{0.92-\exp[-0.57(v-0.01q)]-\exp\left[-1.8(v^2-0.08q)\right]\right\}} \tag{20}$$

4. Concluding remarks

In the last few years, we have developed new methods to treat ion-H_2 collisions with a similar accuracy to those of ion-atom. These methods have been applied to several ions. We plan to extend our calculations to lower velocities of interest in cold regions of fusion plasma. A more detailed treatment of the anisotropy in the ion-target interaction has also been considered for when transitions occur at small distances. Calculations involving projectiles in both ground and metastable states are being carried out where experimental uncertainties in the composition of the initial beams exist.

ACKNOWLEDGEMENTS

This research has been partially supported by the DGICYT Project PB96-0056. IR acknowledges MEC for a Contrato de Incorporación de doctores. CI acknowledges MEC for a postdoctoral grant under the program SGPDE.

REFERENCES

[1] D. ELIZAGA, L.F. ERREA, J.D. GORFINKIEL, A. MACÍAS, L. MÉNDEZ, A. RIERA, A. ROJAS, *J. Phys. B: At. Mol. Opt. Phys.*, 33:2037, 2000.

[2] DAVIDSON. In E. CLEMENTI, editor, *MOTECC, Modern Techniques in Computational Chemistry*. ESCOM Publishers B. V., Leiden, 1990.

[3] L.F. ERREA, J.D. GORFINKIEL, A. MACÍAS, L. MÉNDEZ, A. RIERA, *J. Phys. B: At. Mol. Opt. Phys.*, 30:3855, 1997.

[4] L.F. ERREA, J.D. GORFINKIEL, A. MACÍAS, L. MÉNDEZ, A. RIERA, *J. Phys. B: At. Mol. Opt. Phys.*, 32:1705, 1999.

[5] L.F. ERREA, A. MACÍAS, L. MÉNDEZ, I. RABADÁN, A. RIERA, *J. Phys. B: At. Mol. Opt. Phys.*, 33:L615, 2000.

[6] C.E. MOORE, *Atomic Energy Levels, Nat. Stand. Ref. Data Series vol 1.* (US National Bureau of Standards), 1972.

[7] C. ILLESCAS, A. RIERA, *Phys. Rev. A*, A60:4546, 1999.

[8] J.F. CASTILLO, L.F. ERREA, A. MACÍAS, L. MÉNDEZ, A. RIERA, *J. Chem. Phys.*, 103:2113, 1995.

[9] B.H. BRANSDEN, M.H.C. McDOWELL, *Charge Exchange and the Theory of Ion-Atom Collisions*. (Oxford: Clarendon), 1992.

[10] D. ELIZAGA, L.F. ERREA, A. MACÍAS, L. MÉNDEZ, A. RIERA, A. ROJAS, *J. Phys. B: At. Mol. Opt. Phys.*, 32:L697, 1999.

[11] S.B. SCHNEIDERMAN, A. RUSSEK, *Phys. Rev.*, 181:311, 1969.

[12] C. HAREL, H. JOUIN, *J. Phys. B: At. Mol. Opt. Phys.*, 25:221, 1992.

[13] L.F. ERREA, L. MÉNDEZ, A. RIERA, *J. Phys. B: At. Mol. Opt. Phys.*, 15:101, 1982.

[14] J.H. McGUIRE, L. WEAVER, *Phys. Rev. A*, 16:41, 1977.

[15] V.A. SIDOROVICH, *J. Phys. B: At. Mol. Phys.*, 14:4805, 1981.

[16] H.J. LÜDDE, R.M. DREIZLER, *J. Phys. B: At. Mol. Phys.*, 16:3973, 1983.

[17] F.T. SMITH, *Phys. Rev.*, 179:111, 1969.

[18] L.F. ERREA, J.D. GORFINKIEL, C. HAREL, H. JOUIN, A. MACÍAS, L. MÉNDEZ, B. PONS, A. RIERA, *J. Phys. B: At. Mol. Opt. Phys.*, 33:3107, 2000.

[19] M.W. GEALY, B.I. VAN ZYL, *Phys. Rev. A*, 36:3091, 1987.

[20] L.F. ERREA, A. MACÍAS, L. MÉNDEZ, A. RIERA, *J. Phys. B: At. Mol. Opt. Phys.*, 32:4065, 1999.

[21] P. LEPUTSCH, D. DUMITRIU, F. AUMAYR, H.P. WINTER, *J. Phys. B: At. Mol. Opt. Phys.*, 30:5009, 1997.

[22] G. LUBINSKI, Z. JUHÁSZ, R. MORGENSTERN, R. HOEKSTRA, *Phys. Rev. Lett.*, 86:616, 2001.

[23] G.W. McCLURE, *Phys. Rev.*, 1480:47, 1966.

[24] M. KIMURA, *Phys. Rev. A*, 32:802, 1985.

[25] F. AUMAYR, H.P. WINTER, *At. Data Nucl. Data Tables*, 65:155, 1985.

[26] J. VanECK, J. KISTEMAKER, *Physica*, 26:629, 1960.

[27] E. UNTERREITER, J. SCHWEINZER, H.P. WINTER, *J. Phys. B: At. Mol. Opt. Phys.*, 24:1003, 1991.

[28] A. ITOH, *J. Phys. Soc. Jap.*, 64:3255, 1995.

[29] K. OKUNO, *Tokyo Metropolitan University Report*, 2000.

[30] J.B. GREENWOOD, *Private communication.*

[31] R. HOEKSTRA, J.P.M. BEIJERS, A.R. SCHALATMANN, R. MORGENSTERN, F.J. DE HEER, *Phys. Rev. A*, 41:4800, 1990.
[32] A. PHANEUF, I. ALVAREZ, F.W. MEYER, D.H. CRANDALL, *Phys. Rev. A*, 26:1892, 1982.
[33] D. DIJKKAMP, D. CIRIC, E. VLIEG, A. DE BOER, J. DE HEER, *J. Phys. B: At. Mol. Opt. Phys.*, 18:4763, 1985.
[34] M. GARGAUD, R. McCARROLL, *J. Phys. B: At. Mol. Phys.*, 18:463, 1985.
[35] M. GARGAUD, PhD thesis, Université de Bordeaux I, 1987.
[36] A. KUMAR, B. SAHA, *Phys. Rev. A*, 59:1273, 1999.
[37] W. FRITSCH, *Phys. Rev. A*, 46:3910, 1992.

TABLE 1. FRANCK-CONDON FACTORS FOR H_2, D_2, DT AND T_2

ν'	H_2	D_2	DT	T_2
0	0.088088	0.032798	0.023775	0.015375
1	0.163359	0.086461	0.068723	0.049741
2	0.181715	0.129654	0.111744	0.089406
3	0.159648	0.146563	0.135583	0.118563
4	0.123301	0.139736	0.137472	0.130021
5	0.088460	0.119268	0.123728	0.125349
6	0.060893	0.094501	0.102574	0.110319
7	0.041047	0.071197	0.080280	0.090900
8	0.027458	0.051864	0.060352	0.071390
9	0.018389	0.036974	0.044134	0.054148
10	0.012398	0.026026	0.031692	0.040062
11	0.008440	0.018211	0.022508	0.029137
12	0.005807	0.012731	0.015899	0.020957
13	0.004033	0.008925	0.011218	0.014979
14	0.002816	0.006293	0.007932	0.010679
15	0.001961	0.004470	0.005635	0.007618
16	0.001342	0.003204	0.004030	0.005450
17	0.000873	0.002318	0.002905	0.003919
18		0.001693	0.002112	0.002835
19		0.001247	0.001550	0.002067
20		0.000925	0.001147	0.001519
21		0.000689	0.000857	0.001125
22		0.000513	0.000644	0.000841
23		0.000378	0.000486	0.000634
24		0.000273	0.000368	0.000481
25		0.000189	0.000277	0.000368
26			0.000206	0.000282
27			0.000148	0.000217
28				0.000167
29				0.000127

TABLE 2. CROSS SECTIONS (IN UNITS OF 10^{-16} cm^2) FOR THE REACTIONS $H^+ + H_2(X\ ^1\Sigma_g^+, \nu = 0, 1) \longrightarrow H + H_2^+(X\ ^2\Sigma_g^+)$

v(a.u.)	ν=0	ν=1	C.C
0.040			0.20
0.045	0.02	0.19	
0.063	0.11	0.64	0.43
0.089	0.45	1.68	0.65
0.100	0.69	2.20	0.78
0.141	2.07	4.47	1.68
0.200	4.79	7.00	4.34
0.400	8.99	9.15	

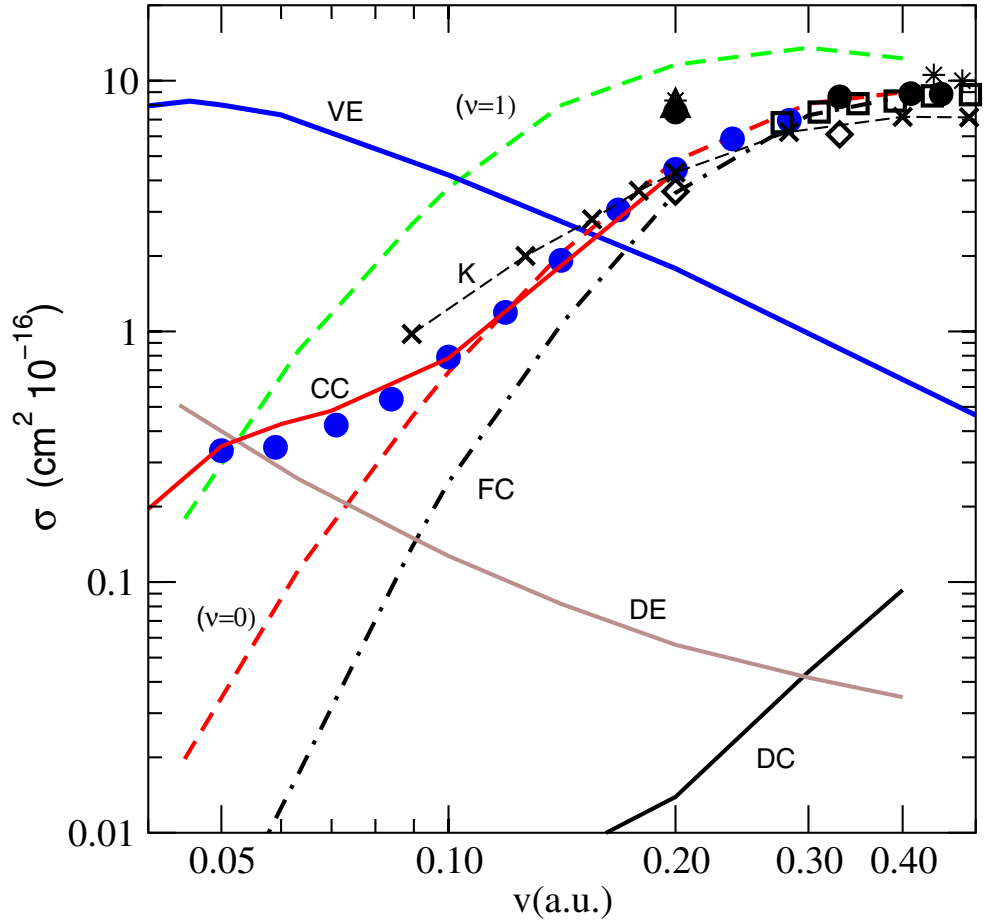

FIG. 1. Cross sections for the reactions $H^+ + H_2(X\ ^1\Sigma_g^+; \nu) \longrightarrow H + H_2^+(X\ ^2\Sigma_g^+)$. (●) Geally [19], (□) [23], (K) [24]; our results: (VE) vibrational excitation, (CC) vibrational close-coupling, (FC) Franck-Condon, (DE) dissociative excitations, (DC) dissociative capture, ($\nu = 0$) capture from $H_2(\nu = 0)$, ($\nu = 1$) capture from $H_2(\nu = 1)$. For other experimental data see ref. [1].

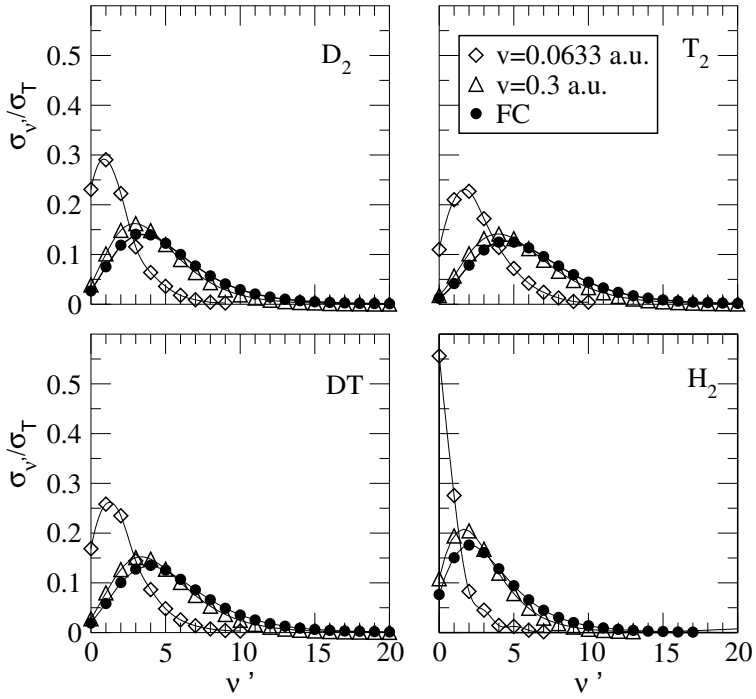

FIG. 2. Cross sections for the reactions $H^+ + H_2(X\,^1\Sigma_g^+;\nu) \longrightarrow H + H_2^+(X\,^2\Sigma_g^+;\nu')$. Empty symbols are from the vibronic CC calculation (see text).

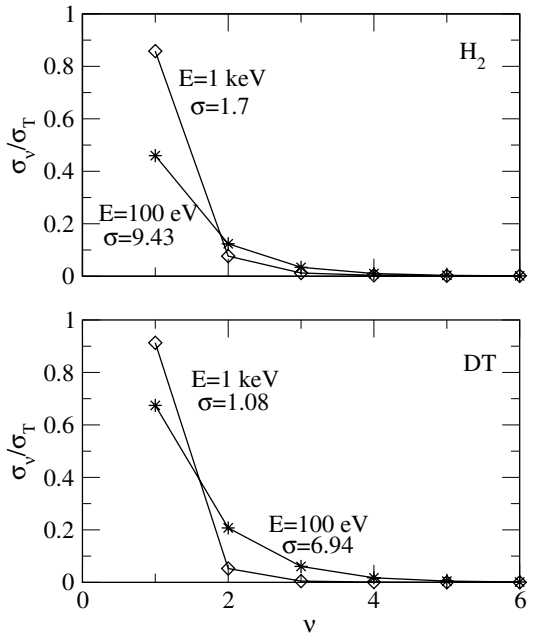

FIG. 3. Cross sections for the reactions $H^+ + H_2(X\,^1\Sigma_g^+;\nu=0) \longrightarrow H^+ + H_2(X\,^1\Sigma_g^+,\nu)$.

TABLE 3. CROSS SECTIONS (IN UNITS OF 10^{-16} cm^2) FOR THE SEC REACTIONS $Li^+ + H_2 \longrightarrow Li(2s) + H_2^+$ AND $Li^+ + H_2 \longrightarrow Li(2l) + H_2^+$, AND THE EXCITATION REACTION $Li^+ + H_2(X\ ^1\Sigma_g^+) \longrightarrow Li^+ + H_2(B\ ^1\Sigma_u^+)$

v(a.u.)	Li(2s)	Li(2l)	$H_2(B\ ^1\Sigma_u^+)$
0.063	0.02	0.03	0.04
0.089	0.04	0.10	0.05
0.100	0.07	0.13	0.06
0.141	0.06	0.21	0.06
0.200	0.18	0.48	0.15
0.250	0.29	0.53	0.23
0.300	0.31	0.63	0.27
0.350	0.31	0.79	0.30
0.400	0.41	0.99	0.29
0.500	0.74	1.46	0.23

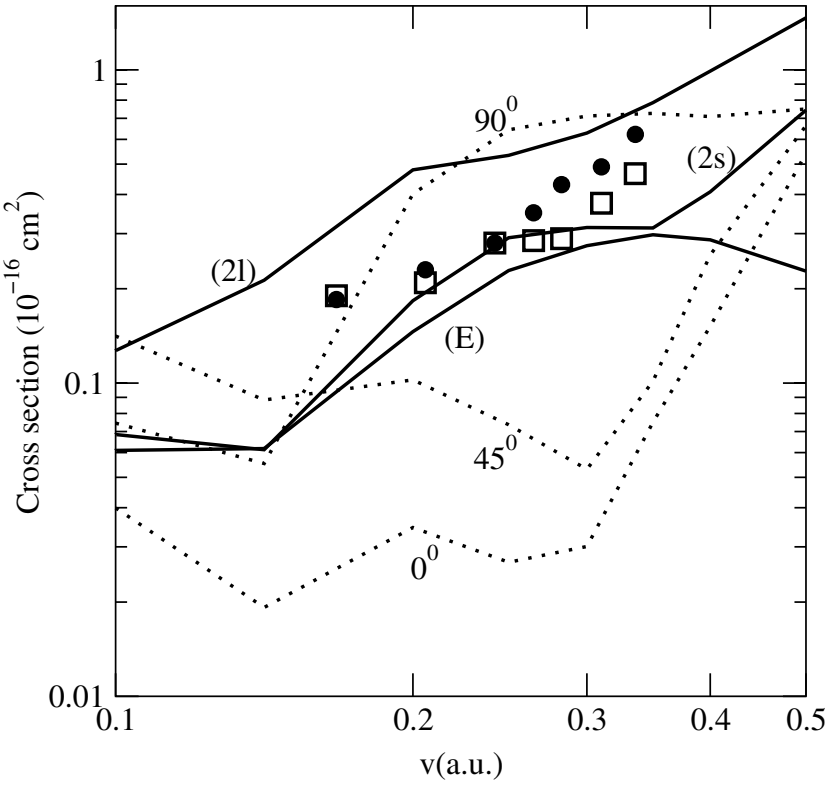

FIG. 4. Cross sections for the SEC reactions (2s) $Li^+ + H_2 \longrightarrow Li(2s) + H_2^+$ and (2l) $Li^+ + H_2 \longrightarrow Li(2l) + H_2^+$, and the excitation reaction (E) $Li^+ + H_2(X\ ^1\Sigma_g^+) \longrightarrow Li^+ + H_2(B\ ^1\Sigma_u^+)$. Also plotted are the isotropic calculation (dotted lines) obtained for three values of the relative orientation angle α for capture to Li(2s). ● [25], □ [26].

TABLE 4. FC SEC CROSS SECTIONS (IN UNITS OF 10^{-16} cm^2) FOR C^{2+}+H_2(X $^1\Sigma_g^+$) COLLISIONS

v (a.u.)	$C^{2+}(^1S)$(FC)	$C^{2+}(^3P)$(FC)	$C^{2+}(^3P)$(sudden)
0.045	6.053	17.606	12.425
0.048	5.808	17.919	12.799
0.052	5.490	17.975	12.803
0.055	5.309	18.440	13.138
0.058	5.140	18.587	13.509
0.060	5.102	18.484	13.650
0.080	5.460	19.219	15.098
0.100	6.143	18.836	15.378
0.115	6.763	17.162	14.646
0.120	6.828	16.475	14.282
0.140	7.379	14.656	13.148
0.160	8.165	14.132	12.546
0.180	8.952	13.738	12.024
0.200	9.302	13.118	11.418
0.220	9.587	12.352	10.753
0.240	9.873	11.556	10.079
0.260	10.130	10.801	9.432

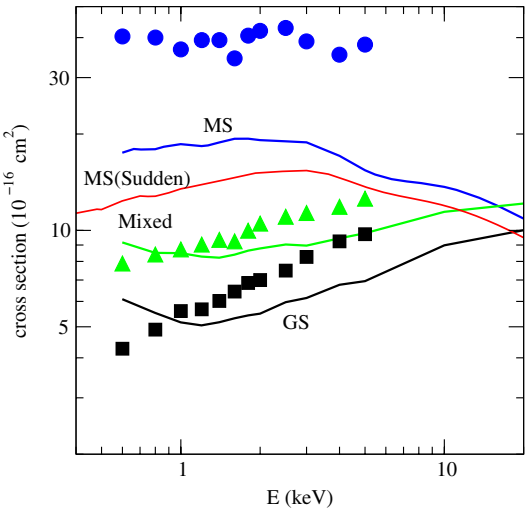

FIG. 5. Franck-Condon charge transfer cross section in the collision (GS) $C^{2+}(^2S)$+H_2→$C^+(^2D)$+H_2^+ and (MS) $C^{2+}(^3P)$+H_2→$C^+(^2D)$+H_2^+. Also included is the sudden cross section with projectile $C^{2+}(^3P)$(eq. (7)). Symbols are experiments of [27].

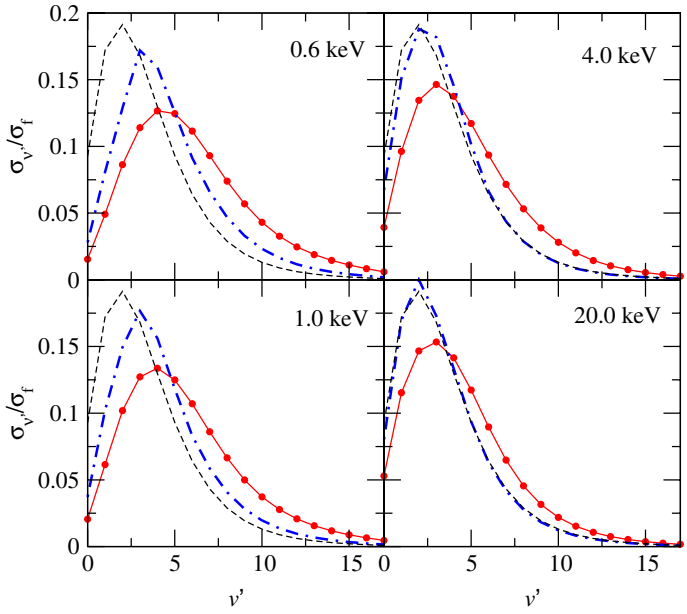

FIG. 6. Relative cross section $\sigma_{\nu'}/\sigma_f$ for the charge transfer reaction (18) as a function of $H_2^+(X^2\Sigma_g^+)$ vibrational state (ν'). Dotted continuous line are the sudden approximation results (equation 4). The dot-dashed line are the corrected FC results of equation (9) of [5] and the dashed line the FC results.

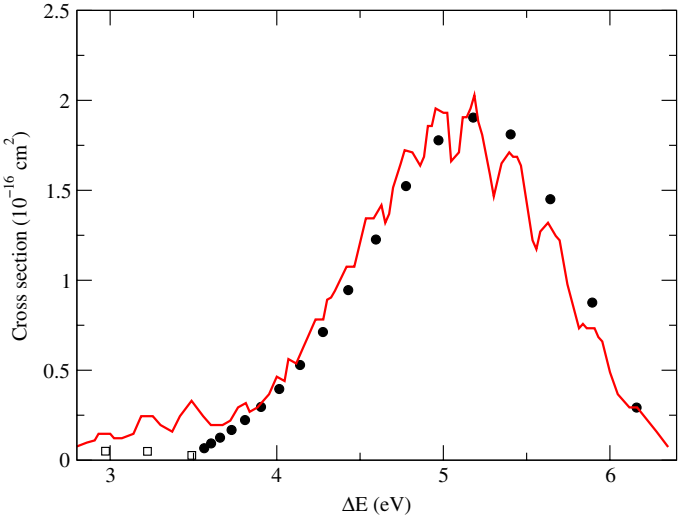

FIG. 7. Calculated cross section for the charge transfer reactions $C^{2+}(^3P)+H_2(X^1\Sigma_g^+,\nu=0)\rightarrow C^+(^2D)+H_2^+(X^2\Sigma_g^+,\nu')$ (●) and $C^{2+}(^3P)+H_2(X^1\Sigma_g^+,\nu=0)\rightarrow C^+(^2S)+H_2^+(X^2\Sigma_g^+,\nu')$ (□) at $E=1$ keV as a function of energy defect. The curve corresponds to [21] experiment, renormalized to the area under the theoretical data.

TABLE 5. FC SEC AND DEC CROSS SECTIONS (IN UNITS OF 10^{-16} cm^2) FOR C^{3+}+H_2 COLLISIONS

v(a.u.)	SEC	DEC
0.100	7.781	4.518
0.120	6.280	4.832
0.150	5.947	4.785
0.200	6.358	4.407
0.250	6.444	3.972
0.300	6.366	3.694
0.350	6.189	3.548
0.400	5.965	3.470
0.450	5.730	3.423
0.500	5.505	3.391

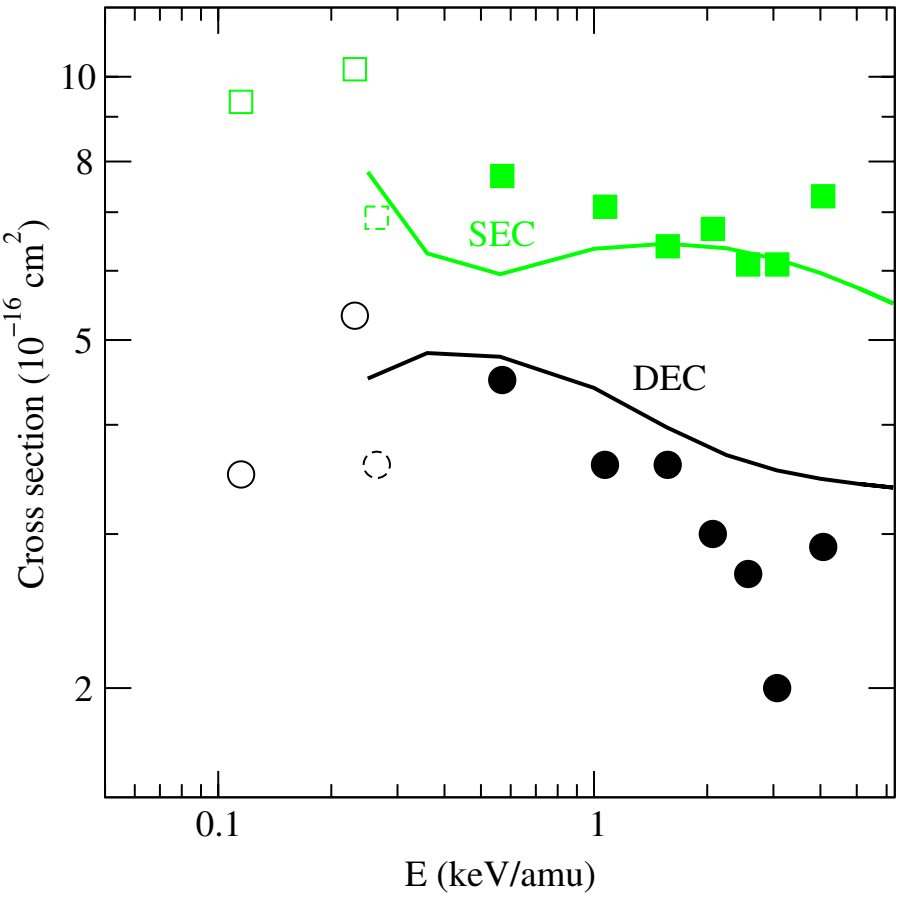

FIG. 8. FC SEC (light grey line and symbols) and DEC (black line and symbols) cross sections for the collision $C^{3+} + H_2$. Lines are our results. Full symbols: ref. [28]; empty symbols [29]; dashed line symbols [30].

TABLE 6. SUDDEN CROSS SECTIONS (IN UNITS OF 10^{-16} cm^2) FOR THE REACTION $C^{4+}+H_2 \longrightarrow C^{3+}(1s^2 3l)+H_2^+(X\ ^2\Sigma_g^+)$

v(a.u.)	l=0	l=1	l=2	Total
0.045	16.9	24.7	1.1	42.8
0.060	20.1	20.7	1.1	42.0
0.071	21.4	18.4	1.2	40.9
0.077	21.8	17.7	1.3	40.8
0.089	22.1	17.3	1.7	41.1
0.100	22.1	16.9	2.2	41.3
0.122	22.2	14.9	3.0	40.0
0.141	22.1	12.4	3.7	38.1
0.200	19.9	9.6	3.8	33.3
0.253	17.1	9.8	3.9	30.8
0.300	14.9	9.7	4.4	29.1

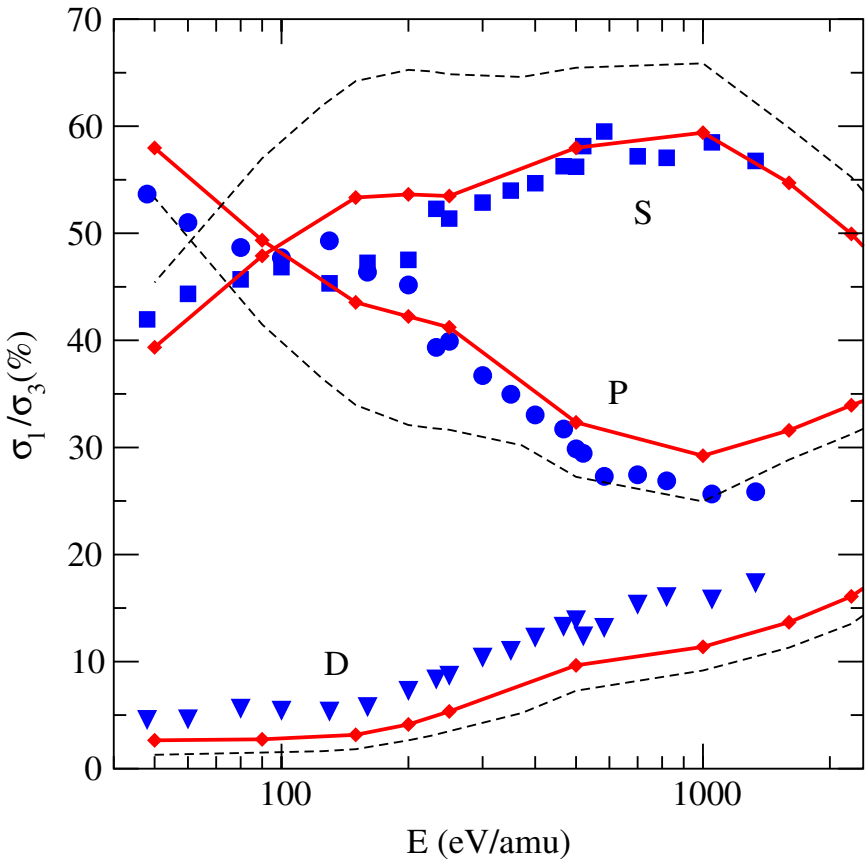

FIG. 9. Cross section fractions σ_l/σ_3 for the reaction $C^{4+}+H_2 \longrightarrow C^{3+}(1s^2\,3l) + H_2^+(X^2\Sigma_g^+)$. Solid line: Sudden approximation; dashed line: FC approximation [4]; symbols: experimental results [31].

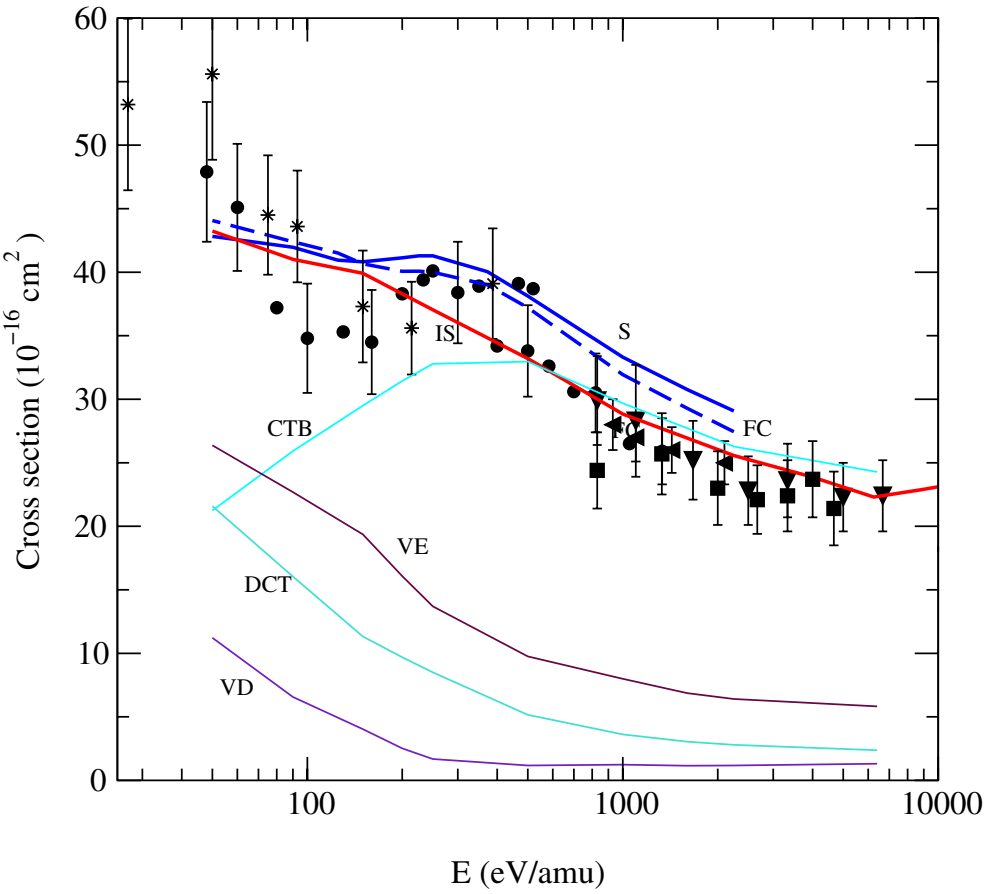

FIG. 10. Sudden cross sections for the reaction $C^{4+} + H_2 \longrightarrow C^{3+}(1s^2 3l) + H_2^+(X\ ^2\Sigma_g^+)$. *Our work: [4]; experimental: [32, 33, 28, 31] and previous effective potential calculations refs. [34–37]. (S) Sudden app.; (FC) Franck-Condon app.; (IS) IMP-SEC; (CTB) charge transfer to bound states; (VE) vibrational excitation; (DCT) dissociative charge transfer; (VD) vibrational dissociation.*

TABLE 7. IPM-SEC TOTAL CHARGE TRANSFER CROSS SECTIONS (IN UNITS OF 10^{-16} cm^2) FOR THE COLLISION N^{5+}+H_2

v(a.u.)	σ	v(a.u.)	σ
0.0447	1.350	0.320	14.308
0.0632	2.271	0.330	14.819
0.089	3.752	0.340	15.453
0.100	4.250	0.350	16.155
0.125	5.427	0.360	16.864
0.150	6.486	0.370	17.532
0.175	7.623	0.380	18.131
0.200	9.236	0.390	18.662
0.210	9.861	0.400	19.095
0.220	10.380	0.410	19.397
0.230	10.743	0.425	19.610
0.240	11.162	0.440	19.565
0.250	11.680	0.450	19.469
0.260	12.200	0.460	19.370
0.270	12.649	0.500	19.428
0.300	13.656	0.540	20.238
0.310	13.938		

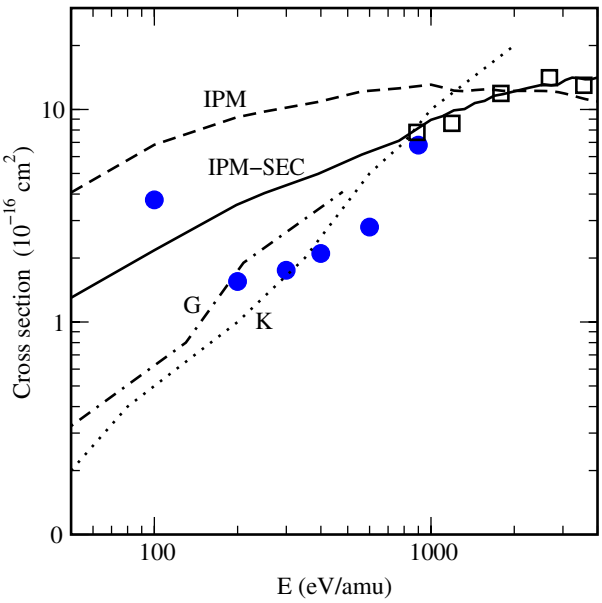

FIG. 11. Cross sections for population of $N^{4+}(1s^2\,3l)$ in $N^{5+}+H_2$ collisions. Our results: lines labelled IPM and IPM-SEC; (G) [34], (K) [36], (□) Exp. *[33], (●)* Exp. *[22].*

TABLE 8. CMTC SINGLE IONIZATION CROSS SECTIONS (IN UNITS OF 10^{-16} cm^2) FOR A^{q+}+H_2 COLLISIONS, AS FUNCTIONS OF THE RELATIVE VELOCITY

v(a.u.)	H^+	He^{2+}	Li^{3+}	Be^{4+}	B^{5+}	C^{6+}	N^{7+}	O^{8+}
0.6	0.235	0.112		0.019				
0.8	0.697	0.405	0.279	0.237	0.164	0.138		
1.0	1.095	1.023	0.877	0.814	0.773	0.684	0.642	0.538
2.0	2.069	5.511	9.036	12.502	15.724	18.893	21.735	24.304
3.0	1.232	3.732	6.549	9.741	13.191	16.697	20.511	24.295
5.0	0.301	1.615	3.119	4.786	6.677	8.750	10.978	13.410
8.0	0.199	0.725	1.486	2.413	3.454	4.613	5.8485	7.163
10.0	0.127	0.488	1.040	1.699	2.475	3.354	4.293	5.282
12.0	0.096	0.368	0.772	1.289	1.874	2.514	3.241	4.044
14.0	0.070	0.292	0.615	1.019	1.487	2.018	2.569	3.212
16.0	0.058	0.214	0.491	0.814	1.195	1.626	2.115	2.615

TABLE 9. CMTC SEC CROSS SECTIONS (IN UNITS OF 10^{-16} cm^2) FOR A^{q+}+H_2 COLLISIONS, AS FUNCTIONS OF THE RELATIVE VELOCITY

v(a.u.)	H^+	He^{2+}	Li^{3+}	Be^{4+}	B^{5+}	C^{6+}	N^{7+}	O^{8+}
0.6	6.451	13.214						
0.8	5.932	12.286	18.396	22.872	29.422	34.684	39.955	45.012
1.0	4.608	10.557	16.251	21.724	27.234	32.679	38.133	43.432
2.0	0.237	0.799	1.491	2.503	3.812	5.210	6.937	8.910
3.0	0.018	0.063	0.133	0.184	0.253	0.341	0.444	0.563
5.0		0.002	0.004	0.004	0.004	0.004	0.005	0.007

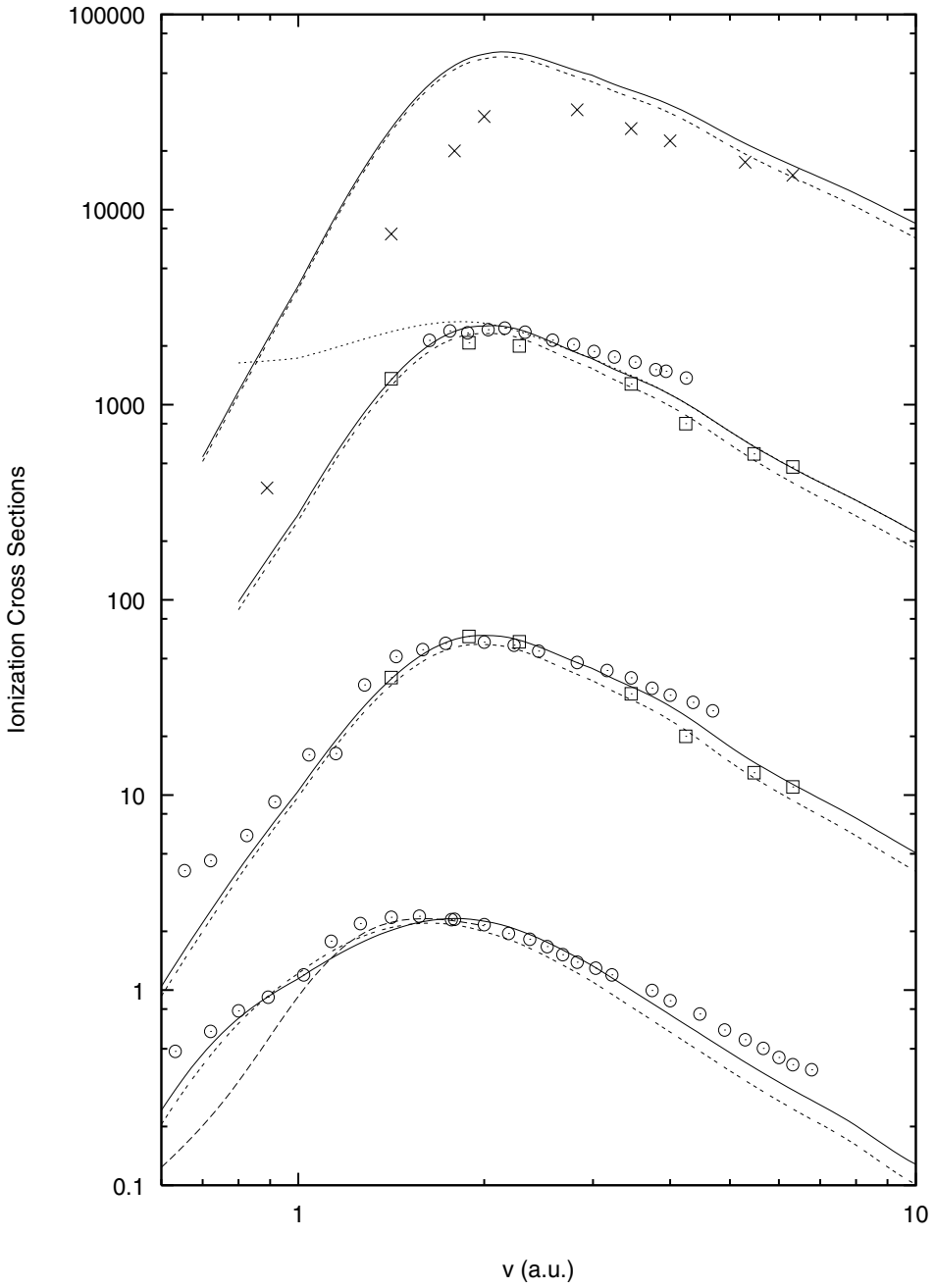

FIG. 12. SI cross sections as functions of the relative velocity v, for A^{q+}+H_2 collisions (in units of 10^{-16} cm^2 and scaled as stated below). From below to above, lines correspond to collisions with different projectiles: H^+ (single plus double ionization), He^{2+} (data × 10, single plus double ionization), Li^{3+} (data × 200, single plus double ionization plus transfer ionization), Be^{4+} (data × 10), B^{5+} (data × 5000, single ionization).

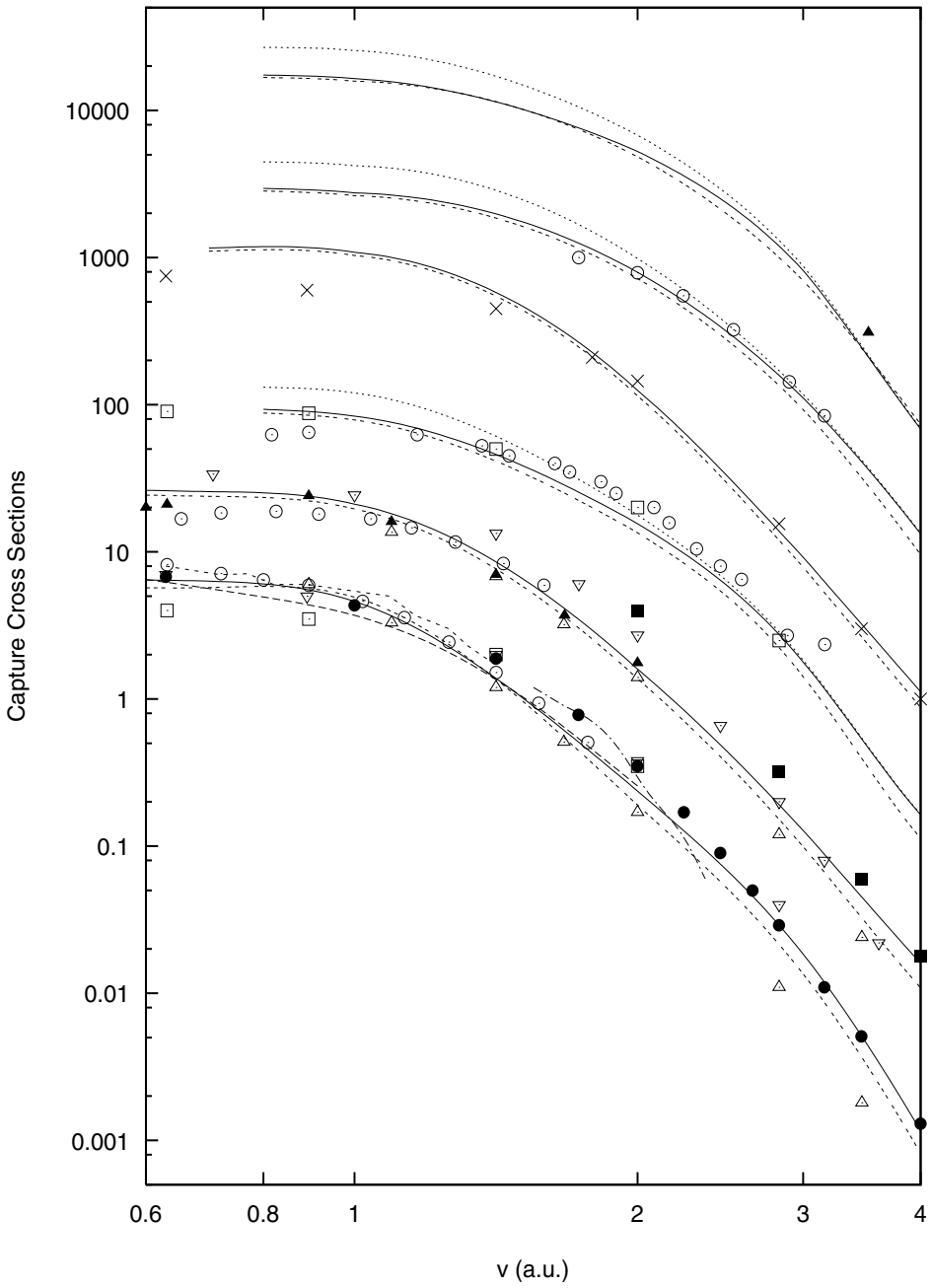

FIG. 13. SEC cross sections, as functions of the relative velocity v in a.u., for $A^{q+}+H_2$ collisions (in units of 10^{-16} cm^2 and scaled as stated below). From below to above, lines correspond to collisions with different projectiles: H^+ (single capture), He^{2+} (data × 2, single capture), Li^{3+} (data × 5, single capture plus transfer ionization), Be^{4+} (data × 50, single capture), B^{5+} (data × 200, single capture plus transfer ionization).

Theoretical study of electron capture and excitation processes in collisions of alpha-particles with helium-like C^{4+}, N^{5+}, O^{6+} ions

V.K. Nikulin, N.A. Guschina
A.F. Ioffe Physical-Technical Institute,
St. Petersburg, Russian Federation

Abstract. The cross section database for the processes of single-electron capture and neutralization of alpha-particles in collisions with helium-like C^{4+}, N^{5+}, O^{6+} ions was produced. The evaluated data were tabulated also for the excitation cross sections of the enumerated He-like ions which are of special importance for fusion research. The maximum values of single-electron capture cross sections were obtained equal to $\sim 2{\cdot}10^{-18}$, $6{\cdot}10^{-19}$, $3{\cdot}10^{-20}$ cm^2 for C^{4+}, N^{5+} and O^{6+} ions, respectively. The maximun values of neutralization cross sections were obtained equal to $4{\cdot}10^{-20}$, $2{\cdot}10^{-21}$, $7{\cdot}10^{-22}$ cm^2 and excitation cross sections were obtained equal to $4{\cdot}10^{-16}$, $2{\cdot}10^{-16}$, $1{,}5{\cdot}10^{-16}$ cm^2.

1. Introduction

The ion-ion collision systems are less suitable for experimental study and there is increasing demand of appropriate data for nuclear-fusion research and astrophysics.

The purpose of our study was to produce cross section databases for the processes of Single-Electron Capture (SEC), Double-Electron Capture (DEC) and of state selective target excitation cross section for collisions of alpha-particles with C^{q+}, N^{q+}, O^{q+} ions – the main impurities released from tokamak surfaces in the form of CO and nitrogen molecules. The study was made of the following reactions in the energy range 20 keV – 3, 4, 5 MeV (depending on whether the velocity of the projectile is lower than that of target electrons):

$$He^{2+} + A^{(Z-2)+}(1s^2) \;\rightarrow\; He^{+}(1s) + A^{(Z-1)+}(nl)\ , \tag{1}$$

$$He^{2+} + A^{(Z-2)+}(1s^2) \;\rightarrow\; He(1s^2) + A^{Z+}\ , \tag{2}$$

$$He^{2+} + A^{(Z-2)+}(1s^2) \;\rightarrow\; He^{2+} + A^{(Z-2)+}(nl, n'l')\ , \tag{3}$$

where $A^{(Z-2)+}$, $A^{(Z-1)+}$, A^{Z+}, respectively, indicate the helium-like, hydrogenic-like and fully stripped ions for atoms C, N and O. If in reaction (1) nl $\neq$ 1s, we have the transfer excitation (TE) process.

The case of alpha-particle projectiles is important for understanding α-losses to walls in TFTR. Particularly important could be the DEC processes which may lead to alpha-particle escape from the central plasma before their complete thermolization. The intensities of emission lines arising from transitions in He-like excited ions are used to determine the electron temperature of fusion plasma.

2. Proposed method

The detailed study of the above reactions was performed by using the close-coupling equation method with nine two-electron quasimolecular states ϕ_i as a basis.

Two-electron states ϕ_i were calculated in the single configuration approximation

$$\phi_i(\vec{r}_k, \vec{r}_l) = \frac{1}{\sqrt{2}}(\psi_k(\vec{r}_k)\psi_l(\vec{r}_l) + \psi_k(\vec{r}_l)\psi_l(\vec{r}_k)) \tag{4}$$

with the basis set of ψ_j (j=k, l) – Screened Diatomic Molecular Orbitals (SDMO), calculated by solving the two-centre problem

$$H\psi(\vec{r}_j) = \left[-\frac{\nabla^2}{2} - \frac{Z_1}{r_{1j}} - \frac{Z_2}{r_{2j}} + V_{eff}(\vec{R}, r_{1j}, r_{2j}) \right] \psi(\vec{r}_j) = \varepsilon_j(R)\psi(\vec{r}_j) \ . \tag{5}$$

Here $\varepsilon(R)_j$ – the energies of SDMO. The effective potential $\mathrm{V}_{eff}(\vec{R}, r_{1j}, r_{2j})$ is specified [1] in the parametric form

$$V_{eff}(\vec{R}, \vec{r}_j) = \frac{1}{2}\left[\frac{a_1 - b_1}{r_{1j}} + \frac{a_1 + b_1}{r_{2j}} + \frac{\widetilde{a}_1 + Ra_0}{r_{1j}r_{2j}} + \frac{b_2(r_{1j} - r_{2j})^2}{Rr_{1j}r_{2j}} \right] \ , \tag{6}$$

where R is the internuclear distance and r_{1j} and r_{2j} are the distances from the $\vec{r}_j$ electron to the nuclei with charges Z_1 ans Z_2, respectively. The scheme for determining the effective potential parameters a_0, $\widetilde{a}_1$, a_1, b_1 and b_2 are given in [1]. The SDMO basis obtained was used for calculating the total energies E_i of the two-electron diabatic states

$$E_i = < \phi_i | H | \phi_i > \ , \tag{7}$$

$$H = \sum_{j=k,l} \left(-\frac{\nabla_j^2}{2} - \frac{Z_1}{r_{1j}} - \frac{Z_2}{r_{2j}} \right) + \frac{1}{r_{kl}} \ . \tag{8}$$

The two-electron energies are calculated to the first order of perturbation theory [2] in residual interaction $\mathrm{W}=1/r_{kl}$–$\mathrm{V}_{eff}(\mathrm{r}_k)$-$\mathrm{V}_{eff}(\mathrm{r}_l)$. The effect of electron screening is important in two-electron quasimolecules.

The matrix elements of dynamic and potential couplings are obtained using the calculated basis SDMO. The dependence of results on the origin of the electronic coordinates for the dynamic matrix elements calculations has been investigated. All final results have been obtained for the origin placed at the centre of the charges of colliding ions.

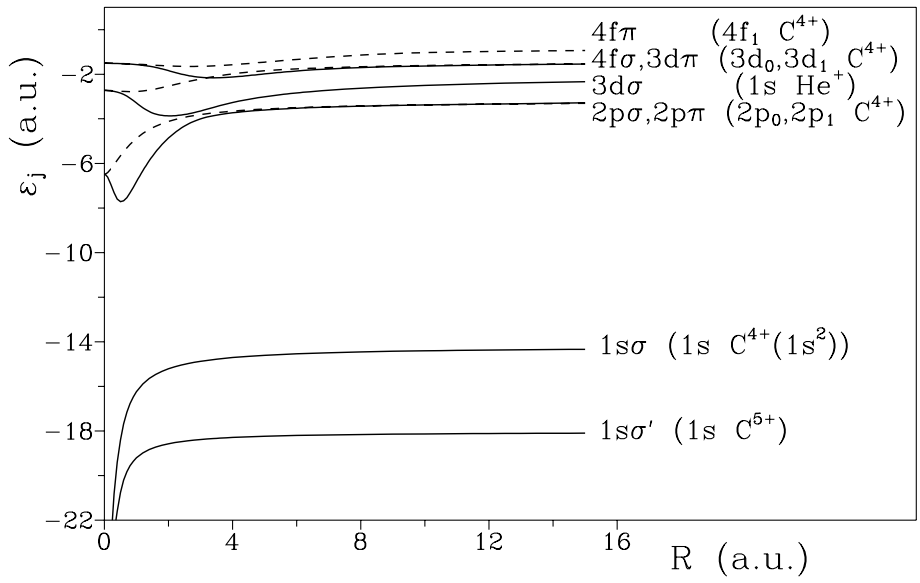

FIG. 1. The energies ε_j of the SDMO for the $(He+C)^{6+}$ quasimolecule.

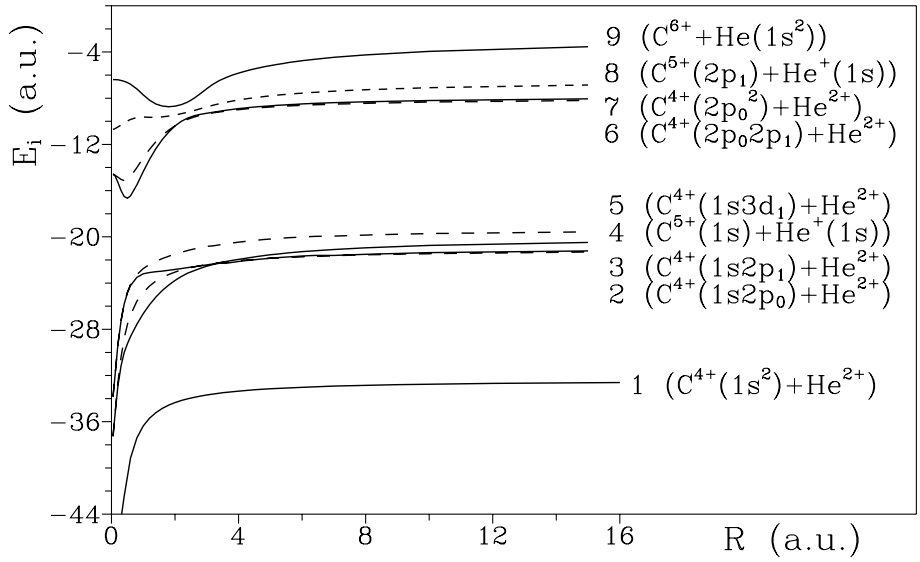

FIG. 2. The energies E_i of two-electron states ϕ_i (i=1 – 9) for the $(He+C)^{6+}$ quasimolecule: a. Entrance channel – $\phi_1(1s\sigma, 1s\sigma)$; b. SEC channel – $\phi_4(1s\sigma', 3d\sigma)$; c. Transfer excitation channel – $\phi_8(3d\sigma, 2p\pi)$; d. DEC channel – $\phi_9(3d\sigma, 3d\sigma)$; e. Single excitation channels – $\phi_2(1s\sigma', 2p\sigma)$, $\phi_3(1s\sigma', 2p\pi)$, $\phi_5(1s\sigma', 3d\pi)$; f. Double excitation channels – $\phi_7(2p\sigma, 2p\sigma)$, $\phi_6(2p\sigma, 2p\pi)$.

The calculated SDMO and two-electron state correlation diagrams for $(He+C)^{6+}$ quasimolecule are shown on figures 1 – 2. The $2p\sigma$–$3d\sigma$ pseudocrossing (Fig. 1) will be of decisive importance in SEC process in He^{2+}– C^{4+} collision. There is a clear-cut distinction between SDMO and two-electron state correlation diagram as to the concrete $2p\sigma$–$3d\sigma$ pseudocrossing in Fig. 1 and the corresponding pseudocrossing between ϕ_2 and ϕ_4 states in Fig. 2.

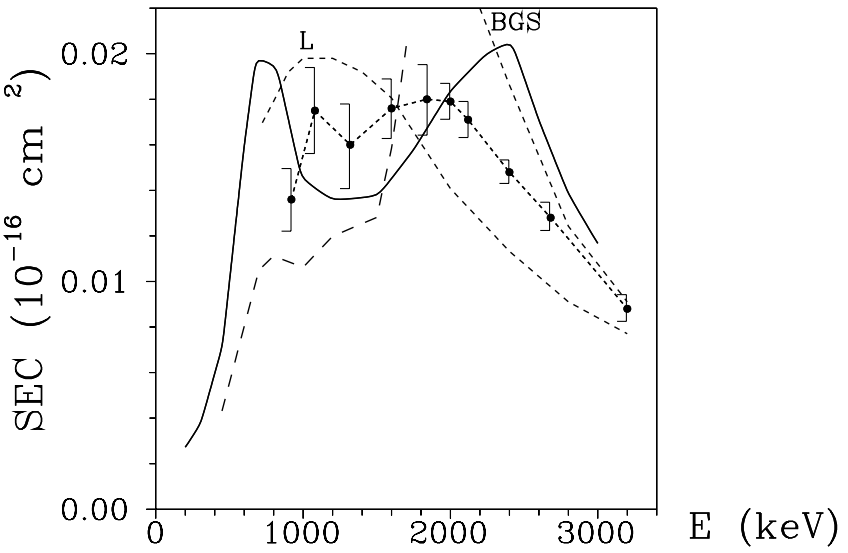

FIG. 3. The cross sections for the single-electron capture in $He^{2+} + C^{4+}(1s^2) \rightarrow He^{+}(1s) + C^{5+}(1s)$ collisions. Solid line – our results, broken line – our results without taking into account $< 2p\sigma|iL_y|2p\pi >$ rotational coupling. • – experimental data by M. Rodbro et al [5]; - - - – theoretical data [5] by Belkić, Gayet and Salin (BGS) and by Lin (L).

3. Results obtained

The results (our preliminary results have been presented early [3], [4]) of our two-electron multistate calculation of SEC cross section for He^{2+}– $C^{4+}(1s^2)$ collision system together with indirect experimental data on 1s – 1s capture in He^{2+} – CH_4 collision [5] are shown in Fig. 3. It is clearly seen that our results are in generally good agreement with experimental data. It is notable that the two-humped structures of the cross section curves are similar in shape. In Fig. 3 our calculation of SEC cross section is presented without taking into account rotational coupling between $2p\sigma$–$2p\pi$ SDMO. In this case the structure has disappeared. One might think that the two-humped structure of the cross section curves is associated with this coupling.

For the same collision systems SEC calculations were reported recently [6] in one-electron two-state approximation. For He^{2+}– O^{6+} system the results by Kuang [6] are an order of magnitude less then ours for alpha-particle energies < 1 MeV .

The results for DEC (reaction (2), neutralization of alpha particles) and for total excitation cross sections (reaction (3)) are shown in Fig. 5 and Fig. 6, respectively.

In Fig. 3 we compare our results for He^{2+}– C^{4+} collision system with the results of previous calculations communicated in work [5]. The results of C.D. Lin (L) are from a close-coupling calculation using basis sets of atomic orbitals (AO), while those of Dź. Belkić, R. Gayet and A. Salin (BGS) are from a continuum-distorted-wave calculation. In the high velocity limit there is agreement between all theoretical results and experiment. For comparison total SEC cross sections for collisions of alpha-particles with He-like C^{4+}, N^{5+}, O^{6+} ions are shown in Fig. 4.

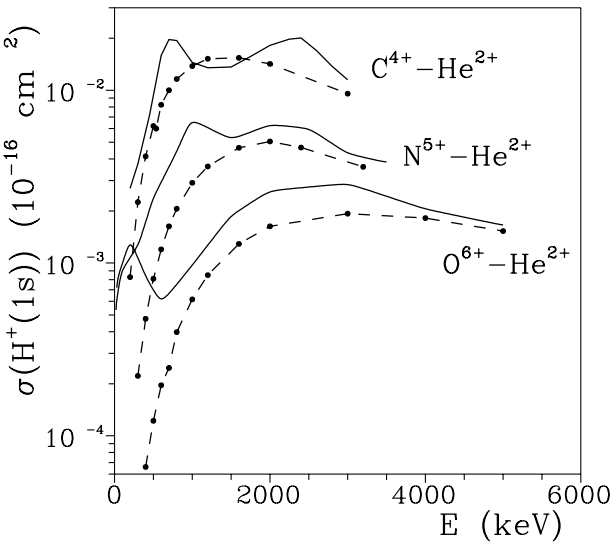

FIG. 4. The comparision of the cross sections for the single-electron capture in He^{2+} + $A^{(Z-2)+}(1s^2)$ collisions for Z=6, 7, 8. Solid line –our results, dash line – data by Y Kuang [6].

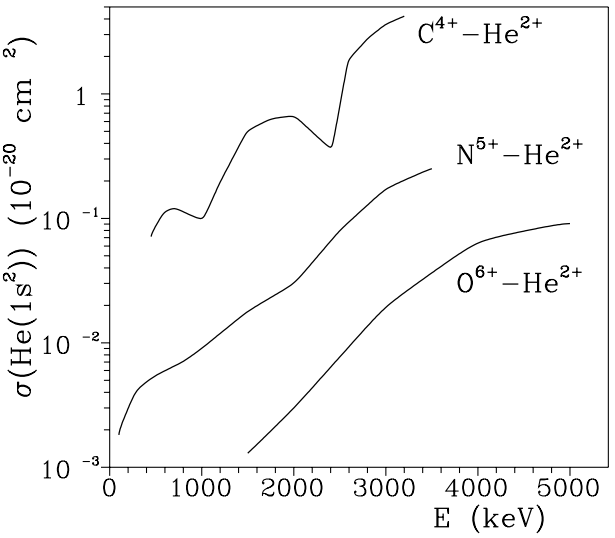

FIG. 5. The cross sections for the double-electron capture in He^{2+} + $A^{(Z-2)+}(1s^2)$ → $He(1s^2)$ + A^{Z+} collisions.

The following excitations have been taken into account: C^{4+}(nl,n'l'), N^{5+}(nl,n'l') (where (nl,n'l') ≡ 1s2p$_0$, 1s2p$_1$, 1s3d$_1$, 2p$_0^2$, 2p$_0$2p$_1$; O^{6+}(nl,n'l') (where (nl,n'l') ≡ 1s2p$_0$, 1s2p$_1$, 1s3d$_0$, 2p$_0^2$, 2p$_0$3d$_0$. The dominant contribution to the excitation cross section was found to be the excitations $C^{4+}(1s^2) \rightarrow C^{4+}(1s2p_1)$; $N^{5+}(1s^2) \rightarrow N^{5+}(1s2p_1)$, $N^{5+}(1s2p_0)$; $O^{6+}(1s^2) \rightarrow O^{6+}(1s2p_1)$, $O^{6+}(1s2p_0)$.

The calculated total SEC and transfer excitation cross sections (SEC+TE, reaction 1), DEC cross section (reaction 2) and dominant partial excitation cross sections of He-like target ions $A^{(Z-2)+}(1s^2)$ (reaction 3) are given in Tables 1 – 3.

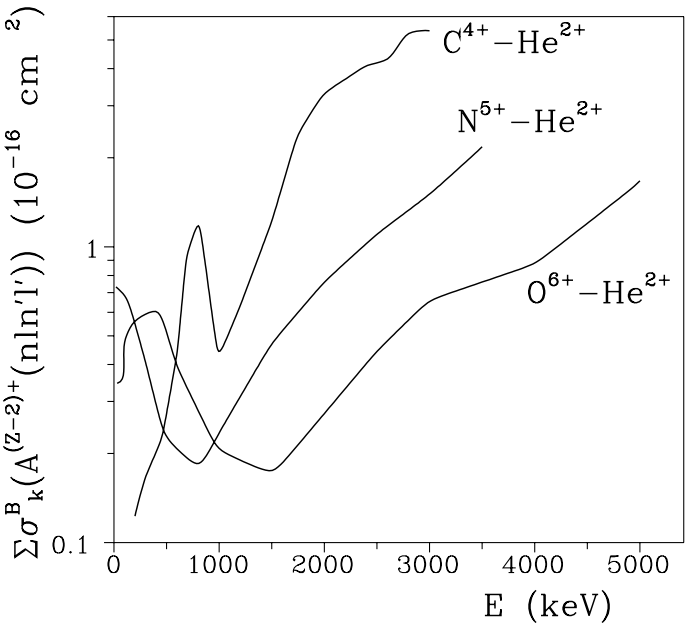

FIG. 6. The total excitation cross sections of He-like target ions $A^{(Z-2)+}(1s^2)$.

Table 1. The total SEC+TE and DEC cross sections and the partial excitation cross sections of $C^{4+}(1s^2)$ ion in He^{2+} – C^{4+} collision

E (keV)	SEC+TE (10^{-16} cm^2)	DEC (10^{-20} cm^2)	$C^{4+}(1s2p_0)$ (10^{-16} cm^2)	$C^{4+}(1s2p_{\pm1})$ (10^{-16} cm^2)
2.00E+02	0.272E-02	0.727E–01	0.420E-01	0.70154E–01
3.00E+02	0.376E-02	0.754E–01	0.419E-01	0.11799E–00
4.50E+02	0.718E-02	0.714E–01	0.498E-01	0.15281E–00
6.00E+02	0.159E-01	0.112E–00	0.741E-01	0.34763E–00
7.00E+02	0.196E-01	0.119E–00	0.143E-00	0.75897E–00
8.00E+02	0.194E-01	0.112E–00	0.179E-00	0.97687E–00
1.00E+03	0.145E-01	0.999E–01	0.668E-01	0.35843E–00
1.20E+03	0.136E-01	0.195E–00	0.866E-01	0.52813E–00
1.50E+03	0.138E-01	0.499E–00	0.162E-00	0.10379E+01
1.75E+03	0.157E-01	0.625E–00	0.479E-00	0.18749E+01
2.00E+03	0.183E-01	0.655E–00	0.727E-00	0.25187E+01
2.25E+03	0.199E-01	0.456E–00	0.870E-00	0.28696E+01
2.40E+03	0.204E-01	0.373E–00	0.925E-00	0.31031E+01
2.60E+03	0.170E-01	0.195E+01	0.835E-00	0.33901E+01
2.80E+03	0.138E-01	0.276E+01	0.925E-00	0.42142E+01
3.00E+03	0.116E-01	0.361E+01	0.918E-00	0.43270E+01

The calculated total SEC, DEC and excitation cross sections for ion-ion collisions He^{2+} – C^{4+}, N^{5+}, O^{6+} may be used in modeling of alpha-particles in thermonuclear plasma and in the design of future experiments.

All results presented above were obtained using our program package [7] for theoretical study of inelastic collisions.

Table 2. The total SEC+TE and dec cross sections and the partial excitation cross sections of $N^{5+}(1s^2)$ ion in He^{2+} – N^{5+} collision

E (keV)	SEC+TE (10^{-16} cm^2)	DEC (10^{-20} cm^2)	$N^{5+}(1s2p_0)$ (10^{-16} cm^2)	$N^{5+}(1s2p_{\pm1})$ (10^{-16} cm^2)
2.00E+01	0.534E-03	0.217E-03	0.496E-00	0.233E–00
1.00E+02	0.898E-03	0.181E-02	0.405E-00	0.265E–00
3.00E+02	0.128E-02	0.415E-02	0.212E-00	0.190E–00
5.00E+02	0.237E-02	0.544E-02	0.962E-01	0.124E–00
8.00E+02	0.444E-02	0.710E-02	0.112E-00	0.624E–01
1.00E+03	0.651E-02	0.904E-02	0.142E-00	0.738E–01
1.50E+03	0.535E-02	0.178E-01	0.241E-00	0.178E–00
2.00E+03	0.627E-02	0.303E-01	0.357E-00	0.373E–00
2.50E+03	0.597E-02	0.795E-01	0.481E-00	0.561E–00
3.00E+03	0.439E-02	0.170E-00	0.458E-00	0.938E–00
3.50E+03	0.391E-02	0.250E-00	0.679E-00	0.141E+01
3.80E+03	0.413E-02	0.261E-00	0.498E-00	0.133E+01
3.90E+03	0.430E-02	0.255E-00	0.516E-00	0.106E+01
4.00E+03	0.465E-02	0.247E-00	0.509E-00	0.905E–00
4.20E+03	0.571E-02	0.226E-00	0.458E-00	0.753E–00

Table 3. The total SEC+TE and DEC cross sections and the partial excitation cross sections of $O^{6+}(1s^2)$ ion in He^{2+} – O^{6+} collision

E (keV)	SEC+TE (10^{-16} cm^2)	DEC (10^{-20} cm^2)	$O^{6+}(1s2p_0)$ (10^{-16} cm^2)	$O^{6+}(1s2p_{\pm1})$ (10^{-16} cm^2)
3.00E+01	0.719E-03	0.300E-05	0.181E-00	0.101E–00
5.00E+01	0.838E-03	0.249E-05	0.204E-00	0.105E–00
1.00E+02	0.990E-03	0.209E-05	0.316E-00	0.132E–00
2.00E+02	0.127E-02	0.148E-05	0.353E-00	0.176E–00
4.00E+02	0.844E-03	0.684E-05	0.364E-00	0.235E–00
6.00E+02	0.619E-03	0.146E-04	0.234E-00	0.131E–00
1.00E+03	0.972E-03	0.460E-03	0.124E-00	0.804E–01
1.50E+03	0.185E-02	0.129E-02	0.799E-01	0.865E–01
2.00E+03	0.257E-02	0.300E-02	0.195E-00	0.263E–00
3.00E+03	0.284E-02	0.192E-01	0.212E-00	0.386E–00
4.00E+03	0.206E-02	0.632E-01	0.258E-00	0.611E–00
5.00E+03	0.165E-02	0.908E-01	0.453E-00	0.116E+01

This work was supported by IAEA (Research Contract N100088), by RFBR (project 99–02–17970) and by INTAS (Ref. N99–1326).

REFERENCES

[1] V.K. NIKULIN, N.A. GUSCHINA, J. Phys. B: Atom. Mol. Phys. **11** (1978) 3553.

[2] V.K. NIKULIN, N.A. GUSCHINA, Physica Scripta T **71** (1997) 134 .

[3] V.K. NIKULIN, N.A. GUSCHINA, "Two-electron description of excitation and charge-transfer in ion-ion He^{2+} – C^{4+}, N^{5+}, O^{6+} collisions". Preprint of Ioffe Physical-Technical Institute N 1740, St. Petersburg, 2000, 27 p.

[4] V.K. NIKULIN, N.A. GUSCHINA, "Electron Capture and Excitation in Ion-Ion Collision of Alpha Particles with He-like HCI". X Int. Conf. on the Physics of Highly Charged Ions, Book of Abstracts, Berkley 2000.

[5] M. RODBRO, E.H. PEDERSEN, C.L. COCKE, et al., Phys. Rev. A **19**, (1979) 1936.

[6] YU RANG KUANG, J. Phys. B: At. Mol. Opt. Phys. **25**, (1992) 199.

[7] N.A. GUSCHINA and V.K. NIKULIN. "The program package for inelastic process computation in slow ion–atom collisions". Preprint of Ioffe Physical-Technical Institute N 1717, St. Petersburg, 1998, 66 p.

Cross sections for electron capture from atomic helium by fully stripped ions

L. Gulyás
Institute of Nuclear Research of the Hungarian Academy of Sciences (ATOMKI),
Debrecen, Hungary

P.D. Fainstein
Comisión Nacional de Energía Atómica,
Centro Atómico Bariloche,
San Carlos de Bariloche, Argentina

Abstract. We give tables of theoretical cross sections for single electron capture from helium by fully stripped projectile ions with nuclear charge (Z) from 1 to 20, in the energy range 80–10000 keV/amu.

1. Introduction

The data produced in the present compilation has been obtained using the Continuum Distorted Wave (CDW) theory where the interaction between the active electron and the target is represented by model potential. We summarize the main concepts of the theory and refer to the literature for full details.

The energy range we are interested in corresponds to the intermediate and high impact energy range for which the first order of perturbative theories (eg. first-Born) is inadequate. At intermediate impact energies the response of the target atom to the projectile field is highly nonlinear while at high projectile velocities the contribution of double scattering cannot be neglected. The usefulness of the CDW theory for describing the electron capture process in the energy range considered has been demonstrated by the comparison with experimental results in a number of previous studies [1, 2].

2. Theory

It is well known that perturbative methods such as the Born series cannot be applied in the case of long range potentials like the Coulomb interaction. The CDW approximation was proposed by Cheshire [3, 4] as a solution to this problem in the case of electron capture. It can be shown that it is the first order of a distorted-wave series and that this series is free of divergences arising from the incorrect treatment of the Coulomb potential [1, 2]. This model belongs to a family of multiple scattering approaches based on the Distorted-Wave Theory and includes contributions from higher order scattering terms in the conventional Born series [2]. Despite a few deficiencies discussed in [5] the CDW model has major advantages: (i) it accounts for the long-range behavior of the Coulomb potential and includes distortions in the entrance and exit channels on equal footing, (ii) the scattering amplitude is given analytically in the case of Coulomb potentials, (iii) the model gives reasonable agreement with experiments for a number of collision systems.

The extension of the CDW model to the case of multi-electronic targets has been done within the framework of the one active electron picture [1]. In this model there is only one active electron which is captured by the impinging projectile while the others remain frozen. Up to now this extension of the model has been limited by the use of Coulomb wave functions with an effective charge to describe the distortion by the residual target. This means that the potential created by the passive electrons is approximated by a Coulomb field. The major problems with this representation is that the target potential is chosen differently in the entrance and exit channels and that in many cases the Coulomb field is not accurate enough, specially at small distances, to represent the field produced by the passive electrons.

In a recent extension of CDW model these problems were solved by the use of spherically symmetric model potentials to represent the potential due to the projectile and target nuclei and the passive electrons bound to them in both the initial and final channels [6]. Therefore the active electron evolves in a two center potential defined by these two model potentials. This allows for a more accurate description of the initial-target and final-projectile bound states and of the distortions in both channels. Here we give the main points in the generalization of the CDW theory and refer to [6, 7] for full details.

Let us consider the transfer of one electron from the target atom B to a projectile ion A. Z_B and Z_A denote the residual-target and projectile charge respectively. The potentials V_A (V_B) describes the interaction between the active electron and the projectile (residual target). In the pure three-body problem the continuum distorted waves are introduced as follows [3, 4]:

$$\begin{aligned}
\xi_i^+ &= \varphi_i(\boldsymbol{x})\; E_{i,-\boldsymbol{v}}(\boldsymbol{r})\; N(\nu_A)\; {}_1F_1(i\nu_A;1;ivs+i\boldsymbol{v}\cdot\boldsymbol{s}) \\
&= \varphi_i(\boldsymbol{x})\; E_{i,-\boldsymbol{v}}(\boldsymbol{r})\; D^+_{-\boldsymbol{v}}(Z_A,\boldsymbol{s}) \\
&= \varphi_i(\boldsymbol{x})\; E_{i,-\boldsymbol{v}}(\boldsymbol{r})\; \exp(i\boldsymbol{v}\cdot\boldsymbol{s})\; \psi^+_{-\boldsymbol{v}}(Z_A,\boldsymbol{s}) \qquad (1)
\end{aligned}$$

$$\begin{aligned}
\xi_f^- &= \varphi_f(\boldsymbol{s})\; E_{f,\boldsymbol{v}}(\boldsymbol{r})\; N(\nu_B)\; {}_1F_1(-i\nu_B;1;-ivx-i\boldsymbol{v}\cdot\boldsymbol{x}) \\
&= \varphi_f(\boldsymbol{s})\; E_{f,\boldsymbol{v}}(\boldsymbol{r})\; D^-_{\boldsymbol{v}}(Z_B,\boldsymbol{x}) \\
&= \varphi_f(\boldsymbol{s})\; E_{f,\boldsymbol{v}}(\boldsymbol{r})\; \exp(-i\boldsymbol{v}\cdot\boldsymbol{x})\; \psi^-_{\boldsymbol{v}}(Z_B,\boldsymbol{x}), \qquad (2)
\end{aligned}$$

with

$$E_{n,\boldsymbol{u}} = \exp\left[i\frac{1}{2}\boldsymbol{u}\cdot\boldsymbol{r} - i\frac{1}{8}u^2t - i\epsilon_n t\right], \qquad (3)$$

where $\boldsymbol{s}$, $\boldsymbol{x}$ and $\boldsymbol{r}$ denote the position vectors of the active electron with respect to a reference frame fixed at the target and projectile nucleus, and to the midpoint of the internuclear separation, $\boldsymbol{v}$ is the collision velocity, ${}_1F_1$ denotes the hypergeometric function and $\epsilon_{i,f}$ are the binding energies of the active electron in the initial and final states. In

the present case, the bound φ and continuum ψ wave functions are obtained from the numerical solutions of the eigen equations:

$$\left(-\frac{1}{2}\nabla_{x,s}^2 + V_X - \epsilon_{i,f}\right)\varphi_{i,f} = 0 \tag{4}$$

$$\left(-\frac{1}{2}\nabla_{x,s}^2 + V_X - v^2\right)\psi_{\boldsymbol{v}}^{\pm} = 0 \tag{5}$$

where V_X is the model potential, $\nu = Z_X/v$ and $N(\nu) = \exp(\nu\pi/2)\Gamma(1-i\nu)$ (X stands for A and B).

Using the straight line version of the impact parameter approximation, the transition amplitude for capture is given by:

$$T_{if}(\boldsymbol{\eta}) = -N(\nu_A)\, N(\nu_B)\, \boldsymbol{I}_A \cdot \boldsymbol{J}_B, \tag{6}$$

where $\boldsymbol{\eta}$ is the transverse component of the momentum transfer, and $\boldsymbol{I}_A$ and $\boldsymbol{J}_B$ are defined as follows:

$$\boldsymbol{I}_A = \int \mathrm{d}\boldsymbol{s}\, \exp(i\boldsymbol{\rho}_A \cdot \boldsymbol{s})\, \varphi_f^*(\boldsymbol{s})\, \boldsymbol{\nabla}_s D_{\boldsymbol{v}}^+(Z_A, \boldsymbol{s}) \tag{7}$$

$$\boldsymbol{J}_B = \int \mathrm{d}\boldsymbol{x}\, \exp(i\boldsymbol{\rho}_B \cdot \boldsymbol{x})\, D_{-\boldsymbol{v}}^-(Z_B, \boldsymbol{x})\, \boldsymbol{\nabla}_x \varphi_i(\boldsymbol{x}) \tag{8}$$

with

$$\boldsymbol{\rho}_{A,B} = \pm\boldsymbol{\eta} - \left(\frac{v}{2} \pm \frac{\epsilon_i - \epsilon_f}{v}\right)\hat{\boldsymbol{v}} \tag{9}$$

where the $+(-)$ sign corresponds to the label A (B). The integrals $\boldsymbol{I}_A$ and $\boldsymbol{J}_B$ can be evaluated numerically (see ref. [7] for details).

The total cross section is obtained as:

$$\sigma_{if} = (2\pi v)^{-2} \int \mathrm{d}\boldsymbol{\eta}\, |T_{if}(\boldsymbol{\eta})|^2 \tag{10}$$

We have applied this generalized CDW model for the calculation of the total cross sections for single electron capture from helium by bare projectile impact. The charge of the impinging ions range from 1-20 and the collision energies from 80 keV/amu to 10 MeV/amu. The interaction of the active electron with the $He+$ ion was represented by the Hartree-Fock-Slater potential [8]. The cross sections were calculated to selective (characterized by the quantum numbers n, l and m) final bound states and the sum of

them over l and m are presented for a given n manifold in the tables. The sum of the state selective cross sections, calculated using the n^3 rule, are also given in the last line of a given table:

$$\sigma_{all} = \sum_{n=1}^{7} \sigma_n + 4.53\sigma_8, \tag{11}$$

provided that $\sigma_8 < \sigma_7 < \sigma_6$, where σ_n is the sum of the cross section for capture to each final bound state with principal quantum number n. All cross sections are given in cm^2. Dashes indicate entries which have been omitted because they are outside the domain of validity of the CDW model [1] defined by E(keV/amu) $\geq$ 80 sup(| ϵ_i | , | ϵ_f |).

REFERENCES

[1] Dž. BELKIĆ, R. GAYET, A. SALIN, Phys. Rep. **56**, 249 (1979).
[2] D.P. DEWANGAN, J. EICHLER, Phys. Rep. **247**, 59 (1994).
[3] I.M. CHESHIRE, Proc. Phys. Soc. (London) **84**, 89 (1964).
[4] R. GAYET, J. Phys. B **5**, 483 (1972).
[5] D.S.F. CROTHERS, L. DUBÉ, Adv. At. Mol. Opt. Phys. **30**, 285 (1993).
[6] S. SUZUKI, L. GULYÁS, N. SHIMAKURA, P.D. FAINSTEIN, T. SHIRAI, J. Phys. B **33**, 3307 (2000).
[7] L. GULYÁS, P.D. FAINSTEIN, T. SHIRAI, Phys. Rev. A: submitted for publication (2001).
[8] F. HERMAN, S. SKILLMAN, *Atomic Structure Calculations* (Prentice-Hall, Inc., Englewood Cliffs, N. J., 1963).

Table 1. Cross-sections for the process $B^+ + He(1s^2) \rightarrow B^{0+}(n) + He^+(1s)$ (in cm^2) from CDW calculations using Hartree-Fock-Slater model potential for the electron target interaction, where B^+ is a fully stripped ion

Final state	Projectile energy (keV/amu)							
n	80	90	100	125	150	200	300	400
1	5.74^{-17}	4.09^{-17}	2.98^{-17}	1.48^{-17}	8.03^{-18}	2.88^{-18}	5.94^{-19}	1.78^{-19}
2	9.76^{-18}	7.08^{-18}	5.23^{-18}	2.63^{-18}	1.43^{-18}	5.03^{-19}	9.96^{-20}	2.88^{-20}
3	3.17^{-18}	2.30^{-18}	1.70^{-18}	8.53^{-19}	4.62^{-19}	1.62^{-19}	3.17^{-20}	9.10^{-21}
4	1.40^{-18}	1.02^{-18}	7.50^{-19}	3.75^{-19}	2.03^{-19}	7.08^{-20}	1.38^{-20}	3.94^{-21}
5	7.38^{-19}	5.34^{-19}	3.94^{-19}	1.97^{-19}	1.06^{-19}	3.70^{-20}	7.18^{-21}	2.05^{-21}
6	4.33^{-19}	3.13^{-19}	2.31^{-19}	1.12^{-19}	6.09^{-20}	2.13^{-20}	4.14^{-21}	1.18^{-21}
7	2.75^{-19}	1.99^{-19}	1.47^{-19}	7.11^{-20}	3.85^{-20}	1.35^{-20}	2.62^{0}	7.48^{0}
8	1.85^{-19}	1.34^{-19}	9.87^{-20}	4.78^{-20}	2.59^{-20}	9.04^{-21}	1.76^{-21}	5.02^{-22}
σ_{all}	7.40^{-17}	5.29^{-17}	3.87^{-17}	1.92^{-17}	1.04^{-17}	3.72^{-18}	7.61^{-19}	2.26^{-19}

Table 1. Cross-sections for the process $B^+ + He(1s^2) \rightarrow B^{0+}(n) + He^+(1s)$ (in cm^2) from CDW calculations using Hartree-Fock-Slater model potential for the electron target interaction, where B^+ is a fully stripped ion

Final state	Projectile energy (keV/amu)							
n	500	600	700	800	900	1000	2000	3000
1	6.68^{-20}	2.92^{-20}	1.43^{-20}	7.58^{-21}	4.30^{-21}	2.57^{-21}	7.61^{-23}	8.84^{-24}
2	1.05^{-20}	4.51^{-21}	2.17^{-21}	1.13^{-21}	6.36^{-22}	3.77^{-22}	1.06^{-23}	1.21^{-24}
3	3.30^{-21}	1.41^{-21}	6.74^{-22}	3.52^{-22}	1.97^{-22}	1.16^{-22}	3.24^{-24}	3.67^{-25}
4	1.43^{-21}	6.08^{-22}	2.90^{-22}	1.51^{-22}	8.46^{-23}	5.00^{-23}	1.39^{-24}	1.57^{-25}
5	7.42^{-22}	3.15^{-22}	1.50^{-22}	7.84^{-23}	4.38^{-23}	2.59^{-23}	7.16^{-25}	8.10^{-26}
6	4.29^{-22}	1.82^{-22}	8.70^{-23}	4.53^{-23}	2.53^{-23}	1.49^{-23}	4.14^{-25}	4.68^{-26}
7	2.71^{-22}	1.15^{-22}	5.49^{-23}	2.86^{-23}	1.60^{-23}	9.43^{-24}	2.61^{-25}	2.95^{-26}
8	1.82^{-22}	7.72^{-23}	3.69^{-23}	1.92^{-23}	1.07^{-23}	6.33^{-24}	1.75^{-25}	1.98^{-26}
σ_{all}	8.43^{-20}	3.67^{-20}	1.79^{-20}	9.46^{-21}	5.35^{-21}	3.19^{-21}	9.35^{-23}	1.08^{-23}

Table 1. Cross-sections for the process $B^{+} + He(1s^2) \rightarrow B^{0+}(n) + He^{+}(1s)$ (in cm^2) from CDW calculations using Hartree-Fock-Slater model potential for the electron target interaction, where B^{+} is a fully stripped ion

Final state	Projectile energy (keV/amu)						
n	4000	5000	6000	7000	8000	9000	10000
1	1.86^{-24}	5.44^{-25}	1.98^{-25}	8.36^{-26}	3.95^{-26}	2.04^{-26}	1.12^{-26}
2	2.51^{-25}	7.31^{-26}	2.65^{-26}	1.12^{-26}	5.28^{-27}	2.72^{-27}	1.50^{-27}
3	7.62^{-26}	2.22^{-26}	8.04^{-27}	3.39^{-27}	1.60^{-27}	8.24^{-28}	4.54^{-28}
4	3.26^{-26}	9.48^{-27}	3.43^{-27}	1.45^{-27}	6.84^{-28}	3.52^{-28}	1.94^{-28}
5	1.68^{-26}	4.89^{-27}	1.77^{-27}	7.73^{-28}	3.53^{-28}	1.82^{-28}	1.00^{-28}
6	9.70^{-27}	2.83^{-27}	1.02^{-27}	4.32^{-28}	2.04^{-28}	1.05^{-28}	5.78^{-29}
7	6.12^{-27}	1.78^{-27}	6.46^{-28}	2.72^{-28}	1.28^{-28}	6.61^{-29}	3.64^{-29}
8	4.10^{-27}	1.20^{-27}	4.33^{-28}	1.82^{-28}	8.61^{-29}	4.43^{-29}	2.44^{-29}
σ_{all}	2.27^{-24}	6.64^{-25}	2.41^{-25}	1.02^{-25}	4.82^{-26}	2.48^{-26}	1.37^{-26}

Table 2. Cross-sections for the process $B^{2+} + He(1s^2) \rightarrow B^{+}(n) + He^{+}(1s)$ (in cm^2) from CDW calculations using Hartree-Fock-Slater model potential for the electron target interaction, where B^{2+} is a fully stripped ion

Final state	Projectile energy (keV/amu)							
n	80	90	100	125	150	200	300	400
1	–	–	–	–	–	2.24^{-17}	5.86^{-18}	2.05^{-18}
2	1.71^{-16}	1.23^{-16}	9.09^{-17}	4.60^{-17}	2.55^{-17}	9.36^{-18}	1.99^{-18}	6.07^{-19}
3	6.70^{-17}	4.86^{-17}	3.59^{-17}	1.82^{-17}	1.00^{-17}	3.60^{-18}	7.39^{-19}	2.19^{-19}
4	3.19^{-17}	2.32^{-17}	1.71^{-17}	8.67^{-18}	4.74^{-18}	1.69^{-18}	3.41^{-19}	9.97^{-20}
5	1.75^{-17}	1.27^{-17}	9.40^{-18}	4.73^{-18}	2.58^{-18}	9.15^{-19}	1.82^{-19}	5.28^{-20}
6	1.05^{-17}	7.61^{-18}	5.63^{-18}	2.83^{-18}	1.54^{-18}	5.23^{-19}	1.05^{-19}	3.07^{-20}
7	6.72^{-18}	4.88^{-18}	3.61^{-18}	1.82^{-18}	9.92^{-19}	3.34^{-19}	6.72^{-19}	1.96^{-20}
8	4.56^{-18}	3.31^{-18}	2.45^{-18}	1.23^{-18}	6.73^{-19}	2.26^{-19}	4.53^{-20}	1.32^{-20}
σ_{all}	–	–	–	–	–	3.99^{-17}	9.49^{-18}	3.14^{-18}

Table 2. Cross-sections for the process $B^{2+} + He(1s^2) \rightarrow B^{+}(n) + He^{+}(1s)$ (in cm^2) from CDW calculations using Hartree-Fock-Slater model potential for the electron target interaction, where B^{2+} is a fully stripped ion

Final state	Projectile energy (keV/amu)							
n	500	600	700	800	900	1000	2000	3000
1	8.63^{-19}	4.11^{-19}	2.14^{-19}	1.20^{-19}	7.13^{-20}	4.43^{-20}	1.59^{-21}	2.00^{-22}
2	2.30^{-19}	1.02^{-19}	4.98^{-20}	2.66^{-20}	1.51^{-20}	9.06^{-21}	2.72^{-22}	3.18^{-23}
3	8.12^{-20}	3.52^{-20}	1.70^{-20}	8.98^{-21}	5.06^{-21}	3.01^{-21}	8.66^{-23}	9.99^{-24}
4	3.66^{-20}	1.57^{-20}	7.58^{-21}	3.98^{-21}	2.24^{-21}	1.33^{-21}	3.77^{-23}	4.33^{-24}
5	1.93^{-20}	8.29^{-21}	3.98^{-21}	2.10^{-21}	1.17^{-21}	6.90^{-22}	1.95^{-23}	2.23^{-24}
6	1.13^{-20}	4.84^{-21}	2.33^{-21}	1.22^{-21}	6.84^{-22}	4.06^{-22}	1.15^{-23}	1.31^{-24}
7	7.17^{-21}	3.07^{-21}	1.48^{-21}	7.74^{-22}	4.34^{-22}	2.57^{-22}	7.25^{-24}	8.27^{-25}
8	4.83^{-21}	2.07^{-21}	9.94^{-22}	5.21^{-22}	2.92^{-22}	1.73^{-22}	4.87^{-24}	5.56^{-25}
σ_{all}	1.27^{-18}	5.89^{-19}	3.01^{-19}	1.66^{-19}	9.73^{-20}	5.98^{-20}	2.05^{-21}	2.54^{-22}

Table 2. Cross-sections for the process $B^{2+} + He(1s^2) \rightarrow B^{+}(n) + He^{+}(1s)$ (in cm^2) from CDW calculations using Hartree-Fock-Slater model potential for the electron target interaction, where B^{2+} is a fully stripped ion

Final state	Projectile energy (keV/amu)						
n	4000	5000	6000	7000	8000	9000	10000
1	4.40^{-23}	1.33^{-23}	4.94^{-24}	2.12^{-24}	1.02^{-24}	5.28^{-25}	2.93^{-25}
2	6.72^{-24}	1.98^{-24}	7.23^{-25}	3.07^{-25}	1.46^{-25}	7.53^{-26}	4.16^{-26}
3	2.09^{-24}	6.14^{-25}	2.24^{-25}	9.45^{-26}	4.46^{-26}	2.31^{-26}	1.27^{-26}
4	9.04^{-25}	2.63^{-25}	9.61^{-26}	4.07^{-26}	1.91^{-26}	9.88^{-27}	5.45^{-27}
5	4.67^{-25}	1.36^{-25}	4.99^{-26}	2.08^{-26}	9.81^{-27}	5.09^{-27}	2.81^{-27}
6	2.73^{-25}	8.00^{-26}	2.91^{-26}	1.23^{-26}	5.83^{-27}	3.01^{-27}	1.66^{-27}
7	1.73^{-25}	5.05^{-26}	1.84^{-26}	7.78^{-27}	3.68^{-27}	1.90^{-27}	1.05^{-27}
8	1.16^{-25}	3.39^{-26}	1.23^{-26}	5.22^{-27}	2.47^{-27}	1.28^{-27}	7.05^{-28}
σ_{all}	5.52^{-23}	1.66^{-23}	6.13^{-24}	2.63^{-24}	1.25^{-24}	6.52^{-25}	3.62^{-25}

Table 3. Cross-sections for the process $B^{3+} + He(1s^2) \rightarrow B^{2+}(n) + He^{+}(1s)$ (in cm^2) from CDW calculations using Hartree-Fock-Slater model potential for the electron target interaction, where B^{3+} is a fully stripped ion

Final state	Projectile energy (keV/amu)							
n	80	90	100	125	150	200	300	400
1	–	–	–	–	–	–	–	3.98^{-18}
2	–	–	3.16^{-16}	1.65^{-16}	9.46^{-17}	3.73^{-17}	8.76^{-18}	2.86^{-18}
3	3.37^{-16}	2.44^{-16}	1.81^{-16}	9.21^{-17}	5.12^{-17}	1.90^{-17}	4.09^{-18}	1.26^{-18}
4	1.81^{-16}	1.31^{-16}	9.71^{-17}	4.93^{-17}	2.73^{-17}	9.91^{-18}	2.06^{-18}	6.18^{-19}
5	1.04^{-16}	7.58^{-17}	5.62^{-17}	2.85^{-17}	1.57^{-17}	5.65^{-18}	1.16^{-18}	3.43^{-19}
6	6.39^{-17}	4.66^{-17}	3.46^{-17}	1.75^{-17}	9.66^{-18}	3.15^{-18}	6.59^{-19}	1.97^{-19}
7	4.17^{-17}	3.03^{-17}	2.25^{-17}	1.15^{-17}	6.30^{-18}	2.03^{-18}	4.24^{-19}	1.26^{-19}
8	2.85^{-17}	2.08^{-17}	1.54^{-17}	7.86^{-18}	4.32^{-18}	1.38^{-18}	2.88^{-19}	8.56^{-20}
σ_{all}	–	–	–	–	–	–	–	9.77^{-18}

Table 3. Cross-sections for the process $B^{3+} + He(1s^2) \rightarrow B^{2+}(n) + He^{+}(1s)$ (in cm^2) from CDW calculations using Hartree-Fock-Slater model potential for the electron target interaction, where B^{3+} is a fully stripped ion

Final state	Projectile energy (keV/amu)							
n	500	600	700	800	900	1000	2000	3000
1	1.97^{-18}	1.06^{-18}	6.11^{-19}	3.69^{-19}	2.33^{-19}	1.53^{-19}	7.25^{-21}	1.02^{-21}
2	1.14^{-18}	5.24^{-19}	2.65^{-19}	1.45^{-19}	8.39^{-20}	5.11^{-20}	1.66^{-21}	2.01^{-22}
3	4.78^{-19}	2.11^{-19}	1.04^{-19}	5.55^{-20}	3.16^{-20}	1.89^{-20}	5.69^{-22}	6.66^{-23}
4	2.31^{-19}	1.01^{-19}	4.90^{-20}	2.60^{-20}	1.47^{-20}	8.74^{-21}	2.54^{-22}	2.95^{-23}
5	1.27^{-19}	5.48^{-20}	2.66^{-20}	1.40^{-20}	7.86^{-21}	4.67^{-21}	1.33^{-22}	1.54^{-23}
6	7.32^{-20}	3.18^{-20}	1.54^{-20}	8.11^{-21}	4.57^{-21}	2.72^{-21}	7.79^{-23}	8.95^{-24}
7	4.69^{-20}	2.03^{-20}	9.83^{-21}	5.18^{-21}	2.91^{-21}	1.73^{-21}	4.94^{-23}	5.67^{-24}
8	3.18^{-20}	1.38^{-20}	6.65^{-21}	3.50^{-21}	1.97^{-21}	1.17^{-21}	3.33^{-23}	3.81^{-24}
σ_{all}	4.22^{-18}	2.07^{-18}	1.11^{-18}	6.39^{-19}	3.88^{-19}	2.46^{-19}	1.01^{-20}	1.36^{-21}

Table 3. Cross-sections for the process $B^{3+} + He(1s^2) \rightarrow B^{2+}(n) + He^{+}(1s)$ (in cm^2) from CDW calculations using Hartree-Fock-Slater model potential for the electron target interaction, where B^{3+} is a fully stripped ion

Final state	Projectile energy (keV/amu)						
n	4000	5000	6000	7000	8000	9000	10000
1	2.39^{-22}	7.50^{-23}	2.86^{-23}	1.26^{-23}	6.11^{-24}	3.22^{-24}	1.81^{-24}
2	4.32^{-23}	1.29^{-23}	4.75^{-24}	2.03^{-24}	9.69^{-25}	5.03^{-25}	2.79^{-25}
3	1.41^{-23}	4.15^{-24}	1.52^{-24}	6.45^{-25}	3.06^{-25}	1.58^{-25}	8.77^{-26}
4	6.18^{-24}	1.81^{-24}	6.64^{-25}	2.80^{-25}	1.33^{-25}	6.89^{-26}	3.79^{-26}
5	3.22^{-24}	9.43^{-25}	3.45^{-25}	1.45^{-25}	6.87^{-26}	3.57^{-26}	1.96^{-26}
6	1.87^{-24}	5.50^{-25}	2.00^{-25}	8.50^{-26}	4.03^{-26}	2.08^{-26}	1.15^{-26}
7	1.19^{-24}	3.48^{-25}	1.27^{-25}	5.37^{-26}	2.55^{-26}	1.32^{-26}	7.29^{-27}
8	7.97^{-25}	2.34^{-25}	8.51^{-26}	3.61^{-26}	1.71^{-26}	8.84^{-27}	4.94^{-27}
σ_{all}	3.12^{-22}	9.67^{-23}	3.66^{-23}	1.60^{-23}	7.73^{-24}	4.06^{-24}	2.28^{-24}

Table 4. Cross-sections for the process $B^{4+} + He(1s^2) \rightarrow B^{3+}(n) + He^{+}(1s)$ (in cm^2) from CDW calculations using Hartree-Fock-Slater model potential for the electron target interaction, where B^{4+} is a fully stripped ion

Final state	Projectile energy (keV/amu)							
n	80	90	100	125	150	200	300	400
1	–	–	–	–	–	–	–	–
2	–	–	–	–	–	7.09^{-17}	1.92^{-17}	6.90^{-18}
3	8.61^{-16}	6.31^{-16}	4.72^{-16}	2.44^{-16}	1.38^{-16}	5.34^{-17}	1.22^{-17}	3.91^{-18}
4	5.57^{-16}	4.04^{-16}	3.01^{-16}	1.54^{-16}	8.58^{-17}	3.20^{-17}	6.90^{-18}	2.12^{-18}
5	3.50^{-16}	2.54^{-16}	1.88^{-16}	9.59^{-17}	5.31^{-17}	1.95^{-17}	4.10^{-18}	1.24^{-18}
6	2.21^{-16}	1.61^{-16}	1.20^{-16}	6.12^{-17}	3.39^{-17}	1.02^{-17}	2.24^{-18}	6.92^{-19}
7	1.47^{-16}	1.07^{-16}	7.99^{-17}	4.08^{-17}	2.26^{-17}	6.66^{-18}	1.46^{-18}	4.50^{-19}
8	1.01^{-16}	7.42^{-17}	5.53^{-17}	2.83^{-17}	1.57^{-17}	4.57^{-18}	1.00^{-18}	3.07^{-19}
σ_{all}	–	–	–	–	–	–	–	–

Table 4. Cross-sections for the process $B^{4+} + He(1s^2) \rightarrow B^{3+}(n) + He^{+}(1s)$ (in cm^2) from CDW calculations using Hartree-Fock-Slater model potential for the electron target interaction, where B^{4+} is a fully stripped ion

Final state	Projectile energy (keV/amu)							
n	500	600	700	800	900	1000	2000	3000
1	–	–	7.97^{-19}	5.27^{-19}	3.60^{-19}	2.51^{-19}	1.67^{-20}	2.71^{-21}
2	2.94^{-18}	1.41^{-18}	7.43^{-19}	4.18^{-19}	2.48^{-19}	1.55^{-19}	5.61^{-21}	7.06^{-22}
3	1.54^{-18}	6.95^{-19}	3.49^{-19}	1.89^{-19}	1.09^{-19}	6.60^{-20}	2.08^{-21}	2.49^{-22}
4	8.10^{-19}	3.58^{-19}	1.76^{-19}	9.42^{-20}	5.37^{-20}	3.22^{-20}	9.62^{-22}	1.13^{-22}
5	4.65^{-19}	2.03^{-19}	9.91^{-20}	5.24^{-20}	2.97^{-20}	1.77^{-20}	5.17^{-22}	5.98^{-23}
6	2.64^{-19}	1.16^{-19}	5.69^{-20}	3.02^{-20}	1.71^{-20}	1.02^{-20}	3.00^{-22}	3.46^{-23}
7	1.71^{-19}	7.50^{-20}	3.67^{-20}	1.95^{-20}	1.10^{-20}	6.58^{-21}	1.91^{-22}	2.20^{-23}
8	1.16^{-19}	5.10^{-20}	2.49^{-20}	1.32^{-20}	7.48^{-21}	4.46^{-21}	1.29^{-22}	1.48^{-23}
σ_{all}	–	–	2.37^{-18}	1.39^{-18}	8.63^{-19}	5.59^{-19}	2.70^{-20}	3.96^{-21}

Table 4. Cross-sections for the process $B^{4+} + He(1s^2) \rightarrow B^{3+}(n) + He^{+}(1s)$ (in cm^2) from CDW calculations using Hartree-Fock-Slater model potential for the electron target interaction, where B^{4+} is a fully stripped ion

Final state	Projectile energy (keV/amu)						
n	4000	5000	6000	7000	8000	9000	10000
1	6.85^{-22}	2.26^{-22}	8.97^{-23}	4.04^{-23}	2.01^{-23}	1.08^{-23}	6.13^{-24}
2	1.55^{-22}	4.69^{-23}	1.75^{-23}	7.51^{-24}	3.60^{-24}	1.88^{-24}	1.05^{-24}
3	5.29^{-23}	1.57^{-23}	5.78^{-24}	2.47^{-24}	1.17^{-24}	6.09^{-25}	3.38^{-25}
4	2.38^{-23}	7.01^{-24}	2.57^{-24}	1.09^{-24}	5.18^{-25}	2.68^{-25}	1.48^{-25}
5	1.26^{-23}	3.69^{-24}	1.34^{-24}	5.70^{-25}	2.70^{-25}	1.40^{-25}	7.70^{-26}
6	7.25^{-24}	2.13^{-24}	7.78^{-25}	3.30^{-25}	1.57^{-25}	8.11^{-26}	4.49^{-26}
7	4.60^{-24}	1.35^{-24}	4.93^{-25}	2.09^{-25}	9.93^{-26}	5.13^{-26}	2.84^{-26}
8	3.10^{-24}	9.09^{-25}	3.31^{-25}	1.41^{-25}	6.67^{-26}	3.49^{-26}	1.91^{-26}
σ_{all}	9.55^{-22}	3.07^{-22}	1.20^{-22}	5.32^{-23}	2.62^{-23}	1.39^{-23}	7.90^{-24}

Table 5. Cross-sections for the process $B^{5+} + He(1s^2) \rightarrow B^{4+}(n) + He^{+}(1s)$ (in cm^2) from CDW calculations using Hartree-Fock-Slater model potential for the electron target interaction, where B^{5+} is a fully stripped ion

Final state	Projectile energy (keV/amu)							
n	125	150	200	300	400	500	600	700
1	–	–	–	–	–	–	–	–
2	–	–	–	2.75^{-17}	1.10^{-17}	5.09^{-18}	2.59^{-18}	1.42^{-18}
3	4.24^{-16}	2.50^{-16}	1.02^{-16}	2.51^{-17}	8.51^{-18}	3.48^{-18}	1.62^{-18}	8.30^{-19}
4	3.35^{-16}	1.90^{-16}	7.25^{-17}	1.64^{-17}	5.20^{-18}	2.03^{-18}	9.15^{-19}	4.57^{-19}
5	2.32^{-16}	1.29^{-16}	4.81^{-17}	1.04^{-17}	3.21^{-18}	1.23^{-18}	5.43^{-19}	2.67^{-19}
6	1.54^{-16}	8.57^{-17}	3.18^{-17}	6.76^{-18}	2.05^{-18}	7.76^{-19}	3.03^{-19}	1.51^{-19}
7	1.05^{-16}	5.87^{-17}	2.16^{-17}	4.56^{-18}	1.37^{-18}	5.16^{-19}	1.97^{-19}	9.80^{-19}
8	7.40^{-17}	4.13^{-17}	1.52^{-17}	3.19^{-18}	9.56^{-19}	3.58^{-19}	1.35^{-19}	6.71^{-20}
σ_{all}	–	–	–	–	–	–	–	–

Table 5. Cross-sections for the process $B^{5+} + He(1s^2) \rightarrow B^{4+}(n) + He^{+}(1s)$ (in cm^2) from CDW calculations using Hartree-Fock-Slater model potential for the electron target interaction, where B^{5+} is a fully stripped ion

Final state	Projectile energy (keV/amu)							
n	800	900	1000	2000	3000	4000	5000	6000
1	–	–	–	2.58^{-20}	4.91^{-21}	1.36^{-21}	4.78^{-22}	1.97^{-22}
2	8.33^{-19}	5.10^{-19}	3.26^{-19}	1.34^{-20}	1.78^{-21}	4.02^{-22}	1.24^{-22}	4.65^{-23}
3	4.58^{-19}	2.68^{-19}	1.65^{-19}	5.53^{-21}	6.75^{-22}	1.46^{-22}	4.35^{-23}	1.61^{-23}
4	2.47^{-19}	1.42^{-19}	8.57^{-20}	2.66^{-21}	3.15^{-22}	6.69^{-23}	1.98^{-23}	7.26^{-24}
5	1.43^{-19}	8.14^{-20}	4.88^{-20}	1.46^{-21}	1.70^{-22}	3.58^{-23}	1.05^{-23}	3.85^{-24}
6	8.11^{-20}	4.64^{-20}	2.79^{-20}	8.42^{-22}	9.79^{-23}	2.06^{-23}	6.07^{-24}	2.21^{-24}
7	5.26^{-20}	3.01^{-20}	1.81^{-20}	5.39^{-22}	6.25^{-23}	1.31^{-23}	3.85^{-24}	1.41^{-24}
8	3.60^{-20}	2.05^{-20}	1.23^{-20}	3.65^{-22}	4.22^{-23}	8.85^{-24}	2.60^{-24}	9.47^{-25}
σ_{all}	–	–	–	5.19^{-20}	8.20^{-21}	2.09^{-21}	6.97^{-22}	2.79^{-22}

Table 5. Cross-sections for the process $B^{5+} + He(1s^2) \rightarrow B^{4+}(n) + He^{+}(1s)$ (in cm^2) from CDW calculations using Hartree-Fock-Slater model potential for the electron target interaction, where B^{5+} is a fully stripped ion

Final state	Projectile energy (keV/amu)			
n	7000	8000	9000	10000
1	9.17^{-23}	4.67^{-23}	2.55^{-23}	1.48^{-23}
2	2.02^{-23}	9.75^{-24}	5.11^{-24}	2.86^{-24}
3	6.88^{-24}	3.29^{-24}	1.71^{-24}	9.50^{-25}
4	3.09^{-24}	1.47^{-24}	7.63^{-25}	4.23^{-25}
5	1.64^{-24}	7.76^{-25}	4.00^{-25}	2.21^{-25}
6	9.41^{-25}	4.47^{-25}	2.31^{-25}	1.28^{-25}
7	5.97^{-25}	2.83^{-25}	1.47^{-25}	8.11^{-26}
8	4.02^{-25}	1.91^{-25}	9.85^{-26}	5.45^{-26}
σ_{all}	1.27^{-22}	6.36^{-23}	3.43^{-23}	1.97^{-23}

Table 6. Cross-sections for the process $B^{6+} + He(1s^2) \rightarrow B^{5+}(n) + He^{+}(1s)$ (in cm^2) from CDW calculations using Hartree-Fock-Slater model potential for the electron target interaction, where B^{6+} is a fully stripped ion

Final state	Projectile energy (keV/amu)							
n	200	300	400	500	600	700	800	900
1	–	–	–	–	–	–	–	–
2	–	–	1.33^{-17}	6.69^{-18}	3.65^{-18}	2.11^{-18}	1.29^{-18}	8.15^{-19}
3	1.49^{-16}	4.04^{-17}	1.45^{-17}	6.20^{-18}	2.98^{-18}	1.57^{-18}	8.86^{-19}	5.28^{-19}
4	1.30^{-16}	3.10^{-17}	1.02^{-17}	4.09^{-18}	1.88^{-18}	9.53^{-19}	5.21^{-19}	3.03^{-19}
5	9.52^{-17}	2.14^{-17}	6.73^{-18}	2.62^{-18}	1.18^{-18}	5.86^{-19}	3.15^{-19}	1.81^{-19}
6	6.54^{-17}	1.44^{-17}	4.46^{-18}	1.71^{-18}	6.24^{-19}	3.18^{-19}	1.74^{-19}	1.01^{-19}
7	4.57^{-17}	9.93^{-18}	3.04^{-18}	1.16^{-18}	4.12^{-19}	2.09^{-19}	1.14^{-19}	6.60^{-20}
8	3.27^{-17}	7.05^{-18}	2.15^{-18}	8.13^{-19}	2.84^{-19}	1.44^{-19}	7.84^{-20}	4.53^{-20}
σ_{all}	–	–	–	–	–	–	–	–

Table 6. Cross-sections for the process $B^{6+} + He(1s^2) \rightarrow B^{5+}(n) + He^{+}(1s)$ (in cm^2) from CDW calculations using Hartree-Fock-Slater model potential for the electron target interaction, where B^{6+} is a fully stripped ion

Final state	Projectile energy (keV/amu)							
n	1000	2000	3000	4000	5000	6000	7000	8000
1	–	3.03^{-20}	6.88^{-21}	2.11^{-21}	7.93^{-22}	3.43^{-22}	1.65^{-22}	8.65^{-23}
2	5.36^{-19}	2.57^{-20}	3.62^{-21}	8.43^{-22}	2.65^{-22}	1.01^{-22}	4.42^{-23}	2.15^{-23}
3	3.29^{-19}	1.19^{-20}	1.49^{-21}	3.27^{-22}	9.87^{-23}	3.66^{-23}	1.57^{-23}	7.54^{-24}
4	1.85^{-19}	6.00^{-21}	7.20^{-22}	1.54^{-22}	4.58^{-23}	1.69^{-23}	7.20^{-24}	3.43^{-24}
5	1.09^{-19}	3.36^{-21}	3.95^{-22}	8.36^{-23}	2.47^{-23}	9.04^{-24}	3.85^{-24}	1.83^{-24}
6	6.15^{-20}	1.94^{-21}	2.28^{-22}	4.81^{-23}	1.42^{-23}	5.19^{-24}	2.20^{-24}	1.05^{-24}
7	4.01^{-20}	1.25^{-21}	1.46^{-22}	3.07^{-23}	9.04^{-24}	3.30^{-24}	1.40^{-24}	6.65^{-25}
8	2.75^{-20}	8.48^{-22}	9.87^{-23}	2.08^{-23}	6.10^{-24}	2.23^{-24}	9.44^{-25}	4.48^{-25}
σ_{all}	–	8.43^{-20}	1.39^{-20}	3.69^{-21}	1.28^{-21}	5.25^{-22}	2.44^{-22}	1.25^{-22}

Table 6. Cross-sections for the process $B^{6+} + He(1s^2) \rightarrow B^{5+}(n) + He^{+}(1s)$ (in cm^2) from CDW calculations using Hartree-Fock-Slater model potential for the electron target interaction, where B^{6+} is a fully stripped ion

Final state	Projectile energy (keV/amu)	
n	9000	10000
1	4.84^{-23}	2.85^{-23}
2	1.13^{-23}	6.38^{-24}
3	3.93^{-24}	2.19^{-24}
4	1.78^{-24}	9.90^{-25}
5	9.46^{-25}	5.26^{-25}
6	5.42^{-25}	3.00^{-25}
7	3.44^{-25}	1.90^{-25}
8	2.32^{-25}	1.28^{-25}
σ_{all}	6.83^{-23}	3.97^{-23}

Table 7. Cross-sections for the process $B^{7+} + He(1s^2) \rightarrow B^{6+}(n) + He^{+}(1s)$ (in cm^2) from CDW calculations using Hartree-Fock-Slater model potential for the electron target interaction, where B^{7+} is a fully stripped ion

Final state	Projectile energy (keV/amu)							
n	400	500	600	700	800	900	1000	2000
1	–	–	–	–	–	–	–	2.95^{-20}
2	–	7.26^{-18}	4.22^{-18}	2.59^{-18}	1.65^{-18}	1.09^{-18}	7.38^{-19}	4.18^{-20}
3	2.08^{-17}	9.33^{-18}	4.66^{-18}	2.52^{-18}	1.46^{-18}	8.84^{-19}	5.60^{-19}	2.21^{-20}
4	1.70^{-17}	7.03^{-18}	3.30^{-18}	1.71^{-18}	9.46^{-19}	5.56^{-19}	3.43^{-19}	1.17^{-20}
5	1.21^{-17}	4.82^{-18}	2.19^{-18}	1.11^{-18}	6.02^{-19}	3.48^{-19}	2.12^{-19}	6.74^{-21}
6	8.33^{-18}	3.25^{-18}	1.08^{-18}	5.64^{-19}	3.16^{-19}	1.87^{-19}	1.15^{-19}	3.85^{-21}
7	5.81^{-18}	2.25^{-18}	7.17^{-18}	3.75^{-19}	2.09^{-19}	1.23^{-19}	7.58^{-20}	2.50^{-21}
8	4.16^{-18}	1.59^{-18}	4.99^{-19}	2.60^{-19}	1.45^{-19}	8.50^{-20}	5.23^{-20}	1.70^{-21}
σ_{all}	–	–	–	–	–	–	–	1.26^{-19}

Table 7. Cross-sections for the process $B^{7+} + He(1s^2) \rightarrow B^{6+}(n) + He^{+}(1s)$ (in cm^2) from CDW calculations using Hartree-Fock-Slater model potential for the electron target interaction, where B^{7+} is a fully stripped ion

Final state	Projectile energy (keV/amu)							
n	3000	4000	5000	6000	7000	8000	9000	10000
1	8.03^{-21}	2.74^{-21}	1.11^{-21}	5.04^{-22}	2.53^{-22}	1.36^{-22}	7.81^{-23}	4.70^{-23}
2	6.29^{-21}	1.52^{-21}	4.89^{-22}	1.89^{-22}	8.40^{-23}	4.12^{-23}	2.19^{-23}	1.24^{-23}
3	2.86^{-21}	6.38^{-22}	1.94^{-22}	7.27^{-23}	3.14^{-23}	1.51^{-23}	7.88^{-24}	4.40^{-24}
4	1.43^{-21}	3.09^{-22}	9.24^{-23}	3.42^{-23}	1.46^{-23}	6.98^{-24}	3.63^{-24}	2.01^{-24}
5	8.02^{-22}	1.71^{-22}	5.05^{-23}	1.85^{-23}	7.89^{-24}	3.76^{-24}	1.95^{-24}	1.08^{-24}
6	4.61^{-22}	9.80^{-23}	2.90^{-23}	1.06^{-23}	4.51^{-24}	2.15^{-24}	1.11^{-24}	6.16^{-25}
7	2.96^{-22}	6.28^{-23}	1.85^{-23}	6.77^{-24}	2.88^{-24}	1.37^{-24}	7.07^{-25}	3.91^{-25}
8	2.01^{-22}	4.25^{-23}	1.25^{-23}	4.57^{-24}	1.94^{-24}	9.21^{-25}	4.76^{-25}	2.64^{-25}
σ_{all}	2.11^{-20}	5.73^{-21}	2.04^{-21}	8.57^{-22}	4.07^{-22}	2.11^{-22}	1.17^{-22}	6.90^{-23}

Table 8. Cross-sections for the process $B^{8+} + He(1s^2) \rightarrow B^{7+}(n) + He^{+}(1s)$ (in cm^2) from CDW calculations using Hartree-Fock-Slater model potential for the electron target interaction, where B^{8+} is a fully stripped ion

Final state	Projectile energy (keV/amu)							
n	400	500	600	700	800	900	1000	2000
1	–	–	–	–	–	–	–	–
2	–	–	–	2.74^{-18}	1.84^{-18}	1.26^{-18}	8.82^{-19}	5.99^{-20}
3	2.56^{-17}	1.22^{-17}	6.37^{-18}	3.56^{-18}	2.11^{-18}	1.31^{-18}	8.44^{-19}	3.66^{-20}
4	2.50^{-17}	1.07^{-17}	5.15^{-18}	2.72^{-18}	1.53^{-18}	9.12^{-19}	5.68^{-19}	2.06^{-20}
5	1.95^{-17}	7.89^{-18}	3.66^{-18}	1.87^{-18}	1.03^{-18}	6.00^{-19}	3.68^{-19}	1.22^{-20}
6	1.38^{-17}	5.51^{-18}	1.60^{-18}	8.70^{-19}	5.01^{-19}	3.03^{-19}	1.90^{-19}	6.87^{-21}
7	9.84^{-18}	3.88^{-18}	1.08^{-18}	5.85^{-19}	3.35^{-19}	2.02^{-19}	1.26^{-19}	4.48^{-21}
8	7.13^{-18}	2.79^{-18}	7.56^{-19}	4.09^{-19}	2.33^{-19}	1.40^{-19}	8.76^{-20}	3.07^{-21}
σ_{all}	–	–	–	–	–	–	–	–

Table 8. Cross-sections for the process $B^{8+} + He(1s^2) \rightarrow B^{7+}(n) + He^{+}(1s)$ (in cm^2) from CDW calculations using Hartree-Fock-Slater model potential for the electron target interaction, where B^{8+} is a fully stripped ion

Final state	Projectile energy (keV/amu)							
n	3000	4000	5000	6000	7000	8000	9000	10000
1	8.15^{-21}	3.11^{-21}	1.35^{-21}	6.51^{-22}	3.40^{-22}	1.90^{-22}	1.11^{-22}	6.85^{-23}
2	9.72^{-21}	2.45^{-21}	8.08^{-22}	3.19^{-22}	1.43^{-22}	7.10^{-23}	3.80^{-23}	2.16^{-23}
3	4.92^{-21}	1.12^{-21}	3.45^{-22}	1.30^{-22}	5.65^{-23}	2.73^{-23}	1.43^{-23}	8.00^{-24}
4	2.57^{-21}	5.61^{-22}	1.68^{-22}	6.25^{-23}	2.68^{-23}	1.29^{-23}	6.69^{-24}	3.72^{-24}
5	1.47^{-21}	3.14^{-22}	9.35^{-23}	3.44^{-23}	1.47^{-23}	6.99^{-24}	3.62^{-24}	2.01^{-24}
6	8.39^{-22}	1.80^{-22}	5.35^{-23}	1.97^{-23}	8.38^{-24}	3.98^{-24}	2.06^{-24}	1.14^{-24}
7	5.43^{-22}	1.16^{-22}	3.43^{-23}	1.26^{-23}	5.35^{-24}	2.54^{-24}	1.32^{-24}	7.28^{-25}
8	3.70^{-22}	7.88^{-23}	2.33^{-23}	8.52^{-24}	3.62^{-24}	1.72^{-24}	8.88^{-25}	4.91^{-25}
σ_{all}	2.99^{-20}	8.21^{-21}	2.96^{-21}	1.27^{-21}	6.11^{-22}	3.22^{-22}	1.81^{-22}	1.08^{-22}

Table 9. Cross-sections for the process $B^{9+} + He(1s^2) \rightarrow B^{8+}(n) + He^{+}(1s)$ (in cm^2) from CDW calculations using Hartree-Fock-Slater model potential for the electron target interaction, where B^{9+} is a fully stripped ion

Final state	Projectile energy (keV/amu)							
n	400	500	600	700	800	900	1000	2000
1	–	–	–	–	–	–	–	–
2	–	–	–	–	–	1.30^{-18}	9.47^{-19}	7.78^{-20}
3	2.85^{-17}	1.43^{-17}	7.83^{-18}	4.53^{-18}	2.77^{-18}	1.75^{-18}	1.15^{-18}	5.55^{-20}
4	3.32^{-17}	1.47^{-17}	7.30^{-18}	3.93^{-18}	2.26^{-18}	1.37^{-18}	8.60^{-19}	3.32^{-20}
5	2.84^{-17}	1.18^{-17}	5.59^{-18}	2.89^{-18}	1.61^{-18}	9.49^{-19}	5.86^{-19}	2.02^{-20}
6	2.08^{-17}	8.51^{-18}	3.96^{-18}	2.02^{-18}	1.11^{-18}	6.47^{-19}	3.95^{-19}	1.29^{-20}
7	1.51^{-17}	6.11^{-18}	2.81^{-18}	1.42^{-18}	7.77^{-18}	4.49^{-19}	2.73^{-19}	8.61^{-21}
8	1.10^{-17}	4.45^{-18}	2.04^{-18}	1.03^{-18}	5.56^{-19}	3.21^{-19}	1.94^{-19}	5.98^{-21}
σ_{all}	–	–	–	–	–	–	–	–

Table 9. Cross-sections for the process $B^{9+} + He(1s^2) \rightarrow B^{8+}(n) + He^{+}(1s)$ (in cm^2) from CDW calculations using Hartree-Fock-Slater model potential for the electron target interaction, where B^{9+} is a fully stripped ion

Final state	Projectile energy (keV/amu)							
n	3000	4000	5000	6000	7000	8000	9000	10000
1	–	3.18^{-21}	1.49^{-21}	7.59^{-22}	4.14^{-22}	2.39^{-22}	1.44^{-22}	9.09^{-23}
2	1.37^{-20}	3.60^{-21}	1.22^{-21}	4.92^{-22}	2.25^{-22}	1.12^{-22}	6.07^{-23}	3.48^{-23}
3	7.77^{-21}	1.81^{-21}	5.65^{-22}	2.15^{-22}	9.40^{-23}	4.56^{-23}	2.40^{-23}	1.35^{-23}
4	4.25^{-21}	9.41^{-22}	2.85^{-22}	1.06^{-22}	4.56^{-23}	2.18^{-23}	1.14^{-23}	6.37^{-24}
5	2.48^{-21}	5.36^{-22}	1.60^{-22}	5.91^{-23}	2.52^{-23}	1.21^{-23}	6.25^{-24}	3.47^{-24}
6	1.41^{-21}	3.06^{-22}	9.16^{-23}	3.37^{-23}	1.44^{-23}	6.87^{-24}	3.56^{-24}	1.97^{-24}
7	9.16^{-22}	1.98^{-22}	5.90^{-23}	2.17^{-23}	9.23^{-24}	4.39^{-24}	2.27^{-24}	1.26^{-24}
8	6.27^{-22}	1.35^{-22}	4.01^{-23}	1.47^{-23}	6.25^{-24}	2.97^{-24}	1.54^{-24}	8.50^{-25}
σ_{all}	–	1.12^{-20}	4.05^{-21}	1.75^{-21}	8.55^{-22}	4.56^{-22}	2.60^{-22}	1.56^{-22}

Table 10. Cross-sections for the process $B^{10+} + He(1s^2) \rightarrow B^{9+}(n) + He^{+}(1s)$ (in cm^2) from CDW calculations using Hartree-Fock-Slater model potential for the electron target interaction, where B^{10+} is a fully stripped ion

Final state	Projectile energy (keV/amu)							
n	500	600	700	800	900	1000	2000	3000
1	–	–	–	–	–	–	–	–
2	–	–	–	–	–	–	9.30^{-20}	1.78^{-20}
3	1.54^{-17}	8.80^{-18}	5.31^{-18}	3.33^{-18}	2.17^{-18}	1.46^{-18}	7.81^{-20}	1.14^{-20}
4	1.88^{-17}	9.59^{-18}	5.29^{-18}	3.09^{-18}	1.90^{-18}	1.21^{-18}	4.99^{-20}	6.58^{-21}
5	1.64^{-17}	7.91^{-18}	4.17^{-18}	2.35^{-18}	1.40^{-18}	8.73^{-19}	3.16^{-20}	3.94^{-21}
6	1.21^{-17}	5.77^{-18}	3.00^{-18}	1.67^{-18}	9.80^{-19}	6.05^{-19}	2.05^{-20}	2.21^{-21}
7	8.86^{-18}	4.18^{-18}	2.15^{-18}	1.19^{-18}	6.93^{-19}	4.24^{-19}	1.38^{-20}	1.45^{-21}
8	6.51^{-18}	3.06^{-18}	1.57^{-18}	8.60^{-19}	5.00^{-19}	3.05^{-19}	9.67^{-21}	9.93^{-22}
σ_{all}	–	–	–	–	–	–	–	–

Table 10. Cross-sections for the process $B^{10+} + He(1s^2) \rightarrow B^{9+}(n) + He^{+}(1s)$ (in cm^2) from CDW calculations using Hartree-Fock-Slater model potential for the electron target interaction, where B^{10+} is a fully stripped ion

Final state	Projectile energy (keV/amu)						
n	4000	5000	6000	7000	8000	9000	10000
1	–	1.51^{-21}	8.17^{-22}	4.65^{-22}	2.78^{-22}	1.73^{-22}	1.12^{-22}
2	4.92^{-21}	1.72^{-21}	7.10^{-22}	3.29^{-22}	1.67^{-22}	9.10^{-23}	5.25^{-23}
3	2.73^{-21}	8.66^{-22}	3.33^{-22}	1.47^{-22}	7.16^{-23}	3.79^{-23}	2.13^{-23}
4	1.48^{-21}	4.52^{-22}	1.69^{-22}	7.30^{-23}	3.51^{-23}	1.83^{-23}	1.02^{-23}
5	8.59^{-22}	2.57^{-22}	9.54^{-23}	4.09^{-23}	1.95^{-23}	1.02^{-23}	5.65^{-24}
6	4.88^{-22}	1.47^{-22}	5.45^{-23}	2.33^{-23}	1.11^{-23}	5.78^{-24}	3.21^{-24}
7	3.17^{-22}	9.51^{-23}	3.51^{-23}	1.50^{-23}	7.14^{-24}	3.70^{-24}	2.05^{-24}
8	2.17^{-22}	6.48^{-23}	2.39^{-23}	1.02^{-23}	4.84^{-24}	2.51^{-24}	1.39^{-24}
σ_{all}	–	5.35^{-21}	2.32^{-21}	1.14^{-21}	6.12^{-22}	3.51^{-22}	2.13^{-22}

Table 11. Cross-sections for the process $B^{11+} + He(1s^2) \rightarrow B^{10+}(n) + He^+(1s)$ (in cm^2) from CDW calculations using Hartree-Fock-Slater model potential for the electron target interaction, where B^{11+} is a fully stripped ion

Final state	Projectile energy (keV/amu)							
n	600	700	800	900	1000	2000	3000	4000
1	–	–	–	–	–	–	–	–
2	–	–	–	–	–	1.04^{-19}	2.17^{-20}	6.32^{-21}
3	9.25^{-18}	5.78^{-18}	3.74^{-18}	2.51^{-18}	1.72^{-18}	1.03^{-19}	1.59^{-20}	3.89^{-21}
4	1.18^{-17}	6.65^{-18}	3.97^{-18}	2.47^{-18}	1.61^{-18}	7.12^{-20}	9.66^{-21}	2.20^{-21}
5	1.06^{-17}	5.66^{-18}	3.24^{-18}	1.95^{-18}	1.23^{-18}	4.66^{-20}	5.93^{-21}	1.31^{-21}
6	7.89^{-18}	4.17^{-18}	2.36^{-18}	1.40^{-18}	8.72^{-19}	3.08^{-20}	3.80^{-21}	8.23^{-22}
7	5.78^{-18}	3.04^{-18}	1.70^{-18}	1.01^{-18}	6.22^{-19}	2.10^{-20}	2.54^{-21}	5.43^{-22}
8	4.27^{-18}	2.23^{-18}	1.25^{-18}	7.34^{-19}	4.51^{-19}	1.48^{-20}	1.77^{-21}	3.75^{-22}
σ_{all}	–	–	–	–	–	–	–	–

Table 11. Cross-sections for the process $B^{11+} + He(1s^2) \rightarrow B^{10+}(n) + He^+(1s)$ (in cm^2) from CDW calculations using Hartree-Fock-Slater model potential for the electron target interaction, where B^{11+} is a fully stripped ion

Final state	Projectile energy (keV/amu)					
n	5000	6000	7000	8000	9000	10000
1	1.44^{-21}	8.22^{-22}	4.89^{-22}	3.03^{-22}	1.94^{-22}	1.29^{-22}
2	2.29^{-21}	9.65^{-22}	4.55^{-22}	2.34^{-22}	1.29^{-22}	7.51^{-23}
3	1.26^{-21}	4.89^{-22}	2.17^{-22}	1.07^{-22}	5.67^{-23}	3.21^{-23}
4	6.80^{-22}	2.56^{-22}	1.11^{-22}	5.37^{-23}	2.81^{-23}	1.57^{-23}
5	3.95^{-22}	1.46^{-22}	6.30^{-23}	3.02^{-23}	1.57^{-23}	8.75^{-24}
6	2.46^{-22}	9.06^{-23}	3.59^{-23}	1.72^{-23}	8.93^{-24}	4.96^{-24}
7	1.61^{-22}	5.91^{-23}	2.32^{-23}	1.11^{-23}	5.74^{-24}	3.18^{-24}
8	1.11^{-22}	4.05^{-23}	1.58^{-23}	7.51^{-24}	3.89^{-24}	2.16^{-24}
σ_{all}	6.97^{-21}	3.01^{-21}	1.47^{-21}	7.90^{-22}	4.56^{-22}	2.78^{-22}

Table 12. Cross-sections for the process $B^{12+} + He(1s^2) \rightarrow B^{11+}(n) + He^{+}(1s)$ (in cm^2) from CDW calculations using Hartree-Fock-Slater model potential for the electron target interaction, where B^{12+} is a fully stripped ion

Final state	Projectile energy (keV/amu)							
n	700	800	900	1000	2000	3000	4000	5000
1	–	–	–	–	–	–	–	–
2	–	–	–	–	1.10^{-19}	2.51^{-20}	7.71^{-21}	2.89^{-21}
3	5.93^{-18}	3.98^{-18}	2.73^{-18}	1.91^{-18}	1.30^{-19}	2.11^{-20}	5.31^{-21}	1.75^{-21}
4	7.90^{-18}	4.83^{-18}	3.07^{-18}	2.01^{-18}	9.66^{-20}	1.35^{-20}	3.14^{-21}	9.80^{-22}
5	7.29^{-18}	4.23^{-18}	2.58^{-18}	1.64^{-18}	6.58^{-20}	8.56^{-21}	1.91^{-21}	5.80^{-22}
6	5.50^{-18}	3.16^{-18}	1.91^{-18}	1.20^{-18}	4.43^{-20}	5.56^{-21}	1.21^{-21}	3.65^{-22}
7	4.05^{-18}	2.31^{-18}	1.39^{-18}	8.66^{-19}	3.06^{-20}	3.75^{-21}	8.08^{-22}	2.40^{-22}
8	3.00^{-18}	1.71^{-18}	1.02^{-18}	6.34^{-19}	2.18^{-20}	2.63^{-21}	5.60^{-22}	1.66^{-22}
σ_{all}	–	–	–	–	–	–	–	–

Table 12. Cross-sections for the process $B^{12+} + He(1s^2) \rightarrow B^{11+}(n) + He^{+}(1s)$ (in cm^2) from CDW calculations using Hartree-Fock-Slater model potential for the electron target interaction, where B^{12+} is a fully stripped ion

Final state	Projectile energy (keV/amu)				
n	6000	7000	8000	9000	10000
1	7.83^{-22}	4.88^{-22}	3.13^{-22}	2.07^{-22}	1.41^{-22}
2	1.25^{-21}	6.00^{-22}	3.13^{-22}	1.74^{-22}	1.03^{-22}
3	6.88^{-22}	3.08^{-22}	1.52^{-22}	8.14^{-23}	4.62^{-23}
4	3.72^{-22}	1.62^{-22}	7.87^{-23}	4.13^{-23}	2.31^{-23}
5	2.16^{-22}	9.31^{-23}	4.47^{-23}	2.33^{-23}	1.30^{-23}
6	1.35^{-22}	5.30^{-23}	2.54^{-23}	1.33^{-23}	7.38^{-24}
7	8.84^{-23}	3.43^{-23}	1.64^{-23}	8.54^{-24}	4.75^{-24}
8	6.08^{-23}	2.34^{-23}	1.12^{-23}	5.81^{-24}	3.22^{-24}
σ_{all}	3.81^{-21}	1.84^{-21}	9.95^{-22}	5.76^{-22}	3.52^{-22}

Table 13. Cross-sections for the process $B^{13+} + He(1s^2) \rightarrow B^{12+}(n) + He^{+}(1s)$ (in cm^2) from CDW calculations using Hartree-Fock-Slater model potential for the electron target interaction, where B^{13+} is a fully stripped ion

Final state	Projectile energy (keV/amu)							
n	800	900	1000	2000	3000	4000	5000	6000
1	–	–	–	–	–	–	–	–
2	–	–	–	1.11^{-19}	2.78^{-20}	8.99^{-21}	3.49^{-21}	1.55^{-21}
3	4.01^{-18}	2.82^{-18}	2.03^{-18}	1.57^{-19}	2.68^{-20}	6.95^{-21}	2.33^{-21}	9.29^{-22}
4	5.60^{-18}	3.62^{-18}	2.42^{-18}	1.26^{-19}	1.83^{-20}	4.31^{-21}	1.36^{-21}	5.21^{-22}
5	5.30^{-18}	3.28^{-18}	2.11^{-18}	8.94^{-20}	1.19^{-20}	2.68^{-21}	8.22^{-22}	3.08^{-22}
6	4.03^{-18}	2.47^{-18}	1.57^{-18}	6.15^{-20}	7.85^{-21}	1.73^{-21}	5.22^{-22}	1.94^{-22}
7	2.98^{-18}	1.82^{-18}	1.15^{-18}	4.30^{-20}	5.34^{-21}	1.16^{-21}	3.46^{-22}	1.28^{-22}
8	2.22^{-18}	1.35^{-18}	8.51^{-19}	3.08^{-20}	3.77^{-21}	8.09^{-22}	2.40^{-22}	8.81^{-23}
σ_{all}	–	–	–	–	–	–	–	–

Table 13. Cross-sections for the process $B^{13+} + He(1s^2) \rightarrow B^{12+}(n) + He^{+}(1s)$ (in cm^2) from CDW calculations using Hartree-Fock-Slater model potential for the electron target interaction, where B^{13+} is a fully stripped ion

Final state	Projectile energy (keV/amu)			
n	7000	8000	9000	10000
1	4.65^{-22}	3.09^{-22}	2.11^{-22}	1.47^{-22}
2	7.58^{-22}	4.02^{-22}	2.27^{-22}	1.35^{-22}
3	4.21^{-22}	2.10^{-22}	1.13^{-22}	6.43^{-23}
4	2.29^{-22}	1.11^{-22}	5.86^{-23}	3.29^{-23}
5	1.33^{-22}	6.40^{-23}	3.35^{-23}	1.87^{-23}
6	8.31^{-23}	3.98^{-23}	2.07^{-23}	1.15^{-23}
7	5.45^{-23}	2.60^{-23}	1.35^{-23}	7.48^{-24}
8	3.75^{-23}	1.78^{-23}	9.23^{-24}	5.11^{-24}
σ_{all}	2.31^{-21}	1.24^{-21}	7.18^{-22}	4.39^{-22}

Table 14. Cross-sections for the process $B^{14+} + He(1s^2) \rightarrow B^{13+}(n) + He^{+}(1s)$ (in cm^2) from CDW calculations using Hartree-Fock-Slater model potential for the electron target interaction, where B^{14+} is a fully stripped ion

Final state	Projectile energy (keV/amu)							
n	900	1000	2000	3000	4000	5000	6000	7000
1	–	–	–	–	–	–	–	–
2	–	–	1.07^{-19}	2.94^{-20}	1.01^{-20}	4.07^{-21}	1.85^{-21}	9.25^{-22}
3	2.81^{-18}	2.07^{-18}	1.82^{-19}	3.29^{-20}	8.79^{-21}	3.01^{-21}	1.22^{-21}	5.56^{-22}
4	4.11^{-18}	2.79^{-18}	1.59^{-19}	2.38^{-20}	5.73^{-21}	1.83^{-21}	7.06^{-22}	3.12^{-22}
5	4.02^{-18}	2.60^{-18}	1.18^{-19}	1.60^{-20}	3.66^{-21}	1.13^{-21}	4.26^{-22}	1.85^{-22}
6	3.07^{-18}	1.98^{-18}	8.24^{-20}	1.07^{-20}	2.39^{-21}	7.24^{-22}	2.70^{-22}	1.16^{-22}
7	2.28^{-18}	1.47^{-18}	5.84^{-20}	7.38^{-21}	1.61^{-21}	4.85^{-22}	1.79^{-22}	7.66^{-23}
8	1.70^{-18}	1.09^{-18}	4.22^{-20}	5.23^{-21}	1.13^{-21}	3.37^{-22}	1.24^{-22}	5.29^{-23}
σ_{all}	–	–	–	–	–	–	–	–

Table 14. Cross-sections for the process $B^{14+} + He(1s^2) \rightarrow B^{13+}(n) + He^{+}(1s)$ (in cm^2) from CDW calculations using Hartree-Fock-Slater model potential for the electron target interaction, where B^{14+} is a fully stripped ion

Final state	Projectile energy (keV/amu)		
n	8000	9000	10000
1	2.94^{-22}	2.06^{-22}	1.47^{-22}
2	4.98^{-22}	2.84^{-22}	1.71^{-22}
3	2.79^{-22}	1.51^{-22}	8.67^{-23}
4	1.53^{-22}	8.07^{-23}	4.55^{-23}
5	8.92^{-23}	4.66^{-23}	2.61^{-23}
6	5.57^{-23}	2.90^{-23}	1.62^{-23}
7	3.66^{-23}	1.90^{-23}	1.05^{-23}
8	2.52^{-23}	1.30^{-23}	7.22^{-24}
σ_{all}	1.52^{-21}	8.76^{-22}	5.36^{-22}

Table 15. Cross-sections for the process $B^{15+} + He(1s^2) \rightarrow B^{14+}(n) + He^{+}(1s)$ (in cm^2) from CDW calculations using Hartree-Fock-Slater model potential for the electron target interaction, where B^{15+} is a fully stripped ion

Final state	Projectile energy (keV/amu)							
n	1000	2000	3000	4000	5000	6000	7000	8000
1	–	–	–	–	–	–	–	–
2	–	–	3.01^{-20}	1.09^{-20}	4.58^{-21}	2.14^{-21}	1.09^{-21}	5.98^{-22}
3	–	2.04^{-19}	3.90^{-20}	1.08^{-20}	3.76^{-21}	1.55^{-21}	7.15^{-22}	3.62^{-22}
4	3.11^{-18}	1.93^{-19}	3.01^{-20}	7.40^{-21}	2.40^{-21}	9.33^{-22}	4.15^{-22}	2.04^{-22}
5	3.12^{-18}	1.50^{-19}	2.09^{-20}	4.85^{-21}	1.51^{-21}	5.72^{-22}	2.50^{-22}	1.21^{-22}
6	2.40^{-18}	1.07^{-19}	1.43^{-20}	3.21^{-21}	9.80^{-22}	3.67^{-22}	1.58^{-22}	7.61^{-23}
7	1.79^{-18}	7.69^{-20}	9.91^{-21}	2.19^{-21}	6.60^{-22}	2.45^{-22}	1.05^{-22}	5.01^{-23}
8	1.34^{-18}	5.60^{-20}	7.08^{-21}	1.54^{-21}	4.62^{-22}	1.70^{-22}	7.27^{-23}	3.46^{-23}
σ_{all}	–	–	–	–	–	–	–	–

Table 15. Cross-sections for the process $B^{15+} + He(1s^2) \rightarrow B^{14+}(n) + He^{+}(1s)$ (in cm^2) from CDW calculations using Hartree-Fock-Slater model potential for the electron target interaction, where B^{15+} is a fully stripped ion

Final state	Projectile energy (keV/amu)	
n	9000	10000
1	–	1.43^{-22}
2	3.46^{-22}	2.10^{-22}
3	1.97^{-22}	1.14^{-22}
4	1.08^{-22}	6.12^{-23}
5	6.35^{-23}	3.55^{-23}
6	3.97^{-23}	2.21^{-23}
7	2.61^{-23}	1.45^{-23}
8	1.79^{-23}	9.95^{-24}
σ_{all}	–	6.45^{-22}

Table 16. Cross-sections for the process $B^{16+} + He(1s^2) \rightarrow B^{15+}(n) + He^{+}(1s)$ (in cm^2) from CDW calculations using Hartree-Fock-Slater model potential for the electron target interaction, where B^{16+} is a fully stripped ion

Final state	Projectile energy (keV/amu)							
n	3000	4000	5000	6000	7000	8000	9000	10000
1	–	–	–	–	–	–	–	–
2	2.99^{-20}	1.15^{-20}	5.00^{-21}	2.41^{-21}	1.26^{-21}	6.99^{-22}	4.10^{-22}	2.52^{-22}
3	4.49^{-20}	1.28^{-20}	4.59^{-21}	1.91^{-21}	8.96^{-22}	4.57^{-22}	2.51^{-22}	1.45^{-22}
4	3.70^{-20}	9.31^{-21}	3.06^{-21}	1.20^{-21}	5.38^{-22}	2.66^{-22}	1.42^{-22}	8.04^{-23}
5	2.67^{-20}	6.28^{-21}	1.97^{-21}	7.52^{-22}	3.30^{-22}	1.60^{-22}	8.44^{-23}	4.73^{-23}
6	1.85^{-20}	4.21^{-21}	1.30^{-21}	4.87^{-22}	2.11^{-22}	1.02^{-22}	5.31^{-23}	2.96^{-23}
7	1.30^{-20}	2.90^{-21}	8.80^{-22}	3.27^{-22}	1.41^{-22}	6.74^{-23}	3.50^{-23}	1.95^{-23}
8	9.35^{-21}	2.05^{-21}	6.18^{-22}	2.28^{-22}	9.77^{-23}	4.66^{-23}	2.42^{-23}	1.34^{-23}
σ_{all}	–	–	–	–	–	–	–	–

Table 17. Cross-sections for the process $B^{17+} + He(1s^2) \rightarrow B^{16+}(n) + He^{+}(1s)$ (in cm^2) from CDW calculations using Hartree-Fock-Slater model potential for the electron target interaction, where B^{17+} is a fully stripped ion

Final state	Projectile energy (keV/amu)							
n	3000	4000	5000	6000	7000	8000	9000	10000
1	–	–	–	–	–	–	–	–
2	2.90^{-20}	1.18^{-20}	5.32^{-21}	2.64^{-21}	1.41^{-21}	7.96^{-22}	4.74^{-22}	2.94^{-22}
3	5.04^{-20}	1.49^{-20}	5.46^{-21}	2.32^{-21}	1.10^{-21}	5.65^{-22}	3.12^{-22}	1.82^{-22}
4	4.45^{-20}	1.14^{-20}	3.81^{-21}	1.52^{-21}	6.84^{-22}	3.39^{-22}	1.82^{-22}	1.03^{-22}
5	3.33^{-20}	7.94^{-21}	2.52^{-21}	9.69^{-22}	4.26^{-22}	2.08^{-22}	1.10^{-22}	6.18^{-23}
6	2.35^{-20}	5.41^{-21}	1.68^{-21}	6.34^{-22}	2.75^{-22}	1.33^{-22}	6.97^{-23}	3.89^{-23}
7	1.67^{-20}	3.76^{-21}	1.15^{-21}	4.29^{-22}	1.85^{-22}	8.87^{-23}	4.62^{-23}	2.57^{-23}
8	1.21^{-20}	2.68^{-21}	8.11^{-22}	3.01^{-22}	1.29^{-22}	6.16^{-23}	3.20^{-23}	1.78^{-23}
σ_{all}	–	–	–	–	–	–	–	–

Table 18. Cross-sections for the process $B^{18+} + He(1s^2) \rightarrow B^{17+}(n) + He^{+}(1s)$ (in cm^2) from CDW calculations using Hartree-Fock-Slater model potential for the electron target interaction, where B^{18+} is a fully stripped ion

Final state	Projectile energy (keV/amu)							
n	3000	4000	5000	6000	7000	8000	9000	10000
1	–	–	–	–	–	–	–	–
2	–	1.18^{-20}	5.54^{-21}	2.83^{-21}	1.54^{-21}	8.88^{-22}	5.36^{-22}	3.37^{-22}
3	5.54^{-20}	1.70^{-20}	6.35^{-21}	2.74^{-21}	1.32^{-21}	6.85^{-22}	3.81^{-22}	2.24^{-22}
4	5.25^{-20}	1.38^{-20}	4.67^{-21}	1.87^{-21}	8.52^{-22}	4.25^{-22}	2.29^{-22}	1.31^{-22}
5	4.07^{-20}	9.86^{-21}	3.17^{-21}	1.23^{-21}	5.42^{-22}	2.65^{-22}	1.40^{-22}	7.90^{-23}
6	2.92^{-20}	6.83^{-21}	2.13^{-21}	8.10^{-22}	3.53^{-22}	1.71^{-22}	8.98^{-23}	5.03^{-23}
7	2.10^{-20}	4.78^{-21}	1.47^{-21}	5.52^{-22}	2.39^{-22}	1.15^{-22}	5.99^{-23}	3.34^{-23}
8	1.53^{-20}	3.43^{-21}	1.04^{-21}	3.89^{-22}	1.67^{-22}	8.00^{-23}	4.16^{-23}	2.31^{-23}
σ_{all}	–	–	–	–	–	–	–	–

Table 19. Cross-sections for the process $B^{19+} + He(1s^2) \rightarrow B^{18+}(n) + He^{+}(1s)$ (in cm^2) from CDW calculations using Hartree-Fock-Slater model potential for the electron target interaction, where B^{19+} is a fully stripped ion

Final state	Projectile energy (keV/amu)							
n	3000	4000	5000	6000	7000	8000	9000	10000
1	–	–	–	–	–	–	–	–
2	–	1.16^{-20}	5.65^{-21}	2.97^{-21}	1.65^{-21}	9.70^{-22}	5.94^{-22}	3.78^{-22}
3	5.95^{-20}	1.89^{-20}	7.26^{-21}	3.19^{-21}	1.55^{-21}	8.15^{-22}	4.57^{-22}	2.70^{-22}
4	6.06^{-20}	1.63^{-20}	5.61^{-21}	2.28^{-21}	1.04^{-21}	5.24^{-22}	2.83^{-22}	1.63^{-22}
5	4.88^{-20}	1.20^{-20}	3.90^{-21}	1.52^{-21}	6.77^{-22}	3.32^{-22}	1.76^{-22}	9.97^{-23}
6	3.57^{-20}	8.45^{-21}	2.66^{-21}	1.02^{-21}	4.46^{-22}	2.17^{-22}	1.14^{-22}	6.39^{-23}
7	2.58^{-20}	5.98^{-21}	1.85^{-21}	6.99^{-22}	3.03^{-22}	1.46^{-22}	7.64^{-23}	4.26^{-23}
8	1.89^{-20}	4.32^{-21}	1.32^{-21}	4.95^{-22}	2.13^{-22}	1.02^{-22}	5.33^{-23}	2.96^{-23}
σ_{all}	–	–	–	–	–	–	–	–

Table 20. Cross-sections for the process $B^{20+} + He(1s^2) \rightarrow B^{19+}(n) + He^{+}(1s)$ (in cm^2) from CDW calculations using Hartree-Fock-Slater model potential for the electron target interaction, where B^{20+} is a fully stripped ion

Final state	Projectile energy (keV/amu)							
n	3000	4000	5000	6000	7000	8000	9000	10000
1	–	–	–	–	–	–	–	–
2	–	–	5.66^{-21}	3.05^{-21}	1.74^{-21}	1.04^{-21}	6.47^{-22}	4.17^{-22}
3	6.28^{-20}	2.07^{-20}	8.15^{-21}	3.64^{-21}	1.79^{-21}	9.53^{-22}	5.39^{-22}	3.21^{-22}
4	6.88^{-20}	1.90^{-20}	6.63^{-21}	2.72^{-21}	1.26^{-21}	6.36^{-22}	3.45^{-22}	1.99^{-22}
5	5.76^{-20}	1.45^{-20}	4.74^{-21}	1.86^{-21}	8.33^{-22}	4.11^{-22}	2.19^{-22}	1.24^{-22}
6	4.28^{-20}	1.03^{-20}	3.28^{-21}	1.26^{-21}	5.55^{-22}	2.70^{-22}	1.42^{-22}	8.00^{-23}
7	3.13^{-20}	7.36^{-21}	2.30^{-21}	8.72^{-22}	3.80^{-22}	1.83^{-22}	9.60^{-23}	5.37^{-23}
8	2.31^{-20}	5.35^{-21}	1.65^{-21}	6.21^{-22}	2.68^{-22}	1.29^{-22}	6.72^{-23}	3.74^{-23}
σ_{all}	–	–	–	–	–	–	–	–

Charge exchange cross section database for proton collisions with hydrocarbon molecules

R.K. Janev[1,2,3], **J.G. Wang**[3,4], **T. Kato**[3]

[1] Macedonian Academy of Sciences and Arts, Skopje, Macedonia

[2] Universite Catholique de Louvain, Dept. de Physique, FYAM, Louvain-la-Neuve, Belgium

[3] National Institute for Fusion Science, Oroshi-cho, Toki, Japan

[4] Dept. of Physics and Astronomy, University of Georgia, Athens, Georgia, United States of America

Abstract. The available experimental and theoretical cross section data on charge exchange processes in collisions of protons with hydrocarbon molecules have been collected and critically assessed. Using well established scaling relationships for the charge exchange cross sections at low and high collision energies, as well as the known rate coefficients for these reactions in the thermal energy region, a complete cross sections database is constructed for proton-C_xH_y charge exchange reactions from thermal energies up to several hundreds keV for all C_xH_y molecules with $x = 1, 2, 3$ and $1 \leq y \leq 2x + 2$.

1. Introduction

The use of carbon as a plasma facing material (in form of graphite or carbon-carbon composities) in fusion devices is attractive because of its low atomic number that keeps the radiation losses low, and its capability to withstand high heat fluxes without being structurally degraded. For this reason, it has been, and is still being used in many fusion machines, and has been included as one of the plasma facing materials in the divertor design of International Thermonuclear Experimental Reactor (ITER)[1]. However, carbon materials are proved to have extensive chemical erosion when bombarded with hydrogenic particles of energies 50-100 eV and higher. The products of chemical erosion are hydrocarbon molecules, C_xH_y, the composition of which varies with the bombarding energy of hydrogenic particles and surface temperature of carbon materials. At higher particle impact energies (30-500 eV), dominant hydrocarbon species in the erosion fluxes are the light hydrocarbons (CH_3, CH_4, C_2H_2), but with the decrease of impact energy, the heavier hydrocarbon (C_2H_4, C_2H_6, C_3H_4, C_3H_6, C_3H_8) become increasingly more present in the erosion fluxes, and dominant at hyperthermal energies ($\leq 1eV$)[2]. The increase of carbon surface temperature (above 300K) also leads to increase of the presence of heavier hydrocarbons in the erosion fluxes [2]. Most of the presently operating large and medium-size fusion devices (JET, JT-60U, ASDEX, TEXTOR, Alcator C-mod, DIII-D, etc) have divertors in which the plasma temperature is lowered (by appropriate additional cooling) down to 1-10 eV [3]. Under these conditions, the composition of chemical erosion fluxes is dominated by heavy hydrocarbons C_2H_y, C_3H_y and methane (CH_4).

After their release in the divertor plasma, the hydrocarbon molecules C_xH_y become subject to numerous collision processes with plasma constituents (electrons, protons and

neutral hydrogen atoms and molecules). Electron impact excitation and ionization processes of C_xH_y are usually accompanied by molecular fragmentation (dissociation). The recombination of plasma electrons with the $C_xH_y^+$ ions, produced by electron impact ionization and proton charge exchange with C_xH_y, also gives fragmented neutral products (dissociative recombination). Therefore, even if a specific set of CH_y, C_2H_y, C_3H_y hydrocarbon molecules were preferentially formed on the surface and released in the plasma, the above fragmentation collision processes rapidly generate all the members of the CH_y, C_2H_y, C_3H_y families of hydrocarbons.

The cross section database for collision processes of C_xH_y with plasma electrons and protons is still not established, but it is urgently needed to model the transport of eroded carbon in the plasma. Two attempts [4,5] were made in the past to construct such a cross section database. The first of them [4] had a limited scope (containing data only for CH_y, $1 \leq y \leq 4$) and the second [5] was based more on speculative arguments (frequently incorrect) for the cross section relationships between the members of the same family of hydrocarbons, rather than using the available cross section data. Only small part of the cross section data in Ref.4 are based on experimental or theoretical sources; its largest part is also based on speculative arguments and unphysical assumptions.

In the present article, we give a critical assessment of the available cross section data for charge exchange processes of protons colliding with C_xH_y molecules ($x = 1, 2, 3; 1 \leq y \leq 2x + 2$). Although the cross section data are available for a limited number of C_xH_y molecules, the analysis of their energy behavior allows to identify the electron capture mechanism governing the process in a given energy region and , thereby, to establish (at least approximately) the corresponding cross section scaling law. These scaling laws, together with the known (from the experiment, or Langevin orbiting model) cross sections at thermal collision energies, give a possibility to predict the experimentally unknown cross sections for all the collision system with an accuracy better than factor of two in the range from thermal energies up to about 1 MeV. In the next section we present the charge exchange cross sections for the collision systems for which such data are available either from experimental or theoretical sources. In section 3 we introduce a scaling form of the experimental cross sections for CH_4, C_2H_6, C_3H_8 and C_4H_{10} based on the revieled electron capture mechanisms for low and high energies. In section 4 we use the cross section scaling properties and other theoretical arguments to construct approximate cross sections for the collision systems for which no data are presently available, and in section 5 we give analytical fits for the recommended cross sections. In section 6 we give some concluding remarks.

2. Proton charge exchange cross sections with CH_4, C_2H_4, C_2H_6, C_3H_8 and C_4H_10

The only C_xH_y molecules for which the proton impact charge exchange cross sections have been measured so far are : CH_4 [6-13], C_2H_2 [13], C_2H_4 [8,9,11],C_2H_6 [9-13], C_3H_8 [10,12,13] and C_4H_10 [8-10]. Quantum-mechanical cross section calculations have been performed for CH_4 [13,14], C_2H_2 [13,15], C_2H_6 and C_3H_8 [13]. While theoretical calculations cover the region of low collision energies (0.1 - 20 keV), the experimental data

cover the energy range from about 0.1 keV up to the MeV region. We note that theoretical calculations in ref.14 (for CH_4) and Ref.15 (for C_2H_2) were done without inclusion of the effects of vibrational excitation of hydrocarbon ionic reaction product and, therefore, they greatly underestimate the corresponding cross sections. The inclusion of these effects in the calculations presented in Ref.13, brings the theoretical cross sections in agreement with experimental data.

We now analyze the cross sections for each of the above $H^+ + C_xH_y$ collision systems separately, excluding the case of $H^+ + C_2H_2$ for which the experimental data are available only in the range 0.2-4.5 keV. (This case will be discussed in Section 4).

2.1. $H^+ + CH_4$

In Fig. 1 we present the experimental cross section data for the $H^+ + CH_4$ charge exchange collisions as function of the collision energy taken from Ref. [6-10, 12, 13]. (The data of Ref.11 lie at still higher energies, but are consistent with the high energy trend of the data from Ref.9.) All data are consistent with each other within their experimental errors, except for the high energy points of the earlier experimental results of Koopman [7]. We have plotted in this figure also the recent low-energy data of Kusakabe [16] for the $O^+ + CH_4$ collision system (expressing the collision energy in units of keV/amu), which nicely follow the trend of low-energy data for the $H^+ + CH_4$ system. The basis for this extension of the $H^+ + CH_4$ data with $O^+ + CH_4$ data toward lower energies (down to 0.012 keV/amu) is the equal reaction energy defect for the two collision systems and the fact that the large cross sections (higher than $10^{-15} cm^2$) in this energy region is determined dominantly by the asymptotic forms of the atomic wave functions of initial and final electronic states (i.e. the process takes place at large internuclear distances where the wave function of the active electron is essentially determined by its binding energy). The low-energy behavior of the $H^+ + CH_4$ charge exchange cross section (supplemented with the data for the $O^+ + CH_4$ collision system) indicates that the electron capture process in this energy region (below $\sim$ 20 keV/amu) takes place in a resonant (or almost resonant) manner, i.e. the reaction energy defect is zero (or very close to it). In an initially (energy-) non-resonant but exothermic collision system (the electron binding energies of H and CH_4 are 13.6 eV and 12.6 eV, respectively), the energy resonance condition can occur only if the reaction exothermicity is expended on excitation of the internal degrees of freedom of the reaction fragments. In the case of $H^+ + CH_4$ (or $O^+ + CH_4$)system, the energy resonance condition for the electron capture process is achieved due to the excitation of vibrational and rotational degrees of freedom of the product CH_4^+ ion during the electron transition process. Indeed, the quantum-mechanical molecular-orbital close-coupling (MOCC) calculations performed in Ref.13 for this system could be brought into agreement with the experimental data of the same reference only with inclusion the vibrationally excited states of CH_4^+ in the calculations.

The revieled resonant character of the electron capture process in the $H^+ + CH_4$ collision system in the low energy region allows us to extend the cross section in the region below the one where experimental data exist (i.e. below 0.01 keV) by using theoretical

arguments. The resonant electron capture theory gives the following expression for the low energy charge transfer cross section [17,18]

$$\sigma = A \ln^2 \left(\frac{B}{v} \right) \tag{1}$$

where A and B are some constants depending on parameters of colliding system and v is the collision velocity. The validity of this expression is restricted to collision velocities $v \ll 1$, in atomic units, (corresponding to energies $E \ll 25keV/amu$), but greater than some $v = v_{pol}$, below which the electron capture is governed by the Langevin orbiting (or polarization capture) mechanism. The Langevin polarization capture cross section formula can be put in the form [19] (in atomic units)

$$\sigma_L = \frac{2\pi}{v} (\frac{\alpha}{\mu_r})^{1/2} P_\lambda \tag{2}$$

where α is the polarizability of the molecule, μ_r is the reduced mass of the collision system and P_λ is the probability of decay of the compound, formed by the orbiting mechanism, into the reaction channel λ. For instance, in the $H^+ + CH_4$ collision system, two reaction channels are possible at thermal energies,

$$\begin{aligned} H^+ + CH_4 \rightarrow (H^+CH_4) &\rightarrow H + CH_4^+ \qquad (a) \\ &\rightarrow H_2 + CH_3^+ \qquad (b) \end{aligned} \tag{3}$$

with decay probabilities $P_{3a} \simeq 0.4$ and $P_{3b} \simeq 0.6$. The total thermal rate coefficient, for both channels, is experimentally known [20] and has the value $3.8 \times 10^{-9} cm^3/s$. This value, converted into cross section by the reaction (2), was used to determine the thermal energy limit of the charge exchange cross section for the $H^+ + CH_4$ system in the thermal energy region. The solid curve in Fig. 1 represent the best fit of the data and their extension with the $O^+ + CH_4$ data.

2.2. $H^+ + C_2H_4$

The experimental cross section data for the electron capture in $H^+ + C_2H_2$ collision system available only for energies above 40 keV [8,9,11]. Kusakabe et al [16] have recently performed electron cross section measurements for the collision system $C^+ + C_2H_4$ in the energy range 0.017-0.38 keV/amu. The charge transfer reaction in this system is exothermic (the ionization potentials of C and C_2H_4 are 11.27 eV and 10.51 eV, respectively) and the data of Kusakabe et al show that in the energy range where the measurements were performed the cross section for this reaction has a behavior consistent with that for the resonant charge exchange processes. The data are shown in Fig. 2. In the thermal energy region (below $\sim$ 0.05 eV), besides the electron capture, there are also two additional exothermic reactions taking place in this collision system

$$\begin{aligned} H^+ + C_2H_4 \rightarrow (H^+C_2H_4) &\rightarrow H + C_2H_4^+ \qquad (a) \\ &\rightarrow H_2 + C_2H_3^+ \qquad (b) \\ &\rightarrow H_2 + H + C_2H_2^+ \quad (c) \end{aligned} \tag{4}$$

The total rate coefficient for reactions (4a)-(4b), according to Eq.(2), is $K_4 = 4.8 \times 10^{-9} cm^3/s$, which is distributed among the channels with the probabilities $P_{4a} \simeq 0.3$, $P_{4b} \simeq 0.5$, $P_{4c} \simeq 0.2$. The solid curve in Fig.2 represents the best fit of the available experimental data with an extension towards the thermal energies by taking into account the above value of the Langevin rate coefficients. We note that the decay probability weights for the reactions (4b) and (4c) are determined in accordance with reaction exothermicities.

2.3. $H^+ + C_2H_6$

Experimental cross section data for the electron capture process in $H^+ + C_2H_6$ system are available in the energy range from 0.2 keV up to a few MeV [9-13]. The reaction is exothermic (the ionization potential of C_2H_6 is 11.52 eV) with an energy defect in the initial channel of 2.08ev. However, this exothermicity can be expended on excitation of internal degrees of freedom of $C_2H_6^+$ ion and the cross section data below 20 keV show a behavior typical for resonant charge exchange (see Fig.3). Moreover, the recent experimental cross section data for the $O^+ + C_2H_6$ system [16] smoothly extend the resonant cross section behavior down to 0.012 keV/amu (also shown in Fig.3). In the thermal energy region (e.g. below $\sim$ 0.05 eV), there are two additional exothermic reactions in the $H^+ + C_2H_6$ system

$$\begin{aligned} H^+ + C_2H_6 \rightarrow (H^+C_2H_6) &\rightarrow H + C_2H_6^+ \quad (a) \\ &\rightarrow H_2 + H + C_2H_4^+ \quad (b) \\ &\rightarrow H_2 + H_2 + C_2H_3^+ \quad (c) \end{aligned} \tag{5}$$

The reaction channel producing $H_2 + C_2H_5^+$ is endothermic and does not participate in the decay of the complex $(H^+C_2H_6)$. The ion $C_2H_6^+$ has a dissociation energy of about 1 eV with respect to dissociation into $C_2H_4^+ + H_2$ products and can rapidly predissociate into this channel. Therefore, the channels (5a) and (5b) are sometimes treated jointly. The total rate coefficient for all the channels (5) is $K_5 = 4.2 \times 10^{-9} cm^3/s$ [21], with channel probabilties $P_{5a} \simeq 0.3$, $P_{5b} \simeq 0.3$ and $P_{5c} \simeq 0.4$. The solid curve in Fig.3 represents a least square fit to the data with an extension towards lower energies consistent with the above rate coefficient value.

2.4. $H^+ + C_3H_8$

Experimental cross section data for the electron capture reaction in this collision system are available in the energy range 0.2-200 keV [10,12,13]. Similar data have recently become available also for the $O^+ + C_3H_8$ system in the energy range 0.012-0.28 keV/amu [16]. The H^+ and O^+ impact data are plotted in Fig.4 and they all show a consistent low energy behavior of the cross section, confirming the resonant character of the process in the region below $\sim$ 20 keV/amu. (The ionization potential of C_3H_8 is 11.08 eV.) In the

thermal energy region (below $\sim$ 0.05 eV), the charge exchange is accompanied also by atom exchange, i.e.,

$$\begin{aligned} H^+ + C_3H_8 \rightarrow (H^+C_3H_8) &\rightarrow H + C_3H_8^+ \quad (a) \\ &\rightarrow H_2 + C_3H_7^+ \quad (b) \end{aligned} \tag{6}$$

with total rate coefficient $K_6 = 5.2 \times 10^{-9} cm^3/s$ [21], and decay channel probabilities $P_{6a} \simeq P_{6b} \simeq 0.5$. The solid curve in Fig.4 is a fit of the data with an extension towards lower energies consistent with the above value of the rate coefficient. In the region above 200 keV/amu, the cross section is derived by using the scaling relation discussed in Section 3.

2.5. $H^+ + C_4H_{10}$

The electron capture cross section data for this collision system are available only in the region above 1 keV (up to 1 MeV) [8-10] and are shown in Fig.5. The low-energy data (below $\sim$ 20 keV) indicate that this reaction also has a resonant character, consistent with its high exothermicity (the ionization potential of C_4H_{10} is 10.53 eV) and the large number of vibrational modes of $C_4H_{10}^+$ product ion (available to absorb the reaction exothermicity during the capture process and provide resonance conditions for the process). Since the rate coefficient for this reaction in the thermal energy region (below $\sim$ 0.05 eV) is unknown, we have calculated it by using the relation

$$K_{10} \simeq K_8 \left(\frac{\alpha_{10}}{\alpha_8} \right)^{1/2} \tag{7}$$

following from Eq.(2), where the subscripts "8" and "10" refer to the C_3H_8 and C_4H_{10} molecules, the polarizabilities of which are known: $\alpha_8 = 42.49$, $\alpha_{10} \simeq 54.7$, in atomic units (a_o^3)[22]. This gives the value for K_{10} of $5.9 \times 10^{-9} cm^3/s$. The solid curve in Fig.5 is a fit to the experimental data, extended towards the low energies in accordance with the above value for K_{10}.

At the end of this section we would like to make the following remark. It can be observed that the high energy dependence of the cross sections for the considered collision system somewhat changes (the cross section curves change their slope) at the energies above 400 - 500 keV (see Figs.1-3,5). The observed increase of the cross sections in this energy region is due to the contribution to the process of electron capture from the inner shells of C_xH_y.

3. Cross section scaling relations

The similarity in the cross section energy behaviors for all the $H^+ + C_xH_y$ collision systems considered in the preceding section indicates that the electron capture process in

these systems is governed by the same physical mechanism at low energies ($E \leq 20keV$) and another physical mechanism (but same for all collision systems) at the high energies (above $\sim 100keV$). We have already argued that the low-energy transition mechanism is the resonant capture mechanism, characterized by a cross section energy behavior in the form of Eg.(1). From the theory of resonant charge exchange reactions (see e.g. [17],[18]), it follows that the constant A in Eq.(1) is proportional to $1/I_p$, where I_p is the ionization potential of the molecule. The constant B in Eq.(1) is proportional to the number of equivalent electrons in the target, which we take to be equal to the number y of H-atoms in the C_xH_y molecule. For $4 \leq y \leq 8$, $ln^2 y$ can be approximated by $y^{1/2}$ to within an accuracy of 37%, or better. Therefore, in the low energy region, the resonant capture cross section can be approximately represented in a reduced form

$$\overline{\sigma}_l = \sigma I_p / y^{1/2}. \tag{8}$$

In the energy region above $\sim 100keV$, most of the theoretical models (e.g. the classical impulse approximation, the first Born approximation, etc) show an I_p^{-2} dependence of the charge exchange cross section (see e.g. [23]). Assuming that the electron donors of the C_xH_y molecule in the electron capture process, are the H atoms, and that at high energies these atoms can be considered as independent donors, it follows that the cross sections at these energies is proportional to the numbers y of H atoms in the C_xH_y molecule. Therefore, in the region above 100-200 keV, the approximate reduced form of charge exchange cross section is

$$\overline{\sigma}_h = \frac{\sigma I_P^2}{y} \tag{9}$$

In the intermediate energy range ($\sim 20 - 100keV$), the electron capture process in any ion-atom or ion-molecule collision system results from the coupling of many electronic states and no simple dependence of σ on I_p and y can be theoretically predicted. For the practical purpose of constructing a reduced cross section $\overline{\sigma}$ in the entire energy region, one can bridge these interval by taking the average value of $\overline{\sigma}_l$ and $\overline{\sigma}_h$,

$$\overline{\sigma}_m = (\overline{\sigma}_l + \overline{\sigma}_h)/2 \tag{10}$$

Using the scaling relations (8)-(10), we have plotted the experimental data for CH_4 , C_2H_6, C_3H_8 and C_4H_{10} in Fig.6 in a reduced form, $\overline{\sigma}(E)$. The scaled data show a pronounced tendency of grouping around a single curve, their dispersion being result of the approximate character of the scalings (8)-(10), but also a reflection of the experimental uncertainties of the original data. The solid line in Fig.6 represents a best-square fit of the data. The extension of this line towards lower collision energy was done by using the scaled fits of the cross section for these systems in the energy region below 1eV.

It should be noted that the scaling relation (8) is valid only for those systems for which the electron capture process has a resonance character. We could expect that the energy resonance conditions for the processes can be met for the C_xH_y molecules with sufficiently large number of H atoms (e.g. $y \geq 2x$, or so). The high energy scaling relation (9), however, should be valid for any C_xH_y molecule.

4. Derived cross sections for other $H^+ + C_XH_Y$ system

In order to perform a complete modeling of the transport of hydrocarbons in the plasma one needs to know the cross sections (or rate coefficients) for all members of the hydrocarbon families C_xH_y, for x=1-3 and $1 \leq y \leq 2x+2$, and for all important processes. Charge exchange is certainly one of those processes, especially for the temperatures characterizing the plasma edge and divertor plasmas. (The C_4H_{10} family of hydrocarbons will be excluded from our further considerations.) Since apart from the systems discussed in Section 2, experimental (and theoretical) information exists only for the $H^+ + C_2H_2$ system (but only in the energy range 0.2-4.5 keV [15]), one is left with the necessity to derive approximate cross sections for the remaining $H^+ + C_xH_y$ collision systems on the basis of the scaling laws discussed in the previous section, the information about the thermal rate coefficients available from Ref.21, and by using the general theory of charge exchange reactions [18,23,24], In deriving the approximate cross sections for the systems for which data are not available (above the thermal energy region) from the literature, it is convenient to separate the $H^+ + C_xH_y$ collision systems into two classes: systems in which the process has resonant character and systems with non-resonant electron capture. This separation is mainly applicable for the low energy region, since at high energies the electron transition mechanism is less sensitive to the energy resonance condition [23,24]. The criteria for the expected fulfillment of the resonant energy condition for the charge exchange process in $H^+ + C_xH_y$ systems were discussed at the end of the preceding section. We should note that the "resonant electron capture" is used here in a broader sense (equality or near equality of the total internal energy in the initial and final reaction states) and is not related to the symmetry properties of the collision system (like in the case of resonant electron capture in isonuclear atomic and molecular collision systems).

4.1. Resonant $H^+ + C_xH_y$ charge exchange reactions

We have seen in Section 2 that the charge exchange reactions in $H^+ + CH_4$, C_2H_4,C_2H_6, C_3H_8 collision systems have a resonant character in the low energy region. In the next sub-section, we shall see that the experimental cross section data for the $H^+ + C_2H_2$ reaction in the energy range 0.2-4.5 keV show a behavior departing (but not drastically) from the resonant cross section behavior. This can be taken as an indication that for the $H^+ + C_xH_y$ with $x = 2, 3$ and $y \geq 2x - 1$ the process already attains its resonant character. Therefore, for these systems, as well as for CH_3, the cross section above the thermal energy region can be derived from the cross section for C_xH_{2x+2} (given in Section 2) by using the scaling relations (8)-(10). Below ~ 0.5 eV, these cross sections should be extended in such a way as to smoothly go over into the values determined by the known reaction rate coefficients [21]. In Table I we give the total rate coefficients for all $H^+ + C_xH_y$ reactions [21], together with the branching ratios (probabilities P_λ) for the different channels of the orbiting compound decay.We note that not in all cases we have used the branching ratios adopted in Ref.21, but rather we have taken into account the trend of the charge exchange cross section behavior as suggested by the recent low-energy experimental data [15,16], (not available in the time when Ref.21 was published), as well as the values of exothermicities of the particular reaction channels. We further note that

in Ref.5, the the total rate coefficient for (H^+,C_xH_y) compound formation, $\sigma_l v = K_L$ was calculated by using the Langevin formula (Eq.(2) with $P_\lambda = 1$)) and then assigning equal branching ratios to all reaction channels. In the calculation of K_L in Ref.5, the unknown polarizabilities α_{xy} for many C_xH_y molecules were determined by using the Lorentz-Lorenz relation between α_{xy} and the molar refraction R_{xy}. The values of R_{xy} were, on their turn, determined by an inter- and extrapolation procedure using the experimental values for R_{xy} for only six C_xH_y molecules. The assignment of equal decay probability P_λ to all reaction channels in Ref.5 leads to significant uncertainties in the derived cross sections.

A further remarks is noteworthy here regarding the energy dependence of the channel cross sections in the thermal energy reactions

$$\begin{aligned} H^+ + C_xH_y \rightarrow (H^+C_xH_y) \;&\rightarrow\; H + C_xH_y^+ \qquad (a) \\ &\rightarrow\; H_2 + C_xH_{y-1}^+ \qquad (b) \\ &\rightarrow\; H_2 + H + C_xH_{y-2}^+ \qquad (c) \\ &\rightarrow\; H_2 + H_2 + C_xH_{y-3}^+ \qquad (d) \\ &\;\;\ldots\ldots \end{aligned} \tag{11}$$

While the $1/v$ dependence is common to the cross sections of all the channels of reaction (11) in the thermal energy region (e.g. below $\sim$ 0.05 eV), the decrease of the cross section with increasing the collision energy is much faster for the particle exchange and break-up channels (11b)-(11d) than for the electron transfer channel (11a), which continues to follow the $1/v$ dependence in a much larger energy region. These different energy dependences of the cross sections for the reaction channels (11a) and (11b)-(11d) have to be taken into account when trying to smoothly connect the cross sections from the resonant region (when experimental electron capture data for the $H^+ + C_xH_{2x+2}$ exist) with the cross section for the channel (11a). If $K_\lambda = K_{tot}P_\lambda$ is the thermal rate coefficient for the reaction channel λ in Eq.(11), and K_{tot} is the total thermal rate coefficient for all channels, expressed in units of cm^3/s, then the thermal energy cross sections of the channel (11a) and channels (11b)-(11d) can be expressed as

$$\sigma_{11a} = 7.26 \times 10^{-7} \frac{K_{11a}(cm^3/s)}{E(eV)^{1/2}} (cm^2) \tag{12}$$

$$\sigma_\lambda = 7.26 \times 10^{-7} \frac{K_\lambda(cm^3/s)}{E(eV)^{1/2} + aE(eV)^\beta} (cm^2), \lambda = (11b) - (11d), \tag{13}$$

where a (< 1) and β (> 1) are constants given in Table I for each of the reaction channels.

The scaling relations (8)-(10) were used for deriving the resonant cross sections for the systems $H^+ + C_xH_y$, $y \geq 2x - 1$ separately for each of the C_xH_y families of hydrocarbons. For instance, the cross sections for the $H^+ + C_3H_y$, $5 \leq y \leq 7$, collision system were derived by relating the cross section for each of them with the cross section for the system $H^+ + C_3H_8$ by using Eqs.(8)-(10). The ionization potentials I_p of the

C_xH_y molecules, needed in the use of Eqs.(8)-(10) are given in Table II. These data were collected from the literature, or calculated from the thermochemical tables [25,26].

The cross sections for the resonant $H^+ + C_xH_y$ ($2x-1 \leq y \leq 2x+2$) charge exchange reactions are given in Fig.7 (for CH_y), Fig.8 (for C_2H_y) and Fig.9(for C_3H_y), together with the cross sections for the non-resonant reactions.

It should be noted that the cross sections for the system $H^+ + C_xH_{2x+1}$ in the low-energy region are larger than the cross sections for the $H^+ + C_xH_{2x+2}$ systems, which is a consequence of the scaling relation (8) and the fact that the ionization potentials of C_xH_{2x+1} are smaller than those for C_xH_{2x+2} (see Table II).

4.2. Non-resonant $H^+ + C_xH_y$ charge exchange reactions

The only non-resonant charge exchange reaction in the $H^+ + C_xH_y$ collision systems for which the cross section has been measured in the energy range 0.2-4.5 keV is the reaction $H^+ + C_2H_2$ [13]. There have been recently cross section measurement also for the charge exchange reaction $O^+ + C_2H_2$ in the energy range 0.012-0.3 keV/amu. These data are shown in Fig.10 and they follow a single line. The solid line through the data represents their fit. This line is smoothly continued towards the low energies in such a way that it goes over into the thermal energy electron capture cross section of the form of Eq.(12) with the value of rate coefficients (K_{11a}) given in Table I.

In the energy region above $\sim 20keV$, the cross section has been determined by using the scaling relations (9) and (10) in conjunction with the known cross section data for the $H^+ + C_2H_4$ and $H^+ + C_2H_6$ reactions. Since the experimental data above 3 eV show already a very slow increase (see Fig.10), a smooth connection of the data below 4.5 keV with those above 20 keV is possible using the fact that the velocity at which the cross section maximum occurs is given by the Massey relation (in atomic units)

$$c\Delta E/v \simeq 1 \tag{14}$$

where v is the collision velocity, $\Delta E = I_P(H) - I_P(C_2H_2) = 2.2eV$, and c is some constant. The cross section maximum at ~ 10 keV for the $H^+ + C_2H_2$ reaction gives the value of $c \simeq 8$. This value of c will be taken as typical also for the other non-resonant $H^+ + C_xH_y$ charge exchange reactions. The relations (14) shows that for reactions with larger ΔE, the cross section maximum appears at larger energies.

The non-resonant charge exchange reaction in ion-atom/molecule collision systems are generally described by Demkov's (two state) model [18] which predicts a rapid decrease of the cross section when the energy decreases below the value at which the cross section maximum occurs. This decrease is faster (exponential) for the reactions with larger energy defect. However, if the polarizability of the neutral reactant is high, like in the case of hydrocarbon molecules (for CH_4, C_2H_6 and C_3H_8 the values of α are 17.56, 30.20 and 42.5 a_o^3, respectively[22]), the mechanism of polarizational capture (Langevin orbiting) starts to operate at larger collision energies and the cross sections starts to increase with decreasing the energy.

In deriving the cross sections for the non-resonant $H^+ + C_xH_y$ charge exchange (other than for C_2H_2), we have used the scalings (9)-(10) for the energies down to ~ 20 keV, Demkov's model [18] for the energies below ~ 20 keV and the polarization capture model, Eq.(12), for the energies below ~ 1 eV. Since the parameters entering in Demkov's model (e.g. the exchange interaction) are not well known for the considered collision systems, and since the Franck-Condon $C_xH_y \rightarrow C_xH_y^+$ transition factors enter the theory in different ways at the higher (~ 10 keV) and lower ($\sim 1-10$ eV)energies (frozen vs. relaxed vibrational motion), the use of Demkov's model was done in a qualitative manner only (to determine the slope of the cross section decrease in the region below the energy of the cross section maximum). Therefore, the cross sections for the $H^+ + C_xH_y$ systems, with $x = 1-3$ and $y = 1, 2$ (except for C_2H_2) have large uncertainties in the energy range 1 eV - 10 keV. The cross sections for the non-resonant reactions derived by the procedures described above are shown in Fig.7 (for CH_y), Fig. 8 (for C_2H_y) and Fig. 9 (for C_3H_y), together with the cross sections of resonant reactions.

5. Analytic fits to the cross sections

For an easy incorporation of the present cross sections into various plasma application codes, we have fitted the cross section data to the following analytic expression

$$ln(\sigma) = \sum_{i=1}^{N} C_i T_i(x) \tag{15}$$

where, $x = [(lnE - lnE_{min}) - (lnE_{max} - lnE)]/[lnE_{max} - lnE_{min}]$, E is the collision energy expresses in units of keV, C_i are the fitting coefficients, the units of σ are $10^{-16}cm^2$, and $T_i(x)$ are the Chebychev orthogonal polynomials ($T_1(x) = 1$, $T_2(x) = x$, and $T_{n+2}(x) = 2T_{n+1}(x) - T_n(x)$). For all the reactions considered, the $E_{min} = 10^{-4}$ keV and $E_{max} = 10^3$ keV, and the fitting coefficients C_i are given in Table III. The r.m.s. deviation of the fits from the cross section values that have been fitted is somewhat different for different reactions and is in the range $2\% - 8\%$. (The r.m.s. value for each reaction is also shown in Table III).

The solid curve on Fig. 6, which represent the fit to the experimental data for the $H^+ + CH_4$, C_2H_6, C_3H_8 and C_4H_{10} systems, can also be represented by the same expression as the Eq.(15). This reduced cross section, which represents the data with an accuracy of about $20-30\%$ in the low energy region, and with an accuracy of $30-40\%$ in the high energy region, can also be used to derive the cross sections for other $H^+ + C_xH_y$ resonant reactions.

6. Concluding remarks

We have compiled and assessed the existing experimental cross section data for the charge exchange process in $H^+ + C_xH_y$ collision systems with $x = 1-3$ and $1 \leq y \leq 2x+2$.

For the systems with $y = 2x + 2$, as well as for C_2H_4, we have observed that in the low energy region (below $\sim$ 20 keV), the cross section has an energy behavior typical for the resonant electron capture processes. The charge exchange cross sections for these systems exhibit scaling properties, the validity of which has been extended also to the collision systems with large number of H atoms in the C_xH_y molecule ($y \geq 2x - 1$). In the high energy region (above $\sim$ 100 keV), the cross sections for all systems investigated experimentally so far, also show scaling properties. These cross section scalings have been used to derive the cross sections for the systems with $y \geq 2x - 1$, which are consistent with the known values in the thermal energy region. For the non-resonant charge exchange processes, the cross sections have been derived by using the high energy scaling, the known thermal energy reaction rate coefficients and theoretical arguments based on Demkov's model and Massey relation (14).

The accuracy of the resonant cross sections for which experimental data were found available both in the low and high energy regions (CH_4, C_2H_4, C_2H_6, C_3H_8) is estimated to be within $15 - 20\%$. Based on the accuracy of the high-energy cross section scaling, all derived cross sections have an estimated accuracy of $30 - 40\%$ in the region above $\sim$ 100 keV. In the energy region below $\sim$ 20 keV, the cross sections of derived resonant reactions ($y \geq 2x - 1$) have an estimated accuracy of about $20 - 30\%$ (based on the accuracy of the low energy scaling), while the accuracy of the cross sections for non-resonant reactions is much larger in this energy region (and in fact is undeterminated). In the energy range between $\sim$ 20 keV and $\sim$ 100 keV, the expected accuracy of all derived cross sections in the range $20 - 30\%$.

ACKNOWLEDGEMENTS

We are indebted to Prof. T. Kusakabe for providing us with his cross section data for $O^+, C^+ + C_xH_y$ collisions prior to publication. Several discussions with Prof. M. Kimura are also greatfully acknowledged.

REFERENCES

[1] Technical Basis for the ITER Final Design Report; ITER EDA Documentation Series No.16 (IAEA, Vienna, 1998).
[2] HAASZ, A.A., STEPHENS, J.A., VIETZKE, E., et al., Atom. Plasma-Mater. Interact. Data Fusion, 7 (part A) (1998) 5.
[3] REITER, D., MAY, Chr., BAELMANS, M., et al., J. Nucl. Mater. 241-243 (1997) 342.
[4] EHRHARDT, A.B., LANGER, W.D., Collisional Processes of Hydrocarbons in Hydrogen Plasmas, Report PPPL-2477 (1987) (Princeton Plasma Physics Laboratory).
[5] ALMAN, D.A., RUZIC, D.N., BROOKS, J.N., Phys. Plasmas 7 (2000) 1421.
[6] CHAMBER, E.S., Report UCRL-14214 (1965).

[7] KOOPMAN, D.J., J. Chem. Phys. 49 (1968) 5203.
[8] COLLINS, J.G., KEBARLE, P., J. Chem. Phys. 46 (1967) 1082.
[9] TOBUREN, L.H., NAKAI Y., LANGLEY, R.A., Phys. Rev. 171 (1968) 114.
[10] ELLIOT, M., J. de Physique 38 (1977) 24.
[11] VARGHESE, S.L., BISSINGER, G., JOYCE, J.M., LAUBERT, R., Nucl. Instrum. Meth. 170 (1980) 269.
[12] JONES, M.L., DOUGHERTY, B.M., DILLINGHAM, T.R., et al., Nucl. Instrum. Meth. B: 10/11 (1985) 142.
[13] KUSAKABE, T., ASAHINA, K., IIDA, A., et al., Phys. Rev. A (submitted).
[14] KIMURA, M., LI, Y., HIRSCH, G., BUENKER, R.J., Phys. Rev. A 52 (1995) 1196.
[15] KIMURA, M., LI, Y., HIRSCH, G., BUENKER, R.J., Phys. Rev. A 54 (1996) 5019.
[16] KUSAKABE, T., (private communication, 2000).
[17] FIRSOV, O.B., Zh. Exp. Theor. Fiz. 21 (1951) 1001 (in Russian).
[18] SMIRNOV, B.M., "Asymptotic Methods in Atomic Collision Theory", (Nauka, Moscow, 1973)(in Russian).
[19] See, e.g., GIOUMOUSIS, G., STEVENSON, D.P., J. Chem. Phys. 29 (1958) 294.
[20] See, e.g., ANICICH, V.G., HUNTRESS, W.T., Astrophys. J., Suppl. Ser. 62 (1986) 553.
[21] MILLAR, T.G., at al., Astron. Astrophys. Suppl. 121 (1997) 139.
[22] HIRSCHFELDER, J.O., CURTIS, C.F., BIRD, R.B., "Molecular Theory of Gases and Liquids" (John Wiley, New York, 1967).
[23] JANEV, R.K., PRESNYAKOV, L.P., SHEVELKO, V.P., "Physics of Highly Charged Ions" (Springer-Verlag, Berlin, 1987).
[24] BRANSDEN, B.H., McDOWELL, M.R.C., "Theory of Charge Exchange Collisions" (Clarendon Press, Oxford, 1992).
[25] WAGMAN, D.D., EVANS, W.H., PARKER, V.B., et al., "Selected Values of Chemical Thermodynamic Properties", NBS Technical Note 270-3 (January, 1968), US Gov. Printing Office, Washington D.C. (1968).
[26] ROSENSTOCK, J., J. Phys. Chem. Ref. Data 6 (1977) 1.

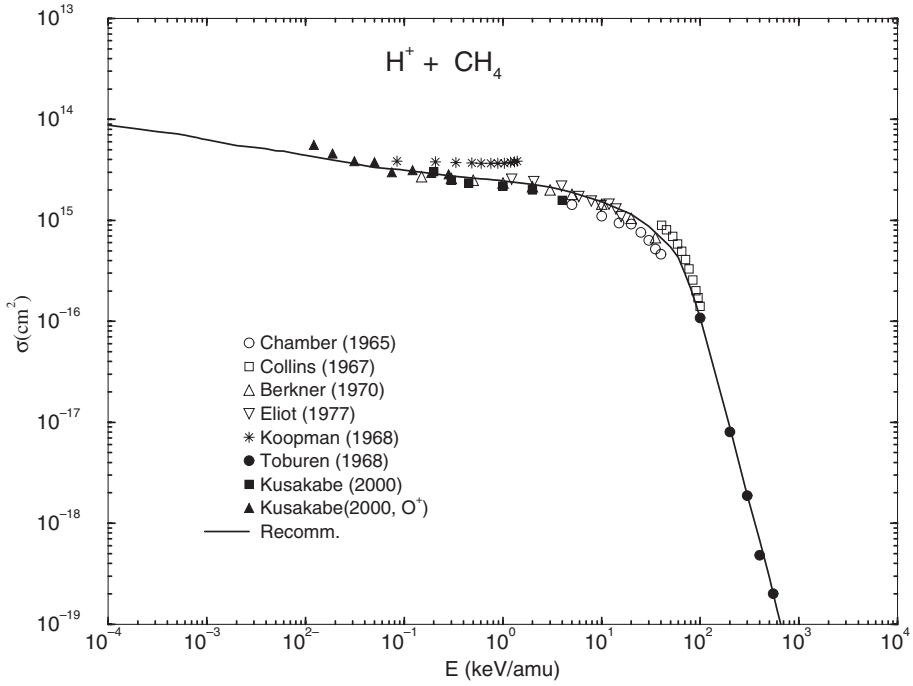

FIG. 1. Total cross sections for the $H^+ + CH_4$ charge exchange collisions as a function of the collisional energy. Symbols represent the experimental data [6-10,12,13,16], and solid curve represents the least square fit of the data (with appropriate extensions;see text).

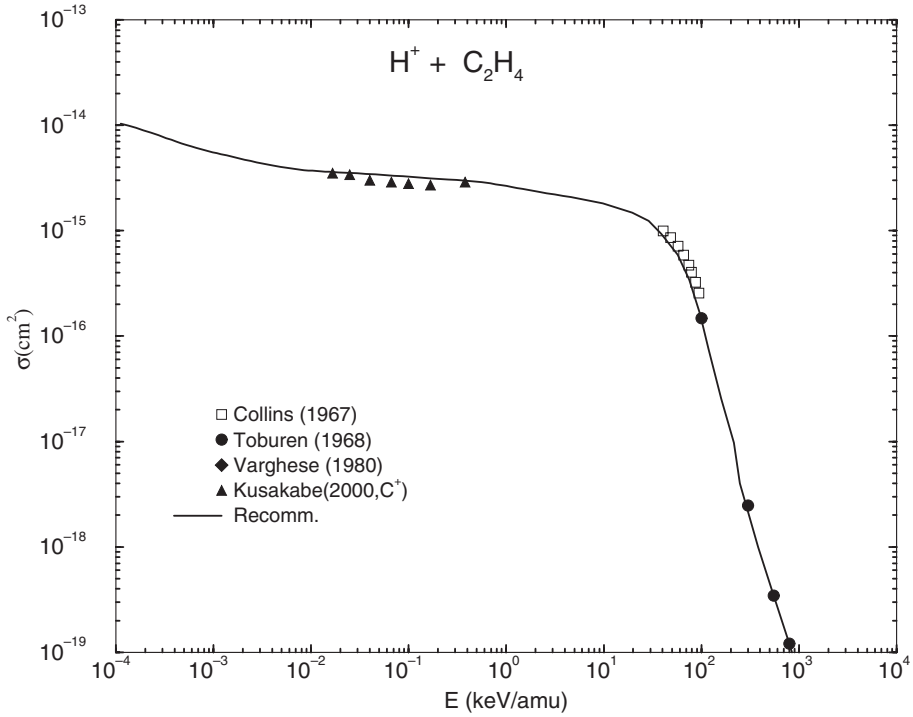

FIG. 2. Total cross sections for the $H^+ + C_2H_4$ charge exchange collisions as a function of the collisional energy. Symbols represent the experimental data [8,9,11,16], and solid curve represents the least square fit of the data (with appropriate extensions;see text).

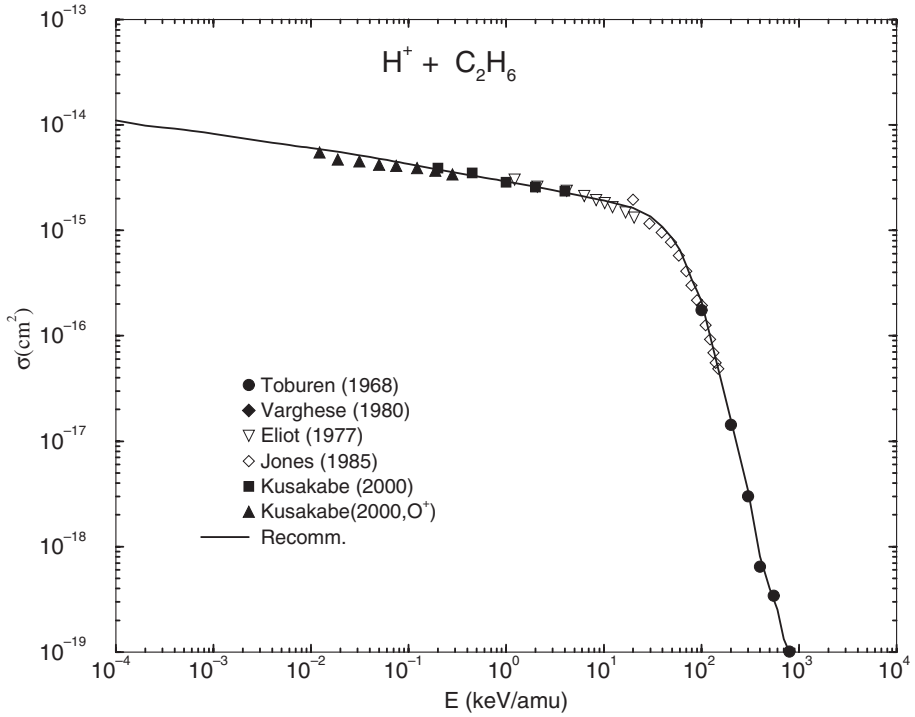

FIG. 3. Total cross sections for the $H^+ + C_2H_6$ charge exchange collisions as a function of the collisional energy. Symbols represent the experimental data [9-13,16], and solid curve represents the least square fit of the data (with appropriate extensions;see text).

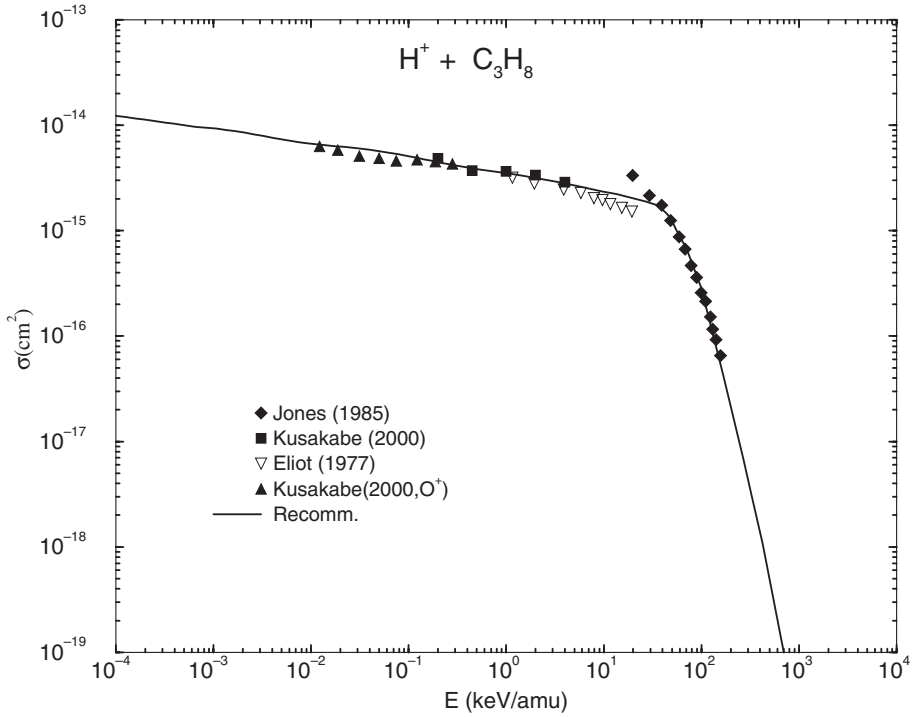

FIG. 4. Total cross sections for the $H^+ + C_3H_8$ charge exchange collisions as a function of the collisional energy. Symbols represent the experimental data [10,12,13,16], and solid curve represents the least square fit of the data (with appropriate extensions;see text).

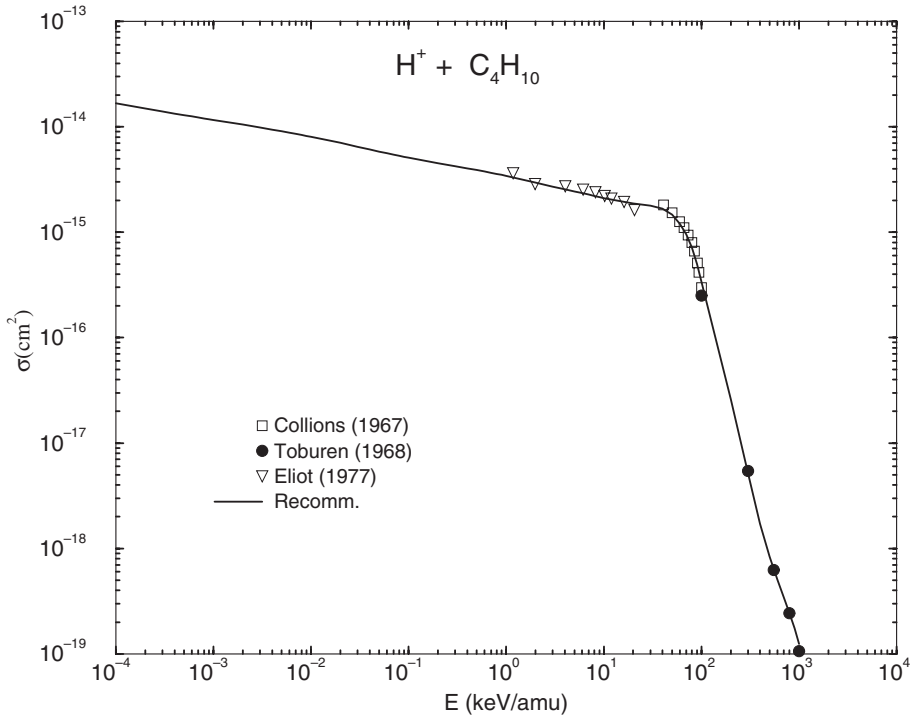

FIG. 5. Total cross sections for the $H^+ + C_4H_{10}$ charge exchange collisions as a function of the collisional energy. Symbols represent the experimental data [8-10], and solid curve represents the least square fit of the data (with appropriate extensions;see text).

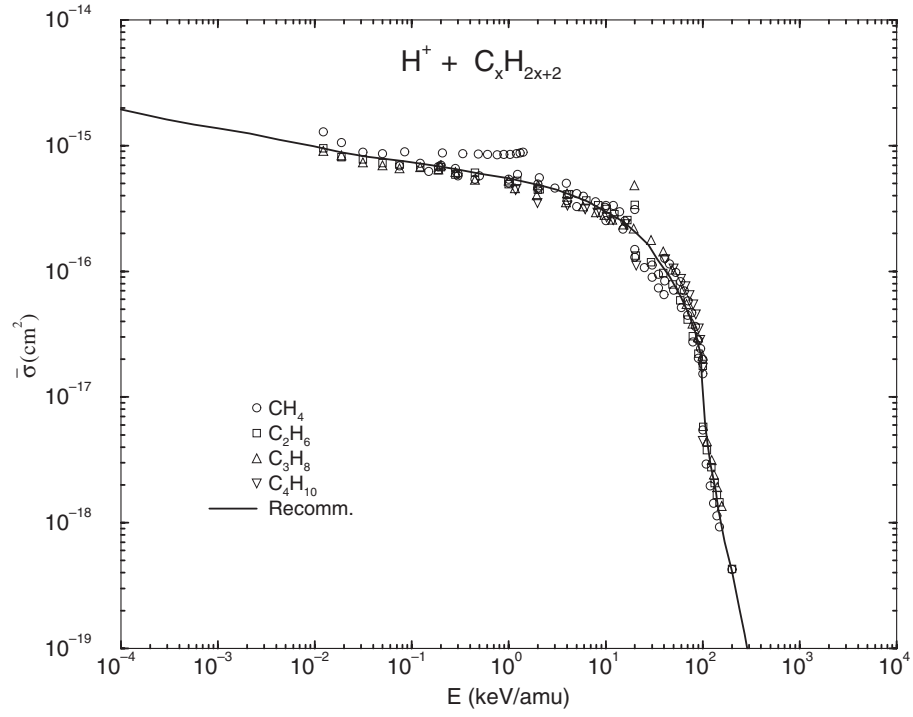

FIG. 6. Total cross sections in a reduced form (Eqs.(8)-(10)) for the CH_4, C_2H_6, C_3H_8 and C_4H_{10} charge exchange collisions as a function of the collisional energy. Symbols represent the experimental data [6-13,16], and solid curve represents the least square fit of the data,extended to scaled thermal-energy cross section values.

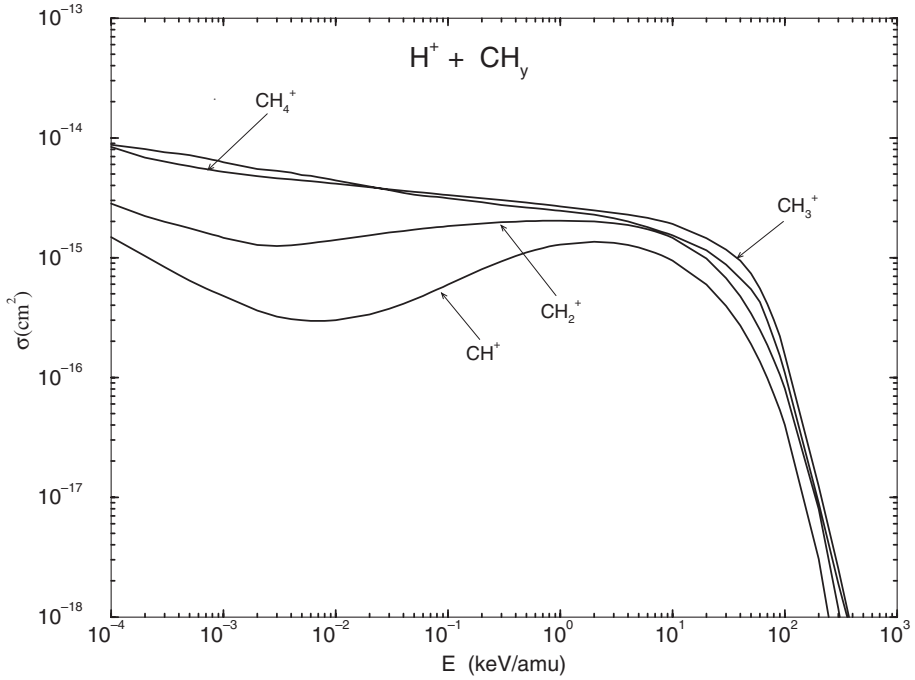

FIG. 7. Cross sections for the $H^+ + CH_y(y = 1 - 4)$ charge exchange collisions as a function of the collisional energy.

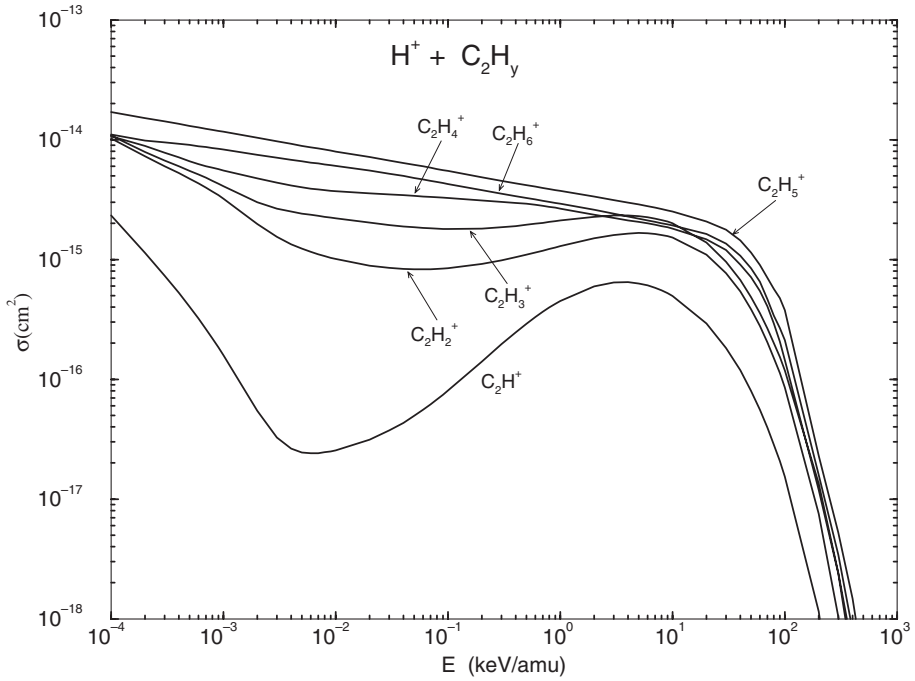

FIG. 8. Cross sections for the $H^+ + C_2H_y(y = 1 - 6)$ charge exchange collisions as a function of the collisional energy.

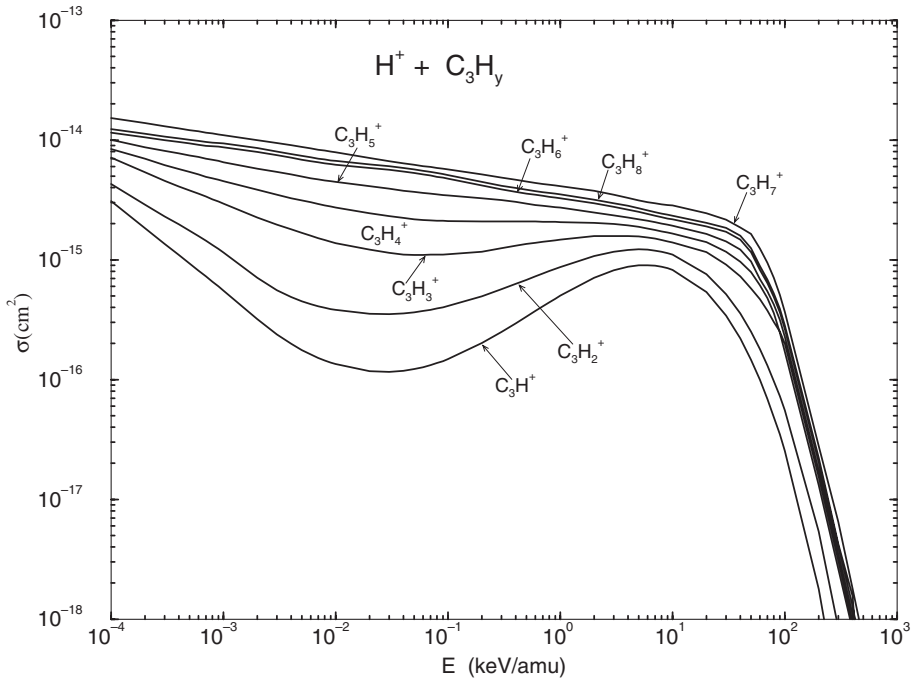

FIG. 9. Cross sections for the $H^+ + CH_y (y = 1 - 8)$ charge exchange collisions as a function of the collisional energy.

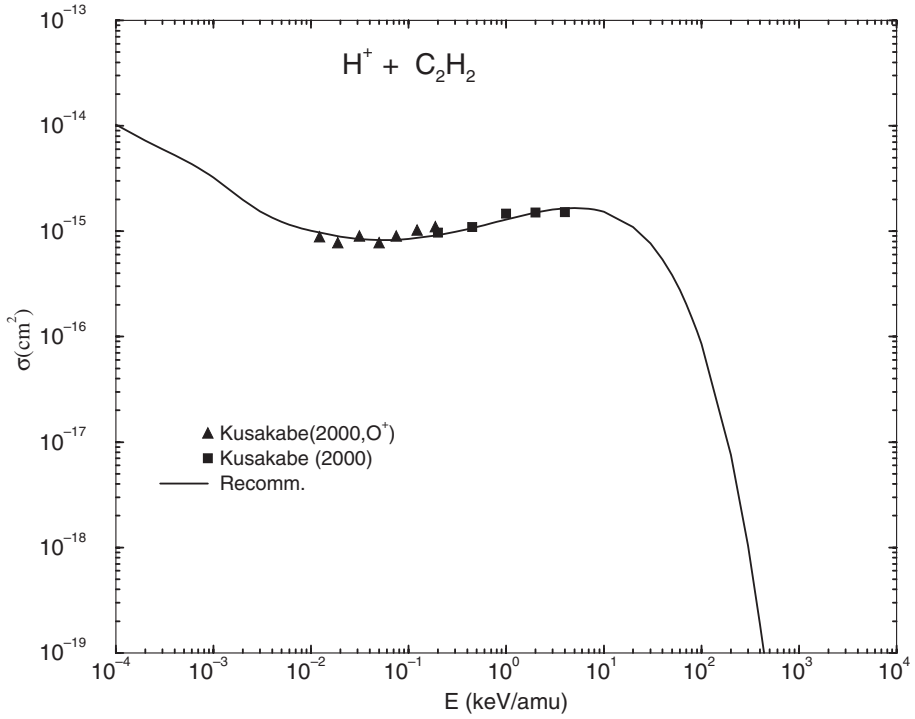

FIG. 10. Total cross sections for the $H^+ + C_2H_2$ charge exchange collisions as a function of the collisional energy. Symbols represent the experimental data [13,16], and solid curve represents the least square fit of the data (with appropriate extensions;see text).

Table I. Total thermal rate coefficients, branching ratios and values of parameters α and β in Eq. (13) for the $H^+ + C_xH_y$ charge exchange reactions

Reaction	Branching Ratios,P_λ	Total Rate Coef.($10^{-9}cm^3/s$)	α	β
$H^+ + CH_4 \rightarrow H + CH_4^+$	0.4	3.8	-	-
$\rightarrow H_2 + CH_3^+$	0.6		0.5	2.5
$H^+ + CH_3 \rightarrow H + CH_3^+$	1.0	3.4	-	-
$H^+ + CH_2 \rightarrow H + CH_2^+$	0.36	2.8	-	-
$\rightarrow H_2 + CH^+$	0.64		0.5	2.5
$H^+ + CH \rightarrow H + CH^+$	0.31	1.9	-	-
$\rightarrow H_2 + C^+$	0.69		0.01	3.5
$H^+ + C_2H_6 \rightarrow H + C_2H_6^+$	0.29	4.2	-	-
$\rightarrow H + H_2 + C_2H_4^+$	0.33		0.45	2.5
$\rightarrow H_2 + H_2 + CH_3^+$	0.38		0.45	2.5
$H^+ + C_2H_5 \rightarrow H + C_2H_5^+$	0.40	4.5	-	-
$\rightarrow H_2 + C_2H_4^+$	0.49		0.45	2.5
$\rightarrow H + H_2 + C_2H_3^+$	0.11		0.45	2.5
$H^+ + C_2H_4 \rightarrow H + C_2H_4^+$	0.31	4.8	-	-
$\rightarrow H_2 + C_2H_3^+$	0.52		0.45	2.5
$\rightarrow H + H_2 + C_2H_2^+$	0.17		0.45	2.5
$H^+ + C_2H_3 \rightarrow H + C_2H_3^+$	0.77	4.0	-	-
$\rightarrow H_2 + C_2H_2^+$	0.23		0.5	2.5
$H^+ + C_2H_2 \rightarrow H + C_2H_2^+$	0.71	3.5	-	-
$\rightarrow H_2 + C_2H^+$	0.29		0.45	2.5
$H^+ + C_2H \rightarrow H + C_2H^+$	0.5	3.0	-	-
$\rightarrow H_2 + C_2^+$	0.5		0.45	2.5
$H^+ + C_3H_8 \rightarrow H + C_3H_8^+$	0.5	5.2	-	-
$\rightarrow H_2 + C_3H_7^+$	0.5		0.6	3.0
$H^+ + C_3H_7 \rightarrow H + C_3H_7^+$	0.5	5.0	-	-
$\rightarrow H_2 + C_3H_6^+$	0.5		0.6	3.0
$H^+ + C_3H_6 \rightarrow H + C_3H_6^+$	0.5	4.8	-	-
$\rightarrow H_2 + C_3H_5^+$	0.5		0.6	3.0
$H^+ + C_3H_5 \rightarrow H + C_3H_5^+$	0.5	4.6	-	-
$\rightarrow H_2 + C_3H_4^+$	0.5		0.6	3.0
$H^+ + C_3H_4 \rightarrow H + C_3H_4^+$	0.5	4.4	-	-
$\rightarrow H_2 + C_3H_3^+$	0.5		0.6	3.0
$H^+ + C_3H_3 \rightarrow H + C_3H_3^+$	0.5	4.2	-	-
$\rightarrow H_2 + C_3H_2^+$	0.5		0.8	3.0
$H^+ + C_3H_2 \rightarrow H + C_3H_2^+$	0.5	4.0	-	-
$\rightarrow H_2 + C_3H^+$	0.5		1.0	3.0
$H^+ + C_3H \rightarrow H + C_3H^+$	0.5	4.0	-	-
$\rightarrow H_2 + C_3^+$	0.5		1.6	3.0

Table II. Ionization potentials of C_xH_y

CH_y	$I_p(eV)$	C_2H_y	$I_p(eV)$	C_3H_y	$I_p(eV)$
CH_4	12.51	C_2H_6	11.52	C_3H_8	11.08
CH_3	9.84	C_2H_5	8.25	C_3H_7	9.10
CH_2	10.46	C_2H_4	10.51	C_3H_6	9.74
CH	11.13	C_2H_3	9.45	C_3H_5	9.90
		C_2H_2	11.51	C_3H_4	$(10.02)_{av}$
		C_2H	17.42	(Propyne)	10.36
				(Allene)	9.69
				C_3H_3	8.34
				C_3H_2	12.50
				C_3H	13.40

Table III. Values of parameters C_i in Eq. (15) for the $H^+ + C_xH_y$ collision systems and their reduced form Eqs (8)–(10). (The r.m.s. deviation of the fits is shown in the bottom line)

	CH_4	CH_3	CH_2	CH	C_2H_6
C_1	3.901564E-1	6.854778E-1	1.118652E-1	-1.060468E+0	1.275456E+0
C_2	-6.426675E+0	-5.810741E+0	-5.216803E+0	-5.662572E+0	-5.408443E+0
C_3	-3.706893E+0	-3.622136E+0	-3.893841E+0	-4.376450E+0	-3.426843E+0
C_4	-1.999034E+0	-2.179920E+0	-2.756865E+0	-3.567226E+0	-2.298691E+0
C_5	-5.625439E-1	-7.801006E-1	-1.192043E+0	-1.433069E+0	-1.310537E+0
C_6	2.279431E-1	-2.421371E-2	-5.200059E-1	-5.789399E-1	-5.555345E-1
C_7	3.443980E-1	2.762333E-1	-1.816781E-1	-3.523295E-1	-1.044490E-1
C_8	1.566892E-1	2.288237E-1	1.129866E-2	-9.956988E-2	5.031086E-2
C_9	-5.398410E-2	6.164797E-2	-3.658702E-3	1.532751E-2	6.306925E-2
C_{10}	-1.822252E-1				-6.864191E-3
C_{11}	-1.593352E-1				
C_{12}	-8.826322E-2				
Deviation	6%	6%	5%	2%	5%

Table III. (continued)

	C_2H_5	C_2H_4	C_2H_3	C_2H_2	C_2H
C_1	1.716499E+00	8.341737E-1	8.888440E-1	2.513870E-1	-1.986507E+0
C_2	-5.230512E+00	-5.821612E+0	-5.243715E+0	-5.812705E+0	-5.720283E+0
C_3	-3.170772E+00	-3.769920E+0	-3.110835E+0	-3.338185E+0	-3.535139E+0
C_4	-2.185277E+00	-2.790407E+0	-2.531330E+0	-3.071630E+0	-4.230273E+0
C_5	-1.232087E+00	-1.480843E+0	-1.113044E+0	-1.433263E+0	-1.254502E+0
C_6	-5.036952E-01	-6.962345E-1	-3.147011E-1	-3.583544E-1	-2.056898E-1
C_7	-7.229334E-02	-2.496726E-1	-5.834419E-2	-1.456216E-1	-4.595756E-1
C_8	8.230586E-02	-8.972341E-3	2.432579E-2	-7.391778E-3	-7.842824E-2
C_9	8.365203E-02	2.066349E-2	-9.508213E-3	1.151712E-2	3.002537E-2
C_{10}	1.283200E-02				-5.626713E-2
C_{11}					6.455583E-2
Deviation	4%	4%	3%	3%	5%

Table III. (continued)

	C_3H_8	C_3H_7	C_3H_6	C_3H_5	C_3H_4
C_1	1.403347E+0	1.732713E+0	1.487291E+0	1.239651E+0	9.386948E-01
C_2	-5.455461E+0	-5.142546E+0	-5.211636E+0	-5.153170E+0	-5.123019E+00
C_3	-3.554360E+0	-3.263284E+0	-3.372781E+0	-3.302519E+0	-3.226687E+00
C_4	-2.464602E+0	-2.274484E+0	-2.304268E+0	-2.360416E+0	-2.473107E+00
C_5	-1.438525E+0	-1.321468E+0	-1.360992E+0	-1.335779E+0	-1.322435E+00
C_6	-6.514340E-1	-5.792384E-1	-6.362773E-1	-5.991178E-1	-5.319703E-01
C_7	-1.712580E-1	-1.275364E-1	-1.832337E-1	-1.796747E-1	-1.598061E-01
C_8	1.920722E-3	3.649298E-2	-2.945122E-2	-3.727936E-2	-5.410573E-02
C_9	1.586834E-2	6.265064E-2	5.310641E-3	1.001740E-2	-5.656260E-03
C_{10}	-4.835895E-2	-1.079800E-2	-8.896402E-2	-7.613230E-2	-7.050675E-02
Deviation	2%	2%	6%	8%	7%

Table III. (continued)

	C_3H_3	C_3H_2	C_3H	C_4H_{10}	Reduced $\overline{\sigma}$
C_1	6.955227E-1	-2.638408E-1	-1.152102E+0	2.083786E+0	-4.977547E-1
C_2	-4.904809E+0	-5.204029E+0	-5.658128E+0	-4.479109E+0	-5.282566E+0
C_3	-2.961972E+0	-3.135821E+0	-3.394316E+0	-2.435900E+0	-3.084821E+0
C_4	-2.610593E+0	-3.021844E+0	-3.551017E+0	-1.560149E+0	-1.686825E+0
C_5	-1.346304E+0	-1.220869E+0	-1.368680E+0	-7.565884E-1	-5.026824E-1
C_6	-5.076411E-1	-2.175365E-1	-1.457613E-1	-1.216295E-1	2.047167E-1
C_7	-2.245476E-1	-1.076868E-1	-7.089518E-2	2.540721E-1	4.754529E-1
C_8	-9.378583E-2	-9.698729E-3	-4.108061E-2	3.300761E-1	3.703372E-1
C_9	-2.851315E-2	8.886834E-3	8.174401E-3	2.530929E-1	2.414728E-1
C_{10}				9.383315E-2	
Deviation	8%	8%	7%	7%	8%

Charge transfer processes in collisions of H^+ ions with H_2, D_2, CO, CO_2 CH_4, C_2H_2, C_2H_6 and C_3H_8 molecules below 10 keV

T. Kusakabe
Department of Nuclear Engineering, Kinki University, Osaka, Japan

R.J. Buenker
Theoretische Chemie, Bergische Universitaet-GesamthochschuleWuppertal,
Wuppertal, Germany

M. Kimura
Graduate School of Science and Engineering, Yamaguchi University, Yamaguchi, Japan

Abstract

Charge transfer processes resulting from collisions of H^+ ions with H_2, D_2, CO, CO_2 CH_4, C_2H_2, C_2H_6 and C_3H_8 molecules have been investigated in the energy range of 0.2 to 4.0 keV experimentally and theoretically. The initial growth rate method was employed in the experiment for studying the dynamics and cross sections. Theoretical analysis based on a molecular-orbital expansion method for H_2, D_2, CO, CH_4 and C_2H_2 targets was also carried out. The present results for the H_2, CO and CO_2 molecules by H^+ impact are found to be in excellent accord with most of previous measurements above 1 keV, but they show some differences below this energy where our result displays a stronger energy-dependence. For CH_4, C_2H_2, C_2H_6 and C_3H_8 targets, both experimental and theoretical results indicate that if one assumes vibrationally excited molecular ions (CH_4^+, $C_2H_2^+$, $C_2H_6^+$ and $C_3H_8^+$) formed in the exit channel, then charge transfer processes sometimes become more favorable since these vibrationally excited fragments meet an accidental resonant condition. This is a clear indication of the role of vibrational excited states for charge transfer, and is an important realization for general understanding.

I. INTRODUCTION

In research on controlled thermonuclear fusion, charge transfer processes of H^+ ions in collisions with H_2 and various carbon-containing molecules at low collision energies play a key role in low temperature edge plasmas of the current fusion devices with carbon-coated or graphite-lined walls as plasma facing materials [1]. In the medical sciences, proton and other heavy-ion beams have been successfully employed for the treatment of deep-seated malignancy [2]. For an astrophysical environment, needless to say, the cosmic rays and solar wind contain a sizable amount of protons which are involved in various types of charge transfer processes, thus initiating a variety of chain chemical reactions [3].

Although many experimental investigations have been performed on the charge transfer of H^+ ions in collisions with various gas atoms and molecules, cross section data are still fragmentary and are not consistent with each other. This is particularly so for hydrocarbon molecules, and more systematic determination of charge transfer cross sections is urgently required. Theoretical approaches applicable to slow ion-molecule collisions are also scarce because of the difficulty of treating the intrinsic multicenter nature of molecules accurately, although some small-scale exploratory studies have been carried out [4 - 6].

For these reasons, we have undertaken a joint experimental and theoretical investigation and determined charge transfer cross sections of H^+ ions colliding with the H_2, D_2, CO, CO_2

CH_4, C_2H_2, C_2H_6, and C_3H_8 molecules in the energy range of 0.2 to 4.0 keV[7, 8]. The specific processes we are concerned with are, with their asymptotic energy defects:

$H^+ + H_2, D_2 (v_I=0) \rightarrow H(1s, {}^2S) + H_2^+, D_2^+ (v_f) - 1.827$ [eV] (1)

$H^+ + CO (v_i=0) \rightarrow H(1s, {}^2S) + CO^+ (v_f) - 0.4155$ [eV] (2)

$H^+ + CO_2 (v_i=0) \rightarrow H(1s, {}^2S) + CO_2^+ (v_f) - 0.1746$ [eV] (3)

$H^+ + CH_4 (v_i=0) \rightarrow H(1s, {}^2S) + CH_4^+ (v_f) + 0.618$ [eV], (4)

$H^+ + C_2H_2 (v_i=0) \rightarrow H(1s, {}^2S) + C_2H_2^+ (v_f) + 2.198$ [eV], (5)

$H^+ + C_2H_6 (v_i=0) \rightarrow H(1s, {}^2S) + C_2H_6^+ (v_f) + 2.078$ [eV], (6)

$H^+ + C_3H_8 (v_i=0) \rightarrow H(1s, {}^2S) + C_3H_8^+ (v_f) + 2.648$ [eV], (7)

where v_i and v_f are the quantum numbers of the initial and final vibrational states of target molecules, respectively. All collision processes which involve hydrocarbon molecules Eqs. (4) - (7) are exothermic with an appreciable energy difference, although it is relatively small in the case of CH_4. Vibrationally excited molecules in the initial channel increase the exothermicity, and hence, are expected to reduce the charge transfer cross section. On the other hand, vibrational excited states in the product channel reduce the exothermicity, which may lead to the larger cross section. Hence, charge transfer to the vibrationally excited molecule needs to be considered.

In the present theory, the molecular - orbital expansion method is applied to the H^+ - H_2, D_2, CO, CH_4 and C_2H_2 collisions. The lowest vibrationally excited level for CO, CH_4-C_3H_8 molecules is in the neighborhood of 0.07 eV due to the C-O and C-H bending modes, and at room temperature, such vibrationally excited species amount to more than 10 % of the total molecules. Hence, it is also important to assess the contribution to charge transfer from vibrationally excited molecules since a small amount of the contamination from them is expected to significantly increase the charge transfer cross section, in addition to the contribution from vibrationally excited final molecular-ion formation described above.

II. EXPERIMENTAL SETUP

A proton beam produced by 30 eV electron impact on H_2 molecules is directed into an electron-impact ion source, was mass-analyzed with a Wien filter and introduced into a 40 mm long collision cell with a 0.5 mm diameter entrance and a 3.5 mm diameter exit apertures. The target gases of high purity (> 99.9 %) were fed into the cell and the gas pressure was measured with a sensitive Pirani gauge [9] which was calibrated with a MKS-Baratron capacitance manometer. The front and main chambers were evacuated down to the base pressure less than about 6ü~10^{-6} Pa by a 500 l/s turbo-molecular pump and a 6" cryo-pump. The ions emerging from the cell after collisions were charge-separated with electrostatic parallel plates and sent into a position-sensitive detector consisting of a microchannel plate and a resistive anode (MCP-PSD). The output signals from both ends of its anode were converted into position information in an analogue divider [10, 11] and recorded on a pulse height analyzer as the charge distribution of ions after collisions. Peak areas corresponding to the singly charged primary ions and energetic neutral particle products were integrated. It is safe to conclude that relative detection efficiencies of MCP-PSD were the same for both the singly charged ions and neutral particles as the front end of the MCP was grounded. After subtracting dark current noises of the MCP-PSD, the fractions of singly charged ions and of neutrals, F_1 and F_0, were determined as a function of the target gas thickness. The electron capture cross sections were derived based upon the growth rate method by fitting the observed fractions F_0 to a quadratic function of the target gas thickness.

The statistical uncertainties of the cross sections are a few percent for most of the present work. Systematic uncertainties due to the determination of the target thickness, the

temperature of target gases and others are estimated to be from 10.6 % to 19.7 % for determining the absolute cross sections. Total experimental uncertainties of the absolute cross sections are given as the quadratic sum of these uncertainties.

III. THEORETICAL MODEL

A. Molecular States

Two sets of calculations for molecular electronic states were carried out. **Configuration interaction (CI) method**: The adiabatic potential energies for H_3^+ are obtained by a CI method modified by an inclusion of a pseudopotential to treat H_2 ($1s^2$: $X\ ^1\Sigma_g$) as an elongated atom, thus replacing the two-electron system by an explicit one-electron problem [4]. The pseudopotential used is of Gaussian type. Slater-type orbitals are employed as basis functions and linear combinations of Slater determinants are used for constructing molecular wave functions. The errors in the present asymptotic energies of the adiabatic potentials are better than 0.2 % compared with those of experiment [12]. The nonadiabatic coupling matrix elements are evaluated numerically by using the wave functions obtained above.

Multireference single- and double-excitation (MRD-CI) CI method: For CO, CH_4 and C_2H_2, adiabatic potentials are obtained by the MRD-CI method [13], with configuration selection and energy extrapolation using the Table CI algorithm [14]. A small selection threshold of 0.32×10^{-6} hartree has been used in the present treatment. The radial coupling matrix elements are obtained using calculated MRD-CI wave functions by a finite-difference method [15] with an increment of 0.0002 a_0.

B. Scattering dynamics

Semiclassical approach [16]**:** A semiclassical MO expansion method with a straight-line trajectory of the incident ion was employed to study the collision dynamics above a few hundred eV/u. In this approach, the relative motion of heavy particles is treated classically, while electronic motion is treated quantum mechanically. The total scattering wave function was expanded in terms of products of molecular electronic state and atomic-type electron translation factors (ETFs), whereby the inclusion of the ETF satisfies the correct scattering boundary condition. A set of first-order coupled equations is thus obtained by substituting the total wave function into the time-dependent Schroedinger equation. Nonadiabatic couplings drive transitions between molecular states. By solving the coupled equations numerically, we obtain the scattering amplitudes for transitions and cross sections.

States included for the dynamical calculation are: the initial, charge transfer, and target excitation channels if this channel lies close to the charge-transfer one. For some cases, charge-transfer and excitation channels are also included. Vibrational levels for final products are considered for both systems by adjusting the ionization potential for each product.

Quantum mechanical approach [16]: Collision dynamics at lower energies are studied on the basis of the fully quantum mechanical formulation of a molecular-orbital expansion method in which dynamical transitions are also driven by nonadiabatic couplings. The total scattering wave function is described as an expansion in products of electronic and nuclear wave functions and the ETF. Substitution of the total scattering wave function into the stationary Schroedinger equation yields coupled, second-order differential equations for the nuclear wave function. It is computationally convenient to solve the coupled equations in a diabatic representation. The transformation from the adiabatic to the diabatic representation can be readily achieved through a unitary transformation matrix. The coupled equations are then solved numerically to obtain the scattering matrix for each partial wave, and the standard procedure can yield the total cross section from the scattering matrix. In the present

calculation, we employed two- and three-state close-coupling treatments with MOs corresponding to the initial and charge transfer channels.

IV. RESULTS AND DISCUSSIONS

A. Cross sections for H_2 and D_2

In Fig. 1 the present cross sections of the charge transfer of H^+ ions in collisions with hydrogen H_2 and D_2 isotopes are compared with those previously measured for different isotope combinations [17 - 22]. In this collision system of relatively large endothermicity, the charge transfer cross sections increase monotonically with collision energy. The present data are found to be in good agreement with the recommended data of Barnett [17], except for that at 4 keV, which is somewhat too small. The calculation using the MO method with inclusion of vibrational excited initial and final states in the range of $v_i = 0 - 3$ and $v_f = 1 - 10$ are found to be in excellent agreement with the present measurement, except for those at energies below 0.3 keV.

Since the difference of the electron binding energy of an electron between H_2 and D_2 is merely 41 meV, there is, within their experimental uncertainties, practically no difference in the present cross sections between $H^+ + H_2$ and $H^+ + D_2$ collisions at energies above 0.45 keV. However it is intriguing that the cross sections for $H^+ + D_2$ collisions at 0.2 keV are found to be about 40 % smaller than those for $H^+ + H_2$ collisions. This difference is outside the uncertainties in the present experiment, and therefore, we regard it as a real ***isotope effect***. The magnitudes of the data for $D^+ + D_2$ collisions measured by Cramer and Marcus [18] are about half of those for $H^+ + H_2$ collisions by Cramer [19]. Recently Elizaga et al. [23] has theoretically shown the possible significant isotope effect in $H^+ + H_2$ and $H^+ + D_2$ collisions, especially at low energies. Their results are consistent to our measurements.

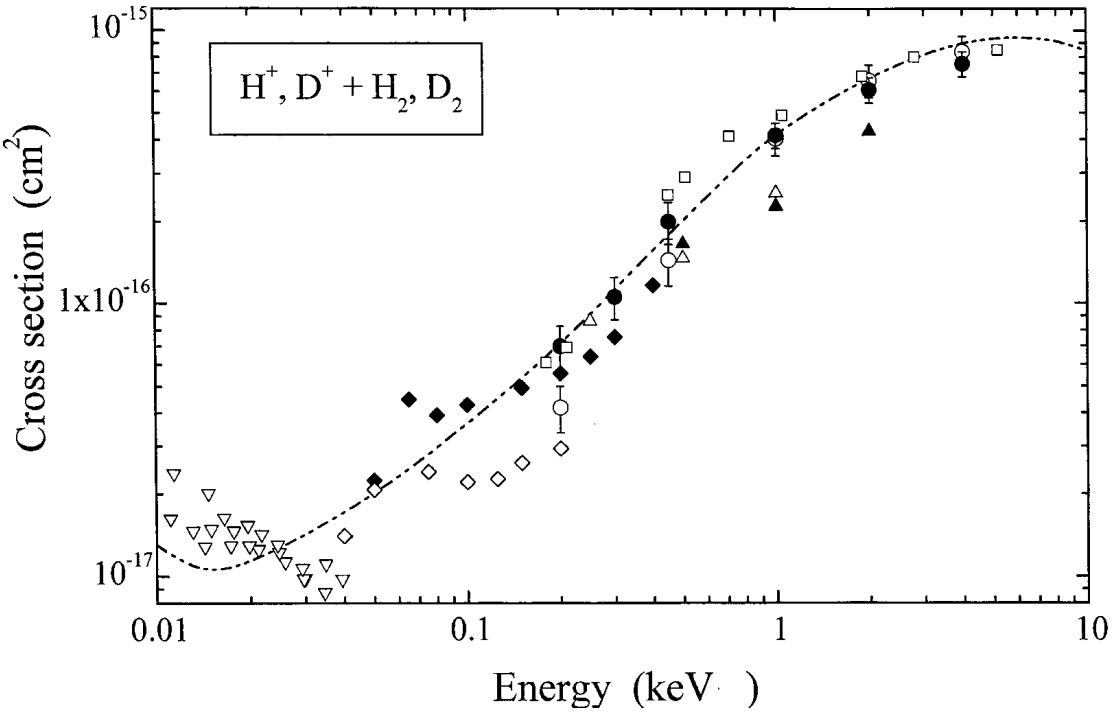

FIG. 1. Comparison of the charge-transfer cross sections for hydrogen ion and molecular isotopes collisions. ●, the present data ($H^+ + H_2$); ○, the present data ($H^+ + D_2$); —●—, the recommended value of Barnett [17]; ◇, Cramer and Marcus ($D^+ + D_2$) [18]; ◆, Cramer ($H^+ + H_2$) [19]; ▲, Abbe and Adloff ($H^+ + H_2$) [20]; Δ, Abbe and Adloff ($D^+ + H_2$) [20]; , Berkner et al. ($D^+ + H_2$) [21]; ∇, Maier II ($H^+ + D_2$) [22].

B. Cross sections for CO and CO_2

CO: The present cross sections of the charge transfer from CO molecules are shown in Fig. 2, together with those from earlier publications [21, 24 - 31]. As the collision energy increases, the present charge transfer cross sections decrease very slowly up to 1 keV and then level off up to 4 keV and finally are smoothly connected with the data at high energies from Chambers [26], McNeal [28], and Gao et al. [31]. There appears to be a shoulder in the cross section around 2 keV, and this shoulder becomes more pronounced for CO_2 as discussed below. The agreement with other experimental data, except for those of Gilbody and Hasted [24], is found to be generally good.

The present calculations for CO molecules in the vibrational ground state show excellent agreement with the present measurements over the entire energy region. If we consider the vibrationally excited $v_i = 1$ molecule in the initial channel, the charge transfer cross section is found to increase by 20 %, thus suggesting the importance of the ***temperature effect***. As the temperature increases above room-temperature, the number of the vibrationally excited molecules is not negligible, and hence their effect should be properly accounted for in the calculation. Below 0.2 keV, the theory indicates a decreasing trend, and this appears to tie up well with those measurements by Gilbody and Hasted [24], and Gustafsson and Lindholm [25] at lower energies. The present theory also suggests a strong molecular ***orientation (steric) effect*** for charge transfer. It is important to examine both the steric effect and temperature effect for understanding charge transfer processes. The calculated values based on a simple analytical formula proposed by Olson [32] with the assumption that the target molecules are in the vibrational ground state ($v_f = 0$) after collisions are larger in the entire energy region studied, but lie near the present data from 0.2 keV to 10 keV. However, they overestimate the values below 0.3 keV and above 20 keV rather significantly.

CO_2: Figure 3 shows the present cross sections for CO_2 molecules, together with earlier measurements [27 - 31, 33 - 34]. They show some interesting collision energy dependence: As the collision energy increases, the present cross sections decrease relatively steeply up to 0.45 keV and then the variation becomes much gentler beyond this energy. Finally the present results are connected smoothly to the data at high energies from McNeal [28], Gao et al. [31], and Greenwood et al. [33]. On the other hand, the data of Koopman [34] at low energies below 2 keV show a monotonic dependence on the collision energy. The origin of the shoulder around 0.3 is highly likely to be that a few different channels contribute to the charge transfer which show a different energy dependence, hence causing some structures when they are summed. Or as for another interpretation, the lowest vibrational excitation for this molecule is the (010) bending mode with the threshold of 0.08 eV. At room temperature, the (010) vibrationally excited CO_2 molecule constitutes about 10 % of the total number, a non-negligible amount. If the molecule is in a vibrationally excited state, this reduces the energy defect so as to increase the near-resonant condition, hence making charge transfer reactions more favorable. This might be the cause of the increasing trend at lower energies. We have also found that there is a similar shoulder around 2 keV in the CO molecule. Because of the smallest energy defect among the three molecules so far, this $H^+ + CO_2$ collision system satisfies the near-resonant condition, and hence, the cross section does not show any hint of the decrease even as the collision energy reaches around 0.2 keV. It should, however, eventually do so at much lower energy because of the endothermic reaction. The calculations based upon the Olson formula for the vibrational ground state are larger than the present observed cross sections, but predict a near-resonant feature for this collision system down to 0.1 keV because of the small energy defect as described. Johnson and Parker [35] have dealt with this collision system in more detail by taking into account the orientation of CO_2 molecules explicitly, and their results show a similar magnitude and energy dependence as

those from the Olson formula. Both calculations simply show a monotonic decrease of the cross sections, and fail to reproduce the structures observed in the present experiment.

C. Cross sections for hydrocarbons (CH_4, C_2H_2, C_2H_6 and C_3H_8)

CH_4: The present cross sections for CH_4 molecules are shown in Fig. 4 together with those previously published [21, 26, 28 - 31, 34, 36 - 37]. Though there are small deviations among the measured data, the general feature seems to be in reasonable accord with each other. As the collision energy increases, the charge transfer cross-sections decrease monotonically, so the present data are in harmony with others. The set of the data by Berkner et al. [21], Eliot [37], and Gao et al. [31] gives slightly larger cross sections, while that of McNeal [28], and Chambers [26] gives somewhat smaller values, and in fact the present results lie in between these two sets of results. The data of Koopman [34] are found to be too large compared to the present data and others. The energy difference of H^+ - CH_4 collisions is 0.618 eV, which is the smallest among all hydrocarbon systems studied. The present theoretical results were obtained by including vibrationally excited states in the product molecular ions, while the energy difference was adjusted in order to match vibrationally excited states of the target molecular ion in the exit channel. The present results show good agreement with most of the experimental data, except for the low energy region. The results indicate a broad peak around 0.3 keV, and on both sides of this energy they gradually decrease. Note that the present result, which includes vibrational excitation in the product molecular ion, is found to be larger by 30 % than those without vibrational excitation, and shows a slightly different energy dependence.

C_2H_2: Figure 5 shows the present cross sections for charge transfer from C_2H_2 molecules. The present cross sections increase slowly as the incident energy increases and level off at around 3 - 4 keV.

We have carried out the calculation by taking the correct energy difference for the vibrationally excited final states (v_f = 1 - 8) of the product molecular ion into account. This change of vibrational states of the product causes the exothermicity to decrease from 2.13 eV to 1.7 eV. The effect of vibrationally excited states is found to be more significant for the H^+ + C_2H_2 system than the H^+ + CH_4 system. The theoretical results, summed over all vibrationally excited final products, are found to be close to the measured values. The vibrational excited state of the target molecular ions of this system is more favorable energetically for the resonant conditions, hence increasing the cross sections rather drastically. As a test for the temperature effect (i.e., the effect of vibrationally excited states to charge transfer), we have performed the calculation for charge transfer from an initial vibrationally excited molecule. As described above, this apparently increases the exothermicity, and hence, the calculation suggests a reduction in the effectiveness of charge transfer in the entire energy range. A vibrationally excited state either in the initial molecule, or the product molecular ion, or in both, is extremely important for correctly assessing the dynamics for charge transfer processes in molecular targets, and hence it is essential for examining the temperature effect more closely. These predictions are very suggestive regarding to the importance of the temperature effect for charge transfer involving molecular targets.

C_2H_6 and C_3H_8: Figures 6 and 7 show the present cross sections for charge transfer in H^+ + C_2H_6 and H^+ + C_3H_8 collisions, respectively, together with those previously published by Eliot [37] and Jones et al. [30]. The present cross-sections decrease almost monotonically for both target molecules as the collision energy increases, a feature similar to that for the CH_4 target. The observed collision energy dependence of the cross sections suggest that the accidental quasi-resonant charge transfer reaction channels involving vibrational excitation of the product target molecular ions play a dominant role. The cross sections calculated by using the

Olson formula [32] for the vibrational ground-to-ground state charge transfer process are found to be too small compared with the experimental results, while those obtained by including the vibrationally excited state of the product molecular ions are drastically improved as similarly as seen for C_2H_2. Although the asymptotic energy differences for C_2H_6 and C_3H_8 are close to that of C_2H_2, the energy dependence of the charge transfer cross section for C_2H_6 and C_3H_8 is different from that for C_2H_2 as seen in Figs 5 - 7. This characteristic seems to arise from the difference in vibrational energies in the two cases.

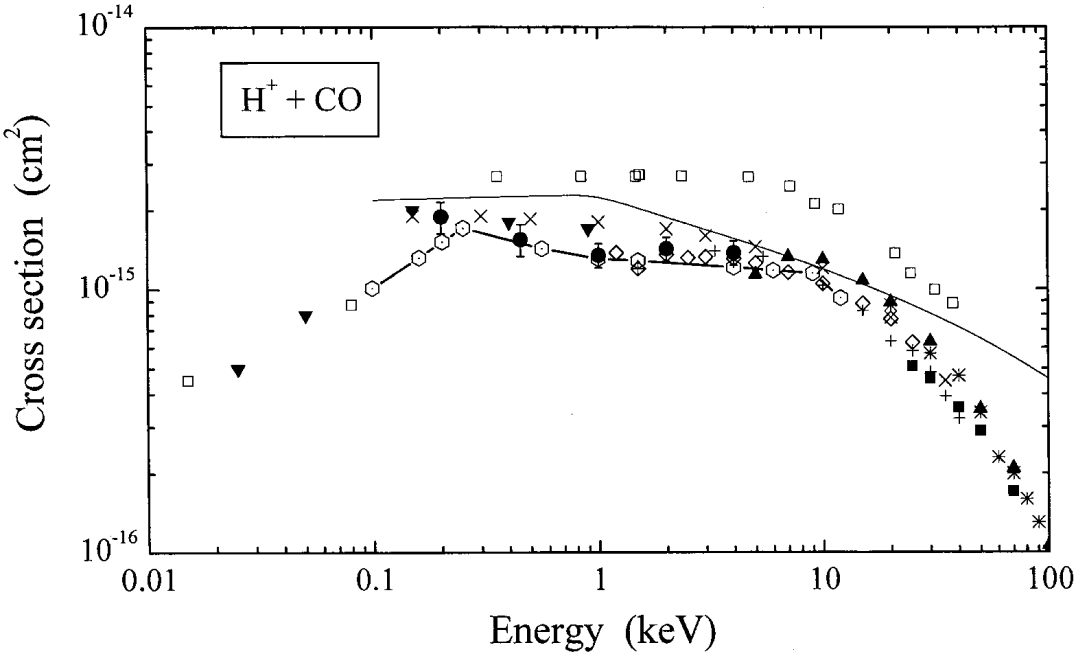

Fig. 2 Charge-transfer cross sections for H^+ ions in collisions with CO molecules. ●, the present data; , Gilbody and Hasted [23]; ▼, Gustafsson and Lindholm [24]; +, Chambers [25]; ■, Desequelles et al. [26]; X, Berkner et al. [20]; ◇, McNeal [27]; ▲, Rudd et al. [28]; ※, Jones et al. [29]; ◇, Gao et al.[30]. Theory; —⊙—, the present calculations based on the MO method; —, Olson formula [31].

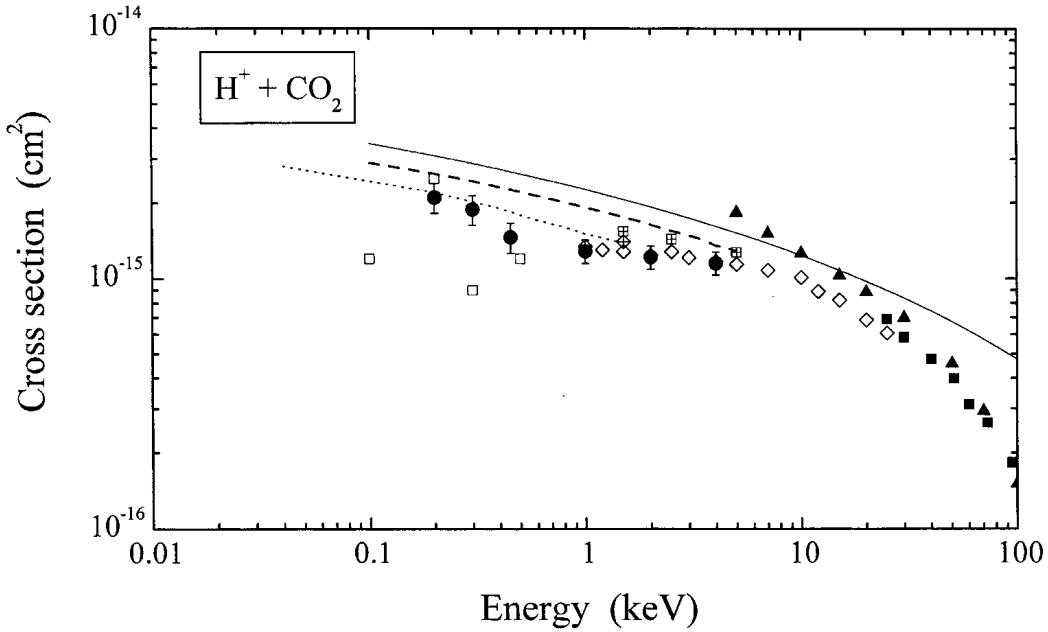

FIG. 3 Charge-transfer cross sections for H^+ ions in collisions with CO_2 molecules. ●, the present data; ■, Desequelles et al. [26]; , Koopman [33]; ◇,McNeal [28]; ▲, Rudd et al. [29]; ◇, Gao et al. [31]; □, Greenwood et al. [33]. Theory; —, Olson formula [32]; – – , Johnson and Parker [35].

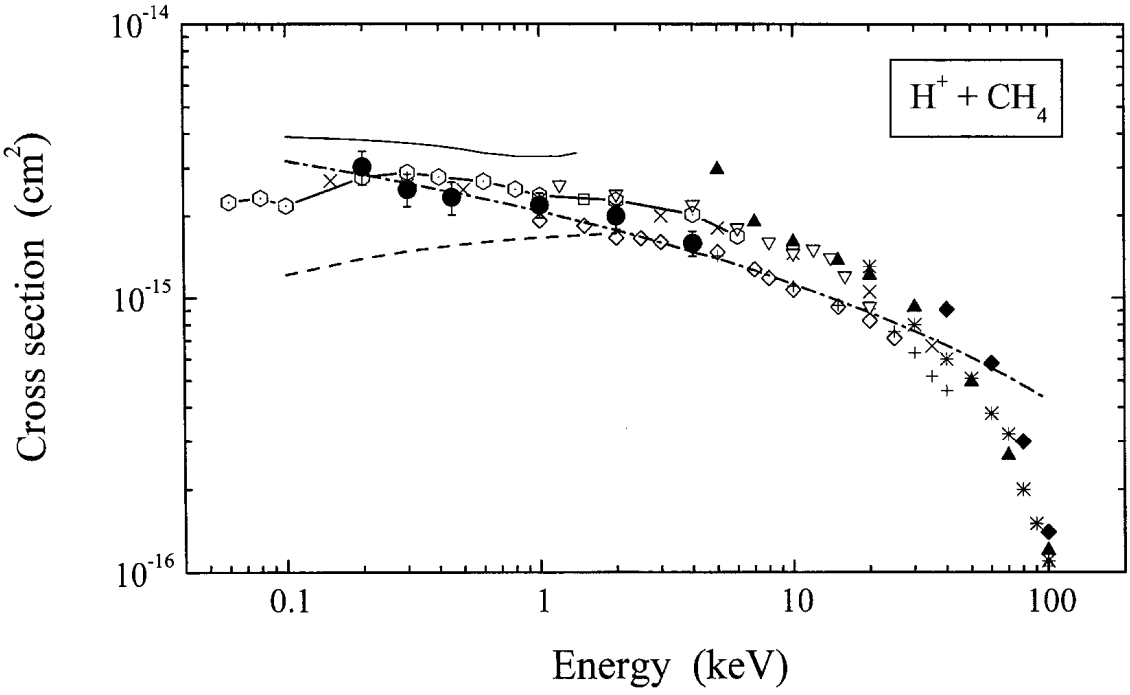

FIG. 4. Charge-transfer cross sections for H^+ ions in collisions with CH_4 molecules. ●, Present data; +, Chambers [26]; –, Koopman [34]; ◆, Collins and Kebarle [36]; ×, Berkner, et. al. [21]; ◇, McNeal [28]; ▽, Eliot [37]; ▲, Rudd et al. [29]; *, Jones et al. [30]; , Gao et al. [31]. The hexagonal symbols with solid lines are the present calculations based upon the molecular expansion method. The dot-chain and dashed curves correspond to the calculations by the Olson formula [32] with and without the vibrational excitation of the product molecular-ion, respectively.

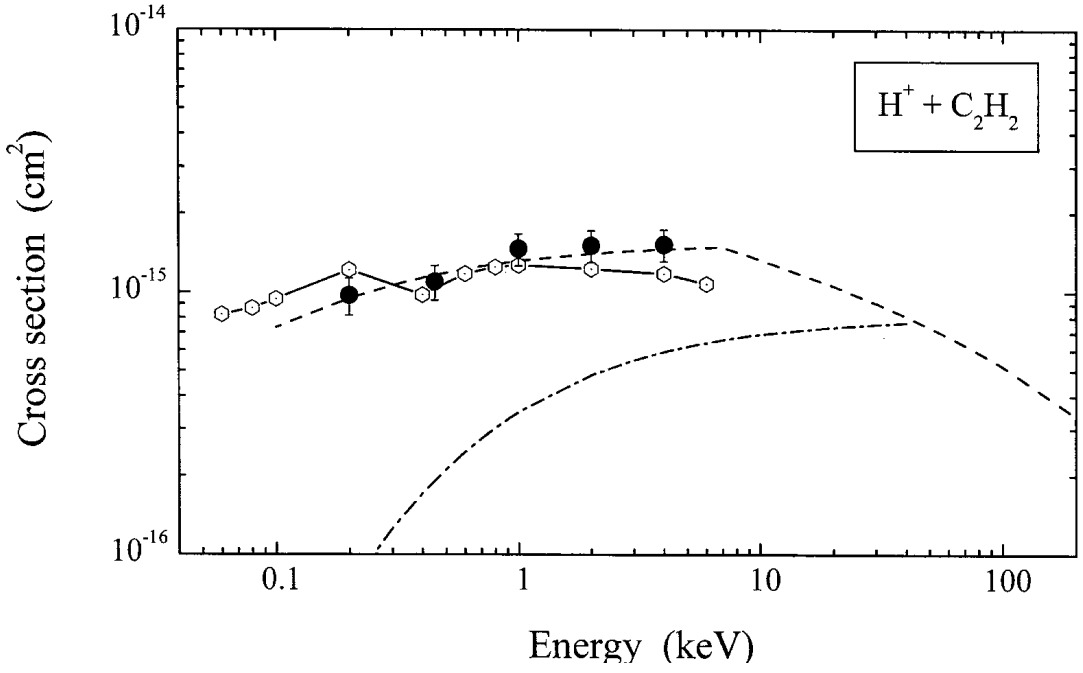

FIG. 5. Charge-transfer cross sections for H^+ ions in collisions with C_2H_2 molecules. ●, Present data. The hexagonal symbols with solid lines are the present calculations based upon the molecular expansion method. The dot-chain and dashed curves correspond to the calculations by the Olson formula [32] with and without the vibrational excitation of the product molecular ion, respectively.

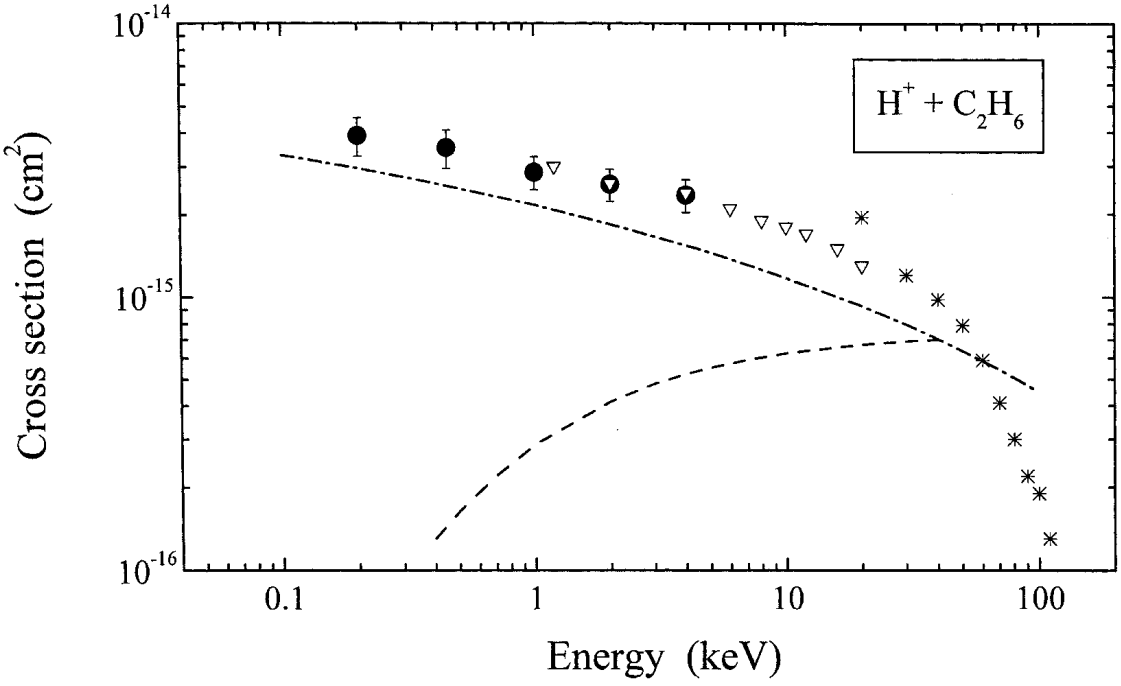

FIG. 6. Charge-transfer cross sections for H^+ ions in collisions with C_2H_6 molecules. ●, Present data; ▽, Eliot [37]; *, Jones et al. [30]. The dot-chain and dashed curves correspond to the calculations by the Olson formula [32] with and without the vibrational excitation of the product molecular-ion, respectively.

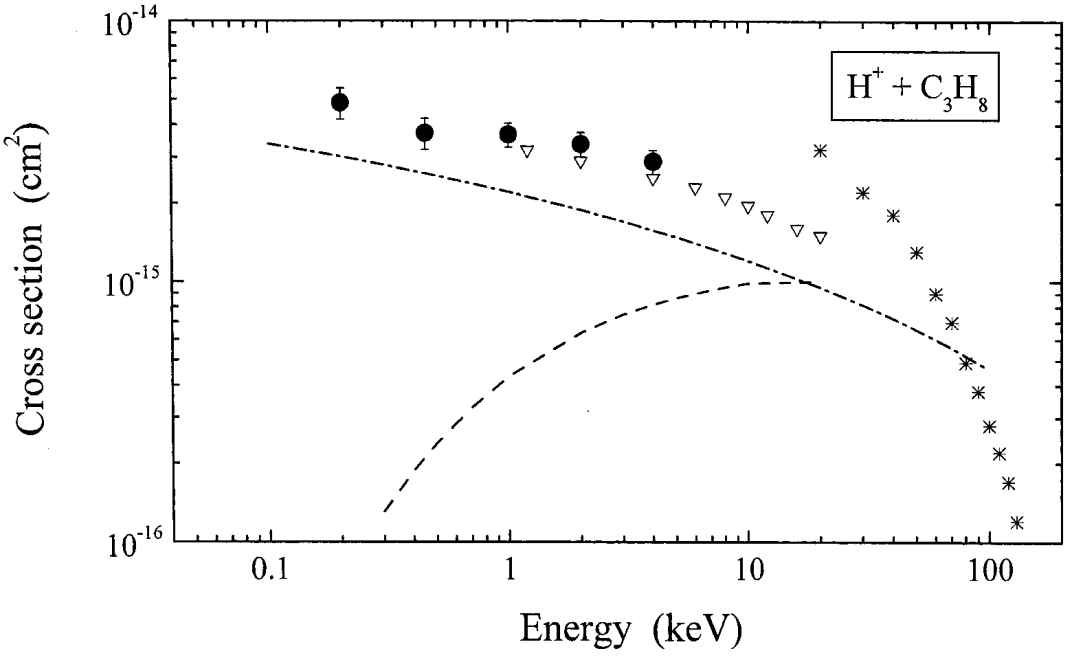

FIG. 7. Charge-transfer cross sections for H^+ ions in collisions with C_3H_8 molecules. ●, Present data; ▽, Eliot [37]; *, Jones et al. [30]. The dot-chain and dashed curves correspond to the calculations by the Olson formula [32] with and without the vibrational excitation of the product molecular-ion, respectively.

V. CONCLUDING REMARKS

We have investigated charge transfer processes from H_2, D_2, CO, CO_2, CH_4, C_2H_2, C_2H_6 and C_3H_8 in collisions with H^+ ions in the energy region from 0.2 keV to 4 keV. We believe that the present measurements are accurate to within 10 - 20 % for all systems and in the entire energy region, hence providing benchmark data which can be used for the normalization of relative data and other applications. We have observed strong evidence that the temperature (vibrational state) of the target molecules significantly affects the charge transfer dynamics and cross sections in $H^+ + CO$, and particularly in $H^+ + C_mH_n$ collisions. The observed cross sections of the charge transfer processes show a gradual increase as the collision energy decreases for all the present collision systems [$H^+ + CH_4$, C_2H_6 and C_3H_8] investigated, except for C_2H_2, in the collision energy range between 0.2 and 20 keV. This feature can be understood arising from charge transfer plus the effect of vibrationally excited product molecular ions, and in fact is confirmed by theoretical calculations based on the MO method by taking a number of the vibrationally excited states of product molecular ions into account. In this way, vibrationally excited product states enforce the ìaccidentalî resonance condition in the charge transfer processes. Even for C_2H_2 targets, where the cross sections increase only slightly as the collision energy increases, it is expected that vibrationally excited states of product $C_2H_2^+$ ions also play a crucial role for charge transfer. Therefore it is extremely interesting and important to study inelastic processes from and to vibrationally excited species to examine the temperature effect more systematically and comprehensively, including the molecules studied here. In addition, it is interesting to study the steric (molecular orientation) effect on charge transfer at intermediate collision energy, which some theoretical studies have suggested that it is in fact very pronounced and hence, might be observable. It should also be noted that the observed cross sections at the present collision energies tend to become large as the ionization energy of the target molecules becomes small, and there seems to be a systematic relationship with the number of electrons or atoms in the target molecules.

ACKNOWLEDGEMENT

This work was performed as a collaborative research of the National Institute for Fusion Science, Japan. TK, and MK were supported in part by a Grant-in-Aid for Science Research (C) from the Ministry of Education, Science, Technology, Sports and Culture in Japan. RJB was supported by Deutsche Forschungsgemeinschaft in the form of a Forschergruppe and Grant No. Bu450/7

REFERENCES

[1] R.K. Janev, in ***Atomic and Molecular Processes in Fusion Edge Plasmas***, edited by R. K. Janev, (Plenum, New York, 1995), pp.1-13.

[2] *Proceedings of NIRS International Seminar on the Application of Heavy Ion Accelerator to Radiation Therapy of Cancer*, NIRS-M-103/HIMAC-008 (1994).

[3] E.F. van Dishoeck, in ***The Molecular Astrophysics of Stars and Galaxies***, T.W. Hartquist and D.A. Williams, eds (Oxford Sci. Pub.,1998).

[4] [4] M. Kimura, Phys. Rev. A **32**, 802 (1985).

[5] [5] M. Kimura, Y. Li, G. Hirsch, and R. J. Buenker, Phys. Rev. A **52**, 1196 (1995).

[6] [6] M. Kimura, Y. Li, G. Hirsch, and R. J. Buenker, Phys. Rev. A **54**, 5019 (1996).

[7] [7] T. Kusakabe, K. Asahina, J. P. Gu, G. Hirsch, R. J. Buenker, M. Kimura, H. Tawara, and Y. Nakai, Phys. Rev. A62, 062714 (2000).

[8] [8] T. Kusakabe, K. Asahina, J. P. Gu, G. Hirsch, R. J. Buenker, M. Kimura, H. Tawara, and Y. Nakai, Phys. Rev. A62, 062715 (2000).
[9] [9] T. Kusakabe, T. Horiuchi, Y. Nakai, and H. Tawara, Jpn. J. Appl. Phys., Part 1 **37**, 369 (1998).
[10] [10] H. Hanaki, N. Nagai, T. Kusakabe, T. Horiuchi, and M. Sakisaka, Jpn. J. Appl. Phys. **22**, 748 (1983).
[11] [11] T. Kusakabe, M. Ohmiya, and K. Wada, Jpn. J. Appl. Phys. **31**, 4093 (1993).
[12] [12] C. E. Moore, ***Atomic energy levels***, NBS (US) Cirl. No. 467, Vol. **1** (US GPO, Washington, D. C., 1949).
[13] [13] R. J. Buenker and S. D. Peyerimhoff, Theor. Chim. Acta **35**, 33 (1974); **39**, 217 (1975); R. J. Buenker, Int. J. Quantum Chem. **29**, 435 (1986); S. Krebs and R. J. Buenker, J. Chem Phys. **103**, 5613 (1995).
[14] [14] R. J. Buenker, in Proceedings of the Workshop on Quantum Chemistry and Molecular Physics, edited by P. G. Burton (University Press, Wollongong, 1980) Vol.**101**, p. 351 ; in ***Studies in Physical and Theoretical Chemistry, Current Aspects of Quantum Chemistry***, edited by R. Carbo (Elsevier, Amsterdam, 1981), Vol. **21**, p. 17; R. J. Buenker and R. A. Phillips, J. Mol. Struct.: THEOCHEM **123**, 291 (1985).
[15] [15] G. Hirsch, P. J. Bruna, R. J. Buenker and S. D. Peyerimhoff, Chem. Phys. **45**, 335 1980).
[16] [16] M. Kimura, and N. F. Lane, in ***Advances for Atomic, Molecular and Optical Physics***, edited by D. R. Bates and B. Bederson (Academic, New York, 1989), Vol. **26**, p.76.
[17] [17] C. F. Barnett, Oak Ridge National Laboratory Report ORNL-6086, (1990).
[18] [18] W. H. Cramer and A. B. Marcus, J. Chem. Phys. **32**, 186 (1960).
[19] [19] W. H. Cramer, J. Chem. Phys., **35**, 836 (1961).
[20] [20] J. C. Abbe and J. P. Adloff, Bull. Soc. Chim. Fr. **6**, 1212 (1964).
[21] [21] K. H. Berkner, R. V. Pyle, and J. W. Stearns, Nucl. Fusion **10**, 145 (1970).
[22] [22] W. B. Maier II, J. Chem. Phys. **54**, 2732 (1971).
[23] [23] D. Elizaga, L. F. Erra, J. D. Gorfinkiel, L. Mendez, A. Macias, A. Riera, and A. Rojas, J. Phys. B**33**, 2037 (2000).
[24] [24] H. B. Gilbody and J. B. Hasted, Proc. Roy. Soc. London, Ser. A **238**, 334 (1956).
[25] [25] E. Gustafsson and E. Lindholm, Arkiv. Fysik **18**, 219 (1960).
[26] [26] E. S. Chambers, UCRL-14214 (1965)
[27] [27] J. Desequelles, G. D. Cao, and M. Dufay, C. R. Acad. Sci. Ser. B **262**, 1329 (1976).
[28] [28] R. J. McNeal, J. Chem. Phys. **53**, 4308 (1970).
[29] [29] M. E. Rudd, R. D. Dubois, L. H. Toburen, C. A. Ratcliffe, T. V. Goffe, Phys. Rev. A **28**, 3244 (1983).
[30] [30] M. L. Jones, B. M. Doughty, T. R. Dillingham and T. A. Jones, Nucl. Instr. & Meth., B**10/11**, 142 (1985).
[31] R. S. Gao, L. K. Johnson, C. L. Hakes, K. A. Smith and R. F. Stebbings, Phys. Rev. A **41**, 5929 (1990).
[32] R. E. Olson, F. T. Smith, and E. Bauer, Appl. Opt. **10**, 1848 (1971); R. E. Olson, Phys. Rev. A **6**, 1822 (1972).
[33] J. B. Greenwood, A. Chutjian and S. J. Smith, Astrophys. J., in press (1999).
[34] D. W. Koopman, J. Chem. Phys. **49**, 5203 (1968).
[35] C. A. F. Johnson and J. E. Parker, Chem. Phys. **111**, 307 (1987).
[36] J. G. Collins and P. Kebarle, J. Chem. Phys. **46**, 1082 (1967).
[37] M. Eliot, J. de Phys. **38**, 21 (1977).
[38] M. A. Coplan and K. W. Ogilvie, J. Chem. Phys. **52**, 4154 (1970).

Ion-molecule reactions in hydrogen systems and charge transfer of multiply charged ions with atoms and molecules in the energy range of 0.5 ~ 2000 eV per ion charge

K. Okuno
Department of Physics, Tokyo Metropolitan University, Hachioji-shi, Tokyo, Japan

Abstract: Ion-molecule reactions in hydrogen systems and charge transfer of multiply charged ions with atoms and molecules have been studied systematically by using the apparatus installed with an octa-pole beam guide (OPIG). In this paper, cross sections of the following collision systems are presented in the energy range of 0.5 ~ 2000 eV per ion charge:

1) Ion-molecule reactions in hydrogen systems;
2) Charge transfer of low-charged inert gas ions with inert gas atoms and atmosphere molecules;
3) Charge transfer of multiply charged ions with helium atoms and hydrogen molecules.

Ion-molecular reactions in hydrogen systems, where many reaction channels compete, have been discriminated by using isotope species. Cross sections of such reactions are essentially important for diagnostics of a fusion plasma and an astronomical plasma. In the study for the group 2), low-charged inert gas ions have been produced by a conventional electron impact type (Nier type) ion source and their charge transfer cross sections have strongly depended on a fraction of low-lying metastable ions in the projectile beam used. On the other hand, a small type of electron beam ion source (Mini-EBIS) has been used in the study for the group 3). The ion beams extracted from the Mini-EBIS have been not contaminated with metastable ions except for C^{2+} and O^{2+} beams. The systematic presentation of cross sections enables us to understand general trends and characteristic features in the low energy region, concerning the collision energy dependence, the charge state dependence, the target species dependence and the contribution of transfer ionization in collisions of multiply charged ions with helium atom and hydrogen molecule.

STRUCTURE

4.1. Part A: Ion-molecular reactions in hydrogen systems.

Table 1. List of hydrogen systems presented in the Part A.

No.	projectile	Targets	No.	projectile	targets
A1	$^{1}H^{+}$	H_2, D_2	A4	$^{2}D_2^{+}$	H_2, D_2
A2	$^{2}D^{+}$	H_2	A5	$^{1}H_3^{+}$	H_2
A3	$^{1}H_2^{+}$	H_2, D_2	A6	$^{2}D_3^{+}$	H_2, D_2

4.2. Part B: Charge transfer of low-charged rare-gas ions produced by a Nier type ion source.

Table 2. List of collision systems presented in the Part B.

No.	projectile	Targets	No.	projectile	targets
B1	$^{20}Ne^{2+}$	He, H_2, N_2	B4	$^{84}Kr^{2+}$	He, Ne, Kr
B2	$^{40}Ar^{2+}$	He, Ne, Ar, Kr	B5	$^{86}Kr^{3+}$	Kr
B3	$^{40}Ar^{3+}$	He, Ne, Ar, Kr			

4.3. Part C: Charge transfer of multiply charged ions produced by a small type electron beam ion source (Mini-EBIS).

Table 3. List of collision systems presented in the Part C.

No.	projectile	Targets	No.	projectile	Targets
C1	$^{3}He^{2+}$	He, H_2	C13	$^{16}O^{3+}$	He, H_2
C2	$^{13}C^{2+}$	He, H_2	C14	$^{18}O^{4+}$	He, H_2
C3	$^{13}C^{3+}$	He, H_2	C15	$^{16}O^{5+}$	He, H_2
C4	$^{12}C^{4+}$	He, H_2	C16	$^{16}O^{6+}$	He, H_2
C5	$^{12}C^{5+}$	He, H_2	C17	$^{40}Ar^{6+}$	He, H_2
C6	$^{13}C^{6+}$	He, H_2	C18	$^{40}Ar^{7+}$	He, H_2
C7	$^{14}N^{2+}$	He, H_2	C19	$^{40}Ar^{8+}$	He, H_2
C8	$^{14}N^{3+}$	He, H_2	C20	$^{40}Ar^{9+}$	He, H_2
C9	$^{14}N^{4+}$	He, H_2	C21	$^{40}Ar^{11+}$	He, H_2
C10	$^{14}N^{5+}$	He, H_2	C22	$^{127}I^{24+}$	He
C11	$^{14}N^{6+}$	He, H_2	C23	$^{127}I^{25+}$	He
C12	$^{16}O^{2+}$	He, H_2	C24	$^{127}I^{26+}$	He

1. Introduction

In the last two decades the advance of ion source devices has contributed to studies on charge transfer of highly charged ions in collision with atoms and molecules. Cross sections for such reactions are not only fundamentally import in atomic physics but also quite valuable for research of fusion and astrophysical plasmas. However, the low energy data below 1 keV/amu which is indispensable for diagnosis of the fusion plasma still is not complete due to technical difficulties, especially in preparation of a stable beam of highly charged ions with a narrow energy spread.

In 1985, we started to measure cross sections of various collision systems in the energy region below 1 keV/amu using an octo-pole ion beam guide (OPIG) technique in which a high frequency oscillating RF field prevents the ion beam from diverging [1] [2]. A small size electron beam ion source (Mini-EBIS) based on a new idea of cooling magnetic solenoid coils with liquid nitrogen was developed in 1987 [3]. Since then the cross section measurements for charge transfer of multiply charged ions with atoms and atmosphere molecules have been performed systematically by combining both techniques of the OPIG and the Mini-EBIS [4].

In the present paper, a comprehensive collection of experimental cross sections measured with the apparatus installed with the OPIG is provided for the following three groups:

1) Ion-molecule reactions in hydrogen systems;
2) Charge transfer of low-charged inert gas ions with inert gas atoms and atmosphere molecules;
3) Charge transfer of multiply charged ions with helium atom and hydrogen molecule.

Cross section measurements have been performed by using a Nier type ion source for the groups of 1 and 2, and by using the Mini-EBIS for the group 3, respectively.

Cross section data, especially for the first and third groups, provides information necessary for diagnostics of the fusion plasma and the astronomical plasma. In the session 2, advantages of the OPIG and the Mini-EBIS for the low energy collision experiments are described in addition to a brief explanation of experimental setup and procedure. General trends and characteristic features of cross sections for each group are summarized in the session 3. In the session 4, graphs and numerical data of cross sections are presented in parts of A, B and C.

2. Experimental setup and experimental procedure

An apparatus used in the present cross section measurements is basically similar to a tandem mass spectrometer that consists of an ion source, a mass selector, a collision cell, a mass analyzer and an ion detector in cascade. The experimental setup equipped with a conventional electron impact type (Nier type) ion source was used for Part A and Part B. The ion source was changed to the Mini-EBIS producing highly charged ions for Part C. In Fig.1, the experimental setup with the Mini EBIS is shown together with the arrangement of electrostatic potentials. Only a

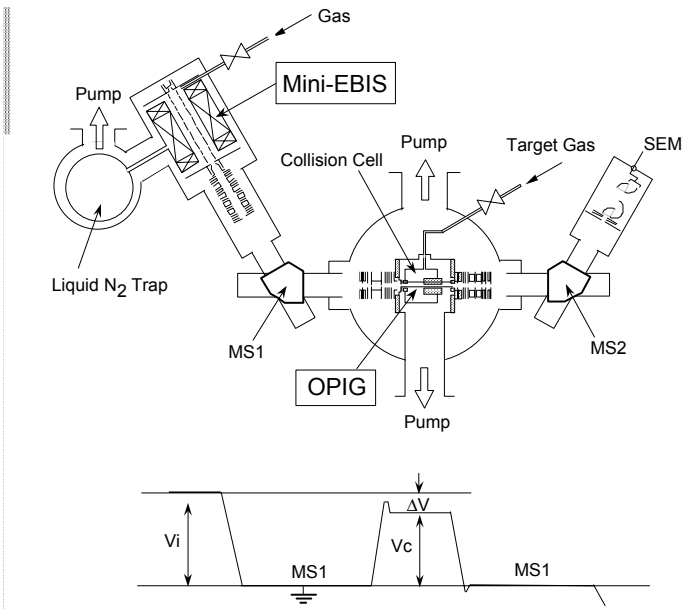

Fig.1. A schematic diagram of the experimental setup and the arrangement of electrostatic potentials. Vacuum envelope is grounded. Vi and Vc are potentials at the ion source and the collision cell, respectively.

brief description is given here since details of experimental setup and procedure have been reported previously [1] [4].

Ions extracted from the ion source are accelerated and mass analyzed by the first electromagnetic analyzer, MS1. Ions with a selected m/q are decelerated just before injection into a collision cell through an entrance aperture of 0.5 mm. In the collision cell, the OPIG system which consists of eight molybdenum poles with a diameter of 1.5 mm and 160 mm length is assembled in inscribing with an outlet ceramic pipe of 7 mm inner diameter. High frequency voltages are supplied to eight poles of the OPIG alternatively in an opposite phase. The oscillatory electric field created in the OPIG modulates and confines only the radial motion of charged particles and never affects the drift motion along the axis. A contour map of the oscillatory potential and the simulated radial trajectory in the OPIG are shown in Fig.2. The ions leaving from the OPIG are accelerated again and their m/q are analyzed by MS2. The

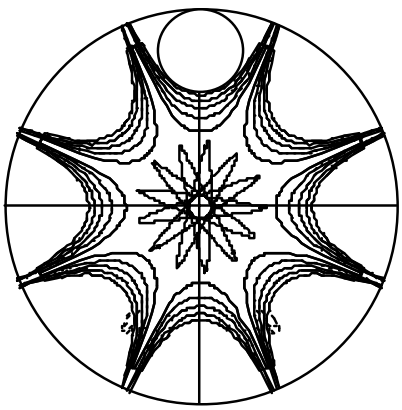

Fig.2. A contour map of the oscillatory potential and the simulated radial trajectory in the OPIG

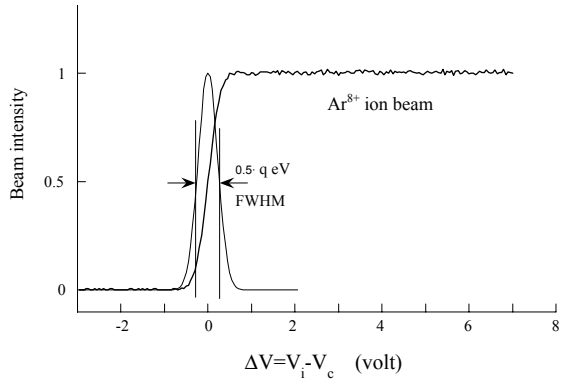

Fig.3. Intensity curve of Ar^{8+} beam extracted from the mini-EBIS as a function of the difference ($\Delta V=V_i-V_c$) between potentials at the ion source (V_i) and the collision cell (V_c).

primary ion and product ions are counted by a secondary electron multiplier. The pressure of target gas is measured indirectly by a MKS Baratron gauge.

The collision energy is determined by the charge q times the potential difference ΔV between V_I at the ion source and V_c at the collision cell, so that $E_{lab}= q\times\Delta V$. When beam intensity is measured as a function of $\Delta V = V_i-V_c$ by changing V_c, it is almost constant until it falls off rapidly near the zero energy as seen in Fig.3. This is a great advantage of using the OPIG for the low energy cross section measurements. Furthermore, the DC mode operation of the Mini-EBIS is very effective not only to eliminate energy spreads of the multiply charged ion beam but also to suppress contamination of excited ions with a long life. Energy spreads of the ion beam were estimated from a differential curve of the beam intensity, as typically $q\times0.3$ eV (FWHM) for using the Nier type ion source and $q\times(0.4\sim0.7)$ eV (FWHM) for using the Mini-EBIS, respectively.

Cross sections for ion-molecule reactions and charge transfer reactions were determined by the initial growth method with increasing the target gas pressure. In addition, in order to check the reliability of measured cross sections and the contamination of long-living excited ions in the ion beam, cross sections of beam attenuation in target gases were routinely measured.

3. Explanation of graphs and tables

All measured cross sections are presented in graphs as a function of collision energy of E_{cm} in the center-of-mass system so as to compare results of different isotope species. Their numerical data are listed in tables as functions of three energies, E_{lab}/q, $E_{cm}=E_{lab}\times m_2/(m_1+m_2)$ and $E_{amu}=E_{lab}/m_1$, where E_{lab}, q, m_1 and m_2 are energy in the laboratory system, charge state of the projectile ion and masses of the projectile ion and the target, respectively.

Statistical uncertainties of presented cross sections were less than ±10% and systematic errors for each parameter measurements were commonly estimated to be around ±5% for the collision length, ±5% for target pressure and less than ±5% for signal counting, respectively.

Thus, the gross uncertainties of measured cross sections can be commonly estimated to be ±25% at the most.

3.1. Part A: Ion-molecule reactions in hydrogen systems

Ion-molecule reactions in hydrogen systems were investigated by the experimental setup equipped with a Nier type ion source. Complicated ion-molecule reactions in hydrogen systems are discriminated by using isotope species and their cross sections are shown in the part A of the session 4 together with attenuation cross sections of σ(att) and contributions of δ from secondary processes. These cross sections are unpublished data measured during 1985-1986. In the cross section measurements for hydrogen systems, attenuation cross sections are much larger than sum of cross sections of ion-molecule reactions. This means that a lot of very slow ions, which are produced in ion-molecule reactions, cause secondary processes and most of them are confined in the OPIG for long times. Also, it should be noted that target excitation processes followed with

Fig.4. Resolved cross sections related following processes for the A^+/B_2 system.

$$A^+ + B_2 \rightarrow AB + B^+ + 0 \text{ eV} \quad \sigma(B^+) \quad (1)$$
$$\rightarrow AB^+ + B - 1.83 \text{ eV} \quad \sigma(AB^+) \quad (2)$$
$$\rightarrow A + B_2^+ - 1.83 \text{ eV} \quad \sigma(B_2^+) \quad (3)$$
$$\rightarrow A + B + B^+ - 4.48 \text{ eV} \quad \sigma(B^+) \quad (4)$$
$$\rightarrow A^+ + B_2^+ + e - 15.43 \text{ eV} \quad \sigma(B_2^+) \quad (5)$$

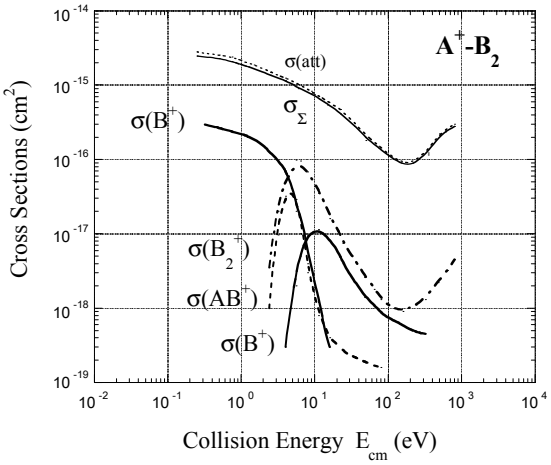

Fig.5. Resolved cross sections related to the following processes for the A_2^+/B_2 system.

$$A_2^+ + B_2 \rightarrow A_2B^+ + B + 2.06 \text{ eV} \quad \sigma(A_2B^+) \quad (6)$$
$$\rightarrow AB_2^+ + A + 2.06 \text{ eV} \quad \sigma(AB_2^+) \quad (7)$$
$$\rightarrow AB^+ + AB + 0 \text{ eV} \quad \sigma(AB^+) \quad (8)$$
$$\rightarrow A + A + B_2^+ - 4.47 \text{ eV} \quad \sigma(B_2^+) \quad (9)$$
$$\rightarrow A^+ + A + B_2 - 2.75 \text{ eV} \quad \sigma(A^+) \quad (10)$$
$$\rightarrow A_2 + B_2^+ + 0 \text{ eV} \quad \sigma_C(B_2^+) \quad (11)$$

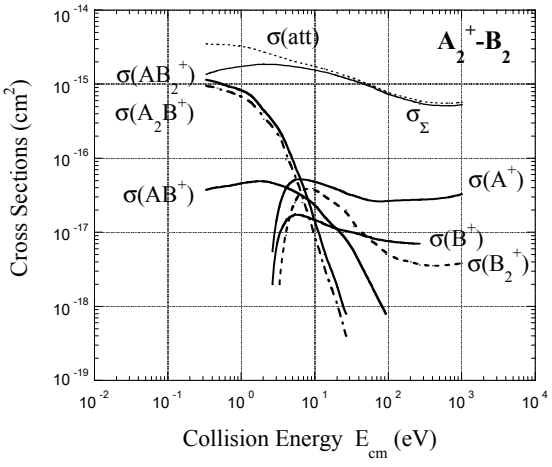

Fig.6. Resolved cross sections related to the following processes for the A_3^+/B_2 system.

$A_3^+ + B_2 \rightarrow A_2B^+ + AB + 0$ eV $\sigma(A_2B^+)$ (12)
$\rightarrow A_2B^+ + A + B - 4.47$ eV $\sigma(A_2B^+)$ (13)
$\rightarrow AB_2^+ + A_2 + 0$ eV $\sigma(AB_2^+)$ (14)
$\rightarrow AB_2^+ + A + A - 4.47$ eV $\sigma(AB_2^+)$ (15)
$\rightarrow AB^+ + A_2 + B - 6.52$ eV $\sigma(AB^+)$ (16)
$\rightarrow AB^+ + AB + A - 6.52$ eV $\sigma(AB^+)$ (16')
$\rightarrow A^+ + A_2 + B_2 - 4.81$ eV $\sigma(A^+)$ (17)
$\rightarrow A_2^+ + A + B_2 - 6.52$ eV $\sigma(A_2^+)$ (18)
$\rightarrow A_2^+ + AB + B - 6.52$ eV $\sigma(A_2^+)$ (18')
$\rightarrow A_2 + AB + B^+ - 4.81$ eV $\sigma(B^+)$ (19)
$\rightarrow A_2 + A + B_2^+ - 6.52$ eV $\sigma(B_2^+)$ (20)

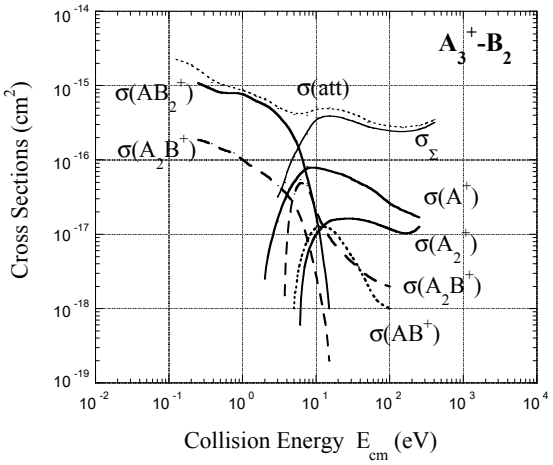

large energy loss which increases the attenuation cross sections.

By comparison of presented data, following cross sections and related processes are resolved for each hydrogen systems of A^+/B_2, A_2^+/B_2 and A_3^+/B_2 types as shown in Fig.4-6, where A and B are element of H or D. The σ_Σ indicates the difference between σ(att) and sum of measured reaction cross sections.

3.2. Part B: Charge transfer of low-charged rare gas ions produced by a Nier type ion source

In the part B, single-, double- and triple-electron capture cross sections of low-charged rare-gas ions in collisions with rare gas atoms and atmosphere molecules, studied using a Nier type ion source again, are presented in graphs and tables as a function of collision energy of E_{cm} in the center-of-mass system.

Studies for symmetric collision systems of Ar^{2+}/Ar, Ar^{3+}/Ar, Kr^{2+}/Kr and Kr^{3+}/Kr were reported in detail [1] [2]. At low energies where the collision is dominated by an attractive potential of an induced dipole, symmetric resonant charge transfer process of $A^{q+} + A \rightarrow A + A^{q+}$ becomes to be most dominant even for q=2 and 3 and their cross sections well agree with a half of the Langevin cross section, $\sigma_L = 2\pi q(\alpha/2E_{cm})^{1/2}$, where α is polarizability of the target atom [5].

Generally, a conventional electron impact type ion source provides doubly charged rare gas ions including low-lying metastable ions in states of $^1D_2$ and $^1S_0$ added to the ground state of $^3P_{1/2,3/2}$. Practically, σ_{21} and σ_{20} measured in collision systems of Ar^{2+}/He and Kr^{2+}/He except for Ne^{2+}/He have strongly depended on the electron impact energy. Accordingly, the electron impact energy E_e used for production of the projectile ions is shown in each graph. From the pressure dependence of product ions, partial cross sections were determined of $\sigma_{21}(^1D_2)$ and $\sigma_{21}(^3P)$ in Ar^{2+}/He system and of $\sigma_{21}(^1S_0)$ and $\sigma_{21}(^1D_2)$ in Kr^{2+}/He. It is worth noting that a very

steep threshold structure of σ_{21} in Ne^{2+}/He near $E_{cm}\approx16$ eV is quite different from others. On the other hand, σ_{21} in Ne^{2+}/H_2, Ne^{2+}/N_2 increases with decreasing collision energy and goes up along the Langevin cross section at the low energy end.

3.3. Part C: Charge transfer of multiply charged ions produced by a small type electron beam ion source (Mini-EBIS).

In the part C, single- and double-charge transfer cross sections of multiply charged ions in collisions with helium atom and hydrogen molecule, which are measured with the Mini-EBIS, are presented in graphs and tables. An ion beam extracted from a plasma based ECR-type ion source very frequently accompanies ions in metastable states which cause significant and dramatic effects on the observed cross sections. However, the DC mode operation of the Mini-EBIS is very effective to suppress contamination of excited ions with a long life in multiply charge ion beams. The Mini-EBIS is operated at very low pressure lower than 10^{-10} torr. At such low densities, there is little probability of metastable production via electron capture collisions and, even if excited ions with a long life are produced, they will be quenched during long ion-confinement times in the DC mode operation. Practically, no existence of long-living excited ions has been found in beams of multiply charged ions extracted from the Mini-EBIS except for C^{2+} and O^{2+} beams. Some of presented data were already discussed in [6] for He^{2+}/He and He^{2+}/H_2, in [4] for C^{4+}, N^{4+} and O^{4+}/He, in [9] for C^{4+}/H_2, in [10] for Ar^{q+}/H_2 (q=6-9,11), in [11] for Ar^{q+}/He (q=6-9,11) and I^{q+}/He (q=24-26), and in [13] for C^{q+}/He and H_2 (q=2-5). In these measurements, it should be noted that the transfer ionization processes have been ignored since product ions are identified by m/q' for the final charge states of q'. Although both of He and H_2 targets have two electrons, measured cross sections for He target are quite different from those for the H_2 target. Especially, single- and double-charge transfer cross sections of C^{q+}, N^{q+} and O^{q+} (q=2~6) with He strongly depend on the collision energy and the charge states of q in contrast to those with H_2.

In charge transfer collisions of multiply charged ions with many electron targets, contribution of multi-electron transfer processes becomes significant and their cross sections have a characteristic minimum structure in their energy dependence around few eV. Their cross sections are not presented here. They are reported in [7] for He^{2+}/CO, N_2 and O_2, and Kr^{q+}/Ne, N_2, O_2 and CO (q=7-9), in [8] for C^{4+}/Ar and $C_nH_{2(n+1)}$ (n=1~4), in [9] for C^{4+}/H_2, N_2 and O_2, in [12] for Ar^{q+}/Ne,

At low collision energies, the collision dynamics changes drastically giving rise to various new effects on the charge transfer reactions. The Coulomb electric field created by the ionic charge polarizes neutral targets and an ion-induced dipole leads to a mutual attraction between the collision partners. The induced dipole interaction can capture the ion in a spiral trajectory close to the collision center at sufficiently small impact parameters and the trajectory takes a

circular orbit around the target at an appropriate impact parameter [5]. At sufficiently low collision energies where the collision is dominated by the ion-induced dipole, the orbiting cross section is enlarged in inverse proportion to the collision velocity. In various thermal reactions of singly charged ions, almost all reaction rates are constant. This signature is well known as the orbiting effects due to the ion-induced dipole interaction.

As the ionic charge-state becomes large, it is expected that the enhancement of cross section due to the orbiting effects can be observed at energies far much higher than thermal energy. This expectation was my initial motivation to start cross section measurements with multiply charged ions at low energies. It has been successfully confirmed that almost all measured charge transfer cross sections tend to increases at the lower end in the energy range studied [10] [11]. Only for Ar^{6+}-H_2 collisions, reported data using Penning trap at near thermal energy are available [14]. The thermal energy data places just on an extrapolation line of presented single charge transfer cross sections converging to the Langevin cross section σ_L in the lower energy side [5]. This agreement newly gives rise to a fundamental interest how far the cross section goes up with decreasing collision energy. Furthermore, quantum mechanical calculation has predicted that the orbiting resonance leads to drastically increase the interaction time and it makes a sharp peak in the electron capture cross section [15] [16]. The experimental verification of the orbiting resonance is still one of future interests with highly charged ions at low energies.

In slow collisions of He^{2+} and Kr^{8+} highly charged ions with H_2, N_2, O_2 and CO, charge transfer processes followed by fragmentation have been perfectly resolved by a new triple coincidence technique for three particle detection using twin OPIG systems [17]. Some new phenomena relevant to collision dynamics and oriented fragmentation have been found at low energies. The OPIG technique is very useful to trap and transport slow charge particles. Recently, Groningen's group also has applied the OPIG in state-selective electron capture experiments with slow highly charged ions [18] [19].

4. Graphs and tables of presented cross sections

4.1. Part A: Ion-molecular reactions in hydrogen systems

A1-a. Graph and table of reaction cross sections in H^+-H_2 collisions

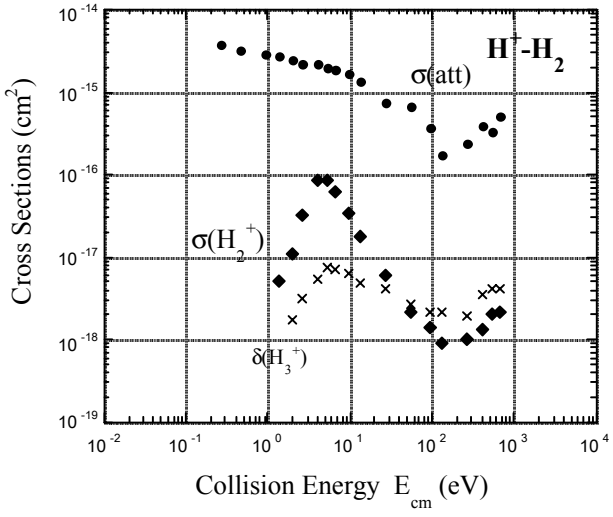

$\delta(H_3^+)$: contribution from the secondary process of slow $H_2^+ + H_2 \rightarrow H_3^+ + H$. See text.

Energy		Cross sections ($\times 10^{-16}$cm^2)		
E_{lab}/q (eV/q)	E_{cm} (eV)	σ_{att}	$\sigma(H_2^+)$	$\delta(H_3^+)$
0.4	0.27	37.0	-	-
0.7	0.47	33.0	-	-
1.4	0.93	29.0	-	-
2.0	1.33	27.0	0.05	-
3.0	2.00	25.0	0.11	0.017
4.0	2.67	22.6	0.32	0.032
6.0	4.00	21.6	0.87	0.054
8.0	5.33	20.3	0.86	0.075
10.0	6.67	18.8	0.63	0.072
14.0	9.33	17.2	0.35	0.062
20.0	13.3	13.7	0.18	0.049
40.0	26.7	7.30	0.061	0.042
80.0	53.3	6.70	0.022	0.026
140	93.3	3.70	0.014	0.021
200	133	1.74	0.009	0.022
400	267	2.35	0.010	0.019
600	400	3.85	0.013	0.035
800	533	3.30	0.020	0.042
1000	667	5.10	0.021	0.042

A1-b. Graph and table of reaction cross sections in H^+-D_2 collisions

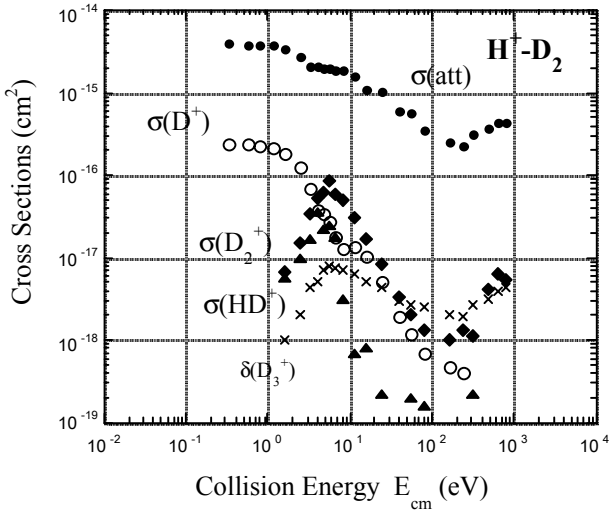

$\delta(D_3^+)$: contribution from the secondary process of slow $D_2^+ + D_2 \rightarrow D_3^+ + D$. See text.

Energy		Cross sections ($\times 10^{-16}$cm^2)				
E_{lab}/q (eV/q)	E_{cm} (eV)	σ_{att}	$\sigma(D^+)$	$\sigma(D_2^+)$	$\sigma(DH^+)$	$\delta(D_3^+)$
0.4	0.32	39.5	2.45	-	-	-
0.7	0.56	37.6	2.38	-	-	-
1.0	0.80	38.6	2.22	-	-	-
1.4	1.12	37.1	2.12	-	-	-
2.0	1.60	34.5	1.81	0.068	0.057	0.010
3.0	2.40	27.6	1.24	0.155	0.096	0.020
4.0	3.20	20.8	0.68	0.332	0.166	0.043
5.0	4.00	20.4	0.39	0.520	0.365	0.051
6.0	4.80	19.9	0.34	0.630	0.223	0.071
7.0	5.60	20.0	0.278	0.870	0.245	0.080
8.0	6.40	19.0	0.174	0.580	0.175	0.075
10.0	8.00	19.1	0.132	0.500	0.032	0.072
14.0	11.2	15.5	0.139	0.300	0.007	0.064
20.0	16.0	10.8	0.102	0.171	0.008	0.051
30.0	24.0	10.4	0.052	0.085	0.002	0.044
50.0	40.0	6.12	0.019	0.034	-	0.030
70.0	56.0	5.85	0.012	0.020	0.002	0.027
100	80.0	3.44	0.007	0.013	0.002	0.025
200	160	2.55	0.005	0.010	-	0.020
300	240	2.22	0.004	0.013	-	0.019
400	320	3.12	-	0.011	0.002	0.027
600	480	3.62	-	0.042	-	0.032
800	640	4.24	-	0.062	-	0.039
1000	800	4.30	-	0.053	-	0.043

A1-c. Graph and table of reaction cross sections in D^+-H_2 collisions

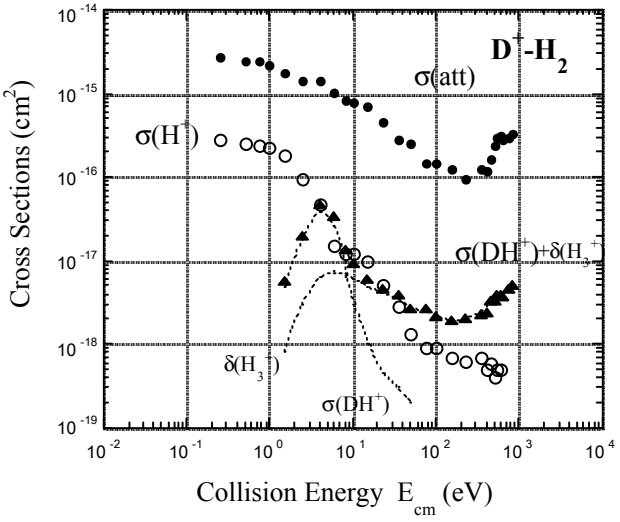

$\delta(H_3^+)$: contribution from the secondary process of slow $H_2^+ + H_2 \rightarrow H_3^+ + H$. See text.

Energy		Cross sections ($\times 10^{-16}$cm^2)		
E_{lab}/q (eV/q)	E_{cm} (eV)	σ_{att}	$\sigma(H^+)$	$\sigma(DH^+) + \delta(H_3^+)$
0.5	0.25	27.0	2.84	
1.0	0.50	24.3	2.53	
1.5	0.75	25.0	2.38	
2.0	1.00	22.0	2.25	
3.0	1.50	17.4	1.80	0.058
5.0	2.50	14.5	0.980	0.20
8.0	4.00	14.0	0.480	0.48
12.0	6.00	10.4	0.150	0.34
16.0	8.00	8.30	0.125	0.13
20.0	10.0	7.70	0.122	0.092
30.0	15.0	6.90	0.099	0.060
45.0	22.5	4.70	0.052	0.046
70.0	35.0	2.80	0.028	0.039
100	50.0	2.50	0.013	0.027
150	75.0	1.50	0.009	0.026
200	100	1.45	0.009	0.021
300	150	1.25	0.007	0.019
450	225	0.95	0.006	0.020
700	350	1.23	0.007	0.023
800	400	1.20	0.005	0.024
900	450	1.65	0.006	0.034
1000	500	2.40	0.004	0.033
1100	550	3.05	0.005	0.039
1200	600	3.06	-	0.040
1300	650	2.80	-	0.038
1500	750	3.00	-	0.045
1700	850	3.40	-	0.050

A2-a. Graph and table of reaction cross sections in H_2^+-H_2 collisions

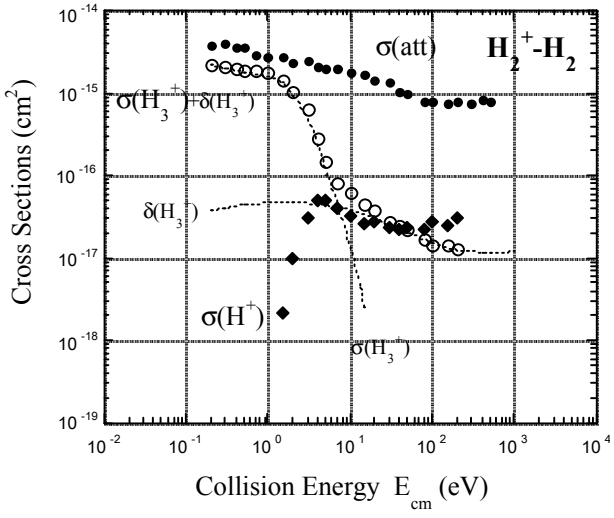

$\delta(H_3^+)$: contribution from the secondary process of slow $H_2^+ + H_2 \rightarrow H_3^+ + H$. See text.

Energy		Cross sections ($\times 10^{-16}$cm^2)		
E_{lab}/q (eV/q)	E_{cm} (eV)	σ_{att}	$\sigma(H_3^+) + \delta(H_3^+)$	$\sigma(H^+)$
0.4	0.20	38.0	22.0	-
0.6	0.30	39.0	20.5	-
0.8	0.40	35.6	20.0	-
1.0	0.50	35.5	18.6	-
1.4	0.70	28.8	18.5	-
2.0	1.0	28.0	17.5	-
3.0	1.5	27.2	14.0	0.02
4.0	2.0	23.5	10.4	0.10
6.0	3.0	24.0	6.20	0.31
8.0	4.0	21.4	2.85	0.51
10.0	5.0	20.0	1.46	0.49
14.0	7.0	19.7	0.82	0.41
20.0	10.0	18.1	0.62	0.33
30.0	15.0	17.2	0.45	0.26
40.0	20.0	14.5	0.38	0.27
60.0	30.0	13.4	0.27	0.24
80.0	40.0	10.5	0.24	0.22
100	50.0	9.6	0.23	0.23
160	80.0	7.7	0.17	0.22
200	100	8.0	0.14	0.28
300	150	7.5	0.15	0.24
400	200	8.1	0.13	0.30
600	300	7.5	-	-
800	400	8.2	-	-
1000	500	8.1	-	-

A2-b. Graph and table of reaction cross sections in H_2^+-D_2 collisions

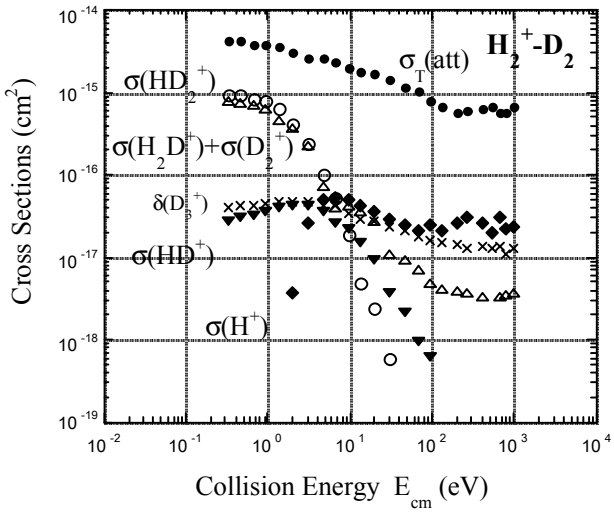

$\delta(D_3^+)$: contribution from the secondary process of slow $D_2^+ + D_2 \rightarrow D_3^+ + D$. See text.

Energy		Cross sections ($\times 10^{-16}$cm^2)					
E_{lab}/q (eV/q)	E_{cm} (eV)	σ_{att}	$\sigma(HD_2^+)$	$\sigma(H_2D^+)$ + $\sigma(D_2^+)$	$\sigma(DH^+)$	$\sigma(H^+)$	$\delta(D_3+)$
0.5	0.33	42.0	9.45	7.85	0.275	-	0.40
0.7	0.47	41.8	9.10	7.55	0.305	-	0.43
1.0	0.67	38.6	8.18	7.25	0.320	-	0.41
1.4	0.93	38.4	8.02	6.25	0.353	-	0.46
2.0	1.33	36.2	6.25	4.54	0.403	-	0.46
3.0	2.00	30.2	4.21	3.62	0.420	0.038	0.47
4.5	3.00	26.5	2.35	2.23	0.432	0.260	0.46
7.0	4.67	25.3	1.03	0.73	0.352	0.490	0.43
10.0	6.67	23.1	0.53	0.41	0.265	0.515	0.42
14.0	9.33	20.0	0.19	0.43	0.222	0.495	0.35
20.0	13.3	18.2	0.05	0.36	0.148	0.434	0.29
30.0	20.0	16.5	0.02	0.28	0.092	0.352	0.27
45.0	30.0	14.0	0.01	0.11	0.038	0.283	0.23
70.0	46.7	11.5	-	0.10	0.021	0.242	0.21
100	66.7	10.1	-	0.07	0.010	0.212	0.18
140	93.3	7.90	-	0.05	0.006	0.245	0.16
200	133	6.81	-	0.04	-	0.205	0.15
300	200	5.65	-	0.04	-	0.262	0.14
400	267	6.00	-	0.04	-	0.310	0.13
600	400	6.25	-	0.03	-	0.265	0.14
800	533	6.60	-	-	-	0.200	0.12
1000	667	5.80	-	0.03	-	0.305	0.14
1200	800	5.61	-	0.03	-	0.225	0.11
1500	1000	6.55	-	0.04	-	0.235	0.13

A2-c. Graph and table of reaction cross sections in D_2^+-H_2 collisions

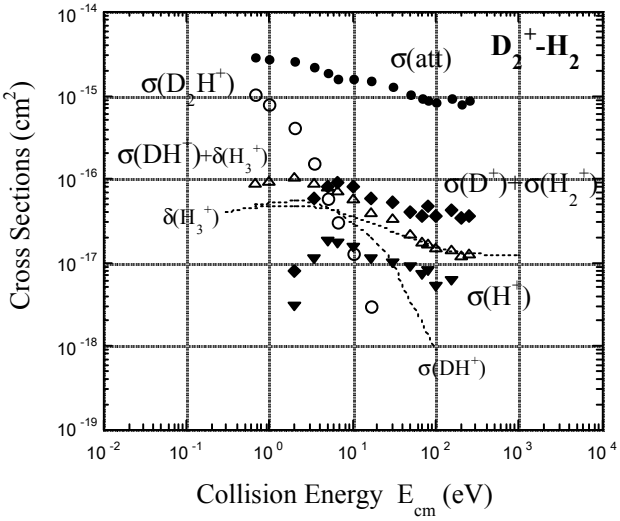

$\delta(H_3^+)$: contribution from the secondary process o slow $H_2^+ + H_2 \rightarrow H_3^+ + H$. See text.

Energy		Cross sections ($\times 10^{-16}$cm^2)			
E_{lab}/q (eV/q)	E_{cm} (eV)	σ_{att}	$\sigma(DH_2^+)$	$\sigma(HD^+)$ + $\delta(H_3^+)$	$\sigma(D^+)$ + $\sigma(H_2^+)$
2.0	0.67	29.0	10.5	0.89	-
3.0	1.00	28.0	8.00	0.95	-
6.0	2.00	25.5	4.15	1.04	0.08
10.0	3.33	21.5	1.54	0.92	0.60
15.0	5.00	18.6	0.58	0.79	0.82
20.0	6.67	16.0	0.31	0.71	0.92
30.0	10.0	16.2	0.13	0.58	0.81
50.0	16.5	15.0	0.03	0.41	0.58
90.0	30.0	13.0	-	0.34	0.52
150	50.0	10.2	-	0.23	0.41
200	66.7	9.5	-	0.18	0.36
240	80.0	8.6	-	0.17	0.48
300	100	8.2	-	0.16	0.36
450	150	9.1	-	0.15	0.42
600	200	8.0	-	0.13	0.35
750	250	8.6	-	0.13	0.36

A2-d. Graph and table of reaction cross sections in D_2^+-D_2 collisions

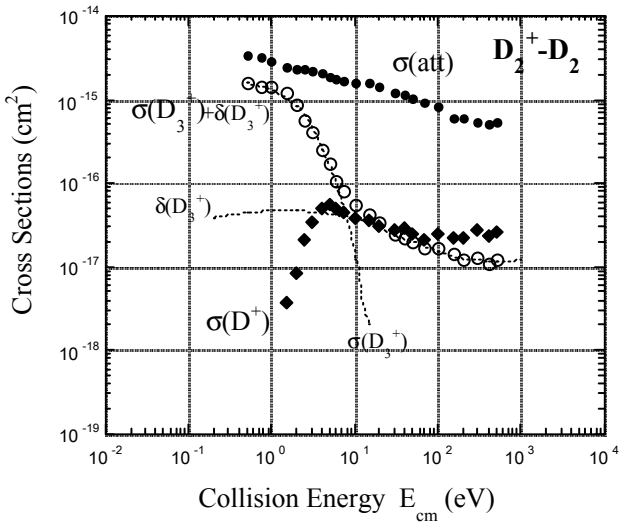

$\delta(D_3^+)$: contribution from the secondary process of slow $D_2^+ + D_2 \rightarrow D_3^+ + D$. See text.

Energy		Cross sections ($\times 10^{-16}$cm^2)		
E_{lab}/q (eV/q)	E_{cm} (eV)	σ_{att}	$\sigma(D_3^+)$ + $\delta(D_3^+)$	$\sigma(D^+)$
1.0	0.50	33.5	16.3	-
1.5	0.75	32.8	14.6	-
2.0	1.0	28.4	14.4	-
3.0	1.5	24.7	12.1	0.036
4.0	2.0	22.7	8.90	0.085
5.0	2.5	23.0	5.80	0.21
6.0	3.0	21.5	4.20	0.34
8.0	4.0	20.5	2.55	0.51
10.0	5.0	19.2	1.71	0.54
12.0	6.0	17.6	1.05	0.50
15.0	7.5	17.0	0.810	0.45
20.0	10.0	16.3	0.568	0.38
30.0	15.0	16.0	0.420	0.36
40.0	20.0	14.0	0.350	0.30
60.0	30.0	12.4	0.250	0.28
80.0	40.0	11.5	0.225	0.29
100	50.0	10.6	0.195	0.24
140	70.0	9.30	0.165	0.21
200	100	8.20	0.165	0.25
300	150	6.10	0.145	0.22
400	200	6.00	0.125	0.22
600	300	5.40	0.130	0.27
800	400	5.00	0.110	0.24
1000	500	5.50	0.125	0.26

A3-a. Graph and table of reaction cross sections in H_3^+-H_2 collisions

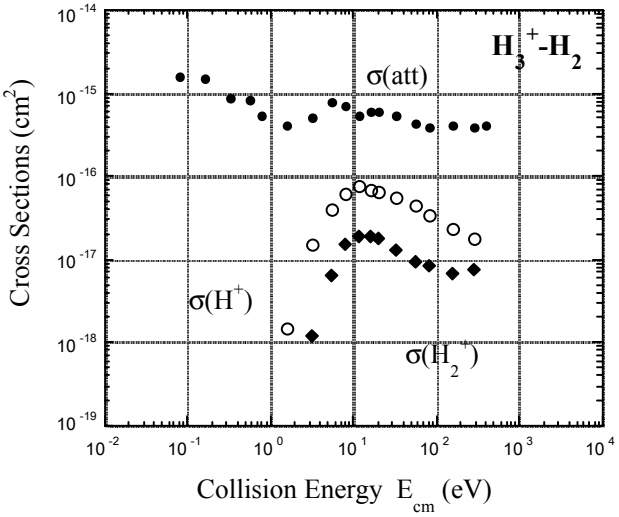

Energy		Cross sections ($\times 10^{-16}$cm^2)		
E_{lab}/q (eV/q)	E_{cm} (eV)	σ_{att}	$\sigma(H^+)$	$\sigma(H_2^+)$
0.10	0.08	15.8	-	-
0.20	0.16	15.2	-	-
0.40	0.32	8.9	-	-
0.70	0.56	8.4	-	-
1.0	0.80	5.5	-	-
2.0	1.60	4.1	0.02	-
4.0	3.20	5.2	0.15	0.012
7.0	5.60	7.7	0.40	0.065
10.0	8.00	7.2	0.62	0.15
15.0	12.0	5.5	0.78	0.19
20.0	16.0	6.0	0.68	0.19
25.0	20.0	6.0	0.65	0.18
40.0	32.0	5.3	0.55	0.13
70.0	56.0	4.3	0.44	0.095
100	80.0	3.8	0.34	0.083
200	160	4.1	0.23	0.067
350	280	3.9	0.18	0.075
500	400	4.2	-	-

A3-b. Graph and table of reaction cross sections in D_3^+-H_2 collisions

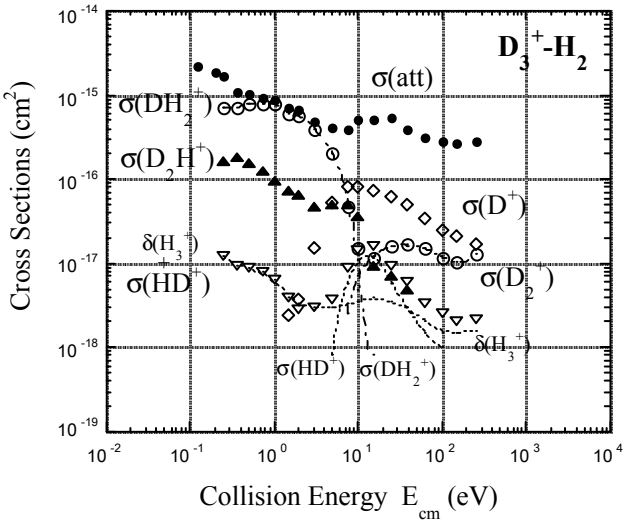

$\delta(H_3^+)$: contribution from the secondary processes of D_2H^+, DH_2^+, $H_2^+ + H_2 \rightarrow H_3^+$. See text.

Energy		Cross sections ($\times 10^{-16}$cm^2)				
E_{lab}/q (eV/q)	E_{cm} (eV)	σ_{att}	$\sigma(DH_2^+) + \sigma(D_2^+)$	$\sigma(D_2H^+)$	$\sigma(D^+)$	$\sigma(DH^+) + \delta(H_3^+)$
0.50	0.13	22.5	-	-	-	-
0.80	0.20	19.2	-	-	-	-
1.0	0.25	16.5	7.08	1.66	-	0.119
1.5	0.38	11.0	7.00	1.78	-	0.095
2.0	0.50	10.2	7.95	1.57	-	0.087
3.0	0.75	9.40	8.01	1.28	-	0.078
4.0	1.0	8.92	7.88	0.97	-	0.063
6.0	1.5	7.21	6.05	0.73	0.02	0.040
8.0	2.0	6.75	5.67	0.67	0.04	0.032
12.0	3.0	4.92	4.00	0.47	0.15	0.030
20.0	5.0	4.08	2.03	0.50	0.54	0.030
30.0	7.5	4.00	0.48	0.51	0.80	0.033
40.0	10.0	5.18	0.15	0.37	0.80	0.035
60.0	15.0	5.03	0.12	0.09	0.71	0.040
100	25.0	5.42	0.16	0.07	0.61	0.035
150	37.5	3.95	0.17	0.05	0.50	0.030
250	62.5	3.21	0.15	-	0.35	0.020
400	100	2.86	0.12	-	0.25	0.015
600	150	2.72	0.10	-	0.21	0.015
1000	250	2.88	0.13	-	0.17	0.016

A3-c. Graph and table of reaction cross sections in D_3^+-D_2 collisions

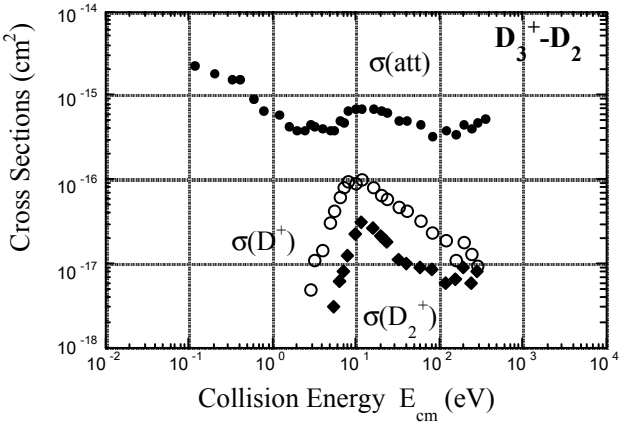

Energy		Cross sections ($\times 10^{-16}$cm^2)		
E_{lab}/q (eV/q)	E_{cm} (eV)	σ_{att}	$\sigma(D^+)$	$\sigma(D_2^+)$
0.3	0.12	23.0	-	-
0.5	0.20	18.0	-	-
0.8	0.32	15.4	-	-
1.0	0.40	15.5	-	-
1.5	0.60	9.3	-	-
2.0	0.80	6.6	-	-
3.0	1.2	6.0	-	-
4.0	1.6	4.4	-	-
5.0	2.0	3.9	-	-
6.0	2.4	3.9	-	-
7.0	2.8	4.5	0.05	-
8.0	3.2	4.3	0.11	-
10.0	4.0	4.1	0.15	-
12.0	4.8	3.8	0.31	-
14.0	5.6	3.9	0.44	0.030
16.0	6.4	5.0	0.62	0.061
18.0	7.2	4.9	0.80	0.083
20.0	8.0	6.6	0.98	0.127
25.0	10.0	7.2	0.90	0.231
30.0	12.0	7.0	1.03	0.310
40.0	16.0	6.9	0.80	0.270
50.0	20.0	6.6	0.66	0.210
60.0	24.0	6.2	0.60	0.180
80.0	32.0	5.1	0.48	0.110
100	40.0	5.0	0.43	0.100
150	60.0	4.5	0.33	0.089
200	80.0	3.3	0.24	0.087
300	120	3.8	0.19	0.060
400	160	3.5	0.114	0.067
500	200	4.5	0.185	0.092
600	240	4.1	0.132	0.060
700	280	4.7	0.096	0.082
900	360	5.5	-	-

4.2. Part B: Charge transfer of low-charged rare-gas ions produced by a Nier type ion source

B1-a. Graph and table of charge transfer cross sections of $^{20}Ne^{2+}$ in He

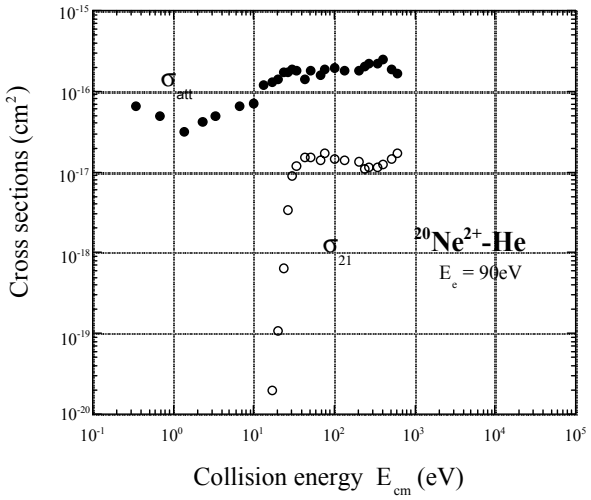

Energy E_{lab}/q (eV/q)	Energy E_{cm} (eV)	Cross sections ($\times 10^{-16}$cm^2) σ_{att}	Cross sections ($\times 10^{-16}$cm^2) σ_{21}	Energy E_{lab}/q (eV/q)	Energy E_{cm} (eV)	Cross sections ($\times 10^{-16}$cm^2) σ_{att}	Cross sections ($\times 10^{-16}$cm^2) σ_{21}
1.0	0.33	0.65	-	130	43.3	1.43	0.15
2.0	0.67	0.50	-	150	50.0	1.80	0.16
4.0	1.33	0.32	-	200	66.7	1.63	0.14
7.0	2.33	0.42	-	230	76.7	1.92	0.17
10.0	3.33	0.50	-	300	100	1.94	0.15
20.0	6.67	0.66	-	400	133	1.85	0.14
30.0	10.0	0.72	-	600	200	1.82	0.13
40.0	13.3	1.20	-	700	233	2.04	0.11
50.0	16.7	1.34	0.000	800	267	2.25	0.12
60.0	20.0	1.42	0.001	1000	333	2.20	0.11
70.0	23.3	1.72	0.007	1200	400	2.55	0.13
80.0	26.7	1.75	0.034	1500	500	1.89	0.15
90.0	30.0	1.92	0.090	1800	600	1.65	0.17
100	33.3	1.84	0.12	-	-	-	-

B1-b. Graph and table of charge transfer cross sections of $^{20}Ne^{2+}$ in H_2

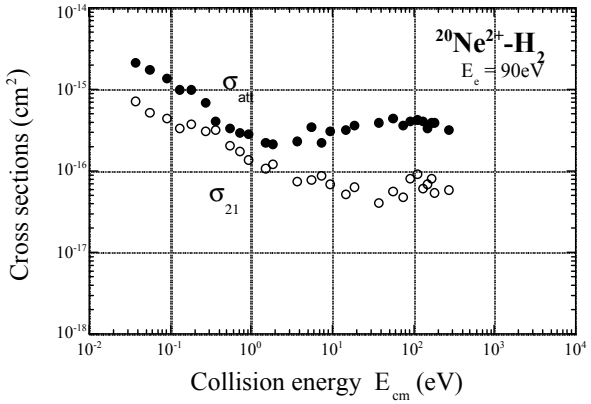

Energy E_{lab}/q (eV/q)	Energy E_{cm} (eV)	Cross sections ($\times 10^{-16}$cm^2) σ_{att}	Cross sections ($\times 10^{-16}$cm^2) σ_{21}	Energy E_{lab}/q (eV/q)	Energy E_{cm} (eV)	Cross sections ($\times 10^{-16}$cm^2) σ_{att}	Cross sections ($\times 10^{-16}$cm^2) σ_{21}
0.2	0.036	21.5	7.18	40.0	7.27	2.28	0.88
0.3	0.055	17.8	5.22	50.0	9.09	3.12	0.69
0.5	0.091	13.8	4.48	80.0	14.5	3.20	0.53
0.7	0.13	9.98	3.33	100	18.2	3.69	0.65
1.0	0.18	10.2	3.85	200	36.4	3.91	0.41
1.5	0.27	7.08	3.15	300	54.5	4.40	0.56
2.0	0.36	4.19	3.25	400	72.7	3.69	0.48
3.0	0.55	3.33	2.09	500	90.9	4.18	0.83
4.0	0.73	2.96	1.76	600	109	4.25	0.92
5.0	0.91	2.91	1.38	700	127	4.10	0.62
8.0	1.45	2.27	1.09	800	145	3.36	0.71
10.0	1.82	2.20	1.21	900	164	4.01	0.83
20.0	3.64	2.38	0.77	1000	182	3.95	0.54
30.0	5.45	3.55	0.78	1500	273	3.18	0.60

B1-c. Graph and table of charge transfer cross sections of $^{20}Ne^{2+}$ in N_2

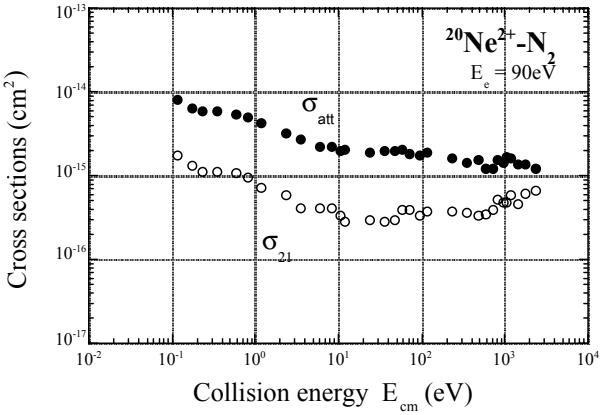

Energy E_{lab}/q (eV/q)	Energy E_{cm} (eV)	Cross sections ($\times 10^{-16}$cm^2) σ_{att}	Cross sections ($\times 10^{-16}$cm^2) σ_{21}	Energy E_{lab}/q (eV/q)	Energy E_{cm} (eV)	Cross sections ($\times 10^{-16}$cm^2) σ_{att}	Cross sections ($\times 10^{-16}$cm^2) σ_{21}
0.1	0.12	82.0	17.4	50.0	58.3	20.8	3.95
0.15	0.18	64.3	13.5	60.0	70.0	18.6	3.91
0.2	0.23	60.1	11.5	80.0	93.3	17.8	3.38
0.3	0.35	60.0	11.1	100	117	18.9	3.82
0.5	0.58	55.2	10.8	200	233	16.3	3.73
0.7	0.82	49.5	9.55	300	350	14.5	3.64
1.0	1.17	42.4	7.32	400	467	15.5	3.39
2.0	2.33	31.7	6.01	500	583	12.1	3.55
3.0	3.50	27.6	4.18	600	700	12.3	3.94
5.0	5.83	22.2	4.08	700	817	15.5	5.24
7.0	8.17	22.3	4.10	800	933	14.7	4.83
9.0	10.5	19.8	3.33	900	1050	16.6	4.93
10.0	11.7	20.7	2.87	1000	1167	16.5	5.95
20.0	23.3	19.2	2.97	1200	1400	13.8	4.64
30.0	35.0	19.8	2.91	1500	1750	14.1	6.21
40.0	46.7	19.6	2.95	2000	2333	12.3	6.68

B2-a. Graph and table of charge transfer cross sections of $^{40}Ar^{2+}$ in He

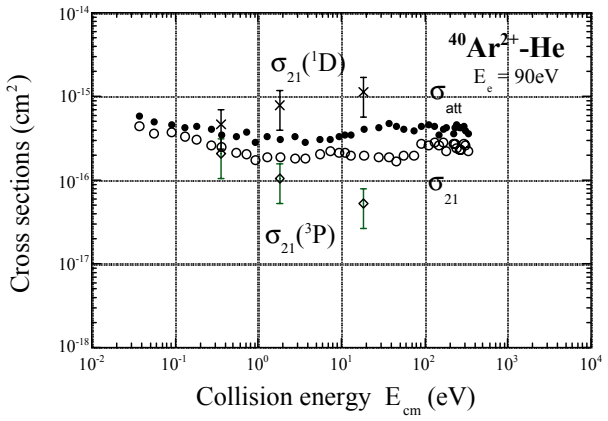

Energy		Cross sections ($\times 10^{-16}$cm^2) E_{el}=90eV			
E_{lab}/q (eV/q)	E_{cm} (eV)	σ_{att}	σ_{21}	$\sigma_{21}(^3P)$	$\sigma_{21}(^1D)$
0.2	0.04	5.82	4.40	-	-
0.3	0.05	5.14	3.60	-	-
0.5	0.09	4.62	3.80	-	-
0.7	0.13	4.28	3.40	-	-
1.0	0.18	4.50	3.15	-	-
1.5	0.27	4.07	2.66	-	-
2.0	0.36	3.51	2.55	2.1	4.7
3.0	0.55	3.31	2.15	-	-
4.0	0.73	3.80	2.10	-	-
5.0	0.91	2.86	1.78	-	-
7.0	1.27	3.30	1.95	-	-
10.0	1.82	3.15	1.93	1.05	7.9
15.0	2.73	3.31	1.87	-	-
20.0	3.64	2.92	1.86	-	-
30.0	5.45	3.09	2.04	-	-
40.0	7.27	3.15	2.24	-	-
50.0	9.09	3.30	2.19	-	-
60.0	10.9	3.54	2.14	-	-
70.0	12.7	3.44	1.96	-	-
100	18.2	4.11	2.02	0.53	11.2
150	27.3	4.26	1.91	-	-
200	36.4	4.82	1.95	-	-
250	45.5	4.53	1.70	-	-
300	54.5	4.08	1.99	-	-
400	72.7	3.88	2.00	-	-
500	90.9	4.41	2.72	-	-
600	109	4.63	2.68	-	-
700	127	4.40	2.89	-	-
800	145	3.52	2.61	-	-
900	164	4.09	2.82	-	-
1000	182	4.21	2.28	-	-
1200	218	3.69	2.75	-	-
1250	227	4.35	2.74	-	-
1300	236	4.58	2.45	-	-

B2-b. Graph and table of charge transfer cross sections of $^{40}Ar^{2+}$ in Ne

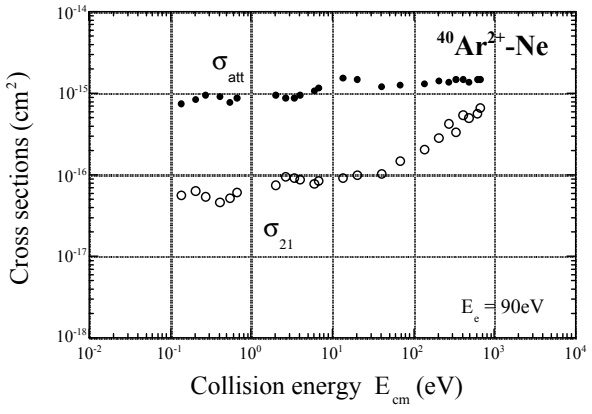

Energy		Cross sections ($\times 10^{16}$cm^2)		Energy		Cross sections ($\times 10^{16}$cm^2)	
E_{lab}/q (eV/q)	E_{cm} (eV)	σ_{att}	σ_{21}	E_{lab}/q (eV/q)	E_{cm} (eV)	σ_{att}	σ_{21}
0.2	0.13	7.5	0.57	20.0	13.3	15.8	0.92
0.3	0.20	8.5	0.65	30.0	20.0	15.0	1.00
0.4	0.27	9.6	0.54	60.0	40.0	12.3	1.06
0.6	0.40	9.1	0.47	100	66.7	12.6	1.52
0.8	0.53	7.9	0.53	200	133	13.1	2.04
1.0	0.67	8.7	0.62	300	200	14.5	2.83
3.0	2.00	9.6	0.74	400	267	13.9	4.22
4.0	2.67	8.7	0.96	500	333	14.8	3.34
5.0	3.33	8.7	0.92	600	400	14.8	5.50
6.0	4.00	9.5	0.90	700	467	13.8	4.95
9.0	6.00	11.0	0.78	900	600	15.0	5.65
10.0	6.67	11.8	0.86	1000	667	15.2	6.72

B2-c. Graph and table of charge transfer cross sections of $^{40}Ar^{2+}$ in Ar

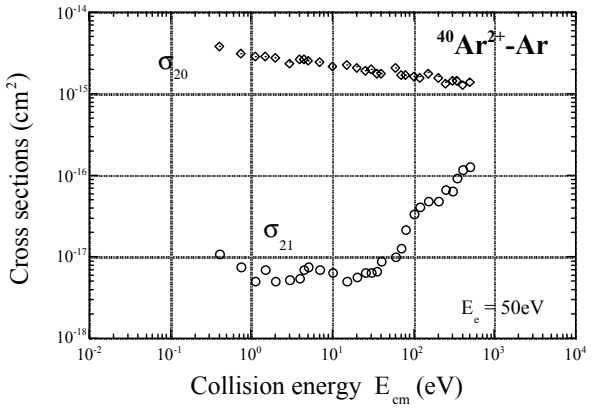

Energy E_{lab}/q (eV/q)	Energy E_{cm} (eV)	Cross sections ($\times 10^{-16}$cm^2) E_{el}=50eV σ_{att}	σ_{21}	σ_{20} *)
0.4	0.4	38.0	0.11	37.9
0.8	0.8	31.0	0.075	30.9
1.1	1.1	28.3	0.051	28.2
1.5	1.5	29.0	0.070	28.9
2.0	2.0	28.0	0.050	28.0
3.0	3.0	23.9	0.053	23.8
4.0	4.0	26.7	0.055	26.6
4.5	4.5	26.0	0.070	25.9
5.0	5.0	25.6	0.075	25.5
7.0	7.0	24.2	0.070	24.1
10.0	10.0	21.5	0.063	21.4
15.0	15.0	22.9	0.050	22.9
20.0	20.0	21.2	0.056	21.1
25.0	25.0	19.0	0.064	18.9
30.0	30.0	20.2	0.065	20.1
35.0	35.0	18.0	0.067	17.9
40.0	40.0	17.9	0.090	17.8
60.0	60.0	21.1	0.099	21.0
70.0	70.0	16.8	0.13	16.7
80.0	80.0	17.0	0.22	16.8
100	100	16.3	0.34	16.0
120	120	16.1	0.41	15.7
150	150	18.1	0.49	17.6
200	200	16.1	0.49	15.6
250	250	14.1	0.67	13.4
300	300	15.2	0.63	14.6
350	350	15.5	0.91	14.6
400	400	13.8	1.20	12.6
500	500	15.1	1.30	13.8

*) σ_{20} was estimated by $\sigma_{20}=\sigma_{att}-\sigma_{21}$.

B2-d. Graph and table of charge transfer cross sections of $^{40}Ar^{2+}$ in Kr

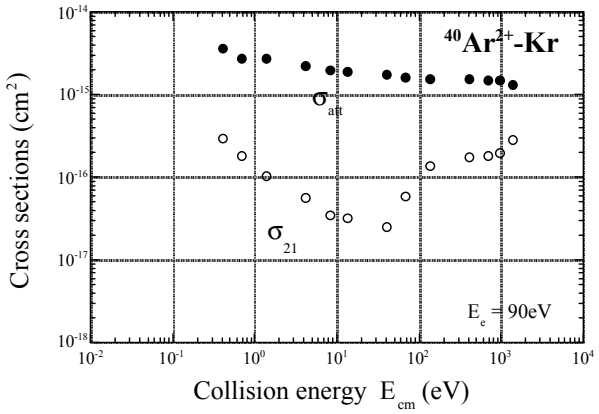

Energy E_{lab}/q (eV/q)	Energy E_{cm} (eV)	Cross sections ($\times 10^{-16}$cm^2) σ_{att}	σ_{21}
0.3	0.41	36.0	2.95
0.5	0.68	27.8	1.87
1.0	1.35	28.0	1.06
3.0	4.06	22.3	0.58
6.0	8.13	19.6	0.35
10.0	13.5	19.1	0.32
30.0	40.6	17.6	0.25
50.0	67.7	16.1	0.59
100	135	15.9	1.37
300	406	15.8	1.77
500	677	15.2	1.82
700	948	15.0	1.96
1000	1355	13.5	2.88

B3-a. Graph and table of charge transfer cross sections of $^{40}Ar^{3+}$ in He

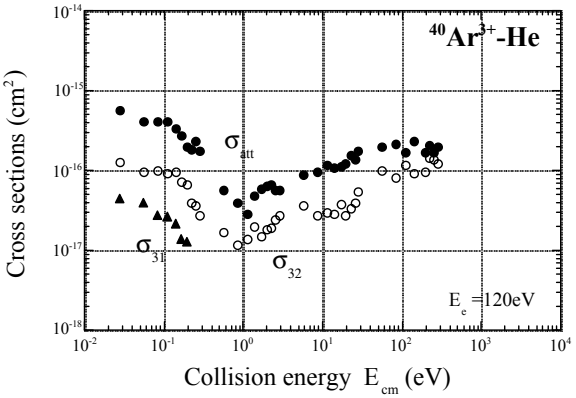

Energy E_{lab}/q (eV)	Energy E_{cm} (eV)	Cross sections ($\times10^{-16}$cm^2) σ_{att}	σ_{32}	σ_{31}
0.1	0.028	5.75	1.26	0.45
0.2	0.056	4.13	0.98	0.39
0.3	0.084	4.17	1.02	0.28
0.4	0.112	4.05	0.92	0.26
0.5	0.140	3.40	0.96	0.22
0.6	0.167	2.77	0.73	0.14
0.7	0.195	2.02	0.66	0.13
0.8	0.223	1.86	0.39	-
0.9	0.251	2.31	0.36	-
1.0	0.279	1.76	0.27	-
2.0	0.558	0.57	0.17	-
3.0	0.837	0.39	0.12	-
4.0	1.12	0.29	0.14	-
5.0	1.40	0.49	0.2	-
6.0	1.67	0.59	0.15	-
7.0	1.95	0.63	0.18	-
8.0	2.23	0.67	0.19	-
10.0	2.79	0.58	0.28	-
20.0	5.58	0.88	0.36	-
30.0	8.37	0.95	0.28	-
40.0	11.2	1.17	0.30	-
50.0	14.0	1.09	0.29	-
60.0	16.7	1.12	0.38	-
70.0	19.5	1.25	0.28	-
80.0	22.3	1.54	0.33	-
90.0	25.1	1.37	0.39	-
100	27.9	1.79	0.55	-
200	55.8	2.00	1.02	-
300	83.7	2.16	0.81	-
400	112	1.71	1.20	-
500	140	2.31	0.92	-
700	195	1.68	0.98	-
800	223	2.10	1.45	-
900	251	1.72	1.40	-

B3-b. Graph and table of charge transfer cross sections of $^{40}Ar^{3+}$ in Ne

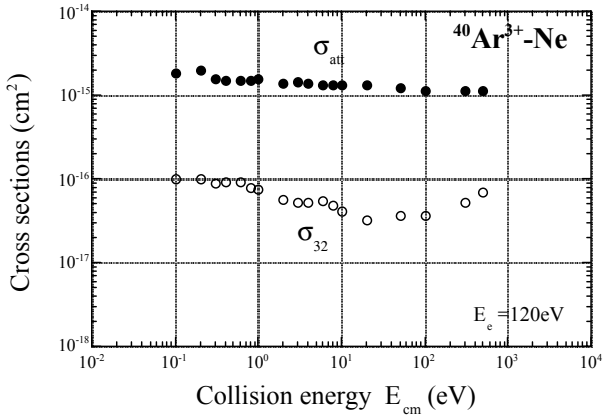

Energy E_{lab}/q (eV/q)	Energy E_{cm} (eV)	Cross sections ($\times10^{-16}$cm^2) σ_{att}	σ_{32}	Energy E_{lab}/q (eV/q)	Energy E_{cm} (eV)	Cross sections ($\times10^{-16}$cm^2) σ_{att}	σ_{32}
0.1	0.1	18.0	1.02	4.0	4.0	14.0	0.53
0.2	0.2	19.6	1.02	6.0	6.0	13.3	0.54
0.3	0.3	15.5	0.9	8.0	8.0	13.5	0.49
0.4	0.4	15.3	0.93	10.0	10.0	13.2	0.42
0.6	0.6	15.0	0.92	20.0	20.0	13.1	0.32
0.8	0.8	14.8	0.8	50.0	50.0	12.1	0.36
1.0	1.0	15.7	0.76	100	100	11.4	0.37
2.0	2.0	14.1	0.58	300	300	11.5	0.53
3.0	3.0	14.3	0.52	500	500	11.2	0.70

B3-c. Graph and table of charge transfer cross sections of $^{40}Ar^{3+}$ in Ar

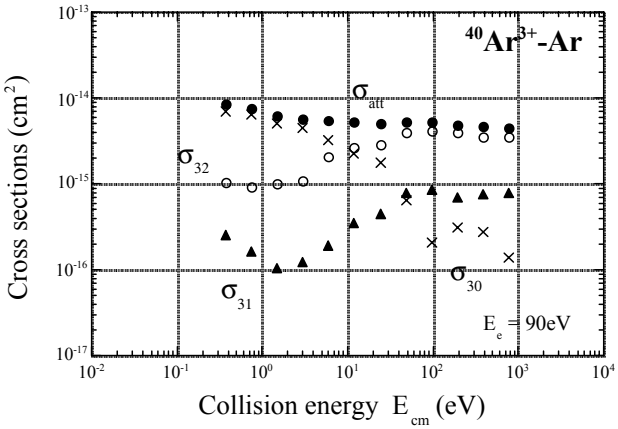

Energy		Cross sections ($\times 10^{-16}$cm^2)			
E_{lab}/q (eV/q)	E_{cm} (eV)	σ_{att}	σ_{32}	σ_{31}	σ_{30} *)
0.25	0.375	83.9	10.4	2.5	71.0
0.5	0.75	75.9	9.2	1.6	65.1
1.0	1.5	62.5	10.1	1.1	51.3
2.0	3.0	56.3	10.9	1.3	44.2
4.0	6.0	55.6	21.1	2.0	32.6
8.0	12.0	52.2	26.2	3.5	22.5
16.0	24.0	51.3	29.0	4.4	17.9
32.0	48.0	53.5	39.3	7.7	6.5
64.0	96.0	52.6	42.0	8.5	2.1
128	192	49.1	38.9	7.1	3.1
256	384	45.8	35.7	7.4	2.7
512	768	44.5	35.3	7.8	1.4

*) σ_{30} was estimated by $\sigma_{30} = \sigma_{att} - \sigma_{31} - \sigma_{32}$

B3-d. Graph and table of charge transfer cross sections of $^{40}Ar^{3+}$ in Kr

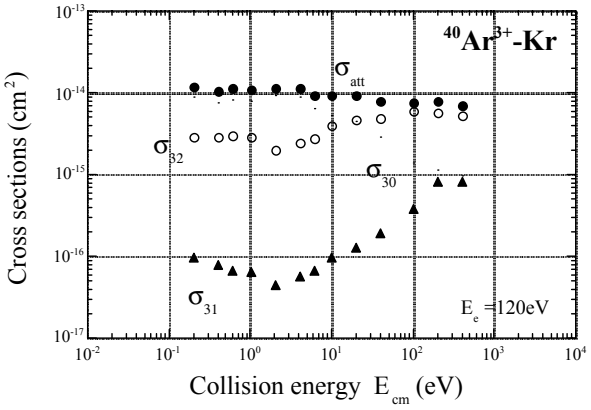

Energy		Cross sections ($\times 10^{-16}$cm^2)		
E_{lab}/q (eV/q)	E_{cm} (eV)	σ_{att}	σ_{32}	σ_{31}
0.1	0.20	118	29	0.96
0.2	0.41	106	28.8	0.78
0.3	0.61	112	29.4	0.68
0.5	1.02	109	29.2	0.64
1.0	2.03	111	19.8	0.45
2.0	4.06	113	24.3	0.57
3.0	6.10	92.2	27.8	0.68
5.0	10.2	92.4	39.1	0.95
10.0	20.3	92.3	46.6	1.28
20.0	40.6	80.0	49.0	1.94
50.0	102	76.6	58.9	3.84
100	203	77.3	57.8	8.08
200	406	70.5	52.6	8.33

B4-a. Graph and table of charge transfer cross sections of $^{84}Kr^{2+}$ in He

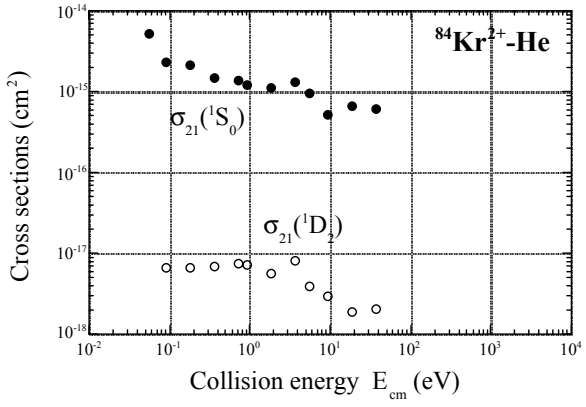

Energy		Cross sections ($\times 10^{-16}$cm^2)	
E_{lab}/q (eV/q)	E_{cm} (eV)	$\sigma_{21}(^1D_2)$	$\sigma_{21}(^1S_0)$
0.6	0.055	-	51.5
1.0	0.091	0.068	23.0
2.0	0.18	0.067	21.2
4.0	0.36	0.070	15.0
8.0	0.73	0.075	13.8
10.0	0.91	0.072	12.5
20.0	1.82	0.058	11.5
40.0	3.64	0.082	13.5
60.0	5.45	0.039	9.7
100	9.09	0.030	5.3
200	18.2	0.019	6.8
400	36.4	0.021	6.3

B4-b. Graph and table of charge transfer cross sections of $^{84}Kr^{2+}$ in Ne

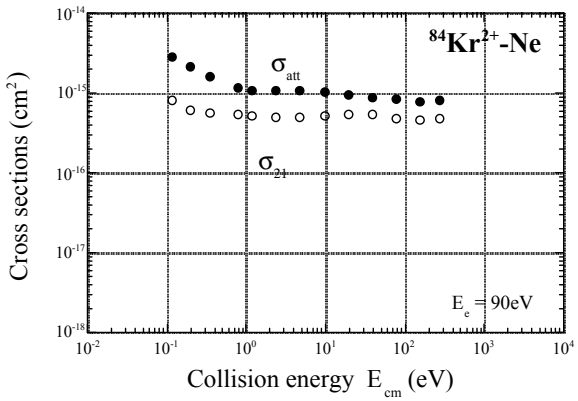

Energy		Cross sections ($\times 10^{-16}$cm$_2$)	
E_{lab}/q (eV/q)	E_{cm} (eV)	σ_{att}	σ_{21}
0.3	0.12	28.6	8.2
0.5	0.19	22.0	6.1
0.9	0.35	16.0	5.6
2.0	0.77	11.8	5.5
3.0	1.15	10.7	5.2
6.0	2.31	11.0	5.1
12.0	4.62	10.9	5.0
25.0	9.62	10.3	5.2
50.0	19.2	9.6	5.4
100	38.5	8.7	5.4
200	76.9	8.5	4.8
400	154	7.9	4.6
700	269	8.1	4.8

B4-c. Graph and table of charge transfer cross sections of $^{84}Kr^{2+}$ in Kr

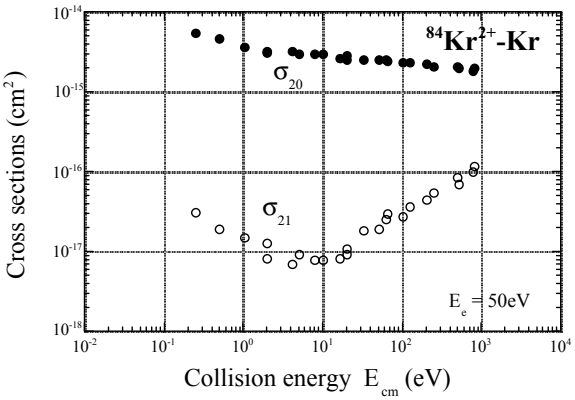

Energy		Cross sections ($\times 10^{-16}$cm^2)		
E_{lab}/q (eV/q)	E_{cm} (eV)	σ_{att}	σ_{21}	σ_{20}
0.25	0.25	55.8	0.31	55.5
0.5	0.5	46.1	0.19	45.9
1.01	1.01	37.1	0.15	37.0
1.98	1.98	31.2	0.08	31.1
2.01	2.01	33.0	0.13	32.9
4.02	4.02	31.8	0.07	31.7
5.03	5.03	30.4	0.09	30.3
7.91	7.91	30.3	0.08	30.2
10.1	10.1	29.3	0.08	29.2
16.1	16.1	26.6	0.08	26.5
19.8	19.8	25.5	0.11	25.4
20.1	20.1	28.4	0.09	28.3
32.7	32.7	25.5	0.18	25.3
50.3	50.3	26.0	0.19	25.8
63.2	63.2	25.9	0.25	25.7
64	64	24.7	0.30	24.4
101	101	23.2	0.27	22.9
126	126	23.4	0.37	23.0
201	201	22.8	0.44	22.4
253	253	21.2	0.54	20.7
503	503	21.6	0.84	20.8
506	506	20.6	0.69	19.9
780	780	19.4	1.0	18.4
804	804	21.0	1.2	19.8

*) σ_{30} was estimated by $\sigma_{20} = \sigma_{att} - \sigma_{21}$.

B5-a. Graph and table of charge transfer cross sections of $^{86}Kr^{3+}$ in Kr

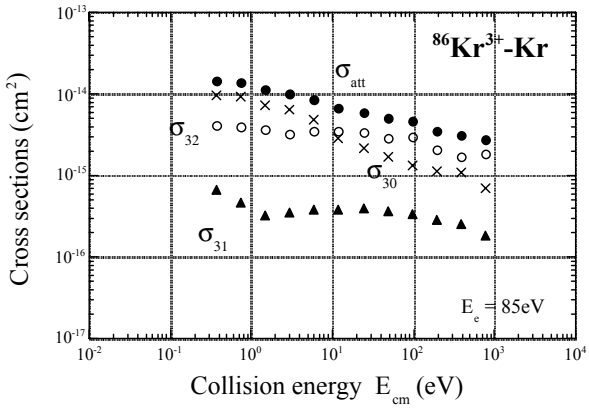

Energy		Cross sections ($\times 10^{-16}$cm^2) E_{el}=85eV			
E_{lab}/q (eV/q)	E_{cm} (eV)	σ_{att}	σ_{32}	σ_{31}	σ_{30} *)
0.25	0.38	144	41.6	6.75	96
0.5	0.75	137	39.0	4.65	93
1.0	1.5	111	36.5	3.18	71
2.0	3.0	99.9	32.1	3.50	64
4.0	6.0	86.8	35.6	3.75	47
8.0	12.0	67.4	34.8	3.74	29
16.0	24.0	59.0	33.2	3.96	22
32.0	48.0	49.5	28.8	3.69	17
64.0	96.0	45.7	29.3	3.32	13
128	192	40.1	20.8	2.88	16
256	384	30.6	17.2	2.50	11
512	768	27.6	18.7	1.84	7

*) σ_{30} was estimated by $\sigma_{30} = \sigma_{att} - \sigma_{32} - \sigma_{31}$.

4.3. Part C: Charge transfer of multiply charged ions produced by Mini-EBIS

C1-a. Graph and table of charge transfer cross sections of $^3He^{2+}$ in He

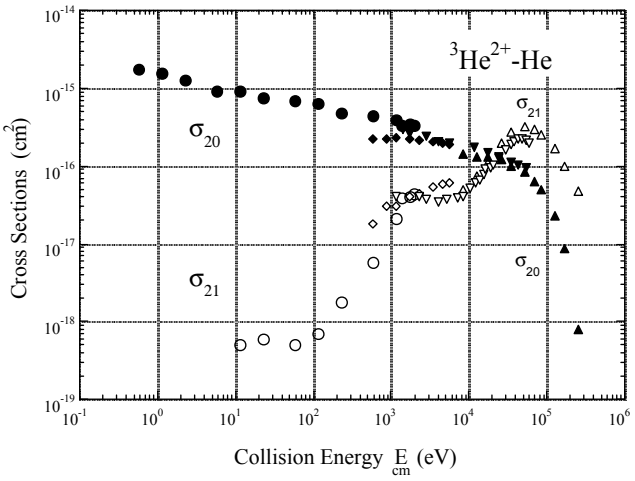

Energy			Cross sections ($\times10^{-16}$cm^2)		
E_{lab}/q (eV/q)	E_{cm} (eV)	E_{amu} (eV/amu)	σ_{att}	σ_{21}	σ_{20}
0.5	0.57	0.33	17.5		17.5
1.0	1.14	0.67	15.9		15.9
2.0	2.29	1.33	12.6		12.6
5.0	5.71	3.33	9.32		9.3
10.0	11.4	6.67	9.38	0.005	9.4
20.0	22.9	13.3	7.49	0.006	7.5
50.0	57.1	33.3	6.82	0.005	6.8
100	114	66.7	6.31	0.007	6.3
200	229	133	4.93	0.018	4.9
500	571	333	4.45	0.059	4.4
1000	1143	667	4.16	0.22	3.9
1200	1371	800	3.75	0.39	3.4
1500	1714	1000	3.84	0.40	3.4
1700	1943	1133	3.77	0.44	3.3

σ_{20} was estimated by $\sigma_{20}=\sigma_{att}-\sigma_{21}$

C1-b. Graph and table of charge transfer cross sections of $^3He^{2+}$ in H_2

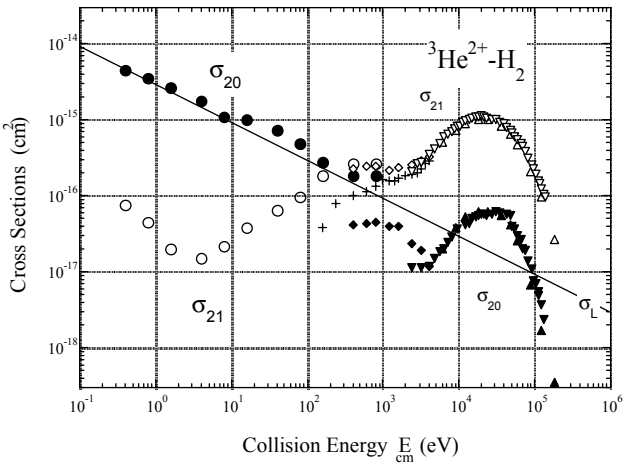

Energy			Cross sections ($\times10^{-16}$cm^2)		
E_{lab}/q (eV/q)	E_{cm} (eV)	E_{amu} (eV/amu)	$\sigma_{\alpha\tau\tau}$	σ_{21}	σ_{20}
0.50	0.40	0.33	45.8	0.75	45.1
1.00	0.80	0.67	36.5	0.44	36.0
2.00	1.60	1.33	27.2	0.20	27.0
5.00	4.00	3.33	17.8	0.15	17.6
10.0	8.00	6.67	11.1	0.22	10.8
20.0	16.0	13.3	10.6	0.38	10.3
50.0	40.0	33.3	8.01	0.66	7.35
100	80.0	66.7	5.78	0.96	4.82
200	160	133	4.60	1.86	2.73
500	400	333	4.52	2.66	1.87
1000	800	667	4.53	2.69	1.85

σ_{20} was estimated by $\sigma_{20}=\sigma_{\alpha\tau\tau}-\sigma_{21}$

C2-a. Graph and table of charge transfer cross sections of $^{13}C^{2+}$ in He

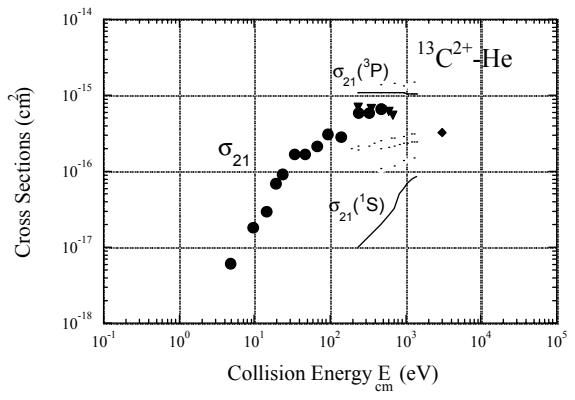

Energy			Cross sections ($\times10^{-16}$cm^2)
E_{lab}/q (eV/q)	E_{cm} (eV)	E_{lab}/q (eV/q)	σ_{21}
10.0	4.71	1.54	0.06
20.0	9.41	3.08	0.18
30.0	14.1	4.62	0.30
40.0	18.8	6.15	0.71
50.0	23.5	7.69	0.93
70.0	32.9	10.8	1.72
100	47.1	15.4	1.73
140	65.9	21.5	2.15
200	94.1	30.8	3.12
300	141	46.2	2.83
500	235	76.9	5.90
700	329	108	6.05
1000	471	154	6.76

C2-b. Graph and table of charge transfer cross sections of $^{13}C^{2+}$ in H_2

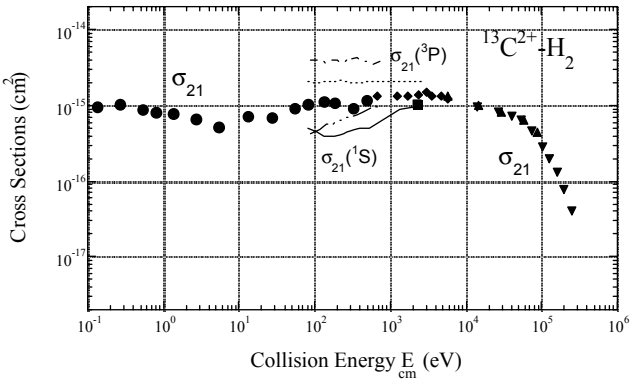

Energy			Cross sections ($\times 10^{-16}$cm^2)
E_{lab}/q (eV/q)	E_{cm} (eV)	E_{lab}/q (eV/q)	σ_{21}
10.0	4.71	1.54	0.06
20.0	9.41	3.08	0.18
30.0	14.1	4.62	0.30
40.0	18.8	6.15	0.71
50.0	23.5	7.69	0.93
70.0	32.9	10.8	1.72
100	47.1	15.4	1.73
140	65.9	21.5	2.15
200	94.1	30.8	3.12
300	141	46.2	2.83
500	235	76.9	5.90
700	329	108	6.05
1000	471	154	6.76

C3-a. Graph and table of charge transfer cross sections of $^{13}C^{3+}$ in He

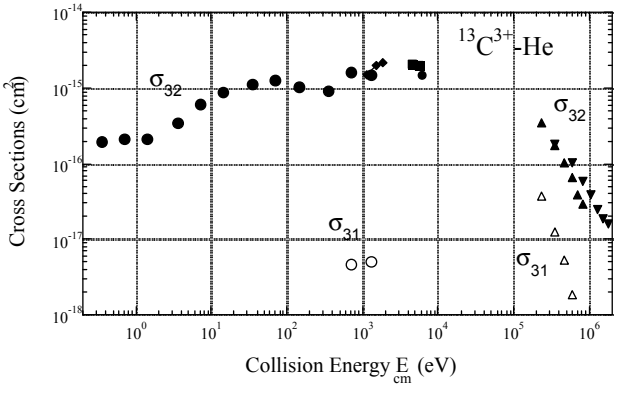

Energy			Cross sections ($\times 10^{-16}$cm^2)	
E_{lab}/q (eV/q)	E_{cm} (eV)	E_{lab}/q (eV/q)	σ_{32}	σ_{31}
0.50	0.35	0.12	2.00	-
1.00	0.71	0.23	2.11	-
2.00	1.41	0.46	2.11	-
5.00	3.53	1.15	3.49	-
10.0	7.06	2.31	6.03	-
20.0	14.1	4.62	8.79	-
50.0	35.3	11.5	11.5	-
100	70.6	23.1	12.9	-
200	141	46.2	10.3	-
500	353	115	9.3	-
1000	706	231	16.5	0.05
1800	1271	415	14.9	0.05

C3-b. Graph and table of charge transfer cross sections of $^{13}C^{3+}$ in H_2

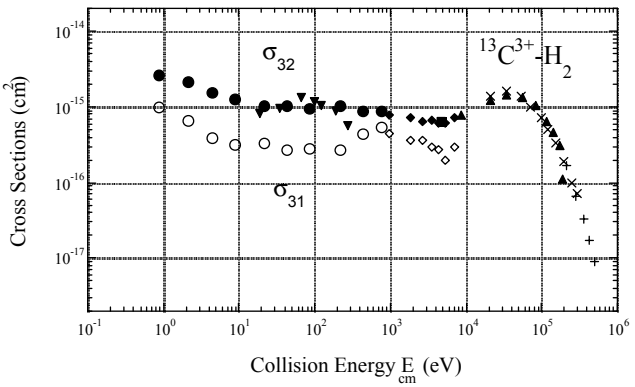

Energy			Cross sections ($\times 10^{-16}$cm^2)	
E_{lab}/q (eV/q)	E_{cm} (eV)	E_{lab}/q (eV/q)	σ_{32}	σ_{31}
2.0	0.8	0.46	26.10	9.80
5.0	2.0	1.15	22.00	6.78
10.0	4.0	2.31	15.30	3.89
20.0	8.0	4.62	12.80	3.22
50.0	20.0	11.5	10.50	3.34
100	40.0	23.1	10.50	2.70
200	80.0	46.2	9.71	2.84
500	200	115	10.30	2.69
1000	400	231	8.72	4.49
1800	720	415	8.73	5.35

C4-a. Graph and table of charge transfer cross sections of $^{12}C^{4+}$ in He

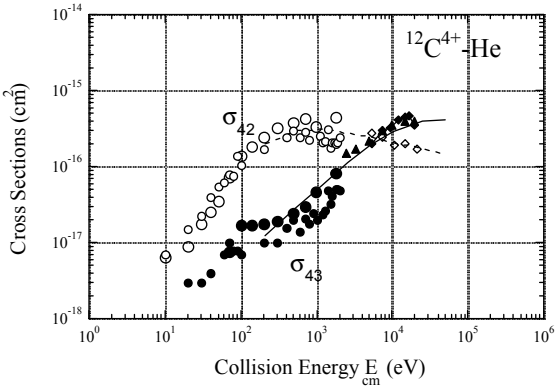

Energy			Cross sections ($\times 10^{-16}$cm^2)	
E_{lab}/q (eV/q)	E_{cm} (eV)	E_{lab}/q (eV/q)	σ_{43}	σ_{42}
10.0	10.0	3.33	-	0.07
20.0	20.0	6.67	0.03	0.15
30.0	30.0	10.0	0.03	0.23
40.0	40.0	13.3	0.04	0.40
50.0	50.0	16.7	-	0.56
60.0	60.0	20.0	0.07	0.63
70.0	70.0	23.3	0.10	0.79
80.0	80.0	26.7	0.08	0.77
90.0	90.0	30.0	0.08	1.39
100	100	33.3	0.07	1.04
200	200	66.7	0.10	1.73
300	300	100	0.10	-
400	400	133	0.16	2.49
500	500	167	0.20	2.99
600	600	200	0.14	2.47
700	700	233	0.21	2.91
800	800	267	0.18	2.24
900	900	300	0.25	-
1000	1000	333	0.20	-
1100	1100	367	-	2.59
1200	1200	400	0.24	2.08
1300	1300	433	0.27	2.22
1400	1400	467	0.46	3.08
1500	1500	500	0.32	1.79
1600	1600	533	0.42	2.05
1700	1701	567	0.81	2.13
1800	1800	600	0.51	2.03
1900	1900	633	0.51	2.06
2000	2000	667	0.49	2.46

C4-e. Graph and table of charge transfer cross sections of $^{12}C^{4+}$ in H_2

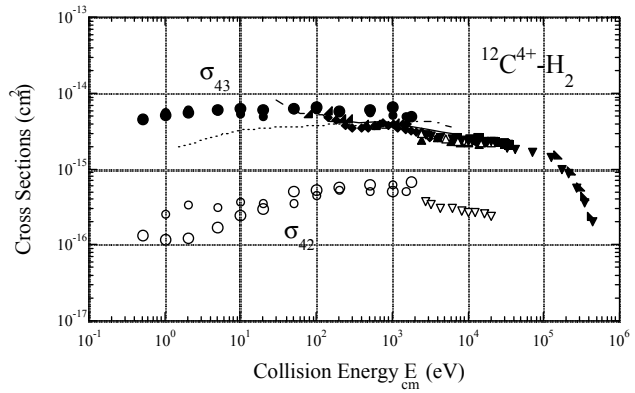

Energy			Cross sections ($\times 10^{-16}$cm^2)	
E_{lab}/q (eV/q)	E_{cm} (eV)	E_{lab}/q (eV/q)	σ_{43}	σ_{42}
0.5	0.29	0.167	47.1	1.33
1.0	0.57	0.333	51.6	1.17
2.0	1.14	0.667	57.4	1.26
5.0	2.86	1.67	61.7	1.69
10.0	5.71	3.33	62.7	2.45
20.0	11.4	6.67	60.7	3.05
50.0	28.6	16.7	65.0	5.15
100	57.1	33.3	65.7	5.33
200	114	66.7	59.8	5.90
500	286	167	60.8	6.36
1000	571	333	66.1	5.20
1800	1029	600	49.5	6.96

C5-a. Graph and table of charge transfer cross sections of $^{12}C^{5+}$ in He

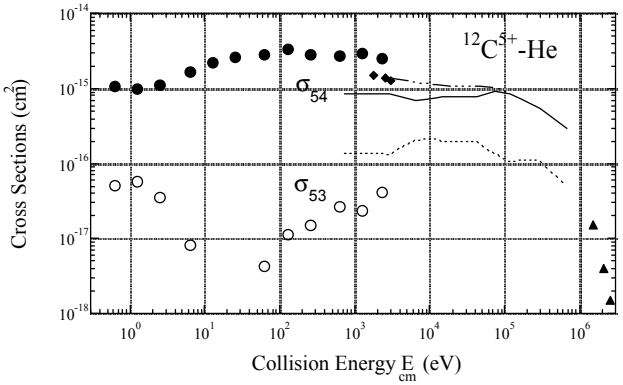

Energy			Cross sections ($\times 10^{-16}$cm^2)	
E_{lab}/q (eV/q)	E_{cm} (eV)	E_{amu} (eV/amu)	σ_{54}	σ_{53}
0.5	0.62	0.21	11.0	0.52
1.0	1.25	0.42	10.0	0.58
2.0	2.50	0.83	11.2	0.36
5.0	6.25	2.08	16.9	0.08
10.0	12.5	4.17	22.7	-
20.0	25.0	8.33	26.9	-
50.0	62.5	20.8	28.2	0.04
100	125	41.7	33.7	0.11
200	250	83.3	28.9	0.16
500	625	208	27.1	0.27
1000	1250	417	29.9	0.24
1800	2250	750	25.7	0.42

C5-b. Graph and table of charge transfer cross sections of $^{12}C^{5+}$ in H_2

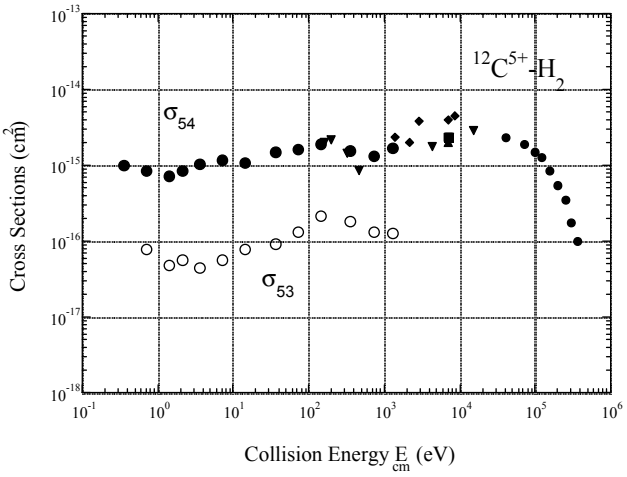

Energy			Cross sections ($\times 10^{-16}$ cm^2)	
E_{lab}/q (eV/q)	E_{cm} (eV)	E_{amu} (eV/amu)	σ_{54}	σ_{53}
0.5	0.36	0.208	10.1	-
1.0	0.71	0.417	8.8	0.79
2.0	1.43	0.833	7.2	0.48
3.0	2.14	1.25	8.6	0.58
5.0	3.57	2.08	10.5	0.46
10.0	7.14	4.17	12.1	0.58
20.0	14.3	8.33	11.1	0.79
50.0	35.7	20.8	15.0	0.94
100	71.4	41.7	16.4	1.33
200	143	83.3	19.0	2.13
500	357	208	15.4	1.84
1000	714	417	13.3	1.35
1800	1286	750	17.1	1.26

C6-a. Graph and table of charge transfer cross sections of $^{13}C^{6+}$ in He

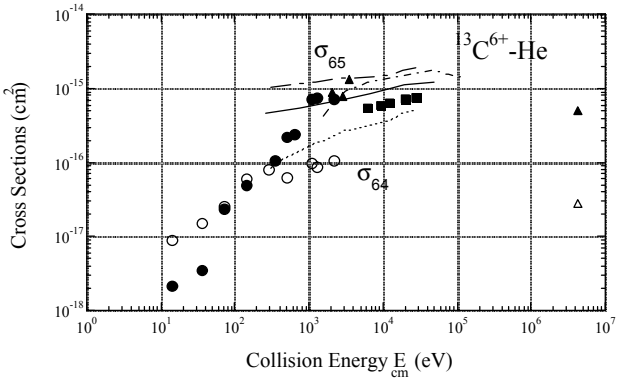

Energy			Cross sections ($\times 10^{-16}$ cm^2)	
Elab/q (eV/q)	Ecm (eV)	Eamu (eV/amu)	σ_{65}	σ_{64}
2.0	0.86	0.50	26.1	9.8
5.0	2.14	1.25	22.0	6.8
10.0	4.29	2.50	15.3	3.9
20.0	8.57	5.00	12.8	3.2
50.0	21.4	12.5	10.5	3.3
100	42.9	25.0	10.5	2.7
200	85.7	50.0	9.71	2.8
500	214	125	10.3	2.7
1000	429	250	8.72	4.5
1800	771	450	8.73	5.3

C6-b. Graph and table of charge transfer cross sections of $^{13}C^{6+}$ in H_2

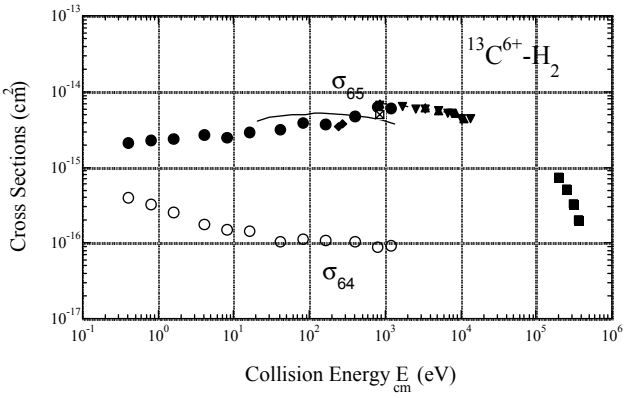

Energy			Cross sections ($\times 10^{-16}$ cm^2)	
E_{lab}/q (eV/q)	E_{cm} (eV)	E_{amu} (eV/amu)	σ_{65}	σ_{64}
0.50	0.40	0.23	21.2	4.03
1.00	0.80	0.46	23.0	3.24
2.00	1.60	0.92	24.0	2.62
5.00	4.00	2.31	27.5	1.76
10.0	8.00	4.62	25.3	1.55
20.0	16.0	9.23	29.6	1.44
50.0	40.0	23.1	31.9	1.07
100	80.0	46.2	38.6	1.16
200	160	92.3	38.4	1.08
500	400	231	49.1	1.06
1000	800	462	63.4	0.91
1500	1200	692	61.3	0.92

C7-a. Graph and table of charge transfer cross sections of $^{14}N^{2+}$ in He

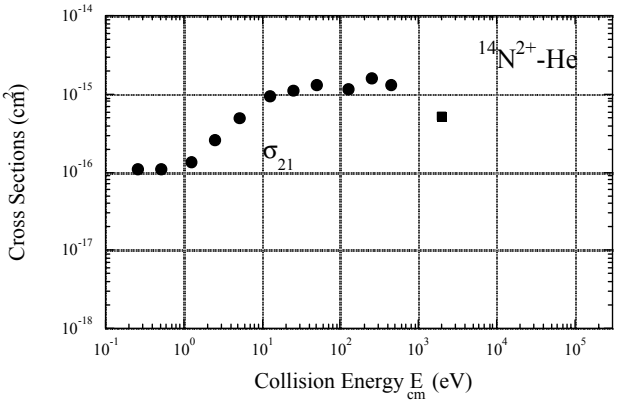

Energy			Cross sections ($\times 10^{-16}$cm^2)
E_{lab}/q (eV/q)	E_{cm} (eV)	E_{amu} (eV/amu)	σ_{21}
1.00	0.25	0.14	1.11
2.00	0.50	0.29	1.11
5.00	1.25	0.71	1.36
10.0	2.50	1.43	2.64
20.0	5.01	2.86	5.08
20.0	25.0	4.29	-
50.0	12.5	7.14	9.76
100	25.0	14.3	11.3
200	50.1	28.6	13.3
500	125	71.4	11.7
1001	250	143	16.2
1799	450	257	13.5

C7-b. Graph and table of charge transfer cross sections of $^{14}N^{2+}$ in H_2

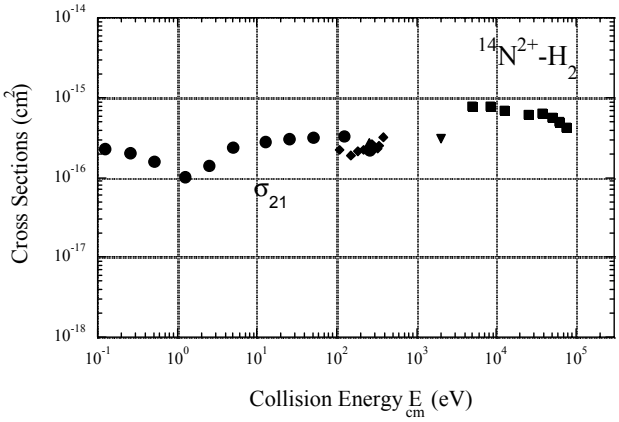

Energy			Cross sections ($\times 10^{-16}$cm^2)
E_{lab}/q (eV/q)	E_{cm} (eV)	E_{amu} (eV/amu)	σ_{21}
0.50	0.12	0.071	2.32
1.00	0.25	0.14	2.07
2.00	0.50	0.29	1.59
5.00	1.25	0.71	1.04
10.0	2.50	1.43	1.42
20.0	5.01	2.86	2.41
50.0	12.5	7.14	2.79
100	25.0	14.3	3.03
200	50.1	28.6	3.16
500	125	71.4	3.32
1000	250	143	2.22

C8-a. Graph and table of charge transfer cross sections of $^{14}N^{3+}$ in He

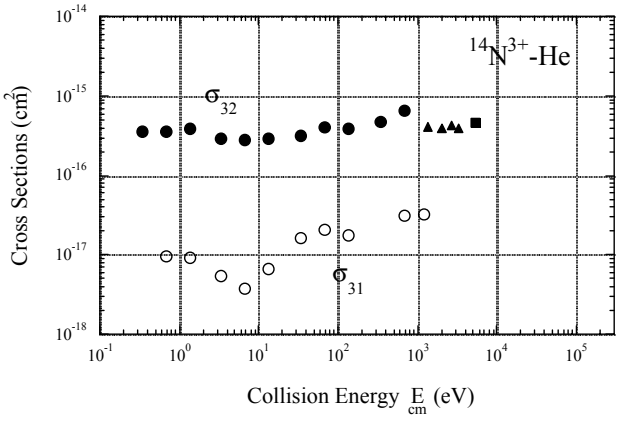

Energy			Cross sections ($\times 10^{-16}$cm^2)	
E_{lab}/q (eV/q)	E_{cm} (eV)	E_{amu} (eV/amu)	σ_{32}	σ_{31}
0.75	0.33	0.11	3.55	-
1.50	0.67	0.21	3.62	0.10
3.00	1.33	0.43	3.99	0.10
7.49	3.33	1.07	2.99	0.06
15.0	6.67	2.14	2.84	0.04
30.0	13.3	4.29	2.97	0.07
74.9	33.3	10.7	3.26	0.16
150	66.7	21.4	4.07	0.21
300	133	42.9	3.89	0.18
749	333	107	4.86	-
1500	667	214	6.66	0.32
2702	1201	386.0	-	0.33

C8-b. Graph and table of charge transfer cross sections of $^{14}N^{3+}$ in H_2

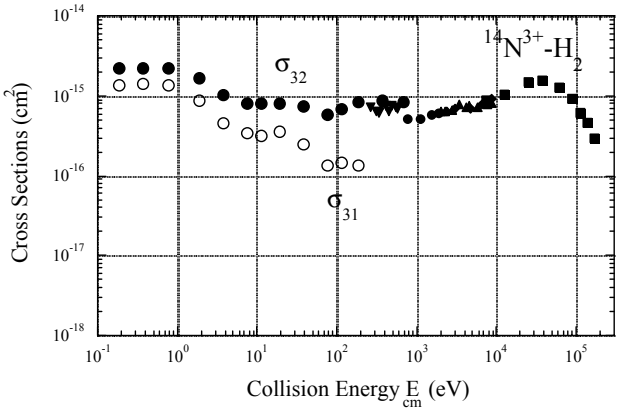

Energy			Cross sections ($\times 10^{-16}$cm^2)	
E_{lab}/q (eV/q)	E_{cm} (eV)	E_{amu} (eV/amu)	σ_{32}	σ_{31}
0.50	0.19	0.11	22.6	14
1.00	0.38	0.21	22.4	14.2
2.00	0.75	0.43	22.3	13.6
5.00	1.87	1.07	16.7	8.7
10.0	3.75	2.14	10.5	4.64
20.0	7.50	4.29	8.17	3.51
30.0	11.3	6.43	8.09	3.19
50.0	18.7	10.7	8.26	3.56
100	37.5	21.4	7.54	2.54
200	75.0	42.9	5.86	1.39
300	113	64.3	6.81	1.47
500	187	107	8.45	1.35
1000	375	214	8.75	-
1800	675	386	8.46	-

C9-a. Graph and table of charge transfer cross sections of $^{14}N^{4+}$ in He

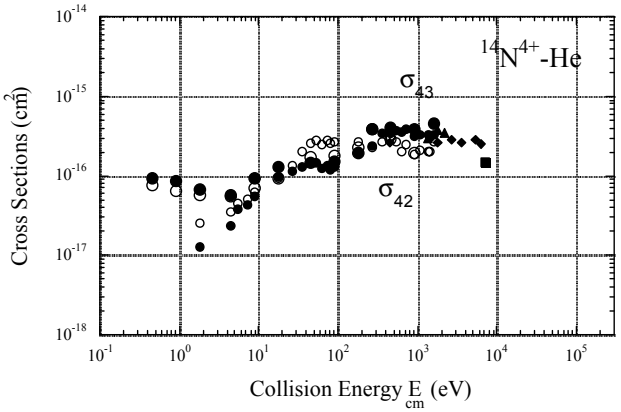

Energy			Cross sections ($\times 10^{-16}$cm^2)	
E_{lab}/q (eV/q)	E_{cm} (eV)	E_{amu} (eV/amu)	σ_{43}	σ_{42}
0.50	0.44	0.14	0.94	0.76
1.00	0.89	0.29	0.87	0.66
2.00	1.78	0.57	0.68	0.59
5.00	4.44	1.43	0.59	0.57
10.0	8.90	2.86	0.94	0.72
20.0	17.8	5.71	1.31	0.95
50.0	44.5	14.3	1.50	1.72
100	89.0	28.6	1.57	1.85
200	178	57.1	1.98	2.27
300	267	85.7	3.98	3.88
500	445	143	4.06	2.90
1000	890	286	3.94	1.94
1800	1600	514	4.53	-

C9-b. Graph and table of charge transfer cross sections of $^{14}N^{4+}$ in H_2

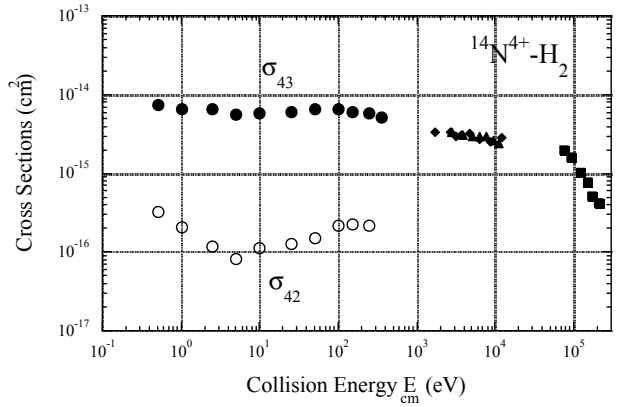

Energy			Cross sections ($\times 10^{-16}$cm^2)	
E_{lab}/q (eV/q)	E_{cm} (eV)	E_{amu} (eV/amu)	σ_{43}	σ_{42}
1.00	0.50	0.29	75.2	3.35
2.00	1.00	0.57	67.5	2.14
5.00	2.50	1.43	65.4	1.21
10.0	5.0	2.86	56.2	0.81
20.0	10.0	5.71	58.8	1.14
50.0	25.0	14.3	60.6	1.27
100	50.0	28.6	66.5	1.51
200	100	57.1	65.7	2.21
300	150	85.7	60.5	2.27
500	250	143	58.2	2.19
700	350	200	51.4	-

C10-a. Graph and table of charge transfer cross sections of $^{14}N^{5+}$ in He

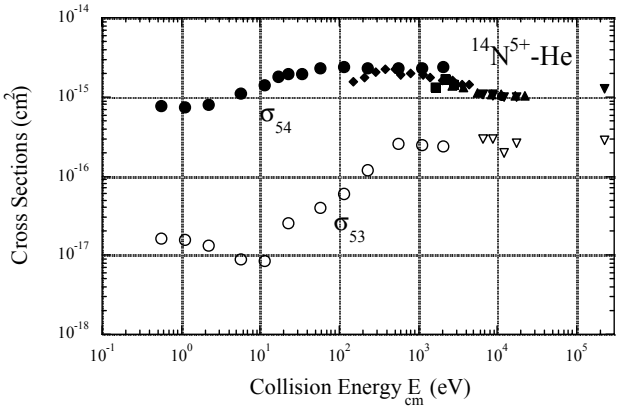

Energy			Cross sections ($\times 10^{-16}$cm^2)	
E_{lab}/q (eV/q)	E_{cm} (eV)	E_{amu} (eV/amu)	σ_{54}	σ_{53}
0.50	0.56	0.179	7.74	0.17
1.00	1.11	0.357	7.58	0.16
2.00	2.22	0.714	8.25	0.13
5.00	5.57	1.79	11.5	0.09
10.0	11.1	3.57	14.2	0.09
15.0	16.7	5.36	18.6	-
20.0	22.2	7.14	20.1	0.26
30.0	33.3	10.7	19.6	-
50.0	55.7	17.9	23.7	0.41
100	111	35.7	24.3	0.61
200	222	71.4	23.3	1.20
500	557	179	23.9	2.66
1000	1111	357	23.3	2.48
1800	2000	643	24.9	2.38

C10-b. Graph and table of charge transfer cross sections of $^{14}N^{5+}$ in H_2

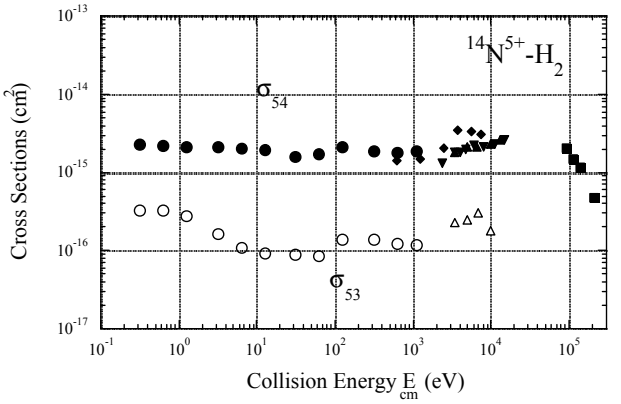

Energy			Cross sections ($\times 10^{-16}$cm^2)	
E_{lab}/q (eV/q)	E_{cm} (eV)	E_{amu} (eV/amu)	σ_{54}	σ_{53}
0.50	0.31	0.18	23.1	3.27
1.00	0.62	0.36	22.1	3.27
2.00	1.25	0.71	21.4	2.77
5.00	3.12	1.79	21.6	1.67
10.0	6.25	3.57	20.1	1.11
20.0	12.5	7.14	19.5	0.95
50.0	31.2	17.9	16.3	0.88
100	62.5	35.7	17.3	0.86
200	125	71.4	21.2	1.38
500	312	179	18.6	1.41
1000	625	357	18.0	1.24
1800	1125	643	18.6	1.19

C11-a. Graph and table of charge transfer cross sections of $^{14}N^{6+}$ in He

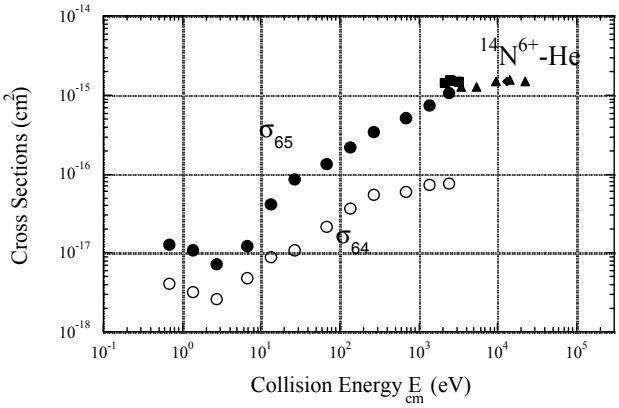

Energy			Cross sections ($\times 10^{-16}$cm^2)	
E_{lab}/q (eV/q)	E_{cm} (eV)	E_{amu} (eV/amu)	σ_{65}	σ_{64}
0.50	0.67	0.21	0.13	0.04
1.00	1.33	0.43	0.11	0.03
2.00	2.67	0.86	0.07	0.03
5.00	6.66	2.14	0.12	0.05
10.0	13.3	4.29	0.43	0.09
20.0	26.7	8.57	0.87	0.11
50.0	66.6	21.4	1.37	0.22
100	133	42.9	2.19	0.37
200	267	85.7	3.46	0.55
499	666	214	5.17	0.61
1000	1335	429	7.49	0.74
1800	2399	771	10.9	0.77

C11-b. Graph and table of charge transfer cross sections of $^{14}N^{6+}$ in H_2

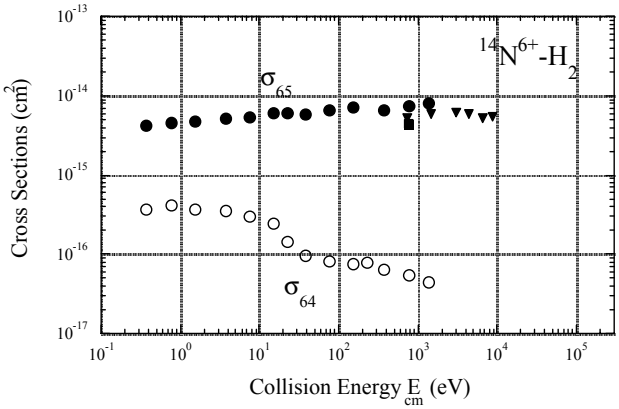

Energy			Cross sections ($\times 10^{-16}$cm^2)	
E_{lab}/q (eV/q)	E_{cm} (eV)	E_{amu} (eV/amu)	σ_{65}	σ_{64}
0.50	0.38	0.21	43.0	3.72
1.00	0.75	0.43	45.5	4.28
2.00	1.50	0.86	48.6	3.77
5.00	3.75	2.14	51.9	3.58
10.0	7.50	4.29	55.3	3.08
20.0	15.0	8.57	61.0	2.50
30.0	22.5	12.9	62.2	1.46
50.0	37.5	21.4	59.8	0.98
100	75.0	42.9	65.6	0.82
200	150	85.7	72.7	0.77
300	225	129	-	0.79
500	375	214	66.0	0.65
1000	750	429	76.5	0.55
1800	1350	771	82.2	0.44

C12-a. Graph and table of charge transfer cross sections of $^{16}O^{2+}$ in He

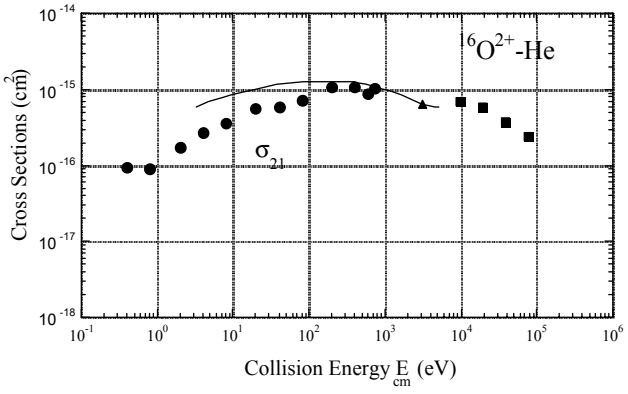

Energy			Cross sections ($\times 10^{-16}$cm^2)
E_{lab}/q (eV/q)	E_{cm} (eV)	E_{amu} (eV/amu)	σ_{21}
1.0	0.40	0.13	0.96
2.0	0.80	0.25	0.90
5.0	2.0	0.63	1.72
10.0	4.0	1.25	2.74
20.0	8.0	2.50	3.68
50.0	20.0	6.25	5.77
100	40.0	12.5	5.82
200	80.0	25.0	7.36
500	200	62.5	10.8
1000	400	125	10.8
1500	600	188	8.68
1800	720	225	10.2

Note: O^{2+} beam contained metastable ions of 3.5%.

C12-b. Graph and table of charge transfer cross sections of $^{16}O^{2+}$ in H_2

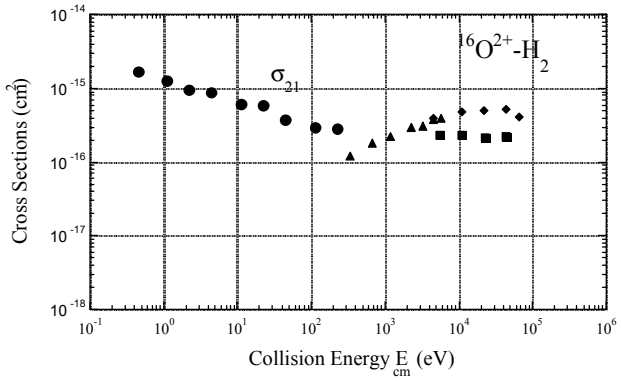

Energy			Cross sections ($\times10^{-16}$cm^2)
E_{lab}/q (eV/q)	E_{cm} (eV)	E_{amu} (eV/amu)	σ_{21}
2.0	0.44	0.25	17.1
5.0	1.11	0.63	12.7
10.0	2.22	1.25	9.76
20.0	4.44	2.50	8.82
50.0	11.1	6.25	6.26
100	22.2	12.5	5.98
200	44.4	25.0	3.84
500	111	62.5	2.99
1000	222	125	2.80

Note: O^{2+} beam contained metastable ions of 3.5%.

C13-a. Graph and table of charge transfer cross sections of $^{16}O^{3+}$ in He

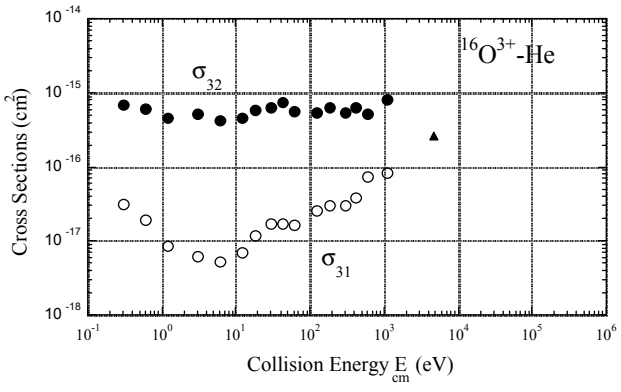

Energy			Cross sections ($\times10^{-16}$cm^2)	
E_{lab}/q (eV/q)	E_{cm} (eV)	E_{amu} (eV/amu)	σ_{32}	σ_{31}
0.5	0.3	0.09	6.81	0.31
1.0	0.6	0.19	6.26	0.19
2.0	1.2	0.38	4.67	0.08
5.0	3.0	0.94	5.25	0.06
10.0	6.0	1.88	4.24	0.05
20.0	12.0	3.75	4.59	0.07
30.0	18.0	5.63	5.84	0.12
50.0	30.0	9.38	6.43	0.17
70.0	42.0	13.1	7.50	0.17
100	60.0	18.8	5.70	0.17
200	120	37.5	5.40	0.26
300	180	56.3	6.30	0.30
500	300	93.8	5.41	0.31
700	420	131	6.44	0.38
1000	600	188	5.21	0.75
1800	1080	338	8.30	0.83

C13-b. Graph and table of charge transfer cross sections of $^{16}O^{3+}$ in H_2

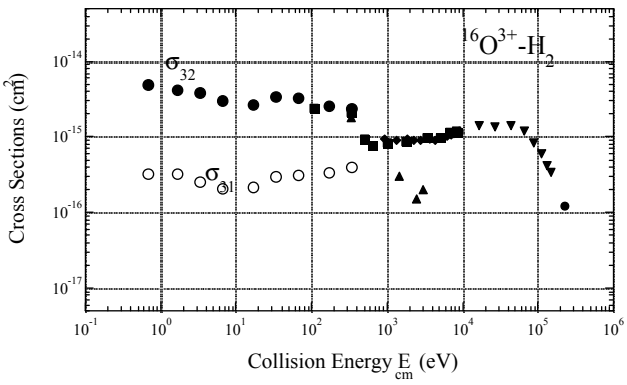

Energy			Cross sections ($\times10^{-16}$cm^2)	
E_{lab}/q (eV/q)	E_{cm} (eV)	E_{amu} (eV/amu)	σ_{32}	σ_{31}
0.5	0.62	0.21	11.0	0.52
2.0	0.67	0.38	48.9	3.25
5.0	1.67	0.94	42.9	3.28
10.0	3.33	1.88	39.5	2.54
20.0	6.67	3.75	31.1	2.09
50.0	16.7	9.38	27.1	2.17
100	33.3	18.8	34.7	3.07
200	66.7	37.5	33.5	3.14
500	167	93.8	25.9	3.42
1000	333	188	23.5	3.95

C14-a. Graph and table of charge transfer cross sections of $^{18}O^{4+}$ in He

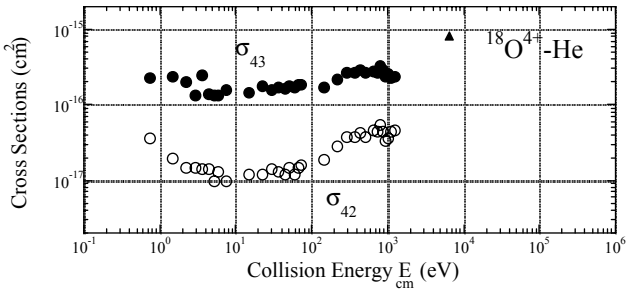

Energy			Cross sections ($\times 10^{-16}$cm^2)	
E_{lab}/q (eV/q)	E_{cm} (eV)	E_{amu} (eV/amu)	σ_{43}	σ_{42}
6.0	4.36	1.33	1.43	0.14
7.0	5.09	1.56	1.37	0.10
8.0	5.82	1.78	1.33	0.13
10.0	7.27	2.22	1.61	0.10
20.0	14.5	4.44	1.49	0.12
30.0	21.8	6.67	1.79	0.12
40.0	29.1	8.89	1.62	0.14
50.0	36.4	11.1	1.70	0.13
60.0	43.6	13.3	1.63	0.12
70.0	50.9	15.6	1.78	0.15
80.0	58.2	17.8	1.71	0.12
90.0	65.5	20.0	1.90	0.15
100	72.7	22.2	1.87	0.16
200	145	44.4	1.75	0.19
300	218	66.7	2.21	0.29
400	291	88.9	2.67	0.38
500	364	111	2.67	0.38
600	436	133	2.91	0.43
700	509	156	2.72	0.38
900	655	200	2.76	0.47
1000	727	222	2.73	0.45
1100	800	244	3.31	0.54
1200	873	267	2.94	0.44
1300	945	289	2.44	0.33
1400	1018	311	2.55	0.36
1500	1091	333	2.30	0.45
1700	1236	378	2.44	0.47

C14-b. Graph and table of charge transfer cross sections of $^{18}O^{4+}$ in H_2

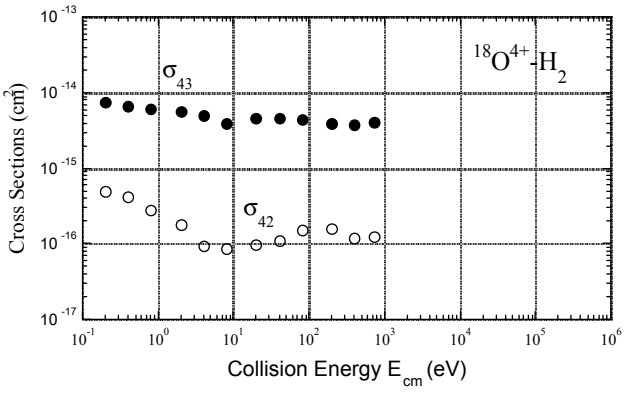

Energy			Cross sections ($\times 10^{-16}$cm^2)	
E_{lab}/q (eV/q)	E_{cm} (eV)	E_{amu} (eV/amu)	σ_{43}	σ_{42}
0.5	0.20	0.11	74.2	4.88
1.0	0.40	0.22	66.6	4.28
2.0	0.80	0.44	62.4	2.79
5.0	2.0	1.11	56.3	1.78
10.0	4.0	2.22	50.3	0.94
20.0	8.0	4.44	39.6	0.86
50.0	20.0	11.1	45.8	0.96
100	40.0	22.2	47.0	1.11
200	80.0	44.4	44.3	1.51
500	200	111	39.3	1.58
1000	400	222	38.1	1.20
1800	720	400	41.5	1.22

C15-a. Graph and table of charge transfer cross sections of $^{16}O^{5+}$ in He

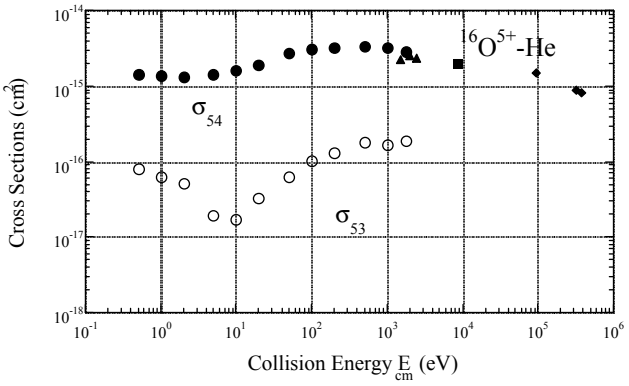

Energy			Cross sections ($\times 10^{-16}$cm^2)	
E_{lab}/q (eV/q)	E_{cm} (eV)	E_{amu} (eV/amu)	σ_{54}	σ_{54}
0.5	0.5	0.16	14.6	0.79
1.0	1.0	0.31	13.6	0.64
2.0	2.0	0.63	13.1	0.52
5.0	5.0	1.56	14.2	0.20
10.0	10.0	3.13	16.0	0.17
20.0	20.0	6.25	19.5	0.33
50.0	50.0	15.6	27.6	0.64
100	100	31.3	31.2	1.04
200	200	62.5	31.9	1.34
500	500	156	33.9	1.85
1000	1000	313	31.9	1.69
1800	1800	563	29.0	1.86

C15-b. Graph and table of charge transfer cross sections of $^{16}O^{5+}$ in H_2

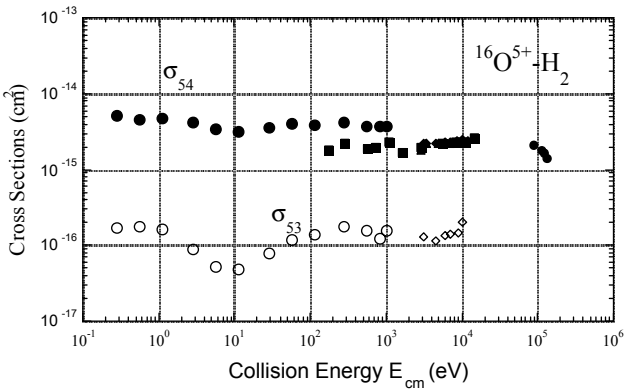

Energy			Cross sections ($\times 10^{-16}$cm^2)	
E_{lab}/q (eV/q)	E_{cm} (eV)	E_{amu} (eV/amu)	σ_{54}	σ_{54}
0.5	0.28	0.16	52.3	1.75
1.0	0.56	0.31	46.8	1.82
2.0	1.11	0.63	48.2	1.67
5.0	2.78	1.56	43.0	0.88
10.0	5.56	3.13	34.4	0.53
20.0	11.1	6.25	31.8	0.48
50.0	27.8	15.6	36.4	0.79
100	55.6	31.3	40.1	1.21
200	111	62.5	39.6	1.40
500	278	156	42.5	1.82
1000	556	313	37.8	1.61
1500	833	469	37.8	1.22
1800	1000	563	37.6	1.59

C16-a. Graph and table of charge transfer cross sections of $^{16}O^{6+}$ in He

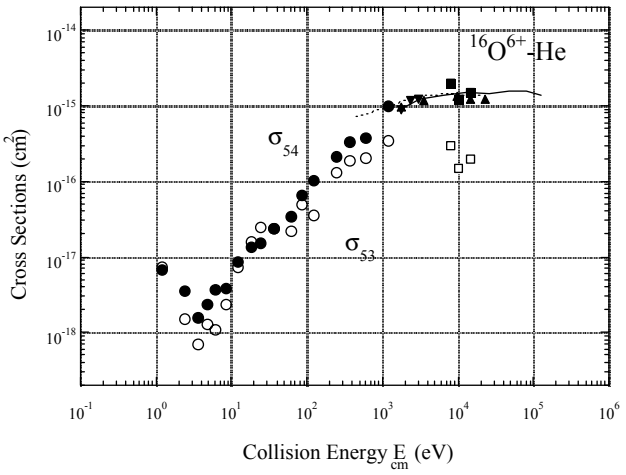

Energy			Cross sections ($\times 10^{-16}$cm^2)	
E_{lab}/q (eV/q)	E_{cm} (eV)	E_{amu} (eV/amu)	σ_{65}	σ_{64}
1.0	1.2	0.38	0.069	0.073
2.0	2.4	0.75	0.035	0.015
3.0	3.6	1.13	0.016	0.007
4.0	4.8	1.50	0.024	0.013
5.0	6.0	1.88	0.037	0.011
7.0	8.4	2.63	0.039	0.024
10.0	12.0	3.75	0.088	0.073
15.0	18.0	5.63	0.14	0.16
20.0	24.0	7.50	0.16	0.25
30.0	36.0	11.3	0.24	0.24
50.0	60.0	18.8	0.35	0.22
70.0	84.0	26.3	0.65	0.50
100	120	37.5	1.05	0.36
200	240	75.0	2.17	1.30
300	360	113	3.32	1.91
500	600	188	3.75	2.04
1000	1200	375	9.86	3.49

C16-b. Graph and table of charge transfer cross sections of $^{18}O^{6+}$ in H_2

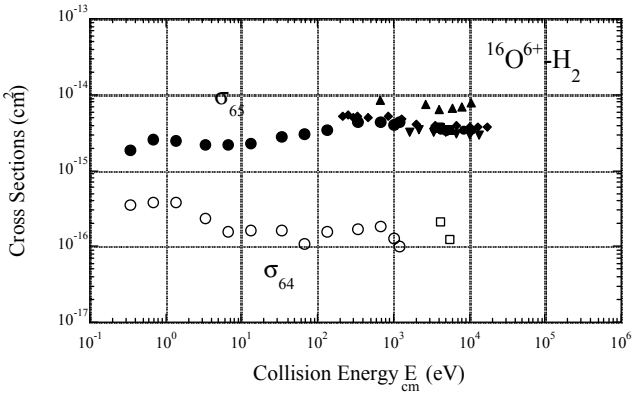

Energy			Cross sections ($\times 10^{-16}$cm^2)	
E_{lab}/q (eV/q)	E_{cm} (eV)	E_{amu} (eV/amu)	σ_{65}	σ_{64}
0.5	0.33	0.19	19.0	3.59
1.0	0.67	0.38	26.2	3.81
2.0	1.33	0.75	25.6	3.83
5.0	3.33	1.88	22.2	2.42
10.0	6.67	3.75	22.1	1.56
20.0	13.3	7.50	23.5	1.65
50.0	33.3	18.8	28.0	1.64
100	66.7	37.5	30.7	1.08
200	133	75.0	34.4	1.56
500	333	188	44.0	1.75
1000	667	375	44.9	1.87
1500	1000	563	41.3	1.28
1800	1200	675	44.9	1.00

C17-a. Graph and table of charge transfer cross sections of $^{40}Ar^{6+}$ in He

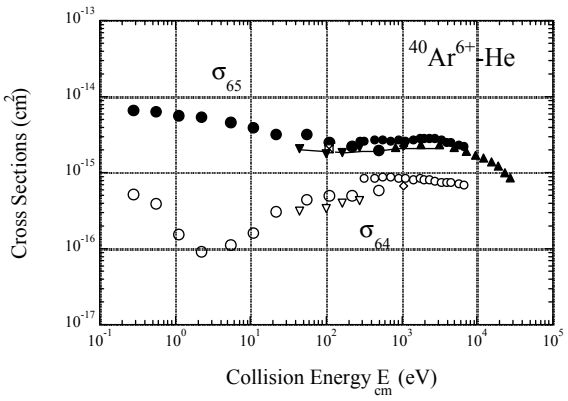

Energy			Cross sections ($\times 10^{-16}$cm^2)	
E_{lab}/q (eV/q)	E_{cm} (eV)	E_{amu} (eV/amu)	σ_{65}	σ_{64}
0.50	0.27	0.08	68.5	5.36
1.00	0.55	0.15	64.5	3.99
2.00	1.09	0.30	58.4	1.57
4.00	2.18	0.60	55.6	0.92
10.0	5.45	1.50	47.2	1.14
20.0	10.9	3.00	40.5	1.64
40.0	21.8	6.00	33.0	3.12
100	54.5	15.0	33.1	4.43
200	109	30.0	26.0	4.99
400	218	60.0	22.7	5.08
900	491	135	20.4	5.88

C17-b. Graph and table of charge transfer cross sections of $^{40}Ar^{6+}$ in H_2

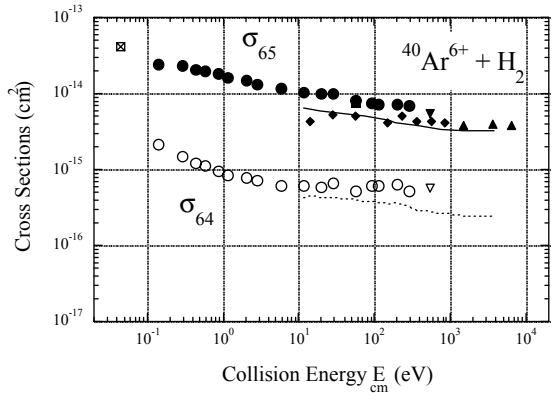

Energy			Cross sections ($\times 10^{-16}$cm^2)	
E_{lab}/q (eV/q)	E_{cm} (eV)	E_{amu} (eV/amu)	σ_{65}	σ_{64}
0.50	0.14	0.075	248	21.4
1.00	0.29	0.150	235	15.2
1.50	0.43	0.225	211	12.5
2.00	0.57	0.300	200	11.2
3.00	0.86	0.450	185	9.72
4.00	1.14	0.600	161	8.69
7.00	2.00	1.05	152	7.86
10.0	2.86	1.50	134	7.19
20.0	5.71	3.00	117	6.27
40.0	11.4	6.00	105	6.16
70.0	20.0	10.5	100	5.91
100	28.6	15.0	103	6.76
200	57.1	30.0	82.6	5.34
320	91.4	48.0	76.7	6.11
400	114	60.0	72.1	6.26
700	200	105	73.6	6.38
1000	286	150	70.5	5.24

C18-a. Graph and table of charge transfer cross sections of $^{40}Ar^{7+}$ in He

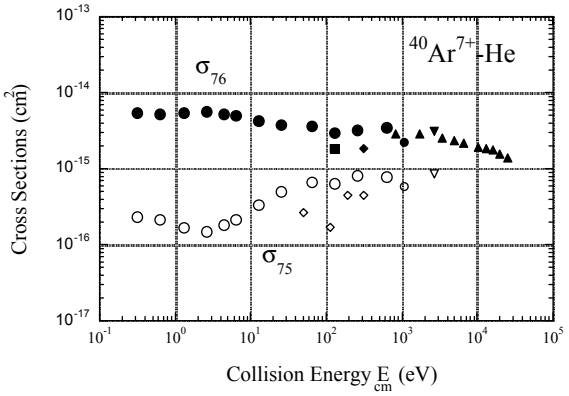

Energy			Cross sections ($\times 10^{-16}$cm^2)	
E_{lab}/q (eV/q)	E_{cm} (eV)	E_{amu} (eV/amu)	σ_{76}	σ_{75}
0.50	0.318	0.087	54.2	2.34
1.00	0.636	0.175	53.9	2.14
2.00	1.27	0.350	54.6	1.71
4.00	2.55	0.700	56.6	1.52
7.00	4.45	1.23	53.3	1.86
10.0	6.36	1.75	49.9	2.16
20.0	12.7	3.50	43.9	3.35
40.0	25.5	7.00	37.7	5.04
100	63.6	17.5	36.3	6.85
200	127	35.0	30.6	6.52
400	255	70.0	32.9	8.20
1000	636	175	36.0	7.92

C18-b. Graph and table of charge transfer cross sections of $^{40}Ar^{7+}$ in H_2

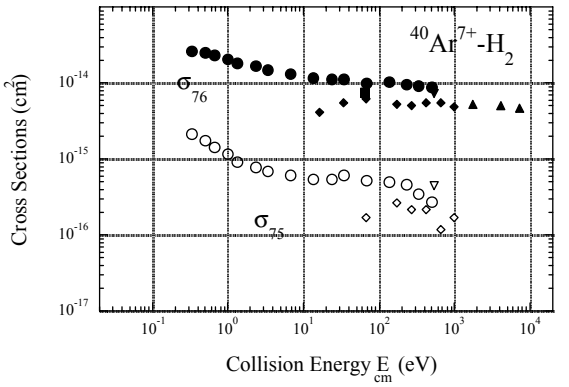

Energy			Cross sections ($\times 10^{-16}$cm^2)	
E_{lab}/q (eV/q)	E_{cm} (eV)	E_{amu} (eV/amu)	σ_{76}	σ_{75}
1.0	0.333	0.175	268	21.4
1.5	0.500	0.263	251	17.7
2.0	0.667	0.350	233	14.2
3.0	1.00	0.525	207	11.6
4.0	1.33	0.700	182	9.40
7.0	2.33	1.23	169	7.97
10.0	3.33	1.75	152	6.94
20.0	6.67	3.50	135	6.14
40.0	13.3	7.00	116	5.56
70.0	23.3	12.3	114	5.52
100	33.3	17.5	114	6.28
200	66.7	35.0	99.0	5.25
400	133	70.0	103	5.08
700	233	123	97.5	4.71
1000	333	175	90.9	3.48
1500	500	263	89.3	2.79

C19-a. Graph and table of charge transfer cross sections of $^{40}Ar^{8+}$ in He

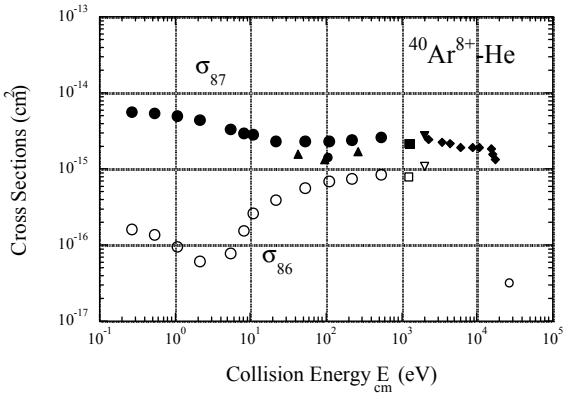

Energy			Cross sections ($\times 10^{-16}$cm^2)	
E_{lab}/q (eV/q)	E_{cm} (eV)	E_{amu} (eV/amu)	σ_{87}	σ_{86}
0.50	0.27	0.10	56.4	1.66
1.00	0.53	0.20	54.5	1.38
2.00	1.07	0.40	49.8	0.98
4.00	2.13	0.80	45.2	0.63
10.0	5.33	2.00	33.2	0.79
15.0	8.00	3.00	30.5	1.60
20.0	10.7	4.00	28.3	2.67
40.0	21.3	8.00	23.4	3.97
100	53.3	20.0	23.2	5.80
200	107	40.0	24.0	6.98
400	213	80.0	24.1	7.69
1000	533	200	26.8	8.65

C19-b. Graph and table of charge transfer cross sections of $^{40}Ar^{8+}$ in H_2

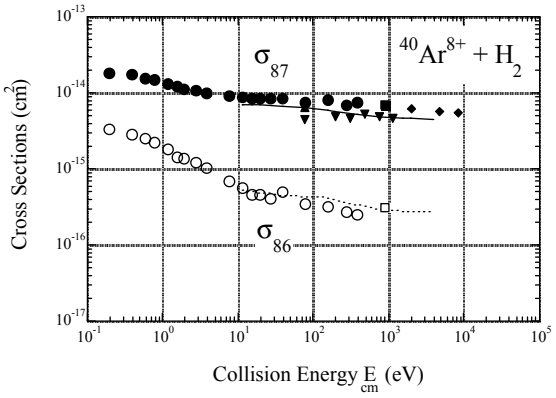

Energy			Cross sections ($\times10^{-16}$cm^2)	
E_{lab}/q (eV/q)	E_{cm} (eV)	E_{amu} (eV/amu)	σ_{87}	σ_{86}
0.50	0.190	0.10	188	34.6
1.00	0.381	0.20	179	28.8
1.50	0.571	0.30	160	25.1
2.00	0.762	0.40	149	22.5
3.00	1.14	0.60	133	18.5
4.00	1.52	0.80	123	14.5
5.00	1.90	1.00	115	13.9
7.00	2.67	1.40	109	12.3
10.0	3.81	2.00	102	10.3
20.0	7.62	4.00	93.3	7.09
30.0	11.4	6.00	87.8	5.77
40.0	15.2	8.00	84.9	4.64
50.0	19.0	10.0	85.8	4.62
70.0	26.7	14.0	85.5	4.12
100	38.1	20.0	87.0	5.00
200	76.2	40.0	75.7	3.48
400	152	80.0	82.2	3.27
700	267	140	71.4	2.77
1000	381	200	75.4	2.58

C20-a. Graph and table of charge transfer cross sections of $^{40}Ar^{9+}$ in He

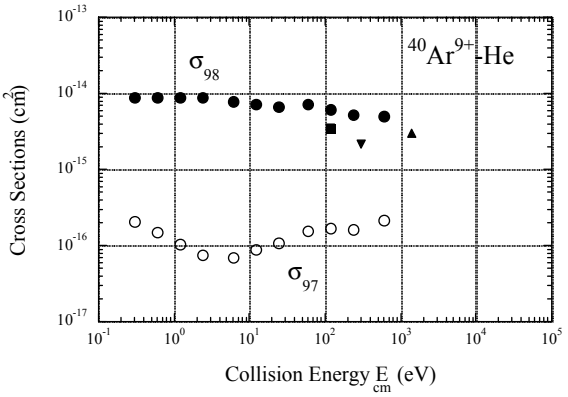

Energy			Cross sections ($\times10^{-16}$cm^2)	
E_{lab}/q (eV/q)	E_{cm} (eV)	E_{amu} (eV/amu)	σ_{87}	σ_{86}
0.50	0.30	0.11	90.4	2.10
1.00	0.60	0.23	88.2	1.53
2.00	1.20	0.45	90.3	1.05
4.00	2.40	0.90	88.7	0.75
10.0	6.00	2.25	78.3	0.70
20.0	12.0	4.50	71.9	0.89
40.0	24.0	9.00	67.6	1.11
100	60.0	22.5	71.9	1.59
200	120	45.0	61.8	1.71
400	240	90.0	53.2	1.62
1000	600	225	50.7	2.19

C20-b. Graph and table of charge transfer cross sections of $^{40}Ar^{9+}$ in H_2

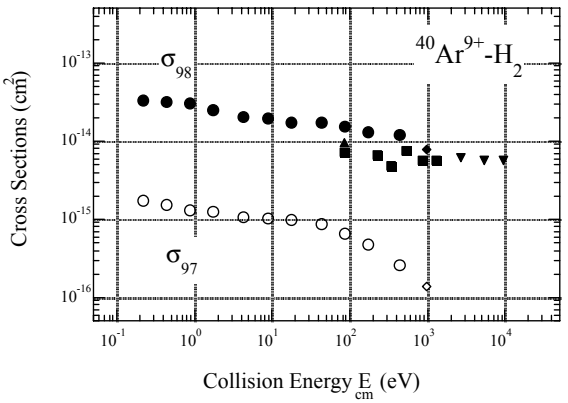

Energy			Cross sections ($\times10^{-16}$cm^2)	
E_{lab}/q (eV/q)	E_{cm} (eV)	E_{amu} (eV/amu)	σ_{87}	σ_{86}
0.50	0.214	0.113	336	17.7
1.00	0.429	0.225	316	15.3
2.00	0.857	0.450	307	13.4
4.00	1.71	0.900	254	12.8
10.0	4.29	2.25	209	10.7
20.0	8.57	4.50	195	10.3
40.0	17.1	9.00	176	9.81
100	42.9	22.5	173	8.70
200	85.7	45.0	158	6.63
400	171	90.0	134	4.81
1000	429	225	121	2.65

C21-a. Graph and table of charge transfer cross sections of $^{40}Ar^{11+}$ in He

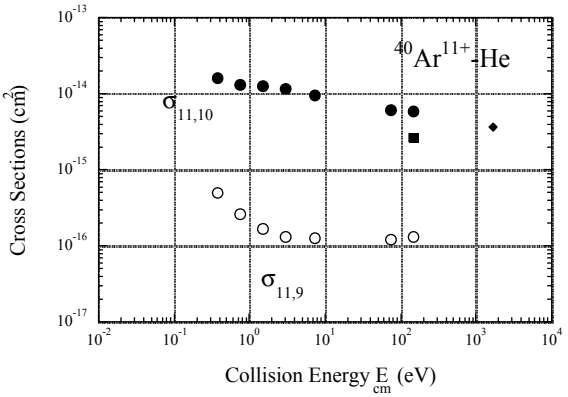

Energy			Cross sections ($\times 10^{-16}$cm^2)	
E_{lab}/q (eV/q)	E_{cm} (eV)	E_{amu} (eV/amu)	σ_{87}	σ_{86}
0.50	0.37	0.14	161	5.07
1.00	0.73	0.28	132	2.65
2.00	1.47	0.55	127	1.70
4.00	2.93	1.10	118	1.32
10.0	7.33	2.75	98.0	1.28
100	73.3	27.5	63.0	1.24
200	147	55.0	58.9	1.34

C21-b. Graph and table of charge transfer cross sections of $^{40}Ar^{11+}$ in H_2

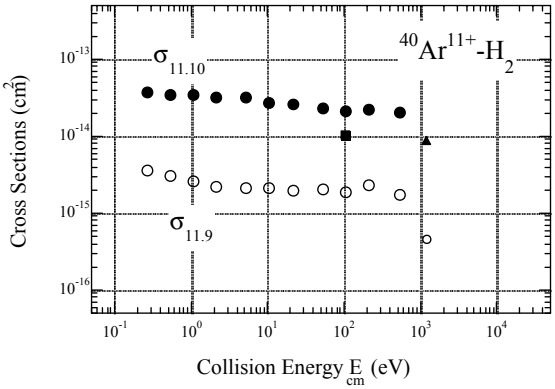

Energy			Cross sections ($\times 10^{-16}$cm^2)	
E_{lab}/q (eV/q)	E_{cm} (eV)	E_{amu} (eV/amu)	σ_{87}	σ_{86}
0.50	0.262	0.138	378	37.0
1.00	0.524	0.275	345	30.3
2.00	1.05	0.550	346	25.8
4.00	2.10	1.10	325	22.2
10.0	5.24	2.75	320	21.5
20.0	10.5	5.50	270	21.6
40.0	21.0	11.0	258	19.5
100	52.4	27.5	229	20.2
200	105	55.0	216	18.9
400	210	110	223	23.0
1000	524	275	205	17.7

C22-a. Graph and table of charge transfer cross sections of $^{127}I^{24+}$ in He

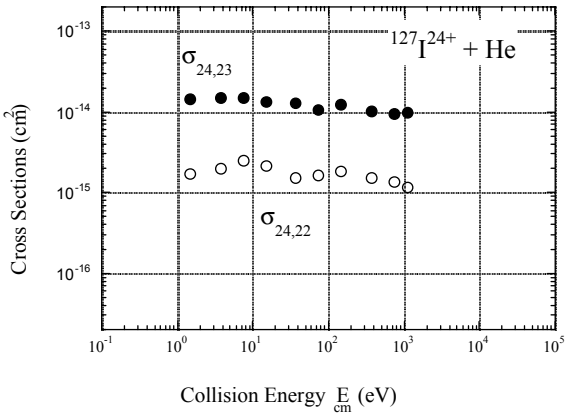

Energy			Cross sections ($\times 10^{-16}$cm^2)	
E_{lab}/q (eV/q)	E_{cm} (eV)	E_{amu} (eV/amu)	$\sigma_{24,23}$	$\sigma_{24,22}$
2.0	1.47	0.38	145	17.0
5.0	3.67	0.95	150	20.0
10.0	7.33	1.89	150	25.3
20.0	14.7	3.78	135	22.0
50.0	36.7	9.46	128	15.3
100	73.3	18.9	108	16.6
200	147	37.8	125	18.3
500	367	94.6	101	15.3
1000	733	189	95.5	13.7
1500	1100	284	100	11.9

C23-a. Graph and table of charge transfer cross sections of $^{127}I^{25+}$ in He

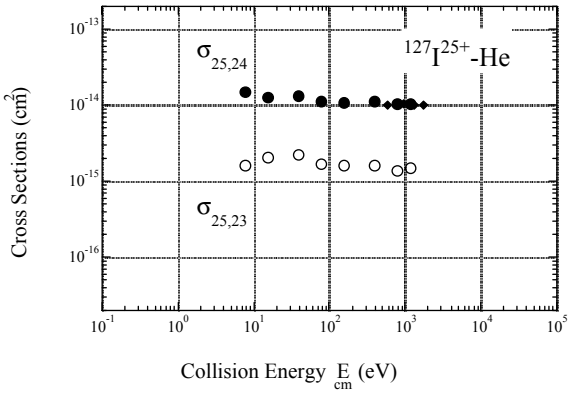

Energy			Cross sections ($\times 10^{-16}$cm^2)	
E_{lab}/q (eV/q)	E_{cm} (eV)	E_{amu} (eV/amu)	$\sigma_{25,24}$	$\sigma_{25,23}$
10.0	7.64	2.0	153	16.1
20.0	15.3	3.9	128	20.6
50.0	38.2	9.9	133	22.2
100	76.4	19.7	114	16.9
200	153	39.4	111	16.6
500	382	98.5	114	16.2
1000	764	197	107	13.7
1500	1144	295	105	15.4

C24-a. Graph and table of charge transfer cross sections of $^{127}I^{26+}$ in He

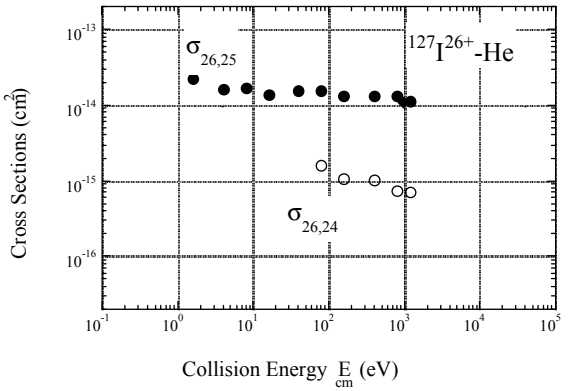

Energy			Cross sections ($\times 10^{-16}$cm^2)	
E_{lab}/q (eV/q)	E_{cm} (eV)	E_{amu} (eV/amu)	$\sigma_{26,25}$	$\sigma_{26,24}$
2.0	0.41	1.59	220	-
5.0	1.02	3.97	164	-
10.0	2.05	7.95	167	-
20.0	4.10	15.9	140	-
50	10.2	39.7	155	-
100	20.5	79.5	159	15.8
200	41.0	159	134	10.7
500	102	397	133	10.4
1000	205	795	135	7.44
1500	307	1192	110	7.20

ACKNOWLEDGEMENTS

The author wishes to express his thanks to Emeritus Professor Yozaburo Kaneko and Professor Nobuo Kobayashi for their ceaseless encouragement. It is also a pleasure to thank all colleagues for their helpful contributions to this subject over many years. This work was partially supported by a Grant-in-Aid for Scientific Research from the Ministry of Education, Science and Culture of Japan.

REFERENCES

[1] K. Okuno, J. Phys. Soc. Jpn., **55**, 1504-1515 (1986).
[2] K. Okuno and Y. Kaneko, Mass Spectrom. Jpn., **34**, 351(1986).
[3] K. Okuno, AIP Conf. Proc. **188**, 33 (1988); Jpn. J. Appl. Phys., **28**, 1124 (1989).
[4] K. Okuno, K. Soejima and Y. Kaneko, Nucl. Instr. Meth. Phys. Res., **B53**, 387 (1991).

[5] G. Gioumousis and D. P. Stevenson, J. Chem.. Phys., **29**, 294 (1958).
[6] K. Okuno, K. Soejima and N. Kaneko, J. Phys. B: At. Mol. Opt. Phys., **25**, L105 (1992).
[7] K. Ishii, K. Okuno and N. Kobayashi, Physica Scripta, **T80**, 176 (1999).
[8] K. Soejima, K. Okuno and N. Kaneko, Org. Mass Spectrometry, **28**, 344 (1993).
[9] K. Soejima, C. J. Latimer, K. Okuno, N. Kobayashi and Y. Kaneko, J. Phys. B: At. Mol. Opt. Phys., **25**, 3009 (1992).
[10] S. Kravis, H. Saitoh, K. Okuno, K. Soejima, M. Kimura, I. Shimamura, Y. Awaya, Y. Kaneko, M. Oura, and N. Shimakura, Phys. Rev., **A52**, 1206 (1995).
[11] K. Okuno, H. Saitoh, K. Soejima, S. Kravis and N. Kobayashi, AIP Conf. Proc., **360**, 867 (1995).
[12] K. Suzuki, K. Okuno and N. Kobayashi, Physica Scripta, **T73**, 172 (1997).
[13] K. Ishii T. Tanabe R. Lomsdze and K. Okuno, Physica Scripta, **T92**, 332 (2001).
[14] S. D. Kravis, D. A. Church, B. M. Johnson, M. Meron, K. W. Jones, J. C. Levin, I. A. Sellin, Y. Azuma, N. Berrah-Mansour, and H. G. Berry, Phys. Rev., **A45**, 6379 (1992).
[15] N. Shimakura and M. Kimura, Phys. Rev., **A44**, 1659 (1991); S. Suzuki, N. Shimakura and M. Kimura, J. Phys. B: At. Mol. Opt. Phys., **31**, 1741 (1998).
[16] P. Stancil, B. Zygelman, N. Clarke, and D. Cooper, J. Phys. B: At. Mol. Phys., **30**, 1013 (1997).
[17] K. Okuno, T. Kaneyasu, K. Ishii, M. Yoshino and N. Kobayashi, Physica Scripta, **T80**, 173 (1999); T. Kaneyasu, K. Matsuda, M. Ehrich, M. Yoshino and K. Okuno, Physica Scripta, **T92**, 341 (2001).
[18] F. W. Bliek, R. Hoekstra and R. Morgenstern, Phys. Rev. **A56**, 426 (1997).
[19] F. W. Bliek, G. R. Woestenek, R. Hoekstra and R. Morgenstern, Phys. Rev., **A57**, 221 (1998).

Contents of previous volumes of Atomic and Plasma–Material Interaction Data for Fusion

Volume 1 (1991)

Volume 2 (1992)

Volume 3 (1992)

Volume 4 (1993)

Volume 5 (1994)

Volume 6 (1995)

Volume 7/A (1998)

Volume 7/B (1998)

Volume 8 (2001)

Volume 9 (2001)